FINAL REPORT

Prediction Model for Impulsive Noise on Structures

SERDP Project WP-1398

Kenneth Plotkin
Yiriy A. Gurovich
Wyle

Louis Sutherland
LCS Acoustics

Vincent Chiarito
U. S. Army - ERDC

SERDP
DOD · EPA · DOE

Intentionally left blank

REPORT DOCUMENTATION PAGE

1. REPORT DATE *(DD-MM-YYYY)*	2. REPORT TYPE	3. DATES COVERED *(From - To)*
9-07-2012	Final Technical Report	March 2004 - March 2012

4. TITLE AND SUBTITLE	5a. CONTRACT NUMBER
Prediction Model for Impulsive Noise on Structures	W912HQ-04-C-0004; P00002

5b. GRANT NUMBER
N/A

5c. PROGRAM ELEMENT NUMBER
N/A

6. AUTHOR(S)
Plotkin, Kenneth J. - Wyle (Principal Investigator)
Yuriy A. Gurovich, Wyle
Louis C. Sutherland, LCS Acoustics
Vincent Chiarito, US Army ERDC

5d. PROJECT NUMBER
WP - 1398

5e. TASK NUMBER
T60092

5f. WORK UNIT NUMBER

7. PERFORMING ORGANIZATION NAME(S) AND ADDRESS(ES)
Wyle, Inc.
241 18th St. Suite 701
Arlington, VA 22202

8. PERFORMING ORGANIZATION REPORT NUMBER
WR 12-3

9. SPONSORING/MONITORING AGENCY NAME(S) AND ADDRESS(ES)
Strategic Environmental Research and Development Program
901 North Stuart Street
Suite 303
Arlington, VA 22203

10. SPONSOR/MONITOR'S ACRONYM(S)
N/A

11. SPONSOR/MONITOR'S REPORT NUMBER(S)
N/A

12. DISTRIBUTION/AVAILABILITY STATEMENT
Approved for Public Release; Distribution is Unlimited

13. SUPPLEMENTARY NOTES
N/A

14. ABSTRACT
A study of impulsive noise propagation and its effect on structures has been performed. Propagation and response measurement were conducted on eleven buildings at three military facilities. Sources included artillery and tank gun firing and explosive ordinance disposal. Propagation measurements demonstrated that the primary path is airborne, not groundborne. Frequency Response Functions were developed for the measured structures, and a general single degree of freedom model for structural velocity response was prepared. A model for Probability of Damage from impulsive noise sources was developed and is presented. That model addresses a wide range of structure types, and provides guidance for impulsive noise criteria in communities.

15. SUBJECT TERMS
impulsive noise, blast noise, structural response, structural damage, explosives, sonic boom, environmental noise

16. SECURITY CLASSIFICATION OF:			17. LIMITATION OF ABSTRACT	18. NUMBER OF PAGES	19a. NAME OF RESPONSIBLE PERSON
a. REPORT	b. ABSTRACT	c. THIS PAGE			Kenneth J. Plotkin
				212	19b. TELEPHONE NUMBER *(Include area code)* (703) 413 4700

Intentionally left blank

Table of Contents

Table of Contents - *continued*

Table of Contents - *continued*

List of Figures

Table of Contents - *continued*

List of Figures

Table of Contents - *continued*

List of Figures

Table of Contents - *continued*

List of Figures

Table of Contents - *concluded*

List of Figures

List of Tables

List of Acronyms

ANSI	American National Standards Institute
APG	Aberdeen Proving Ground
ASD	Auto-Spectral Density
BOM	Bureau of Mines
BRL	Ballistic Research Laboratory
CSD	Cross Spectral Density
DAF	Dynamic Amplification Factor
DoD	Department of Defense
ERDC	Engineer Research and Development Center
FFT	Fast Fourier Transform
FOS	Factor of Safety
FRF	Frequency Response Function
HVAC	Heating, Ventilation and Air Conditioning
IRIG	Inter-Range Instrumentation Group
MCAAP	McAlester Army Ammunition Plant
MIF	Mode Indicator Function
NAPS	Noise Assessment and Prediction System
ODS	Operating Deflection Shape
POD	Probability of Damage
RVSS	Residual Velocity Shock Spectrum
SDOF	Single Degree of Freedom
SERDP	Strategic Environmental Research and Development Program
SIPS	Sound Intensity Prediction System
TF	Transfer Function
TNT	Tri Nitro Toluene
UBC	Uniform Building Code

Intentionally left blank

Keywords

Impulsive noise
Blast noise
Structural response
Structural damage
Explosives
Sonic boom
Environmental noise

Intentionally left blank

Acknowledgements

Intentionally left blank

Abstract

The objective of this project was to develop relationships and models for the propagation of impulsive noise generated by military operations into communities such that the resultant vibration of and potential damage to structures can be assessed. Key elements of the objectives included establishing the importance of ground-borne propagation versus air-borne propagation, to identify or establish models to predict the waveforms that could impact a community, to predict the response of structures to impulsive noise, to collect response properties of a variety of buildings exposed to impulsive noise sources, and to establish the probability of damage of different structural types and materials.

The technical approach taken was a combination of analytical and field studies. The basic mechanisms of air-borne and ground-borne propagation were reviewed. Existing air-borne propagation models BNOISE and SIPS were identified. An approach to assessing ground versus air propagation paths, based on the relative timing of primary and secondary ground motion relative to air wave timing, was identified. A single degree of freedom model for structural response was prepared, and the key elements of a probability of damage model outlined. Propagation and response measurements were conducted on eleven buildings at three military facilities. Sources included artillery and tank gun firing and explosive ordinance disposal. Propagation data collected consisted of pressure wave measurements at heights of 4, 20 and 40 feet above the ground, and motion of the ground. These measurements were made near each structure and at several intermediate points between the source and the structure. Vibration was recorded on key elements - walls, windows and window frames - of all eleven structures. Modal analysis measurements were made on a selected subset of the buildings.

Results of the field measurements included demonstration that propagation was dominated by airborne mechanisms (even for the shallow buried ordnance disposal sources) and a database of structural response data. Structural response measurements were processed into frequency response functions and resonant frequencies identified. These are key elements in the single degree of freedom structural response model. The response model extended to multimodal for damage assessment, where the additional detail was necessary for the estimation of peak stress. A Probability Of Damage (POD) model was prepared, including data for a wide range of structural element types. The POD model has two parts: prediction of the incident wave and its statistics, and prediction of the resultant probability of damage. If the incident wave and its statistics are known (e.g., from SIPS or BNOISE) then that becomes the input to the structural part. If the incident wave is not known, then a source model based on distance and equivalent TNT weight is used.

The benefit of this research is quantification of the response of structures to military impulsive noise. An understanding of propagation mechanisms and structural response is presented. The models developed permit planners and range managers to perform risk analysis of proposed activities and provide guidance for impulsive noise criteria in communities.

Intentionally left blank

1.0 Objectives

The objective of this research project, WP-1398, addresses the Statement of Need CPSON-04-03 "Characterization and Prediction of Potential Impact of Military Generated Noise On Structures," by developing models for military impulsive noise that accurately characterizes the noise propagation from these classes of noise sources and assesses resulting vibration of and probable damage to building components.

The specific goals of the current effort are as follows:

1. To develop relationships for the response of structures to the impulsive waveforms generated by military operations, and select appropriate metrics for describing the effects of the waveforms on structures.

2. To establish the probability of damage of different structural types and materials as a function of the wave characteristics for each source.

3. To establish the importance of ground-borne transmission in the propagation of impulsive noise.

4. To prepare models to predict the response of structures to impulsive noise

5. To develop updated guidelines for assessing damage to structures.

Development of this noise predictive model is necessary for noise management on DoD ranges. Specifically, this model helps to enable unrestricted training while minimizing noise impacts on community health and welfare. This model is structured to provide fast, accurate, and economical processing by interfacing with and leveraging emerging and existing computer noise models.

Routine testing and training range operations can generate complaints and damage claims from civilian communities around DoD installations. These claims can result in testing and training restrictions and expenditure of funds for damage. This new noise prediction model for military impulsive noise fills a deficiency in current noise modeling capabilities. This new capability can be used in the management of noise at DoD ranges and installations to document potential impacts that may influence testing and training. This management tool can assist in the assessment of noise levels from day-to-day operations, the development of mitigation measures and in support of NEPA documentation.

Intentionally left blank

2.0 Background

2.1   Introduction

Military training exercises involving artillery, tanks, small arms, and helicopters inevitably generate impulsive noise from weapon firings and explosions during their operation. These impulsive noises can generate transient loads on surrounding structures, which result in vibrations felt by its occupants. The same is true of supersonic aircraft operations and explosive ordnance demolition programs. It has been claimed that such activities have resulted in actual structural damage, such as window breakage, cracked plaster, etc. DoD has developed models to predict the level of impulsive sound from blast operations (BNOISE), and has established guidelines for the maximum allowable levels to minimize structural damage.

Experience indicates that the current assessment guidelines used by the U.S. Army for blast damage are overly conservative for long-range propagation. In contrast, an in-house analysis conducted by Wyle to study window failures in an apartment complex as a result of an accidental explosion in the adjacent Wyle facility showed quite clearly that the existing DoD "quantity-distance" guidelines for storage of explosives were not accurate for close-range sites and substantially underestimated the risk of window damage. Clearly, it is necessary to develop updated guidelines that are based on current knowledge of blast waveforms and the probability of damage.

To accomplish this with the goals identified in Section 1.0, the following tasks and subtasks were conducted:

- Source/Propagation modeling

- Review airborne propagation mechanisms
    − Review groundborne propagation mechanisms
    − Conduct field measurements of propagation and structural response

- Assess structural response and potential damage
    − Formulate damage model
    − Develop structural transfer functions
    − Develop damage probabilities

- Prepare guidelines

Section 4.0 contains a model for the velocity response of structures to blast noise, and a Probability of Damage model which establishes damage risk. These models, together with recommended blast noise prediction models, provide tools and guidelines suitable for use by range managers and environmental planners.

The following subsection reviews the noise propagation mechanisms from impulsive military sources under consideration.

2.2 Propagation Review

There are two potential propagation paths from an impulsive noise source into the community. One is direct airborne propagation. The other is seismic propagation through the ground. These are illustrated in Figure 2-1. Physically, airborne propagation is direct and appears obvious, while groundborne propagation is somewhat indirect: the sound must enter the ground at the source and exit it at the receiver. In practice, the dominant mechanism is airborne[1,2]. Because impulsive noise effects are predominantly low frequency, however, and are felt rather than heard, there is a common perception that propagation is through the ground. This study has therefore addressed both paths. Emphasis is on quantifying airborne propagation, and addressing groundborne propagation to a degree adequate to ensure that it is not ignored in the event that may be a significant mechanism in a particular case.
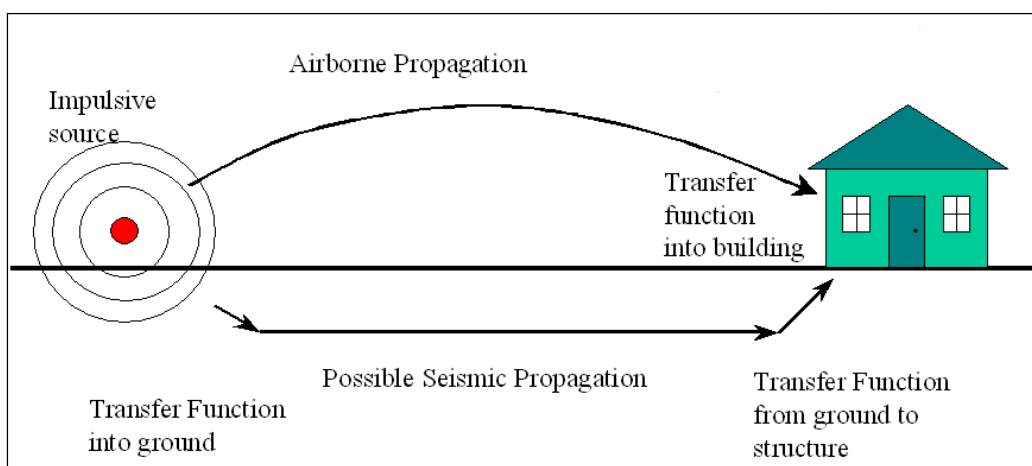
Figure 2-1. Airborne and Groundborne Propagation from Source to Receiver

2.2.1 Airborne Propagation

Figure 2-2 is a sketch showing the key phenomena involved in outdoor propagation of sound, from a ray acoustics perspective. Sound propagates outward from the source, spreading spherically. Sound decays from atmospheric absorption, which tends to be controlled by temperature and humidity. If there are wind and/or temperature gradients, the rays curve. There is a change in amplitude associated with ray tube area changes. Rays will intercept the ground. Reflection from the ground, and the interaction between direct and reflected rays, introduces a complex ground effect. Over soft ground this is generally an attenuation. Upwind, shadow zones can form, while downwind there can be multiple paths to a given receiver location. Turbulence introduces variability to the propagation. Turbulence and diffraction cause the geometric shadow on the upwind side to fill in. Terrain (not shown in the sketch) introduces the possibility of shielding, which carries with it additional diffraction effects. Terrain also alters the geometry of the intersection of sound rays with the ground. Embleton[3] gives a very good description of the effects sketched in Figure 2-2.
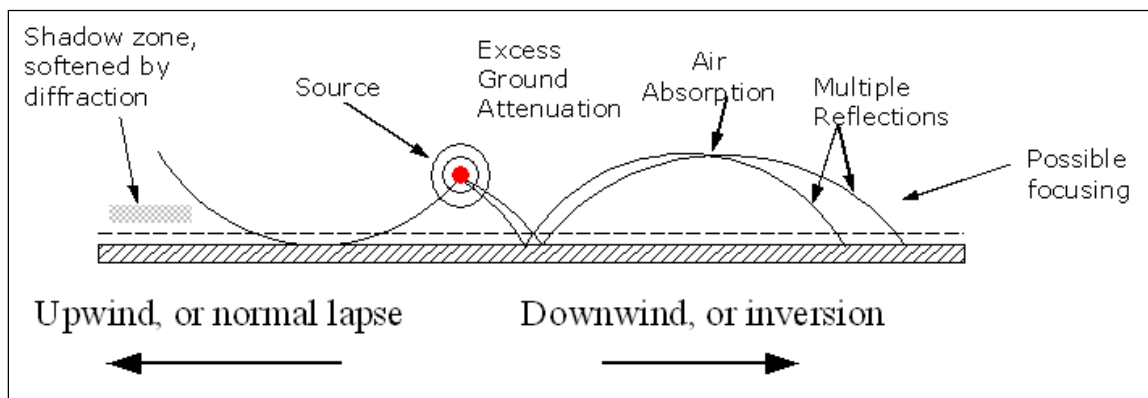
Figure 2-2. Sound Propagation in the Atmosphere, with Wind

2.2.1.1 BNOISE2

The standard model for predicting impulsive noise from weapon fire is BNOISE2.[4] BNOISE2 contains a database of weapon sources and propagation effects. Propagation is computed using Fast Field Program[5] (FFP) and Parabolic Equation[6] (PE) methods. Local terrain can be taken into effect.

The FFP and PE methods employed in BNOISE2 are more sophisticated than ray tracing. They are numeric solutions of the wave equation. There are two drawbacks to the use of these improved methods. The first is that they require more computational time than ray tracing. With current computer capabilities, that limits their use for real time analysis, such as daily range planning using pre-shot weather data. The propagation libraries in BNOISE2 are based on multiple runs using historic data, and provide probability distributions that are used for planning and risk assessment. The second is that they are implicitly linear acoustic methods that operate in the frequency domain. Impulsive noise is high amplitude, and tends to exhibit nonlinear propagation effects. Nonlinear propagation can be directly incorporated in ray tracing programs, such as sonic boom models[7] that operate in the time domain. BNOISE2 accommodates nonlinearity by using effective spectra, based on dominant low frequency bands, in its source models. This method is successful for predicting aggregate metrics such as peak overpressure and sound exposure level. This method is also successful at predicting the levels of dominant frequency components, but would be expected to be less accurate for complete spectra and waveforms.

2.2.1.2 SIPS

Sound Intensity Prediction System[8] (SIPS) and Noise Assessment and Prediction System[9] (NAPS) are two ray tracing models that are successfully used for real time range operation planning. SIPS begins with the following relation for blast wave overpressure, in units of pounds per square inch (psi), in a uniform atmosphere at sea level:

$$P = 226.62 \left[\frac{W^{1/3}}{R} \right]^{1.407} \tag{2.1}$$

where W is the TNT-equivalent charge weight in pounds and R is the radius in feet. Expressed as a sound level re 20 µPa, this is

$$L_{pk} = 20 \log_{10} \left(\frac{226.62 W^{.47}}{R^{1.41}} \right) + 170.75 \tag{2.2}$$

Equation 2.2 is one of a number of experimental blast curves reviewed in Reference 10, and is called the BRL model, named after the Ballistic Research Laboratory. A number of such fits are available (see also Reference 11), and they are generally similar. These fits generally originate from Brode's numerical study, which developed the parameter scaled distance:

$$Z = \frac{R}{W^{1/3}} \tag{2.3}$$

Note that Equations 2.1 and 2.2 contain a factor of $Z^{1.41}$. Equations 2.1 and 2.2 provide only the peak pressure. The complete waveform for a blast is modeled as

$$P(t) = P_{max} \left(1 - \frac{t}{T_s} \right) e^{-\frac{bt}{T_s}} \tag{2.4}$$

where P_{max} corresponds to P in Equation 2.1, T_s is the positive phase duration, and b is a wave amplitude decay factor. Figure 2-3 illustrates Equation 2.4. T_s, b and the ratio of P_{max} to P_{min} correlate with Z. Reference 13 shows typical relations of these parameters with Z and with each other. For artillery, which has horizontal directivity characteristics, that directivity may be applied to the source.
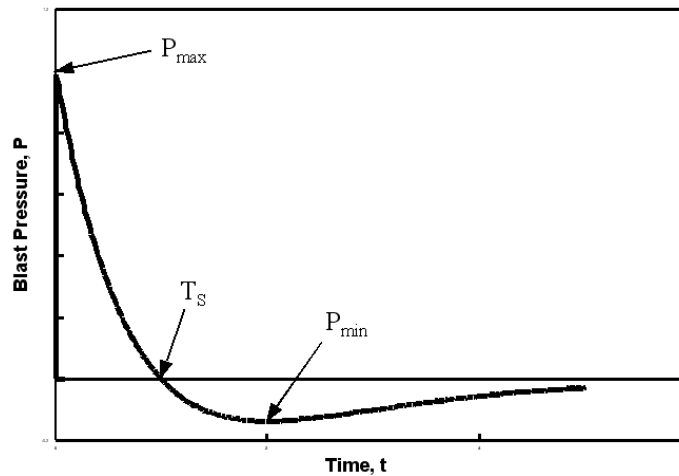
Figure 2-3. Blast Wave Shape

Equations 2.1 and 2.2 apply directly to propagation in a uniform atmosphere, with spherical spreading. SIPS accounts for atmospheric gradients with a simplified version of ray tracing. Acoustic ray tracing in a moving medium[14] is implicitly three dimensional because rays are convected by the wind vector. Winds in the atmosphere are, however, predominantly horizontal and the propagation direction of interest for environmental analysis of blast waves is generally near-horizontal. In that case, it is reasonable to represent the combination of sound speed and wind gradients by an effective sound speed profile that consists of the actual sound speed plus the component of the wind vector in the direction of propagation. A different effective profile is needed for each direction, but in a given direction propagation becomes two dimensional and is much easier to analyze than full three dimensional propagation. SIPS uses a single original vector atmospheric profile, but can base that profile on the average of several soundings within a study area.

SIPS traces rays using Snell's law.[15] The calculation is further simplified by modeling each layer of the atmosphere with a linear effective sound speed profile. Ray paths within each layer are arcs of circles, and may be handled analytically rather than requiring numeric integration. SIPS computes, for an initial ray elevation angle, the distance at which the ray intercepts the ground. SIPS also computes a ray tube area amplitude multiplication factor M_F that accounts for the refracted rays diverging differently than pure spherical spreading.

For propagation upwind or for normal temperature lapse, as sketched in the left part of Figure 2-2, shadow zones can form. While no rays penetrate a shadow zone, sound does enter from diffraction and turbulent scattering effects. SIPS does not estimate sound levels in shadow zones. Levels in shadow zones are generally up to 30 dB less than levels in adjacent non-shadow regions,[3] so those regions are not of particular interest for the current problem.

For propagation downwind or under inversion conditions, as sketched in the right part of Figure 2-2, there can be multiple paths to a given receptor. It is also possible for focus points to occur. SIPSs ray tracing accounts for both of these. At a focus, differentially separated rays cross, and the geometric amplitude is singular. The actual amplitude at a focus is limited by diffraction effects. SIPS limits its prediction of focus amplitude to M_F of 15 dB. Focus points are highlighted in SIPS output.

SIPS accounts for the presence of terrain. Ray paths are computed for the horizontally stratified atmosphere, as if the ground were flat, but the ground surface is represented by the actual terrain profile in the propagation direction. Ground intercept points are based on intersections of rays with the actual terrain. In the version of SIPS described in Reference 8, terrain profiles were manually prepared from USGS topographic maps. Plans were under way to automate the process, using available Digital Terrain Elevation Data.[16] That process is straightforward, and is easily adaptable to any available database. The Advanced Acoustic Model,[17] developed under SERDP Project WP-1304, performs such terrain cuts from a variety of elevation data sources.

In validation tests of SIPS at the Utah Test and Training Range,[18] levels were overpredicted by as much as 30 dB and underpredicted by as much as 10 dB. This is not a defect in SIPS. Large variability often occurs in propagation from identical charges under controlled conditions. This is typical for outdoor sound propagation near the ground, and is seen even at distances of two thousand feet[19]. SIPS provided reasonable predictions of average levels, with a tendency to overpredict. Overprediction provides a degree of conservatism. This was considered to be

beneficial in application at UTTR and Sierra Army Depot where community relations were significant, and it did not adversely affect the firing schedules.

2.2.1.3 NAPS

Noise Assessment and Prediction System[9] (NAPS) is a ray tracing program similar to SIPS. There are several differences:

- The source level model is similar to Equations 2.1 and 2.2, except that there is a factor of $Z^{-1.1}$ instead of $Z^{-1.41}$ and the leading constant is different.

- NAPS is employed in a system where profiles from 4DWX weather forecasts[20] are available on a 3.3 km grid. In the current version of NAPS, profiles are used in an ensemble mode. Rather than average profiles across the study area, as SIPS does when multiple soundings are available, NAPS ray tracing is performed for every profile. The results are treated as an ensemble, and the user is presented with a probability distribution of outcomes, rather than a single prediction.

- 4DWX is in place at six Army test ranges. NAPS is incorporated into 4DWX at Aberdeen Proving Ground, and contains facility-specific data.

Validation testing of NAPS single-event predictions[21] showed a range of underprediction of up to 20 dB and overprediction of up to 20 dB, with a mean underprediction of about 5 dB. The variation of levels is consistent with that observed for SIPS and other long range outdoor propagation studies.

The ensemble approach that NAPS uses for multiple atmospheric profiles is superior to the single profile method used by SIPS. The atmosphere is constantly changing, and the use of a single profile gives a snapshot that may not be valid even a few minutes later. The spread in measured levels of up to 30 dB[18, 21] is a consequence of this variability. An ensemble provides probabilities that a range operator can use in a risk assessment process.

2.2.1.4 General Considerations

The three models reviewed above - BNOISE2, SIPS and NAPS - are all successful at predicting average levels from ground and near-ground impulsive noise sources. BNOISE2 uses modern numeric propagation methods, but that limits propagation calculations to pre-set libraries. BNOISE2 does provide statistical distributions of expected levels, but for a general pre-computed ensemble rather than probabilities for particular days. The FFP and PE methods used in BNOISE2 operate in the frequency domain, so impulsive sources are represented by effective linear spectra that focus on their dominant low frequency content. This method provides the peak levels and CSEL that are required for noise analysis according to current criteria. It does not, however, address the spectral changes that occur from nonlinear stretching as the waves propagate.

SIPS and NAPS are more similar to each other than different. Both use ray tracing in a horizontally stratified atmosphere. They predict peak amplitude using empirical relations like Equation 2.2, adjusted for ray tube area. If more details of the predicted waves are needed, they can be obtained by using the empirical waveform given by Equation 2.4, or the waveform evolution can be computed within the ray tracing as is done in sonic boom analysis.[7] Because ray

tracing is faster than the numeric methods employed in BNOISE2, both SIPS and NAPS can be applied in real time. This improves range utilization, since potentially unacceptable events can be actively managed.

There is some potential to update the technology in SIPS and NAPS. Some of the ray tracing simplifications used when these programs were written in the 1990s are not needed for today's faster computers. Wyle's ORTHANC ray tracing model, used for analysis of airport noise[22], performs full three dimensional ray tracing fairly quickly - perhaps a minute or so to compute propagation from 30 source altitudes over a 10 km square study area. The basic technology in SIPS and NAPS, and the assumptions in their implementations are, however, quite adequate. The biggest practical differences in the two models are associated with their installations. NAPS is embedded in the 4DWX system at Aberdeen, and can make use of forecast weather profiles for ensemble predictions. For general use at non-test ranges, SIPS is designed as a portable system, and is preferred for that reason. Ensemble forecasting would depend on available weather data at a given location.

Overall, it was concluded for airborne propagation that the combination of BNOISE2 and SIPS is the best approach for range management purposes. Ensemble averaging, as done in the NAPS model, as well as incorporation of some elements of newer ray tracing/geometric theory of diffraction models may be also beneficial.

2.2.2   Groundborne Propagation

Figure 2-1 shows a potential groundborne propagation path: airborne sound near the source enters the ground near the source, then propagates through the ground to the receiver. For surface explosions, coupling to the ground is more direct. A deeply buried charge, such as used in mining operations, the charge would couple directly to the ground with no direct air coupling. Military impulsive noise sources are generally not buried. Most, such as artillery fire, are above the ground. Some, such as artillery impacts, are at the surface. Ordnance disposal charges are often thought of as buried. They are not, however, deeply buried the way mining charges would be. They are on the surface or in shallow pits with an overburden of dirt that serves to partly muffle the air blast. Reference 23 presents the results of a series of experiments testing the airborne noise reduction capability of various degrees of overburden, blast mats and foam. The possibility of burying explosive items is discussed, but significant operational and safety issues were identified.

Groundborne propagation is more complex than airborne because the ground, as a solid, can support both compressive and shear waves, while air can support only compressive waves. In general, there are four types of seismic waves:

- P - primary (compressional);
- S - secondary (shear);
- Love; and
- Rayleigh.

The first two are body waves, and propagate spherically from a disturbance such as an earthquake epicenter. The compressional P wave is called primary because it propagates fastest.

S waves are secondary, so denoted because they propagate slower. The last two are surface waves, induced by interaction of the P and S waves. Love waves are transverse shear waves, while Rayleigh waves are a combination of horizontal compressive wave and vertical shear. Rayleigh waves have an elliptical rolling motion, and are generally the most destructive waves in an earthquake. Surface waves propagate cylindrically along the surface, and decay exponentially with depth. Rayleigh waves are the slowest of these four types, but still have a speed of 1000 to 5000 m/s, much faster than the speed of sound in air of about 340 m/s.

The bulk of literature on seismic propagation is directed at earthquakes (naturally!), long range detection of nuclear tests, and geological soundings as used for mineral exploration. Literature relevant to the current project is focused on battlefield acoustics, with the primary objective of detection of surface disturbances. Seismic disturbances generated by ground vehicles can be unambiguously detected at considerable distances,[24] and numeric modeling of the propagation of these disturbances is successful.[25] The Army's Acoustic Battlefield Aid model[26] (ABFA) originally developed for acoustic detection has been extended to include seismic detection.[27] The algorithms define targets for which only acoustic or seismic signatures are available, and those for which both are available. Seismic signatures are available only for ground vehicles. Incorporation of seismic detection improves the performance of the model, particularly at upwind positions where the acoustic signal is low. The seismic signals are, however, based on mechanisms that directly impact the ground, not ground penetration of aboveground acoustic signals.

The key to a seismic propagation mechanism is the coupling of the acoustic wave in a manner that can generate propagating surface waves. Local interaction of sound with the ground is an implicit part of the attenuation of sound by the ground. Traditionally, ground is considered to be semi-infinite and locally reacting[28,29], with its behavior depending on its porosity[30]. Introduction of elastic properties of the ground, and its layered nature[31,32], does not substantially affect the interaction of the ground with the acoustic wave and its consequent effect on sound attenuation. It does, however, provide the possibility of propagating seismic waves[33]. An experiment to test the coupling theory by modifying the surface layering[34] demonstrated the generation of seismic waves. The method of modifying the layering was to dig a square hole one or two meters across, of various depths, in desert soil and fill the hole with pumice. The pumice was about twice as porous and one-third as dense as the soil. The transfer function increased by an order of magnitude at some frequencies, consistent with the theory in Reference 33. Those frequencies, however, tended to correspond to the resonant frequencies of the rectangular hole. It is not clear how much the resonance enhanced the generation of the seismic waves.

There is a simple method to assess the significance of seismic propagation of an airborne sound. Propagation of Rayleigh waves, the most significant and slowest of the surface waves, is generally several times faster than the speed of sound in air. It is expected that there will be some ground motion at a receiver. Motion that occurs before the air wave arrives is seismic propagation, via the mechanism sketched in Figure 2-1. Motion that occurs at the same time as the air wave is just local reaction, and does not represent propagation of energy through the ground.

Albert and Orcutt[35] conducted experiments to test seismic coupling via this simple principle. Using pistol shots as an impulsive source, signals at distances from 1 to 274 meters were

measured with geophones and microphones. A seismic precursor was detected, but that was typically one to two orders of magnitude smaller than the local reaction when the air wave passed. The mechanism sketched in Figure 2-1 thus did exist, but was not significant. The decay of the air wave was consistent with theoretical calculations, further supporting the conclusion that the ground motion was local reaction to the passing sound wave.

The results obtained by Albert and Orcutt were also obtained in measurements of detonation noise at the Tooele Army Depot[36] and also in measurements conducted in the current project, as will be discussed in Section 3.0. These are consistent with the results noted earlier for References 1 and 2. These support the preponderance of literature that suggests the seismic propagation mechanism is generally not significant. The only place in the reviewed literature where seismic propagation exceeded airborne propagation was for upwind propagation in the ABFA sample calculation[26]. In that case, however, the seismic excitation was direct impact of a ground vehicle, not coupling of an acoustic wave.

Overall, it can be concluded that groundborne propagation is situation dependent. It can be significant if the blast energy is directed into the ground, as it is for mining operations. For air and surface sources of interest in this project, there is usually a combination of air and ground coupling, and the significance of ground propagation depends on that coupling. Prior studies for pistol shots and ordnance disposal detonation found that airborne propagation was dominant.

The same result – dominance of airborne propagation – was found in the field measurements conducted for the current project, as will be discussed in Section 4.0. Based on current results, as well as those in the literature, it has been concluded that seismic propagation mechanism sketched in Figure 2-1 is not significant, and it is not necessary to develop a user model for groundborne propagation.

Intentionally left blank

3.0   Materials and Methods

This project consists of two functional areas: (a) Field Measurements of Impulsive Noise Propagation and Structural Vibration Response and (b) Development of Structural Damage Prediction Models. These areas are contained within the first three technical objectives and are described below.

3.1   Field Measurements

3.1.1   Test Plan and Measurement Locations

A test plan for field measurements was prepared.[37] Measurements were conducted at:

- Aberdeen Proving Ground, MD, 4-10 November 2004. Impulsive sources were 105 mm and 120 mm tank guns.

- Fort Sill, OK, 2-4 and 9-10 August 2005. Impulsive sources were 105 mm Howitzers, plus a variety of unidentified large weapons.

- McAlester Army Ammunition Plant, OK, 8-13 August 2005. Impulsive sources were open pit ordnance disposal, with charges up to 200 pounds NEW.

Figure 3-1 illustrates the basic measurement arrangement. Several "propagation stacks" were deployed, each consisting of:

- 1/4 inch or 1/2 inch condenser microphones at heights of 4, 20 and 40 feet above the ground. These were on a single vertical pole.

- A triaxial geophone on the ground near the base of the microphone pole.

- Signal conditioning amplifiers for the transducers.

- At least three accelerometers were placed on the structure. Those were placed in the center of a window, on a window frame or muntin, and on the adjacent sill or framing member.

- Additional accelerometers (from five to eight) were placed in key locations on the building to monitor the vibration responses related to global building movements, primarily for conducting modal tests and also as auxiliary blast response sensors.

- A multi-channel digital recorder. A variety of DAT and direct-to-disk recorders was used. All were either 16 or 24 bit, and recorded lossless uncompressed data streams. Each recorder was operated continuously during periods of expected firing.

All recordings were synchronized with IRIG-B time codes, usually derived from GPS signals. Data time and field notes were maintained in UTC. The choice of 1/4 inch or 1/2 inch microphones was based on expected peak sound level, with 1/4 inch microphones used for higher levels. The placement of accelerometers on a structure depended on the details of the building. The objective was to measure response of the window glass (the most fragile structural element), the motion of the window structure other than glass, and the motion of the wall itself in

the vicinity of the window. For most measurements, all transducers described above were recorded on a common recorder. An exception was some sites at Aberdeen. Ground motion at some of those sites was measured with a Blastmate, which is a self-standing package consisting of a triaxial geophone, a microphone, and an internal digital recorder. Blastmate records only when triggered either by an acoustic or seismic signal. Data from these systems was synchronized with data on the main digital recorders by aligning the signal on its microphone with the 4-foot stack microphone.
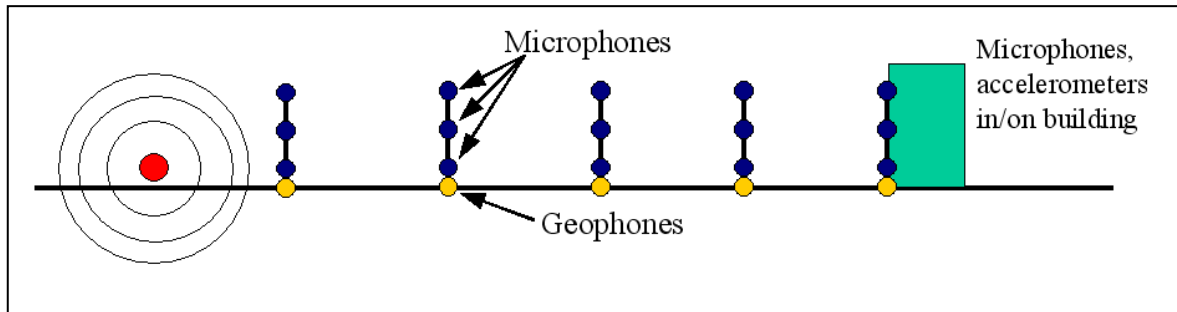
Figure 3-1. Schematic of Measurement Arrangement

Measurements at the three sites are described in Subsections 3.1.2 through 3.1.4. The analysis procedure, developed originally using Aberdeen data, is described in Subsection 4.1.2.

In addition to propagation and blast response measurements, ERDC conducted modal tests in most of the instrumented buildings. The modal tests are described in Subsection 4.6. In some cases, blast response data were collected using the modal analysis transducers.

Analysis results of the data collected in the field measurements for the three military bases are provided and discussed in Section 4.0.

3.1.2 Measurements at Aberdeen Proving Ground

The first set of field measurements were completed on 4-10 November 2004 at Aberdeen Proving Ground (APG). Events recorded were firings of 105 and 120 mm tank guns from Trench Warfare firing points. About 80 events were recorded. Measurement sites were:

      A. Reference position;
      B. Building 4031, a one-story frame structure;
      C. Building 2001, a two-story frame structure;
      D. Building 2006, a one-story brick façade frame house;
      E. Building 379, a two-story frame house; and
      F. Mitchell house site.

Figure 3-2 shows the locations of these sites.
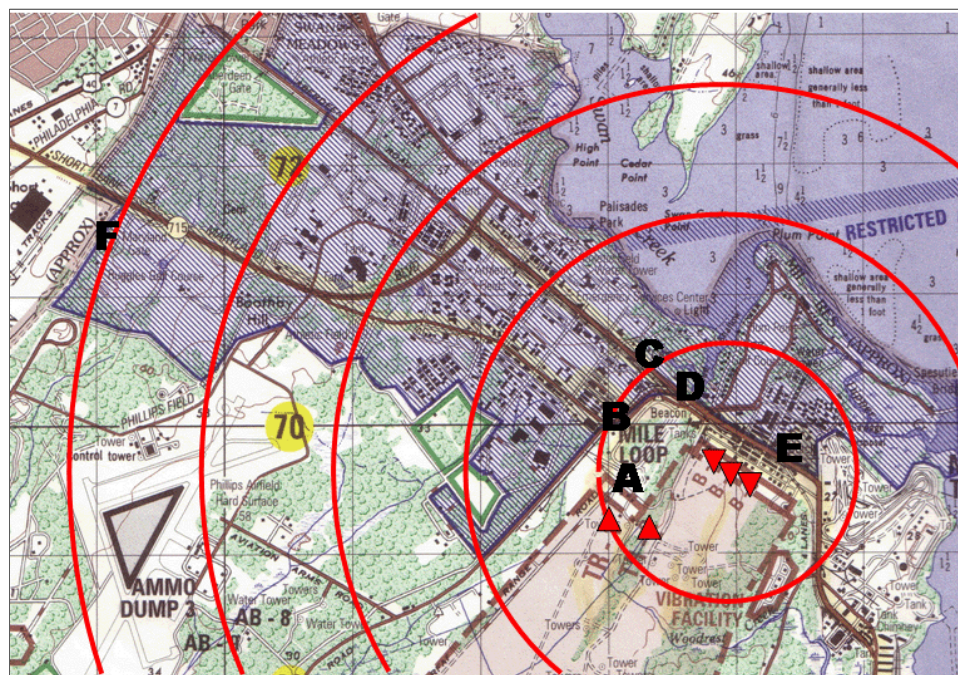
Figure 3-2. Firing Points and Measurement Sites at Aberdeen Proving Ground

(Triangles: Trench Warfare firing points. Inverted triangles: Main Front firing points.

1 km radii from Main Front indicated. High Velocity points around southern part of 1 km circle.
Firing direction is downrange, to the south and south-southwest.)

Site A was about 1 km from the firing points, and Site F about 5 km. The others were about 2 to 3 km from the firing points. Instrumentation at all sites included microphones at 4, 20 and 40 feet above the ground, and tri-axial geophones on the ground. The buildings at Sites B through E were instrumented with accelerometers on a wall, window frame and window glass facing the firing points. Buildings 2001 and 2006 at Sites C and D, respectively, were instrumented with additional building-specific accelerometers for modal testing. Those were also used for recording global building motion response to gun firing.

Data were recorded at Sites A, C and F on all measurement days. Recorders were moved among the other sites from day to day, typically two to three days at each. Recording systems consisted of a National Instruments PXI digital recording system at Site B and DAT recorders at the other sites. Those were operated continuously during measurement periods. Blastmate systems were also deployed at all sites, with geophones deployed at A and B.

The buildings at Sites C, D and E fronted on the north side of the road running from west northwest to east southeast, and were generally on the north side. The building at Site B was on the west side of the road running from southwest to northeast. In the description of orientation in the following photographs and floor plans, the side of each building facing its frontage road is denoted as being "south." That is the side that is generally toward the firing points.

Meteorological data, consisting of hourly atmospheric profiles from Aberdeen's 4DWX system, were obtained. The Aberdeen Noise Office provided the as-fired range schedules for the measurement periods.

Table 3-1 lists the as-fired schedule of tank guns. Rain on 4 November precluded data collection, and the firings on 6 November occurred during modal testing. Data were successfully collected for the entire tank gun firing periods on 9 and 10 November. All sites except D were instrumented for at least part of those two days. Good recordings were obtained for 65 105 mm and five 120 mm shots on those days.

Table 3-1. As-Fired Tank Gun Schedule, Aberdeen

Date	Time (EST)	Firing Point	Weapon	Number
4 Nov	0950-1250	High Velocity	120 mm	18
6 Nov	1316-1345	Trench Warfare	105 mm	8
9 Nov	0926-1026 1149-1219	Trench Warfare	105 mm	36
9 Nov	0934-1140	High Velocity	105 mm	3
9 Nov	1750-1821	Trench Warfare	120 mm	5
10 Nov	1000-1050 1302-1338	Trench Warfare	105 mm	36

3.1.2.1 APG Building 2001 (Site C)

Building 2001 is aligned such that the front faces nearly south and the longitudinal direction is almost aligned with the east-west line. This is a two-story wood frame structure with a concrete slab for the first floor. Conventional footings are assumed supporting the perimeter exterior walls. Only schematics of floor plans were made available. The building is 60 feet long by 30 feet wide and fairly symmetric in plan in both directions. This building could represent a very large two-story family residence or a wood framed office building in size and construction. Details of the actual foundation, framing design, and as-built dimensions were not available. On site measurements and observations were made as possible.

Figures 3-3 through 3-5 show views from the front, east and west sides, and rear of Building 2001, respectively.

Figure 3-3. APG Building 2001: View of the Front (south) Exterior (to the right is E)

Figure 3-4. APG Building 2001: View of the East (left) and West (right) Elevations

Figure 3-5. APG Building 2001: View of the Back (north) Exterior (to the right is W)

Figure 3-6 shows the microphone pole installed at this site. Figure 3-7 shows the wall microphone and accelerometer placement on one window. The first-floor leftmost window on the front façade (close to SW corner) of the building was instrumented to measure the window transient response to gun firing.

Figures 3-8 through 3-17 show the additional transducer locations applied primarily for modal testing of Building 2001 using a shaker or a hammer excitation, as well as for structural response to gun firing. Transducer set up details for the locations shown in Figures 3-8 through 3-17 are provided in Appendix B.

Figure 3-6. Microphone Pole and Blastmate at APG Site C, Building 2001

Figure 3-7. Transducers On and Around Window at APG Site C, Building 2001

APG Building 2001: ground floor elevation – sensor locations
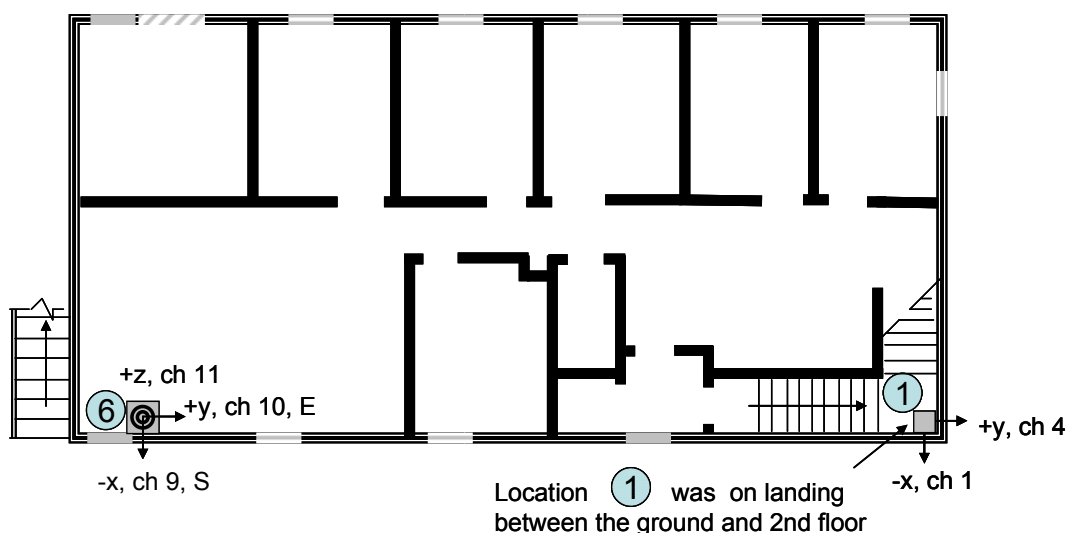
Figure 3-8. Plan Schematic Showing Numbered Locations and Orientations of Accelerometers for Ground Floor

APG Building 2001: 2nd floor elevation – sensor locations
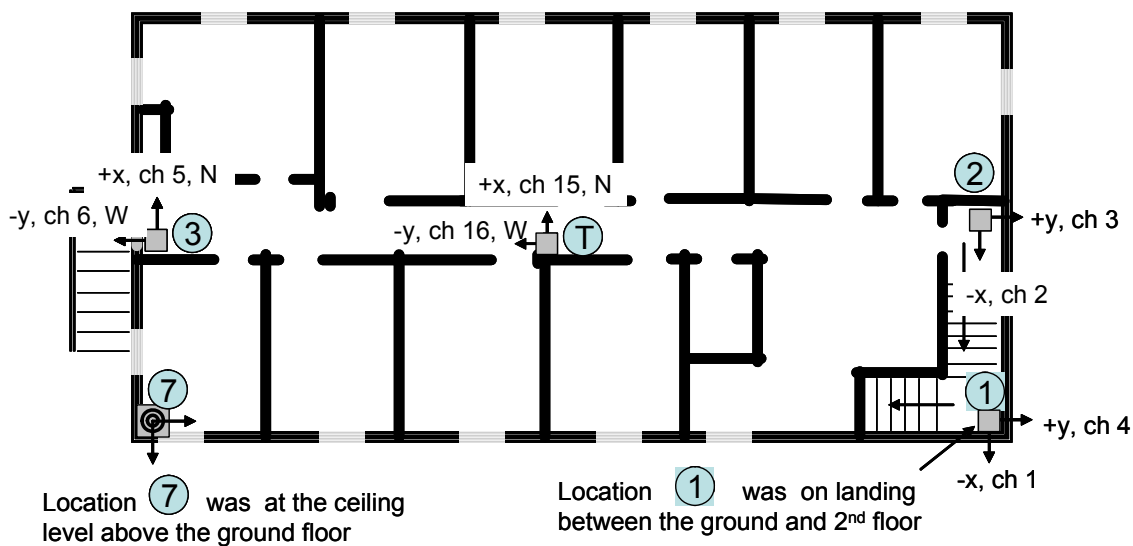
Figure 3-9. Plan Schematic Showing Numbered Locations and Orientations of Accelerometers for the Second Floor Level

APG Building 2001: ceiling elevation - sensor locations
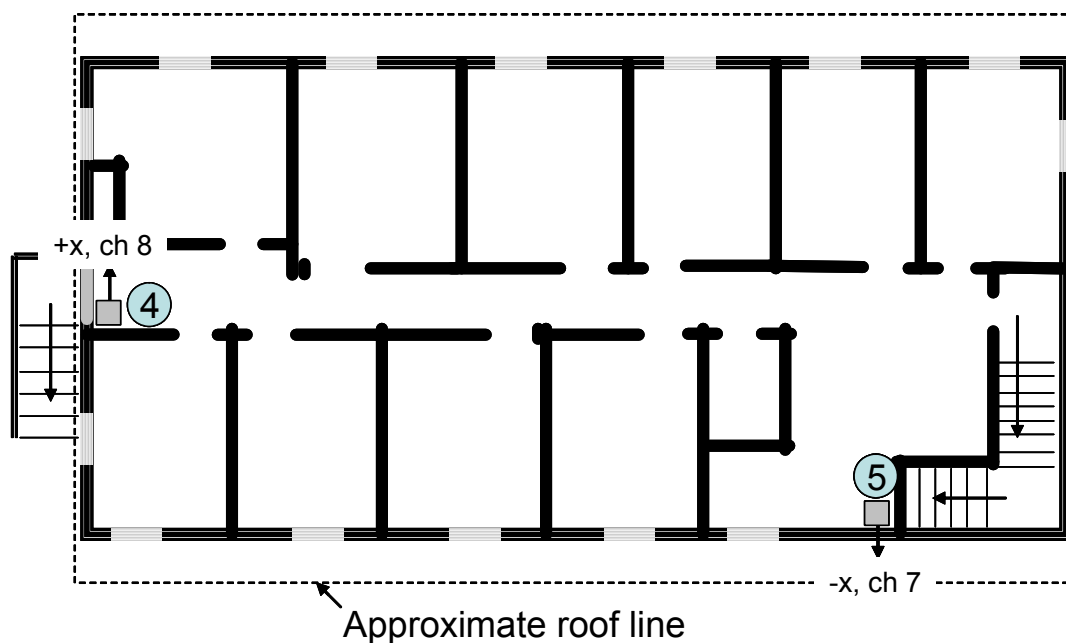
Figure 3-10. Plan Schematic Showing Numbered Locations and Orientations of Accelerometers for the Ceiling Level Above the Second Floor

APG Building 2001 Schematic of south elevation of sensor locations
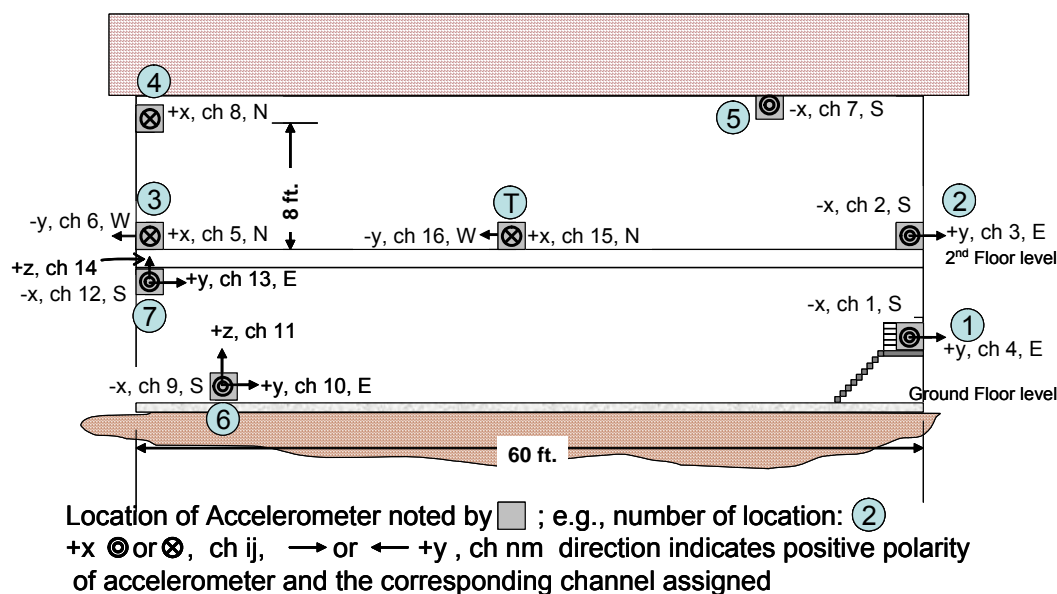
Figure 3-11. South Elevation Schematic Showing Numbered Locations and Orientations of Accelerometers

APG Building 2001Schematic of north elevation of sensor locations

Location of Accelerometer noted by ▢ ; e.g., number of location: ②
+x ◎ or ⊗, ch ij, ⟶ or ⟵ +y , ch nm direction indicates positive polarity
of accelerometer and the corresponding channel assigned
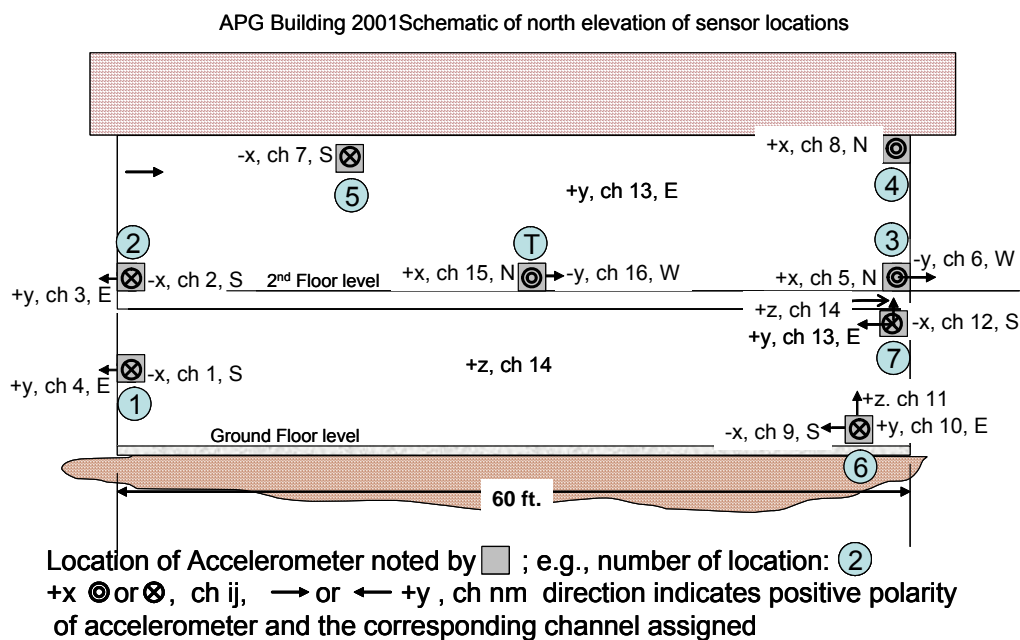
**Figure 3-12. North Elevation Schematic Showing Numbered Locations and
Orientations of Accelerometers**

APG Building 2001 Schematic of east and west elevation views of selected sensor locations

Location of Accelerometer noted by ▢ ; e.g., number of location: ②
+x ◎ or ⊗, ch ij, ⟶ or ⟵ +y , ch nm direction indicates positive polarity
of accelerometer and the corresponding channel assigned
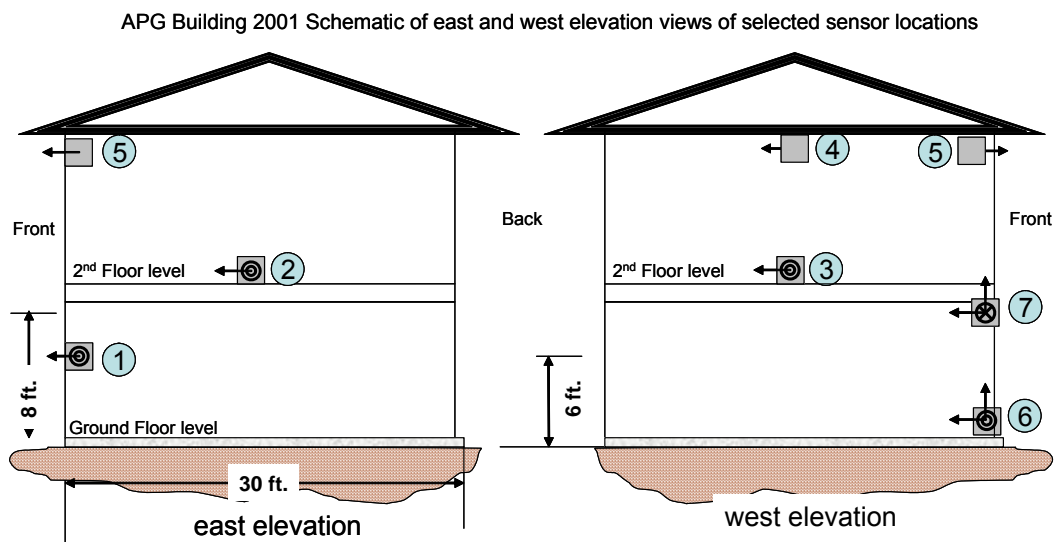
**Figure 3-13. End Elevation Schematics Showing Numbered Locations and
Orientations of Accelerometers**

APG Building 2001: 2nd floor elevation – shaker orientations
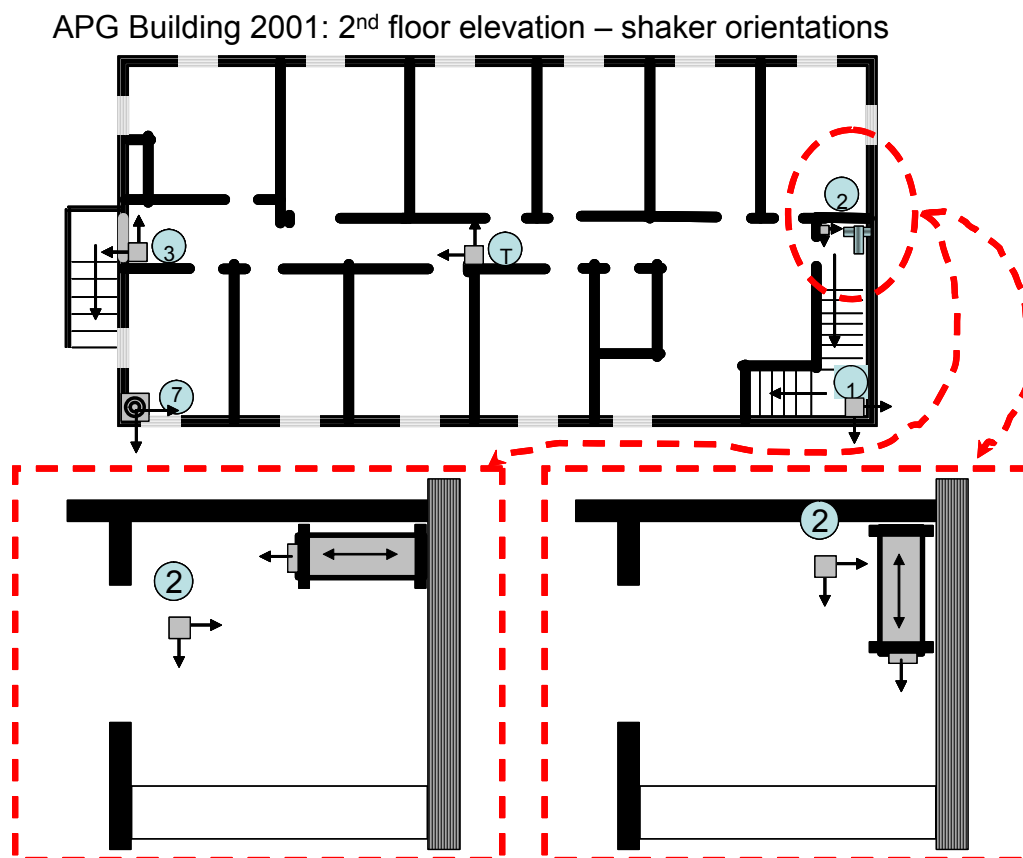
Figure 3-14. Plan Schematic Showing Shaker Locations on the Second Floor Level
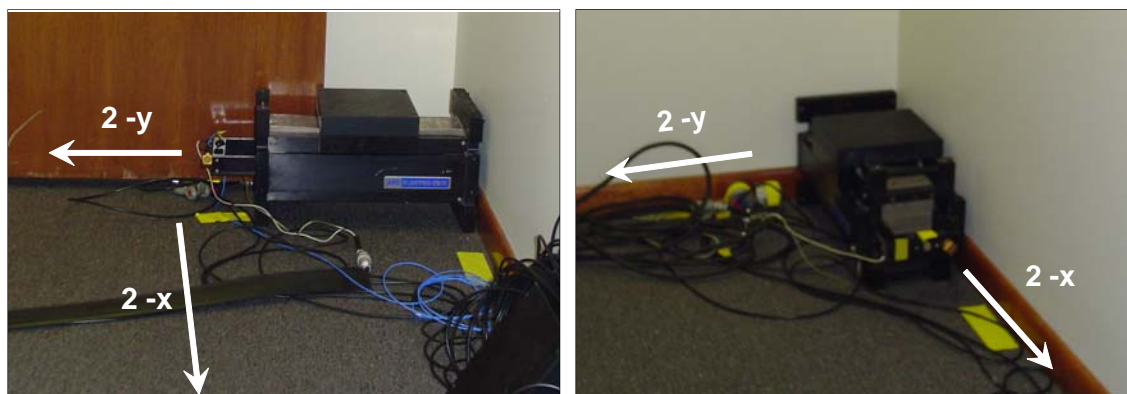
Figure 3-15. Views Showing the Shaker Positioned for the Two Orientations on the Second Floor Level
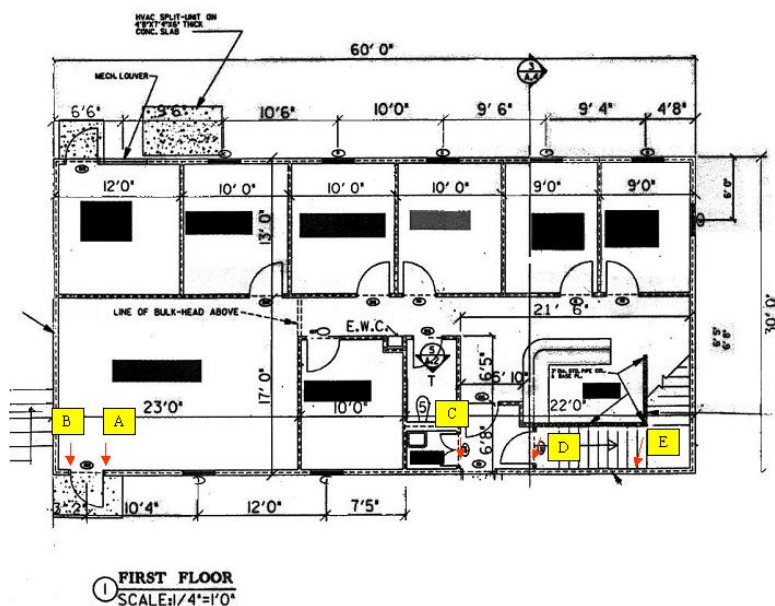
Figure 3-16. First Floor Plan – Excitation Locations A through E for Hammer Impacts
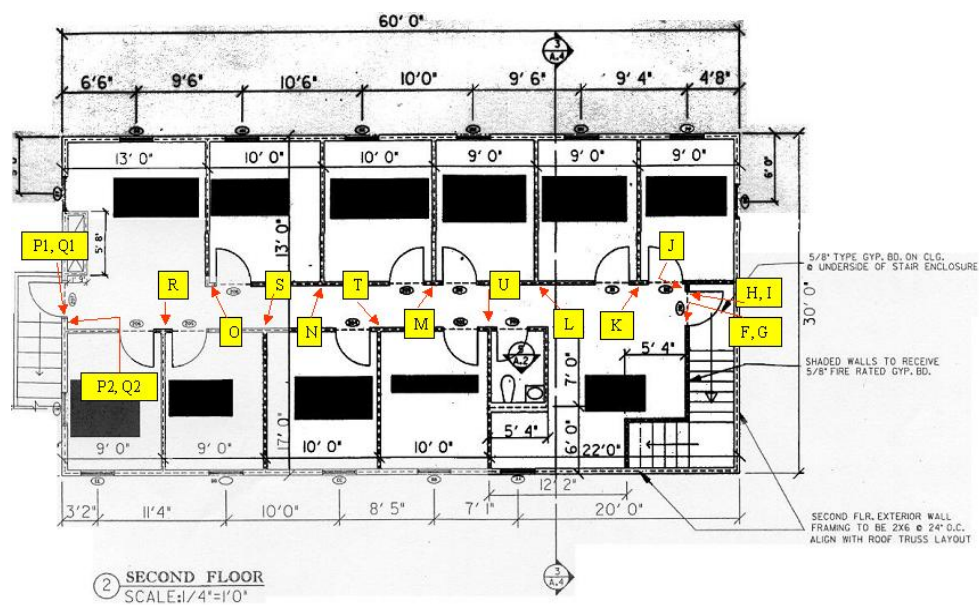
Figure 3-17. Second Floor Plan – Excitation Locations F through U for Hammer Impacts

3.1.2.2 APG Building 2006 (Site D)

Building 2006 is aligned similarly to Building 2001, such that the front faces nearly south and the longitudinal direction is almost aligned with the east-west line. Building 2006 is one-story wood frame structure with a conventional foundation (crawl space under the wood floor joist system) and conventional brick veneer on the front face. The other three sides have siding down to the level just above the crawl space. The building is approximately 88 feet long by 36 feet wide and fairly symmetric in plan in both directions. It appears to have a conventional foundation, with a crawl space. The grade level is slightly higher on the SE portion compared to the back and west sides. This building could represent a typical one-story family residence in size and construction. Details of the actual foundation, framing design, and as-built dimensions were not available. On site measurements and observations were made as possible.

Figures 3-18 through 3-21 show views from the front, rear, east side, and west side, respectively.

Figure 3-18. APG Building 2006: View of the Front (south) Exterior (to the right is E)

Figure 3-19. APG Building 2006: View of Back (north) Exterior (to the right is W)

Figure 3-20. APG Building 2006: Side View of the East Exterior (to the right is N)

Figure 3-21. APG Building 2006: Side View of the West Exterior (to the right is S)

The site was originally instrumented with the microphone pole and window accelerometers, but inclement weather precluded the noise propagation and transient response data collection from tank gun firing. Building 2006 was used primarily for modal testing to monitor global structural movements during the electro-dynamic shaker and impact hammer excitations.

For this purpose, accelerometers were placed nearest to the load transfer connections or joints. Examples of load transferring connections are where the rafters tie in to the top plate of an exterior framed wall, in corners of the building at or above the ceiling height (while still close to or mounted directly on structural framing members). In a one-story structure such as Building 2006, typically all sensors are placed near or at the level of top of the framing wall.

Accelerometers were mounted at five main locations numbered 1 through 5 in Figures 3-22 through 3-24, which present schematics of the main measurement locations. Transducer set up details for the locations shown in Figures 3-22 through 3-24 are provided in Appendix B.

APG Building 2006
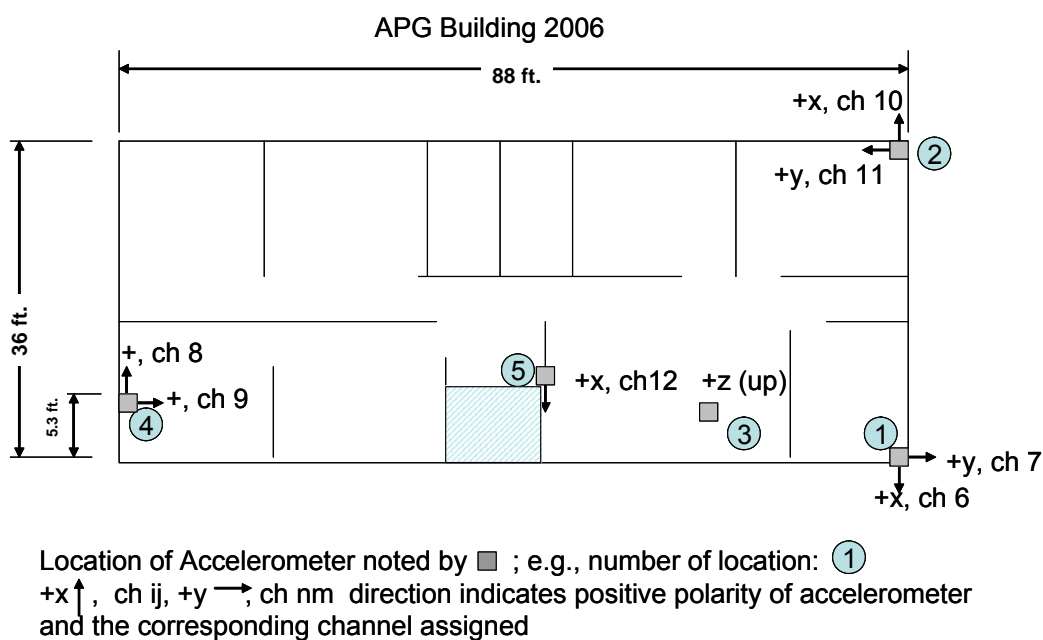
Figure 3-22. Plan Schematic Showing Numbered Locations and Orientations of Accelerometers

APG Building 2006
Schematic of front elevation: sensor locations
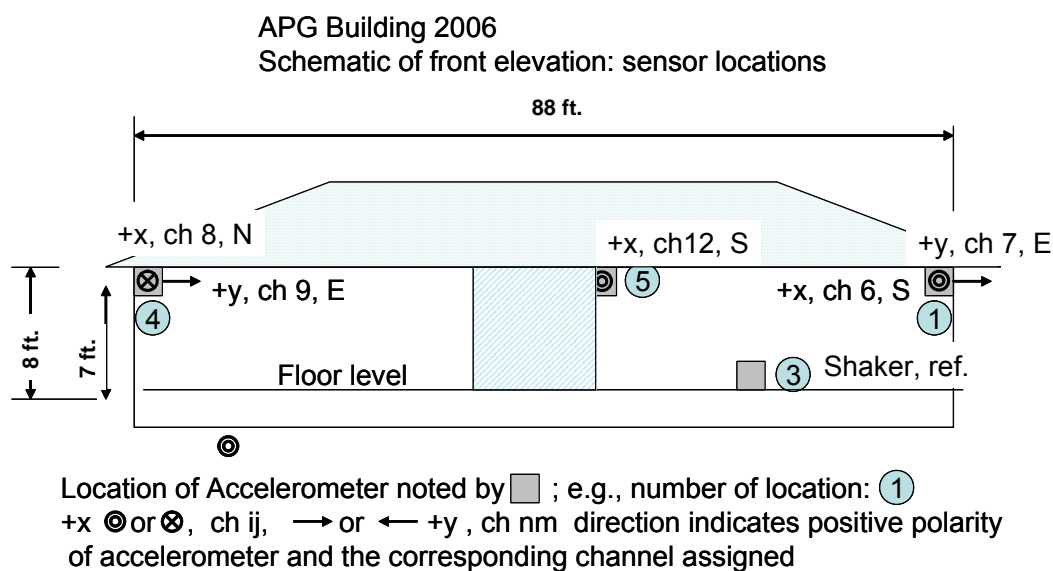
Figure 3-23. Front Elevation Schematic Showing Numbered Locations and Orientations of Accelerometers

APG Building 2006
Schematic of south elevation of sensor locations
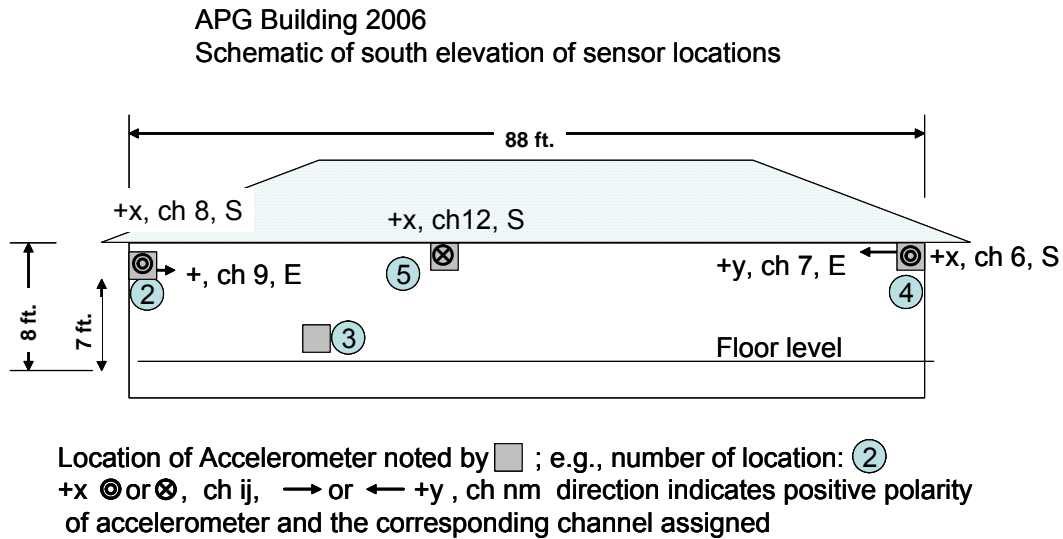
Figure 3-24. Rear Elevation Schematic Showing Numbered Locations and Orientations of Accelerometers

Figures 3-25 through 3-29 depict the accelerometer locations in Building 2006.

Figure 3-25. APG Building 2006: Horizontal Biaxial Accelerometer at Location 1; Interior SE Corner Above the Drop Panels of the Ceiling (to right is S)

Figure 3-26. APG Building 2006: Horizontal Biaxial Accelerometer for Location 2, NE Corner (to right is S)

Figure 3-27. APG Building 2006: View Down the Interior Hall (toward west end)

.
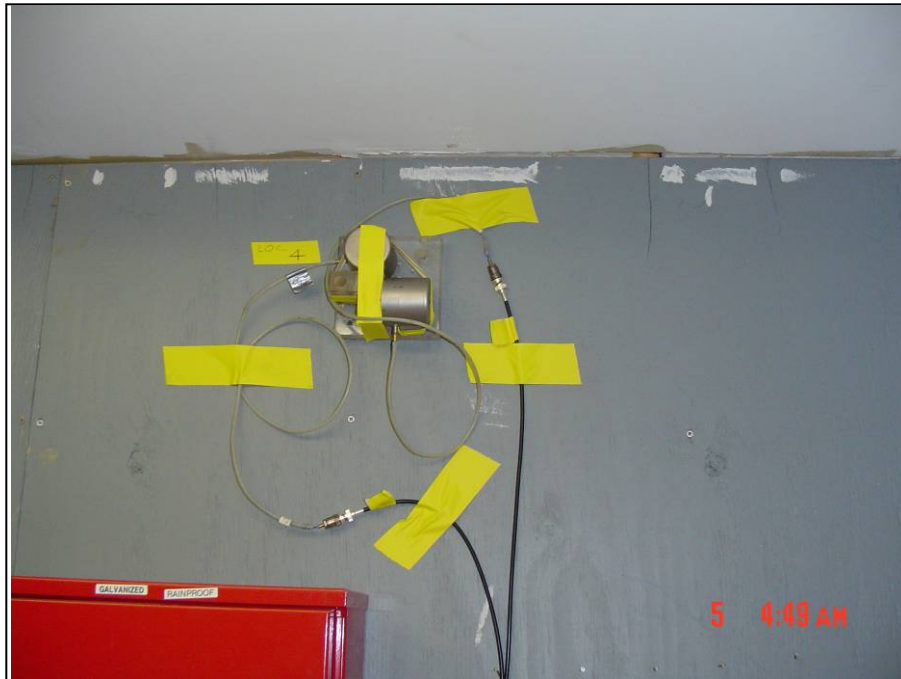
**Figure 3-28. APG Building 2006: Horizontal Biaxial Accelerometer for Location 4,
S of Middle of W Wall (to right is N)**

**Figure 3-29. APG Building 2006: Horizontal Uniaxial Accelerometer Array for Location 5,
E of S Front Door Entrance (to right is S)**

Figures 3-30 and 3-31 show the vertical and horizontal shaker setups, respectively, for the stationary force excitation testing of Building 2006.

**Figure 3-30. APG Building 2006: Vertical Shaker Setup at Location 3 (floor level)
Near the Interior Front Wall, in the East Half (to right is S)**

**Figure 3-31. APG Building 2006: View of the Horizontal Shaker Setup at
Location 3 (floor level) Near the Interior Front Wall, in the East Half (to right is S)**
(*The shaker is aligned to the east-west direction*)

Figure 3-32 indicates locations for the impact hammer tests conducted at Building 2006, and Figures 3-33 through 3-36 illustrate the performance of these tests.
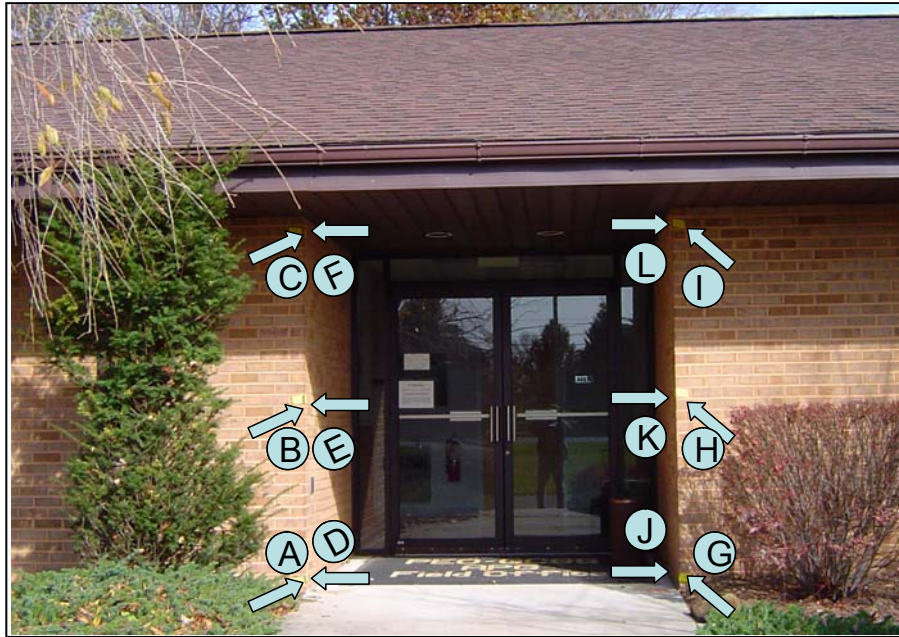
Figure 3-32. APG Building 2006: Close Up View of Front Door Entrance (to right is S)
Where Impact Hammer Tests were Conducted
(_Block Arrows Indicate the Horizontal Directions for Six Impact Locations._
The hammer impacts were applied in two horizontal orientations at each location.**)**
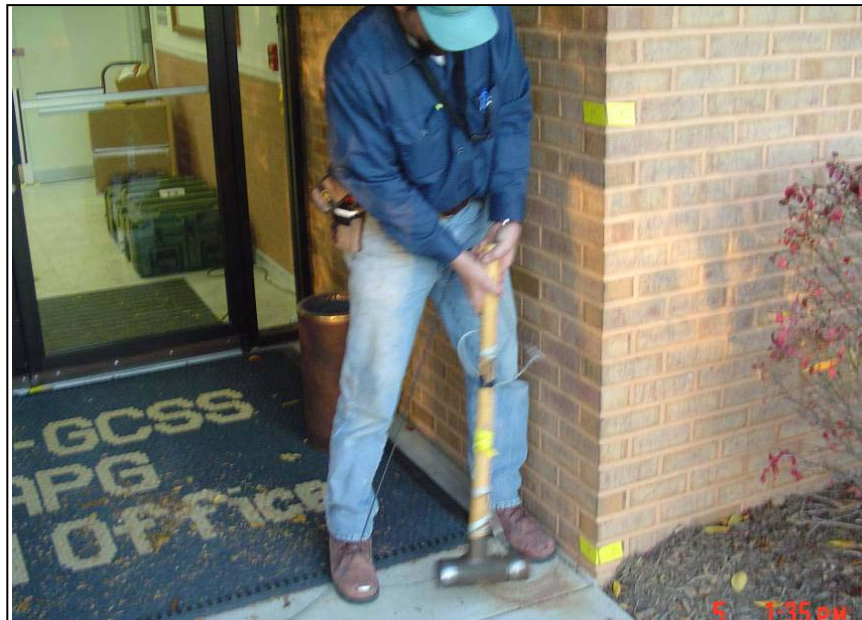
Figure 3-33. APG Building 2006: Close Up View of Front Door Entrance (to right is S)
(This shows an example of the application of the impact hammer to provide measurable transient force inputs while simultaneously measuring acceleration responses) - The hammer in this view is drawn back in preparation to impact the brick veneer wall near the bottom) (Location J in Figure 3-32)

Figure 3-34. APG Building 2006: Close Up View of Front Door Entrance (to right is S)
In this view the hammer has impacted the brick veneer wall near the bottom (Location J in Figure 3-32)
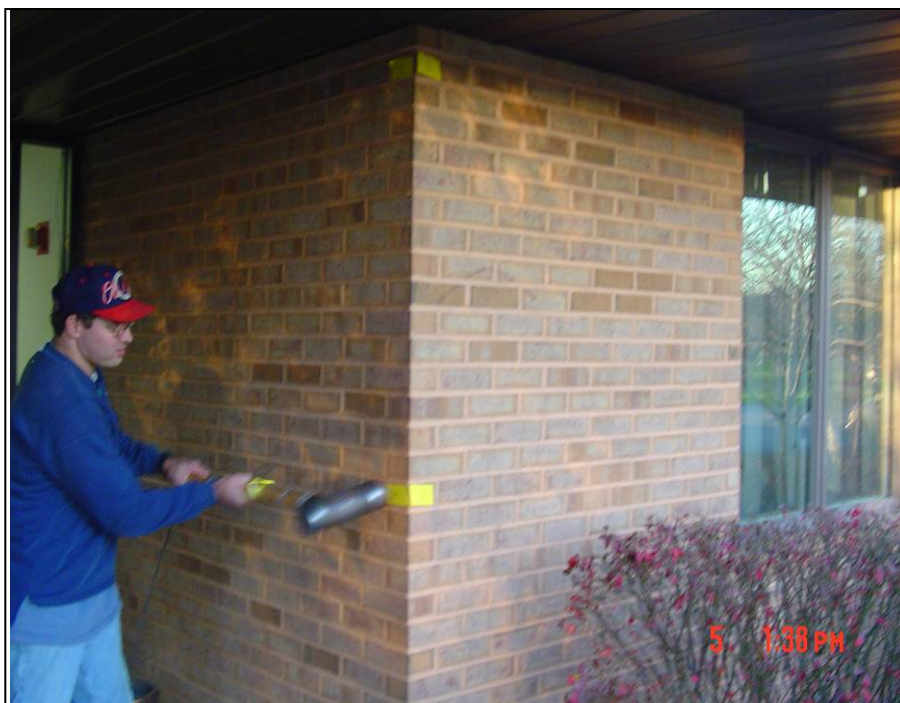
Figure 3-35. APG Building 2006: Close Up View of Front Door Entrance (to right is S)
*In this view the hammer has impacted the brick veneer wall near the mid-height in the east direction
(Location K in Figure 3-32)*

Figure 3-36. APG Building 2006: Close Up View of Front Door Entrance (to right is S)
In this view the hammer has impacted the brick veneer wall near the top (near ceiling height)
in the east direction (Location L in Figure 3-32)

3.1.2.3 APG Building 4031 (Site B)

Building 4031 is aligned perpendicularly to the road passing in front of Buildings 2006 and 2001, such that the long direction of the building is aligned somewhat in a north-south orientation. No drawings or plans for this building were made available.

Building 4031 is one-story wood frame structure and appears to have a concrete slab for the floor with conventional footings. However, the actual foundation details are not known (e.g., whether there is a crawl space or not). The building is approximately 100 feet by 25 feet in plan. This building could represent a small multi-family or a single-family ranch style, one-story residence in size and construction. Details of the actual foundation, framing design, and as-built dimensions were not available. Figures 3-37 through 3-40 show the west, east, north, and south exterior of the building, respectively.

The site was instrumented with microphone pole and Blastmate shown in Figure 3-41, and window accelerometers and exterior wall microphone shown in Figure 3-42. An additional tri-axial accelerometer was placed in the SW corner above the ceiling tile, as shown in Figure 3-43. Measurement data at this site were recorded using a multi-channel National Instruments PXI digital recording system.

Figure 3-37. APG Building 4031: View of the West Exterior (to the right is S)

Figure 3-38. APG Building 4031: View of the East Exterior (to the right is N)

Figure 3-39. APG Building 4031: View of the North Exterior (to the right is W)

Figure 3-40. APG Building 4031: View of the South Exterior (to the right is E)

Figure 3-41. APG Building 4031: Microphone Pole and Blastmate

(a)   (b)

Figure 3-42. APG Building 4031: (a) Interior View of Accelerometers Mounted on the Window and Window Sill; (b) Exterior View of the South Wall with Accelerometer on Window Sill and Wall Microphone

Figure 3-43. APG Building 4031: Interior View of the Transducer Mounted Above the Ceiling in the Southwest Corner

3.1.2.4 APG Building 379 (Site E)

Building 379 is aligned similarly to Buildings 2001 and 2006, such that the front faces nearly south and the longitudinal direction is almost aligned with the east-west line. No pictures of this building were allowed or provided. No drawings or plans were made available. The schematic in Figure 3-44 was drawn from the room dimensions measured on site.

Building 379 is two-story frame structure with a concrete slab for the first floor. Conventional footings are assumed supporting the perimeter exterior walls with the crawl space. The upper story of the building is approximately 60 feet long by 30 feet wide. This building could represent a typical two-story family residence in size and construction. Details of the actual foundation, framing design, and as-built dimensions were not available. On site measurements and observations were made as possible.

Figures 3-44 shows a floor plan with the measurement locations noted. As illustrated in the figure, accelerometers were installed at the second floor near the northeast corner (on the floor of a conference room), on the floor of the second floor hallway near the front (south) wall under a window, and on the second floor front (south) window.

Two four-channel SONY DAT tape recorders were used to record the data during gun firings on 10 November, 2004. The setup information is listed in Appendix B.
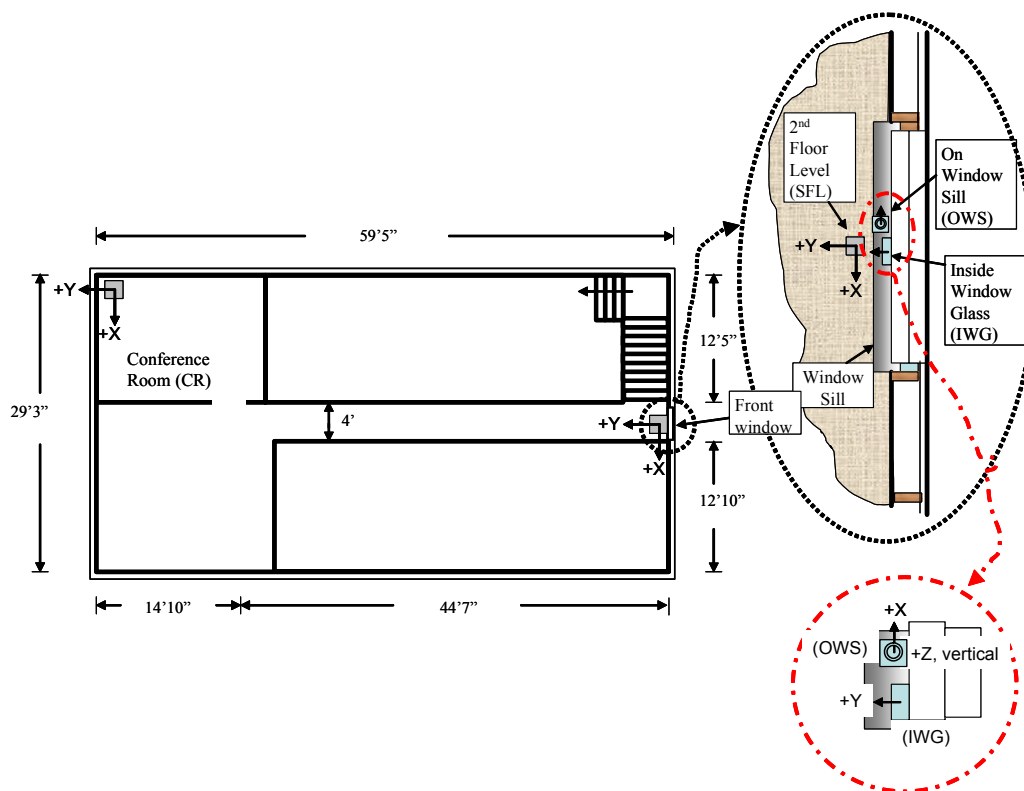
Figure 3-44. Schematic Plan of Second Floor of Building 379 (to the right is S)
Transducers in NE Corner Floor of Conference Room (CR), Second Floor Level under Front Window (SFL), on Inside Window Glass (IWG), and on Window Sill (OWS)

3.1.3   Measurements at Fort Sill

Measurements were made at Fort Sill, OK, on 2-4 and 10 August 2005. The intention was to collect data from firings of Howitzers from Firing Points 8, 9 and 10 on the North Arbuckle Range during the Red Leg Challenge exercise on 2-4 and 9-11 August. Measurement sites were:

- Building 6482 at Site 45W, block building, 3.1 km;

- Building 6429 at Site MK19, metal structure, 3.2 km;

- Building 216, wood frame construction warehouse, 4.8 km;

- Reference site, 1.3 km;

- Building 1230, single-story residence, 4.5 km; and

- Building 6961B, single-story duplex residence, 8.5 km.

Distances, in km, from Firing Point 9 are noted. Figure 3-45 shows the locations of the firing points and measurement sites.
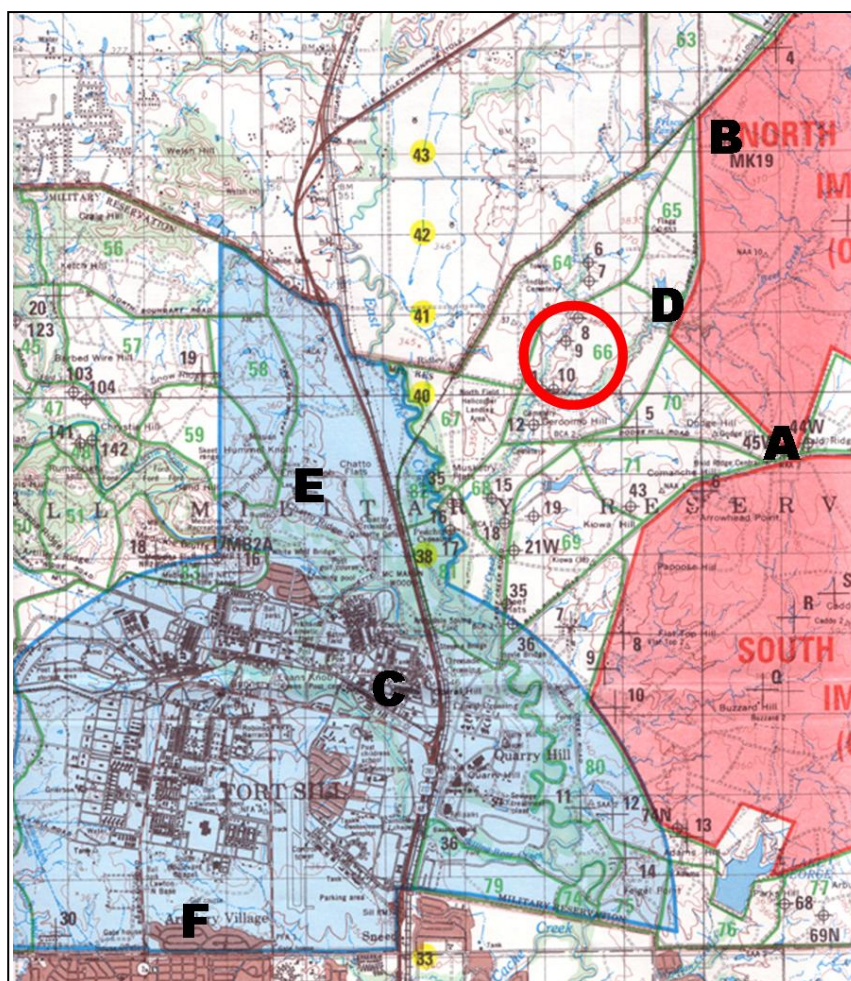
Figure 3-45. Measurement Sites at Fort Sill
(Firing Points 8, 9, 10 are in Circle SW of Site D)

Figures 3-46 through 3-51 show the sites and typical instrumentation placement. Table 3-2 lists the large-weapon firing schedule for the Arbuckle ranges during the measurement period. The scheduled Red Leg Challenge on 2-4 August ended around mid-day on 4 August. Because of setup time and the early end of the exercise, Red Leg Challenge data collected on 2-4 August were limited. For that reason additional measurements were conducted at Site C on 9-10 (during the second week of Red Leg Challenge) and 15-16 August. A number of unknown events on the range complexes were recorded throughout the measurement period.

Table 3-2. Large Weapon Firing Schedule, Arbuckle Range

Date	Weapon	From	Into
2, 3, 4 Aug	105 mm*	08, 09, 10	North Arbuckle
	105 mm	59N	South Arbuckle
	MLRS	01NA	South Arbuckle
9, 10 Aug	105 mm*	08, 09, 10	North Arbuckle
38938	105 mm	59N	South Arbuckle
38939	105 mm	45W	North Arbuckle
15, 16 Aug	MLRS	01NA	South Arbuckle
	MLRS	45W	North Arbuckle

Red Leg Challenge

Figure 3-46. Building 6482 at 45W, Fort Sill

Figure 3-47. Building 6429 at MK19, Fort Sill

Figure 3-48. Building 216 (Warehouse) at Fort Sill *(Propagation Stack in Foreground)*

Figure 3-49. Building 1230, Fort Sill (*Instrumented Window on Left Side*)

Figure 3-50. Rear View of Building 6961B, Fort Sill

**Figure 3-51a. Triaxial Geophone: Geophone Placement,
Partly Embedded Prior to Backfilling**

**Figure 3-51b. Triaxial Geophone: Geophone in Use,
Wiring Harness Connected and Covered with Plastic Bag**

Figure 3-52. Installation of Triaxial Accelerometer, Building 216

Figure 3-53 Accelerometer Placement on Top Plate (Through Ceiling), Building 6961B

Figure 3-54. Accelerometer Placement On and Around Window, Building 6961B, Exterior

Figure 3-55. Accelerometer Placement On and Around Window, Building 6961B, Interior

3.1.3.1 Fort Sill Building 216 (Warehouse)

Building 216 is an approximate one-and-a-half-story wood frame structure. The building is 169 feet long, 38 feet wide, and approximately 20 feet high to the roof peak. No drawings were available, however, a list of plans or modifications were listed as on file. The age of the building is approximately 60 years or more. The structure design of the building in timber framework is made of wood dimensional lumber, connected by fabricated joints and the roof system is generally made of the joists, rafter and ridge board. The building is used for storage of supplies and equipment. This building has office space, too. The building generally has a symmetric structural system for resisting lateral loads in the long and short directions. The building view is shown in Figure 3-48. Figure 3-56 shows the end elevation of Building 216.

Figure 3-56. Elevation View of One End of Building 216, Warehouse

The building plan with transducer locations at the attic level is shown in Figure 3-57. Six accelerometers were mounted to the roof rafters in each corner of the building and two to the middle rafters. An installation detail in Figure 3-58 shows the measurement directions for one of the tri-axial accelerometers, which is connected by black BNC plug (ac) cable to the data recorder located in the corners of the building.
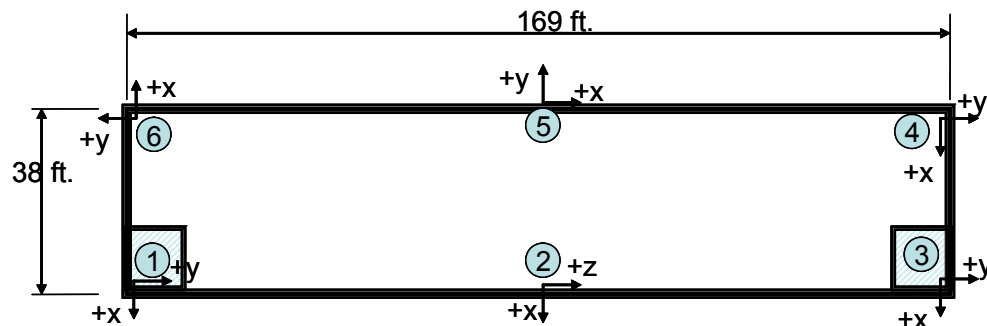
Figure 3-57. Plan of Building 216 with Sensor Locations at the Attic Level

Figure 3-58. Transducer Installation at Building 216 Attic Level

Additional accelerometers were mounted on a walls, window frame and windows glass facing the firing points. Recording system consisted of several DAT recorders were operated continuously during measurement periods in this building (24 hour) measuring impulsive sound from the blast operations.

Shaker testing was also performed on the building in two horizontal directions (X and Y) to measure the response of the frame structure. Figure 3-59 shows two shakers installed in the X direction.

Figure 3-59. Shaker Installation at Building 216, Fort Sill

3.1.3.2 Fort Sill Building 6429

Building 6429 is a one-story steel frame structure of a 800-square feet area with the following approximate dimensions: 40 feet long, 20 feet wide, 9 feet high at the sides, 11 feet high to the peak. It used as short-term storage of supplies and equipments. The building view is shown in Figure 3-47, above.

Accelerometers were mounted to the roof rafters in two opposite corners of the building. Figure 3-60 shows one of the mountings.
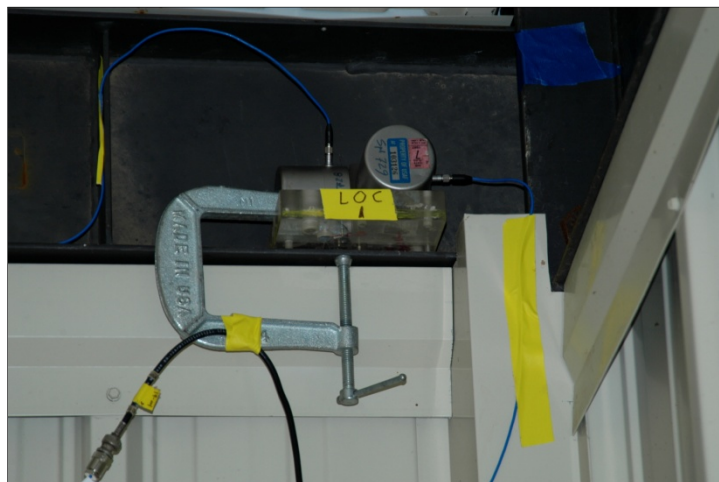
Figure 3-60. Accelerometer Mounting at Building 6429, Fort Sill

Recording system consisted of National Instruments PXI digital recording system and several DAT recorders operated continuously during measurement periods in this building (24 hour), measuring impulsive sound from the blast operations. Figure 3-61 shows the recording system.
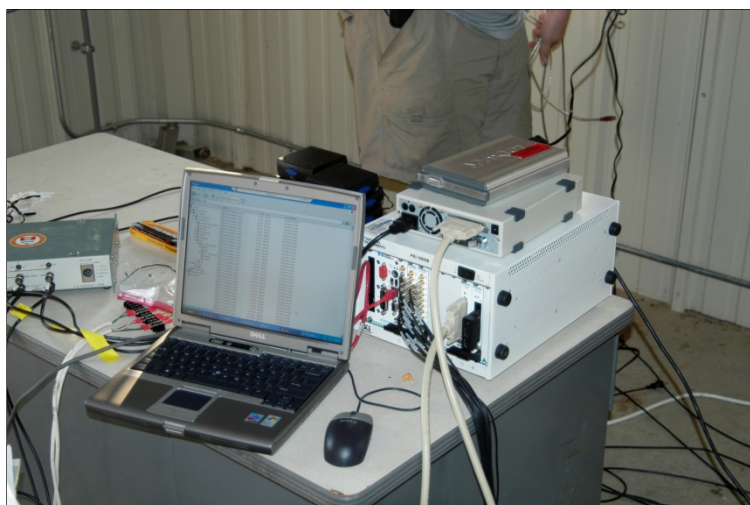
Figure 3-61. Data Collecting System at Building 6429, Fort Sill

Modal testing was performed on the buildings using instrumented hammer. The test was performed with a 12 pound brown tip on PCB 206m06 hammer, impacted 16 points marked inside and outside of the building structure. Figure 3-62 shows an exterior and an interior impact locations.

<table>
<tr><td>(a)</td><td>(b)</td></tr>
</table>

Figure 3-62. Fort Sill, Hammer Testing at (a) Exterior and (b) Interior of Building 6429.

3.1.3.3 Fort Sill Building 1230

Building 1230 is a residential type one-story wood frame structure 60 feet long and 30 feet wide with brick/wood exterior siding. The building is shown in Figure 3-49, above, and Figure 3-63.

Figure 3-63. Fort Sill, Building 1230

Recording system consisted of several DAT recorders operated continuously during measurement periods in this building (24 hour), measuring impulsive sound from the blast operations.

In addition to a stack with microphones at 5, 20 and 40 feet above the ground, and tri-axial geophones on the ground, the building was instrumented with accelerometers mounted on a wall, window frame and window glass facing the firing points. Additional accelerometers were mounted to the roof rafters in the building corners.

Modal testing was performed on the building in both directions (X and Y) using a shaker mounted to the rafter in a deck, as shown in Figure 3-64.

Figure 3-64. Fort Sill, Building 1230: Shaker Installation for Modal Test

3.1.4   Measurements at McAlester Army Ammunition Plant

Measurements were made at McAlester Army Ammunition Plant (MCAAP, Oklahoma) on 8-13 August 2005. Impulsive noise events were from ordnance disposal at the "old" disposal pits. Measurement sites, and their distances (km) from the pits, were:

A. Cabin 75A, a duplex transient residence on the shore of Brown Lake, 4.9 km;
B. Building 97A, a one story frame structure near the plant entrance, 6.7 km;
C. Reference, propagation point, 1.0 km;
D. Building 92, a one story frame building, 4.6 km; and
E. 36AT, propagation point, 2.6 km.

Figure 3-65 shows the locations of these sites and the pits. This is a complex of 26 pits, arranged as shown in Figure 3-66. The pits are notches cut into the side of a network of berms. Figure 3-67 is a view of Pits 8 through 10 during preparation; the earthmover is working in Pit 8. The explosive material is placed on the floor of each pit and covered with at least two yards of dirt. Figure 3-68 shows one pit with a charge in place, covered and ready for detonation.
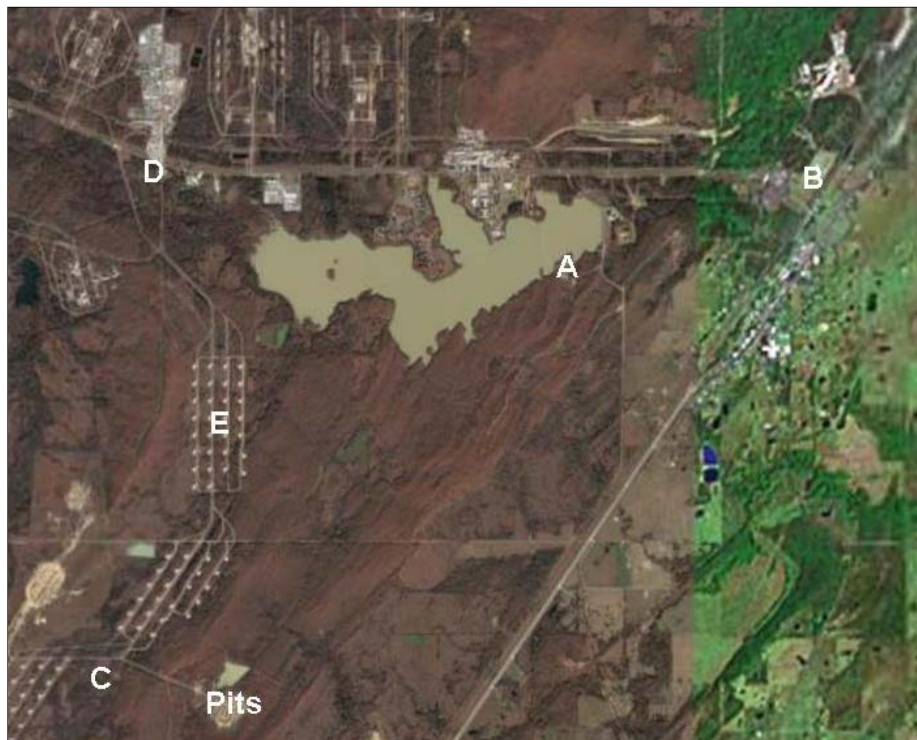
Figure 3-65. Disposal Pit and Measurement Site Locations, MCAAP

Figure 3-66. Arrangement of Disposal Pits, MCAAP

Figure 3-67. MCAAP Disposal Pits 8 Through 10, During Cleanup

Figure 3-68. Disposal Charge, Covered with Dirt, In Pit Prior to Detonation

The disposal schedule consisted of firing the charges in all pits at intervals of about 20 seconds. Firing occurred at around noon local time each day, and pits were fired in the numeric order indicated in Figure 3-66. All 26 pits were fired each day of measurements, with typical charges

of 200 pounds NEW. The firings were preceded by one or two calibration detonations as precursor events for range management purposes.

Modal analysis tests were conducted at B and C, and also at Cabin 72, a building very similar to 75A and in the same complex adjacent to Brown Lake. Figures 3-69 through 3-76 show the sites and typical transducer placement. PXI digital recording systems were used for response measurements at Sites A and B, and DAT recorders at the other sites.

3.1.4.1 MCAAP Building (Cabin) 75A

Building 75 is a residential type one-story wood frame structure. The building has the dimensions of 46 ft long and 30 ft wide. The building has two single bedroom units with full kitchens. A floor plan was available, but no other structural details were. The attic space was not accessible for inspection. It is assumed that roof trusses, either prefabricated or constructed on site, were used. The building is shown in Figure 3-69.

Recording system consisted of several DAT recorders and operated continuously during measurement periods in this buildings measuring impulsive sound and building elements response to the blast operations.

Figure 3-69. MCAAP Building 75A
(Instrumented Window to Left)

3.1.4.2 MCAAP Building (Cabin) 72

Building (cabin) 72 is a residential type one-story wood frame structure very similar, if not identical, to building 75A located nearby and described above. Building 72, shown in Figure 3-70, was available for modal testing.

The building has the dimensions of 46 ft long and 30 ft wide. A floor plan was available, but no other structural details were. The attic space was not accessible for inspection. It is assumed that roof trusses, either prefabricated or constructed on site, were used.

Figure 3-70. MCAAP Building 72

Accelerometers were mounted to the roof rafters in the building corners. Shaker testing was performed on the building in both directions (X and Y) to measure the response of the frame structure. The shakers used in modal tests are shown in Figure 3-71.
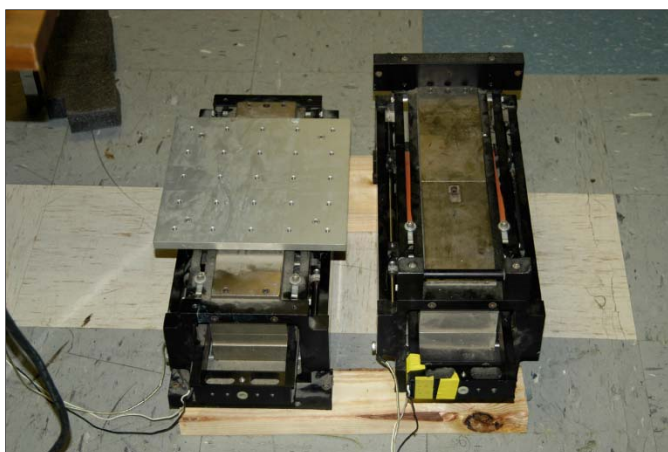
Figure 3-71. Electrodynamic Shakers Used for Modal Tests

3.1.4.3 MCAAP Building 97A

Building 97A is a residential type of one-story frame structure. The building has the approximate dimensions of 40 ft long, 30 ft wide, with an 8 foot interior ceiling height. The structure design of the building is timber framework. Construction drawings were not available for this building. Measurements were made on site of rooms and the outside dimensions of the building. The attic space was accessible for inspection. A typical wood frame truss system supports the roof. This building could represent a single family residence. The age of the building is unknown, but estimated at about 60 years. The building is shown in Figure 3-72.

Recording system consisted of several DAT recorders operated continuously during measurement periods in this building recording impulsive sound from the blast operations. Accelerometers were mounted on and around a window facing the direction of the disposal pits, and to the top plates in building corners. Figure 3-73 shows the instrumented window and corner accelerometer installations.

Shaker testing was also performed on the building in both directions (X & Y) to measure the response of the frame structure. A hammer test was performed with a 12 pound brown tip on PCB 206m06 instrumented hammer on 12 points marked inside the building on the frame structure. Figure 3-74 shows the hammer test execution.

(a) Front View

(b) Rear View

Figure 3-72. MCAAP Building 97A: (a) Front View; (b) Rear View

<div align="center">(a)   (b)</div>

Figure 3-73. MCAAP Building 97A: (a) Instrumented Window; (b) Accelerometers at Top Plate

Figure 3-74. MCAAP Building 97A: Instrumented Hammer Testing

3.1.4.4 MCAAP Building 92

Building 92 is a residential type one-story frame structure of a 900 sq. ft. footprint, 9ft high, 45 ft long and 20 ft wide. The structure design is timber framework. The building is shown in Figure 3-75.

Figure 3-75. MCAAP Building 92: Instrumented Window and Top Corner Seen

Recording system consisted of several DAT recorders operated continuously during measurement periods in this building recording impulsive sound from the blast operations. Accelerometers were mounted on and around a window facing the direction of the disposal pits, and outside to the frame structure of the building, as seen in Figure 3-75.

A hammer test was performed with a 12 pound brown tip on PCB 206m06 instrumented hammer on 5 points marked outside the building on the frame structure. Figure 3-76 shows the impact test execution.

Figure 3-76. Modal Impact Test Using Instrumented Hammer

3.2 Measurement Data Processing and Analysis

Following each set of field measurements, the data collected were extracted from the recording systems into a common format for analysis. Original data from the PXI systems was in disk file format, with data values in the form of single precision (32 bit) floating point numbers representing voltages, multiplexed across channels. Original data from the DAT recorders were transferred to computer disk using the appropriate manufacturer-provided software. The result was data values in the form of 16 bit 2's complement values representing digitized counts, multiplexed across channels, together with header or log file information specifying the count-to-voltage factor and other parameters. MATLAB and Fortran programs, from Wyle's and ERDC's in-house data processing software, were used to convert the original data to physically scaled format. Transducer sensitivities and amplifier gain settings were used in this process. The final processed result was a set of files of type BIN which contained pressure data in Pa, acceleration data in g, or velocity data in inches per second. These were in the form of single precision floating point values. The BIN files were de-multiplexed, i.e., the original data tracks were separated so there would be one channel per file. BIN files from a given data sample were split from a single file per event, so they remained time-synchronized. Each file was given a name that identified the site, included the nominal time and/or run log number, and the sampling rate. IRIG-B time code channels were included in this processing.

Further processing consisted of analysis of waveforms, calculation of Frequency Response Functions for the structures and elements, and identification of global building response characteristics from modal testing performed. This analysis and its results are described and discussed in Section 4.0.

Intentionally left blank

4.0   Results and Discussion

This section describes in-depth analysis of the measurement data collected during activities at the three DoD facilities introduced in Section 3.0, presents and discusses the results of that analysis, and presents the development of models for the probability of structural damage to, or rattle of, building components from impulsive sounds.

4.1   Response Analysis and Transfer Functions

4.1.1   Structural Response to Impulsive Loads

Sutherland et al. developed relations for the response of structures to impulsive loads from sonic booms[38]. Because of the similarity between sonic booms and other impulsive loads, that method was initially selected as a basis for the analysis in the current project. There are, however, detailed differences in waveforms among the various impulsive sources of interest. As a task in the current project, Sutherland confirmed the applicability of the basic methodology and extended the analysis to artillery and ordnance blasts, as described in Reference 39.

Structural response measurement data collected during firing tests at APG were initially analyzed. The goal of this analysis was to obtain measurement characteristics describing vibration response of buildings to the acoustic load from blast waves generated by tank gun firings.

The measurement data collected in the current project, as described in Section 3.0, included the simultaneous sound pressure time histories recorded with microphones placed at poles near the tested buildings (at three different heights) and at the building walls, as well as the acceleration time histories recorded with accelerometers placed at critical structural elements of the buildings, including window glass, sash frame, and sill. Coupling between the blast pressure and vibration response of a structure is described by the Frequency Response Function (FRF) representing a ratio of the frequency spectra for structural response and blast pressure. Response of a structural element can be expressed in terms of its acceleration, velocity, or displacement. Often, the term Transfer Function (TF) is used instead of the FRF for simplicity; however, in a strict physical definition TF is related to the Laplace transforms of the time-dependent input and output signals for a system in the time domain rather than to the Fourier spectra of the signals in the frequency domain.

Pressure waves generated by artillery or ordnance explosive blasts provide impulsive pressure load on structures, so that vibration response of structures to such loads is transient in nature. This distinguishes it from well-studied response to steady-state types of acoustical excitation. The analysis of the current data was based, in general, on relationships between various spectral measures developed in References 38 and 39. Prior to processing of all field data into transfer functions, a pilot analysis was performed on a subset of the data. The subset chosen was that obtained for two buildings at APG in response to tank gun firing. A hands-on method was used that provided results for vibration response of buildings to the acoustic load from a blast wave generated by tank gun firings, and also defined a method which could be automated for processing of the remaining data.

4.1.2   Pilot Analysis Methodology (APG Data)

The analysis of the APG measurement data was performed using a 01dB-Stell[©] PC-based digital signal acquisition system with the dBFA32 spectrum analyzer software package[40] utilized in a post-processing mode. The system allows performing narrow-band and broad-band spectrum analysis for single-channel input signals based on Fast Fourier Transform (FFT) or digital filtering, as well as computing various narrow-band cross-spectrum and frequency response functions in dual-channel signal analysis mode for stationary and transient signals. Inputs to the software are either through the acquisition hardware or through WAV files that include a proprietary 01dB data chunk.

The analysis was conducted in several steps that are described below.

4.1.2.1 Initial Data Post-Processing and Spectrum Analysis

For processing of the measurement data using the dBFA32 software, the digital time-history BIN files for each tank gun firing (run) recorded during the APG tests were initially converted into WAV data files. Fourteen-second-long time histories for each recorded signal encompassing blast pressure or related building response for individual runs were utilized. The conversion was performed using a Fortran program developed for this purpose.

The WAV data files for each run were imported in dBFA32 in pairs for the appropriate microphone and accelerometer signals and subjected to narrow-band dual-channel spectral analysis in the frequency range from 0 to 4687.5 Hz with the resolution of 1.465 Hz. The output of the analysis was configured to include the auto-spectrum for each of the two signals, as well as the frequency response function H1 between the signals. (In spectral analysis, the term auto-spectrum is used to describe the Fourier transform of a signal and distinguish it from the cross-spectrum of two signals. The *frequency response function H1* represents ratio of the Fourier transform of the system response signal to the Fourier transform of the system input signal. The dBFA32 software calculates H1 using auto-spectra and cross-spectrum for the two signals averaged over their duration.)

The same WAV data files for microphone and accelerometer signals for each run were also subjected individually to broad-band spectrum analysis using dBFA32 to obtain one-third octave spectra for each signal. Again, the FFT based algorithm was utilized (as opposed to digital filtering), to produce average spectra for each signal in the frequency range from 3.15 Hz to 8 kHz.

Typical example of a transient pressure load recorded for a tank gun blast with a microphone located on a building wall and structural vibration response recorded with an accelerometer at a window glass is illustrated in Figure 4-1 for one of the runs. The resulting narrow-band spectra for these two signals are shown in Figure 4-2, and the respective one-third octave spectra – in Figure 4-3.
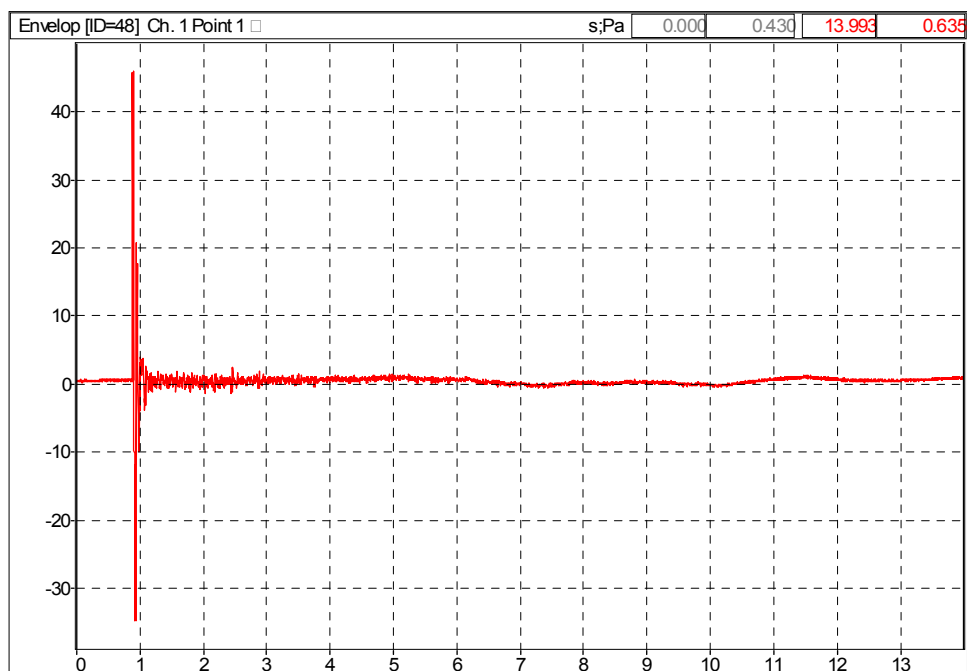
(a) Sound pressure at Wall, Pa, versus time, seconds
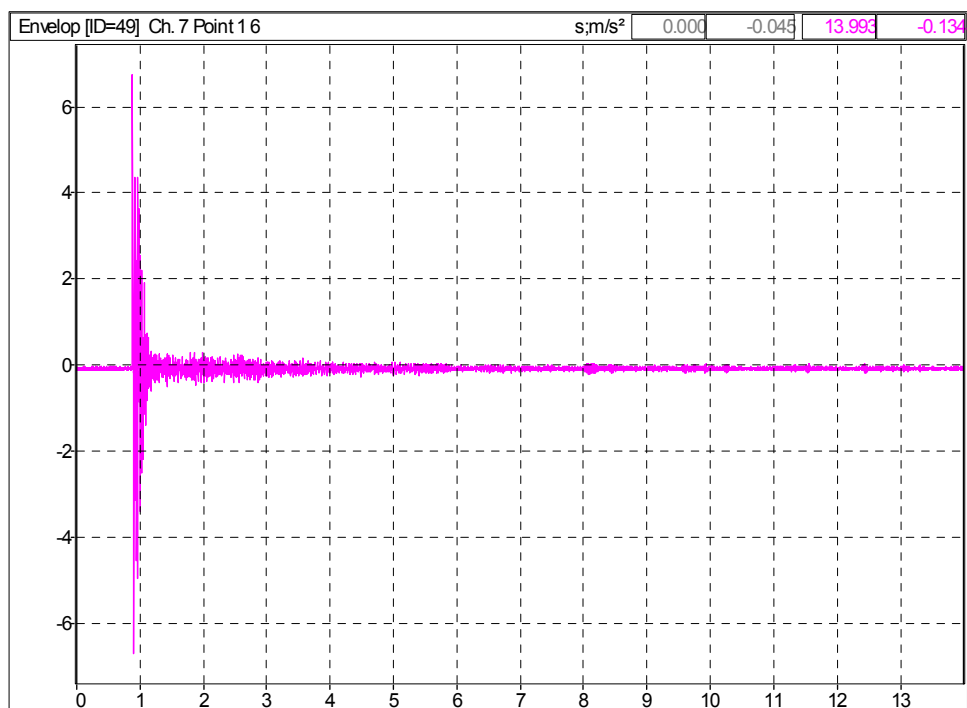
(b) Glass acceleration, m/sec², versus time, seconds

Figure 4-1. Signal Time Histories for APG Building 2001; Run025 – 105 mm; 11/10/04:
(a) Sound pressure at Wall, Pa, versus time, seconds; (b) Glass acceleration, m/sec², versus time, seconds
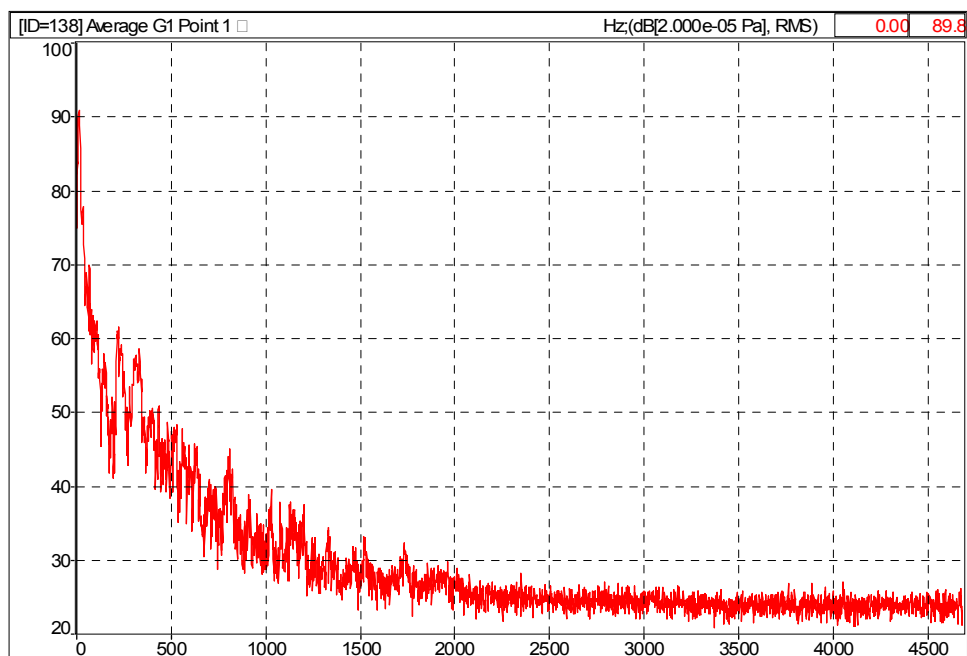
(a)
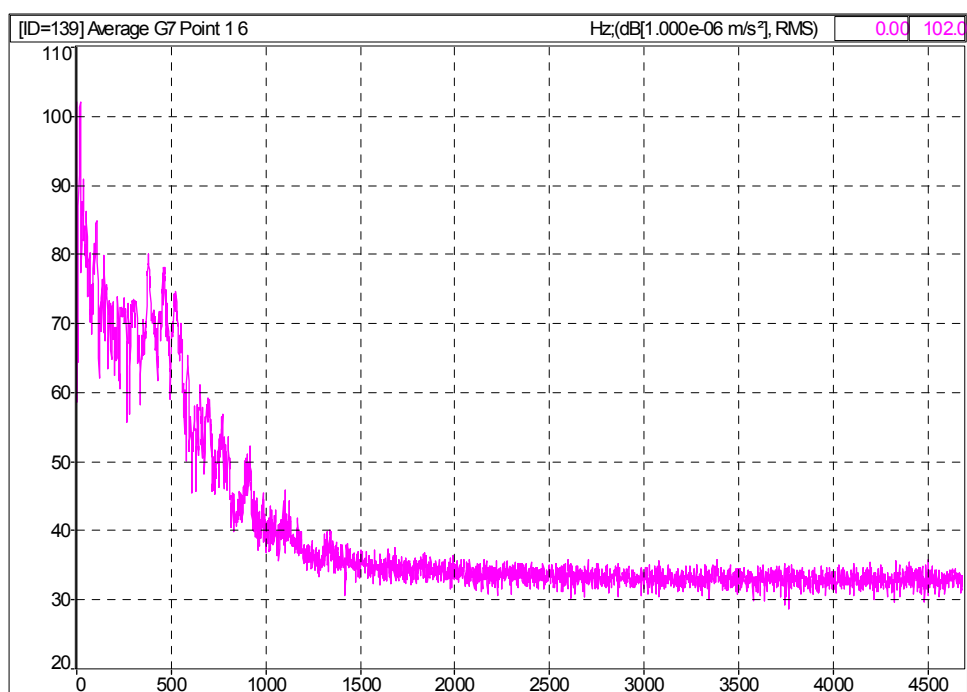
(b) Glass acceleration power spectrum, dB re: 1 μm/sec^2 rms, versus frequency, Hz

Figure 4-2. Narrow Band Spectra for APG Building 2001; Run025 – 105mm; 11/10/04
(a) Sound power spectrum, dB re 20 μPa rms versus frequency, Hz;
(b) Glass acceleration power spectrum, dB re: 1 μm/sec^2 rms, versus frequency, Hz
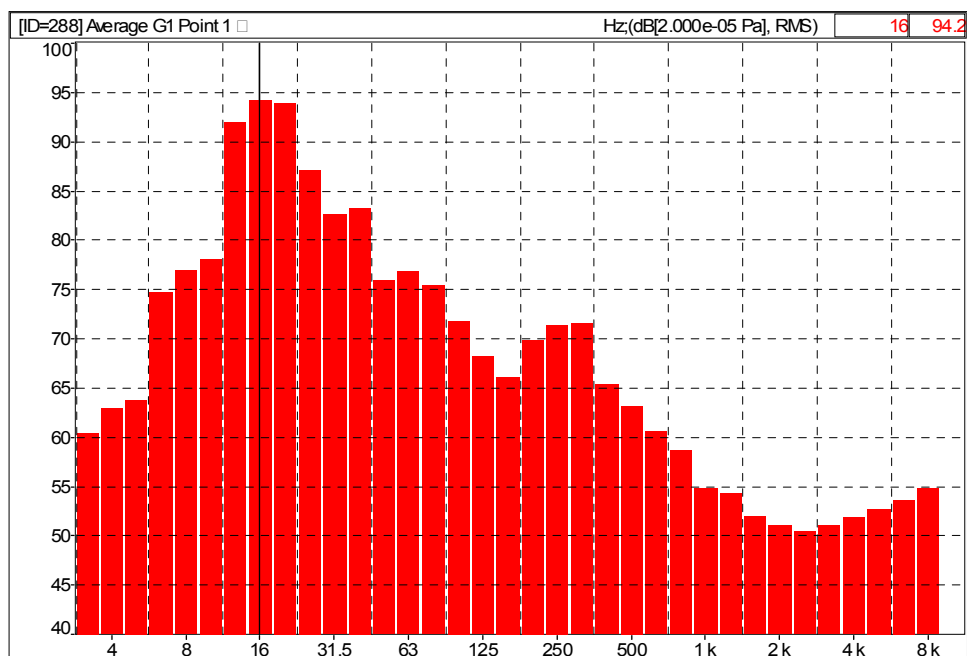
(a) Sound power spectrum, dB re 20 µPa rms versus band center frequency, Hz
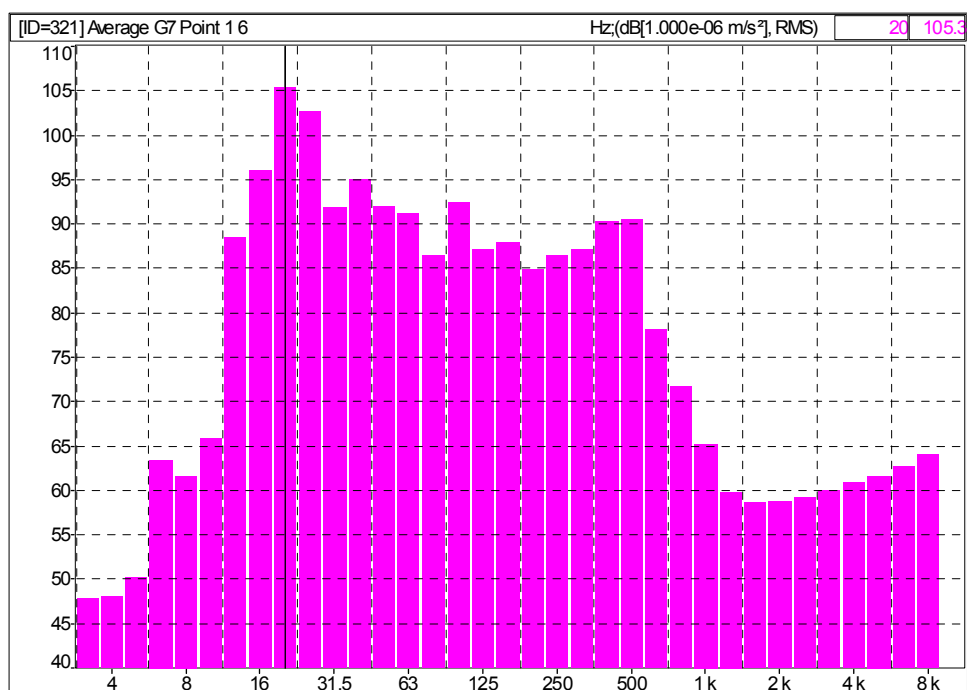
(b) Glass acceleration power spectrum , dB re: 1 µm/sec^2 , versus band center frequency, Hz

Figure 4-3. One-third-octave Spectra for APG Building 2001; Run025 – 105 mm; 11/10/04:
(a) Sound power spectrum, dB re 20 µPa rms versus band center frequency, Hz;
(b) Glass acceleration power spectrum , dB re: 1 µm/sec^2 , versus band center frequency, Hz

4.1.2.2 Validation of Initial Analysis Results

The results of the initial data analysis were exported in Excel spreadsheets for further processing for each tested building, test date, and type of gun. To validate the results, they were compared with the results of the previous study for sonic booms[38]. As shown in Section 1 and Appendix C of Reference 38, the most useful structural response parameter is peak velocity, which can be evaluated using the concept of Residual Velocity Shock Spectrum (RVSS). RVSS represents the envelope of maximum values of the velocity response of a dynamic (ideally, undamped) SDOF system to a transient excitation, after the excitation has ceased, as a function of the system resonance frequency. The same approach is used in this study, as summarized and further developed in Reference 39.

It is also shown in References 38 and 39 [see Equation 41 of the latter] that RVSS of an undamped SDOF system is related by a simple expression to the measured values of the sound pressure spectrum (absolute value of the Fourier transform for the sound pressure), as follows:

$$V_R(f_0) = (g/w)|P(f)| \tag{4.1}$$

where $V_R(f_0)$ = Residual Velocity Shock Spectrum, in/s

f_0 = resonance frequency of SDOF system, Hz

g = acceleration of gravity = 386 in/s^2

w = surface weight of responding system, psi

$P(f)$ = Fourier transform of the sound pressure, psi·s

f = frequency, Hz

For comparison with the results presented in Reference 38, the values of $V_R(f_0) \cdot w/P_{pk}$ were calculated as the product $g \cdot |P(f)|/P_{pk}$, where the peak pressure P_{pk} applied to the structure during each run was determined from the time history for the microphone located at the building wall. Where necessary, the data were converted from the measurement and reference units used in the dBFA32 software (modified SI/metric units) into the mixture of English lb-in-sec and lb-ft-sec units utilized in Reference 38[*]. As an example, a plot showing $V_R(f_0) \cdot w/P_{pk}$ as a function of frequency is demonstrated in Figure 4-4 for the same run as in Subsection 4.1.2.1.

---

[*] While most results in this study are presented in metric units, as generally preferred, the English units employed in Reference 38 are widely used for structural damage analysis. Those units are adopted here as necessary for consistency.
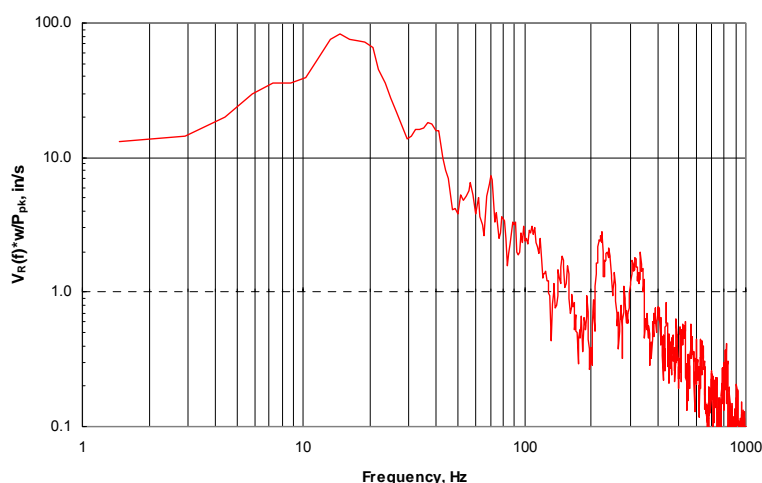
Figure 4-4. [Residual Velocity Shock Spectrum] / [P_{pk}/w]
APG Building 2001; Run025 – 105 mm; 11/10/04

For comparison purposes, Figure 4-5 shows a copy of Reference 38's Figure 4-4, representing theoretical RVSS for the response of an undamped SDOF system to an ideal sonic boom N-wave. It can be seen from Figures 4-4 and 4-5 that the RVSS measured for the tank gun blast resembles the shape and variability with frequency of the RVSS predicted theoretically for the sonic boom, indicating certain similarities in dynamic response of structures under the two different types of transient excitation. Such similarities were also found in comparison with other theoretical and experimental results presented in Reference 38.
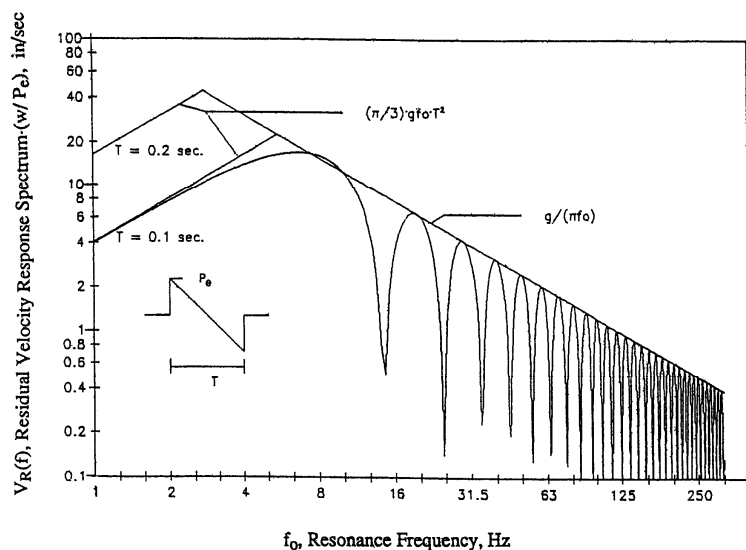
Figure 4-5. Normalized Residual Velocity Shock Spectrum for Predicting Peak Velocity Response of Structures with a Surface Weight w (psf) to a Sonic Boom with an Effective Peak Pressure Pe (psf) (from Figure 4-4 of Reference 38)

These similarities, as well as consistency of the resulting RVSS for different tank firings during the APG tests, as illustrated in Figure 4-6, serve to validate the measurement data and analysis results obtained using the described technique.
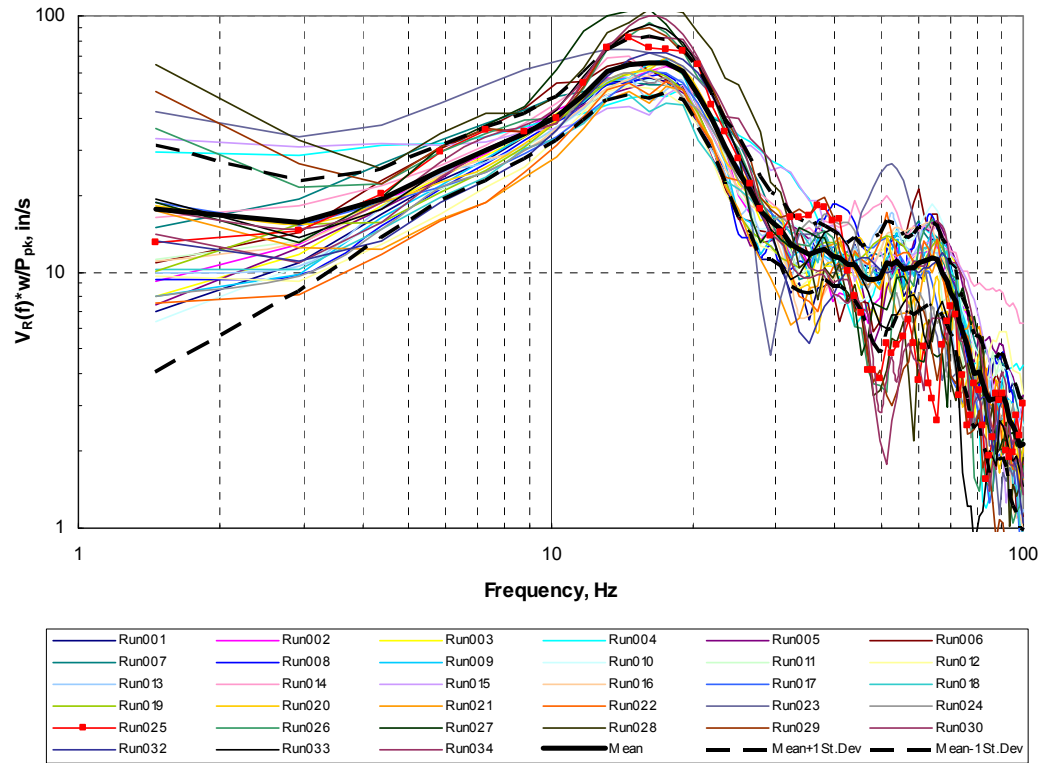
Figure 4-6. [Residual Velocity Shock Spectrum] / [P$_{pk}$/w]
APG Building 2001; 34 Runs – 105 mm; 11/10/04

4.1.2.3 Frequency Response Function

As indicated above, frequency response function is used to describe coupling between the blast pressure and vibration response of a structure. The measurement data collected during the APG tests and the analysis technique described above allow a few different formulations of the FRF to be explored. First is the narrow-band frequency response function H1 output from dBFA32, calculated using the auto-spectra and cross-spectrum for the two signals (dual-channel analysis). This is a complex ratio of the Fourier transform for structural response acceleration, A(f), to the Fourier transform for blast pressure, P(f), represented by a real part and an imaginary part or by a modulus and a phase. Figure 4-7 shows the modulus of H1 for one of the tank gun firings, in the logarithmic form $20 \cdot \log_{10}(|H1|)$.
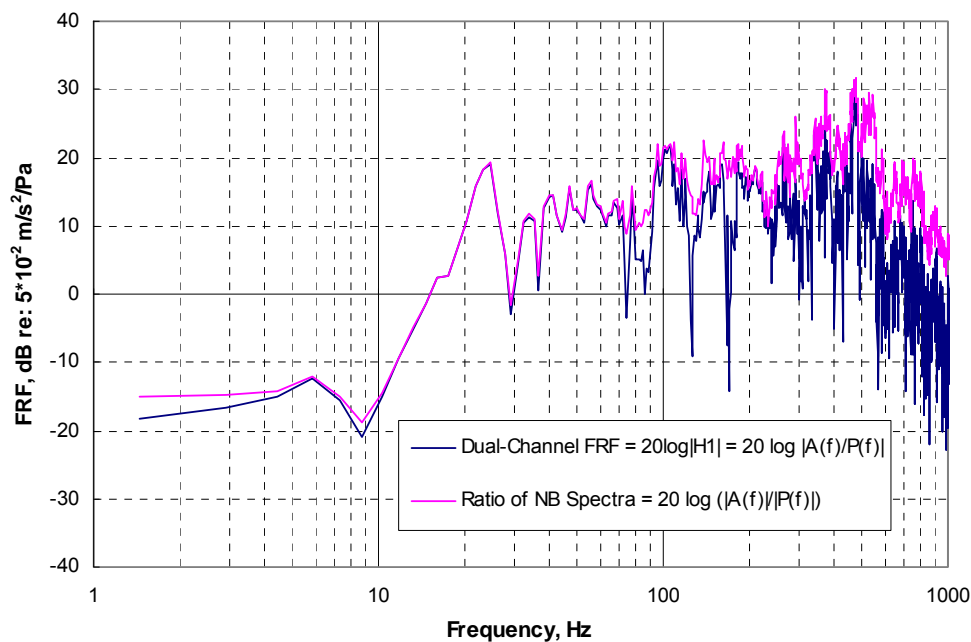
**Figure 4-7. Frequency Response Function (Glass Acceleration/Pressure)
ARG Building 2001; Run001 - 105 mm; 11/09/04**

The second curve in Figure 4-7 represents the frequency response function calculated as a ratio of the two individual narrow-band auto-spectra for acceleration and pressure (single-channel analysis) for the same run, also in the logarithmic form, as $20 \cdot \log^{10}(|A(f)|/|P(f)|)$. It can be seen from the figure that these two formulations for FRF provide almost identical results at frequencies below approximately 70 Hz. At higher frequencies, H1 demonstrates more fine structure with multiple sharp minima, apparently due to phase relationships between pressure and acceleration, which are taken into account by the algorithm for computing H1, but are neglected in the individual auto-spectra.

The FRFs presented in this section thus far relate the sound pressure measured at the building wall and the acceleration measured at the building element. As indicated in References 12 and 13, velocity is a more useful descriptor for evaluating structural stress response and predicting potential damage to structures. By applying a usual factor of $(2\pi f)^{-1}$ to the acceleration values during calculations, FRFs for acceleration/pressure are easily converted into the FRFs for velocity/pressure. For practical purposes, it is also convenient to translate the FRFs obtained by the narrow-band analysis described above into one-third octave frequency bands. Such a frequency recombination was performed using the energy summation of the narrow-band FRF values within the frequency limits of the related one-third octave band. (It is accepted that this approach provides only approximate values at the low end of the measured frequency range). The results of these operations on the two FRFs discussed in this section are shown in Figure 4-8. (Note also transition from the metric reference units used in Figure 4-7 into English units in Figure 4-8.)
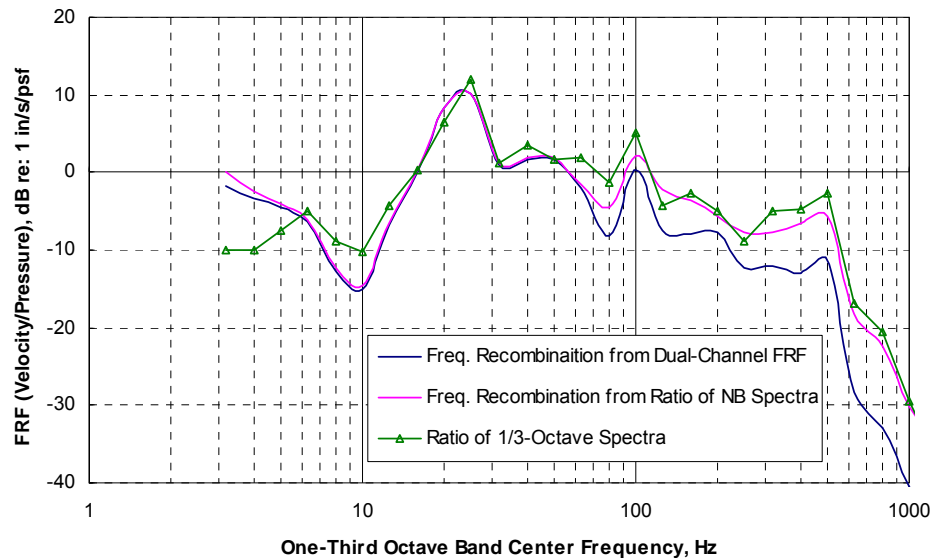
**Figure 4-8. One-Third Octave Frequency Response Function (Glass Velocity/Pressure)
APG Building 2001; Run001 – 105 mm; 11/09/04**

The third curve in Figure 4-8 presents the frequency response function calculated as a ratio of the one-third octave spectrum for acceleration, converted to velocity, to the one-third octave spectrum for pressure. Both individual spectra were obtained using the dBFA32 broad-band spectrum analysis for each signal, as described in Subsection 4.1.2.1, above. Such a formulation is, in actuality, a classic representation for the FRF, which has been in use for years due to its relative simplicity, since it involves only two easily measurable one-third octave spectra. It can be seen from Figure 4-8 that all three curves are generally in good agreement, especially in the frequency range from approximately 6 to 100 Hz. A classic ratio of the one-third octave spectra (direct one-third octave analysis) provides a slightly conservative estimate for the FRF, particularly at its peak near the structural resonance (in this case, approximately 25 Hz), in comparison with the other two formulations using the narrow-band spectrum analysis.

Based on this conclusion, most of the data collected during the measurements at APG, Fort Sill and MCAAP were analyzed using the classic formulation for the frequency response function as a ratio of the one-third octave spectra for structural velocity and sound pressure. The results of this analysis are discussed in the following subsections.

4.2   APG Data Study Results

The one-third octave frequency response functions for velocity/pressure were computed for tested structural elements of two APG buildings using the dBFA32 broad-band spectrum analysis software for all 65 rounds of the 105 mm tank guns and 5 rounds of the 120 mm tank guns recorded on November 9 and 10, 2004. After reviewing the data, several recordings with anomalous outcome were dismissed from further consideration due to irregular time histories (instrument overload or double "events"). The following subsections summarize and illustrate results of the analysis. Unless noted, the sound pressure signal used in calculations of FRFs was

the one recorded with a microphone located on a building wall, approximately 6 feet above the ground. Particular cases when the sound level signals used in the analysis were measured at the poles near the buildings are reviewed in Subsection 4.2.4.

4.2.1   Frequency Response Function Variability

Figure 4-9 shows the resulting one-third octave FRFs obtained for window glass at Building 2001 for 29 rounds of the 105 mm tank guns measured on November 9, 2004. It can be observed from the figure that FRFs for different runs are rather consistent throughout the frequency range of interest, with slightly increased variability toward the ends of the range.
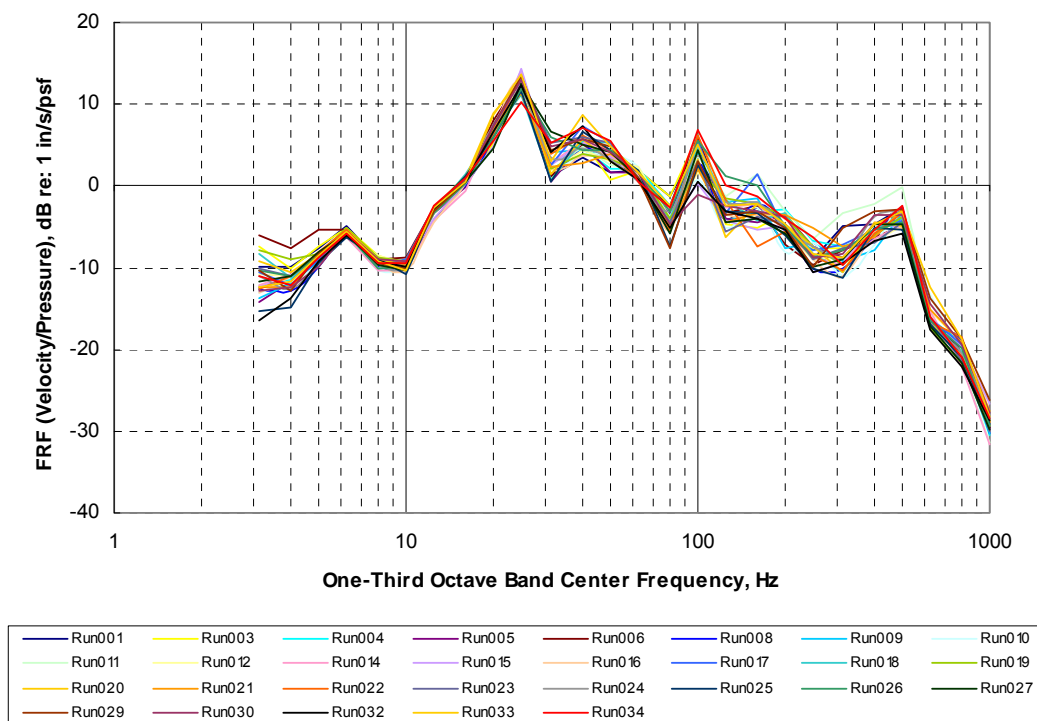
**Figure 4-9. One-Third Octave Frequency Response Function (Velocity/Pressure)
APG Building 2001; 29 Runs – 105 mm; 11/09/04**

Similar FRF consistency was observed for the measurements performed on the same day for the 120 mm guns (5 rounds) and for the second day of testing for the 105 mm guns (30 rounds), as well as for different construction elements at both buildings. This stability reflects the fact that FRF is an attribute of a particular construction, which allows averaging to be performed for different guns and days of testing without losing important information.

4.2.2   Various Tank Guns

Figure 4-10 compares the one-third octave FRFs for window glass at Building 2001 resulted from averaging for the 105 mm and 120 mm tank guns on the two days of testing. It can be seen again that the FRF is practically independent of the type of gun or testing time. A similar

conclusion was drawn based on the related results for sash frames and window sills of the two buildings.
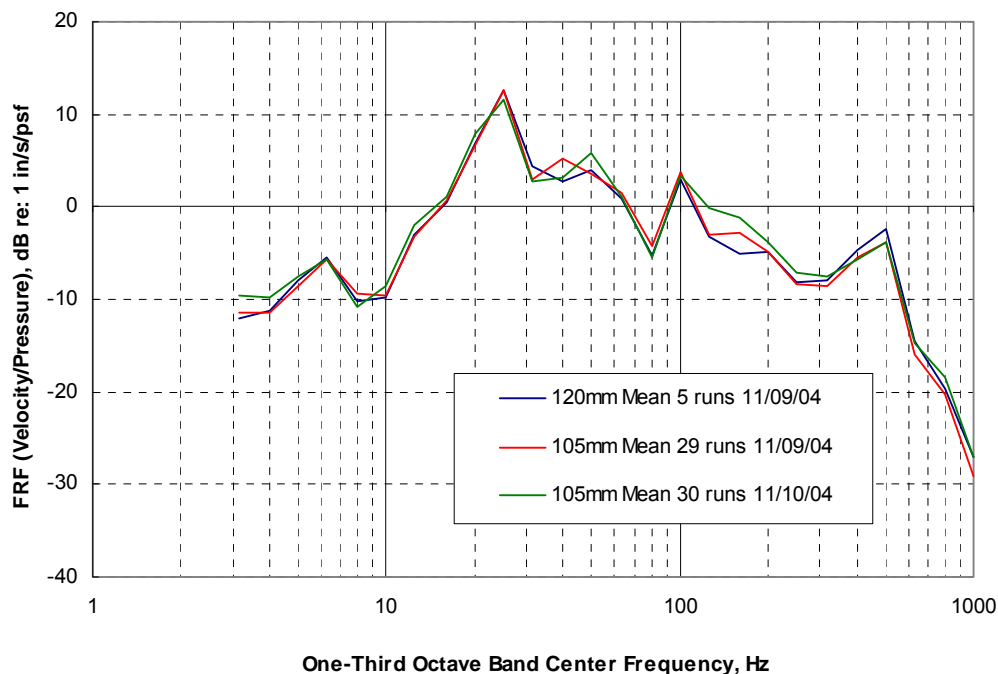
Figure 4-10. Mean One-Third Octave Frequency Response Function (Velocity/Pressure) APG Bldg. 2001; 11/09/04 and 11/10/04

4.2.3 Various Building Elements

Two windows tested at the APG buildings were both of double-hung type. At Building 2001, a relatively new wood/vinyl window was glazed with ½-inch insulating glass in tightly fit sashes. At Building 4031, the old and somewhat loose wood window was glazed with 3/32-inch single strength glass. It should be noted that response of the glass (upper sash) and sash frames (bottom sash) was measured in all the cases in the horizontal direction; on the exterior sills, however, the accelerometers were mounted perpendicular to their nearly horizontal sloping surface and thus measured the nearly vertical response component.

The mean FRFs (105 mm guns on November 9) for window glass, sash frames, and window sills at Buildings 2001 and 4031 are presented in Figures 4-11 and 4-12, respectively. The results for Building 2001 (Figure 4-11) indicate that all three FRFs peak in the same frequency band (25 Hz), but the glass and sash frame respond to the applied pressure pulse with approximately the same amplitude (in the horizontal direction) at the resonance, and much stronger than the exterior sill (in the vertical direction).
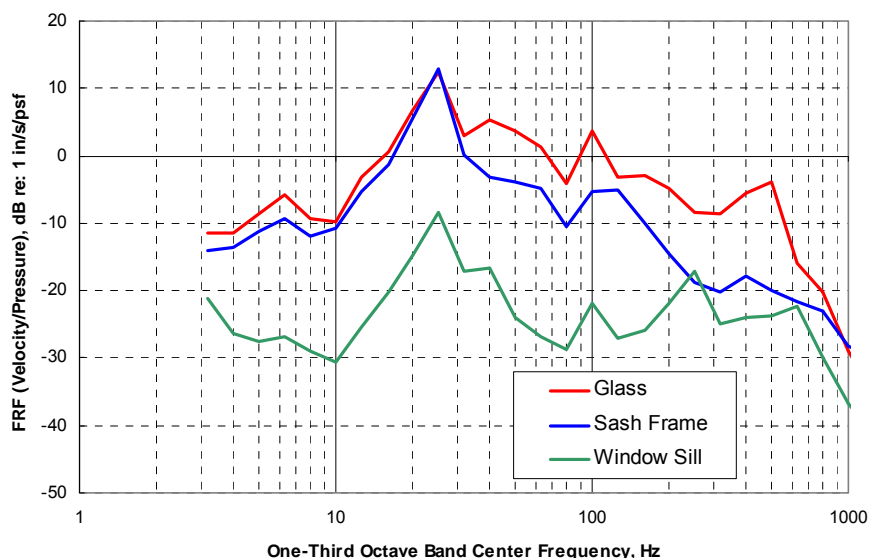
**Figure 4-11. One-Third Octave Frequency Response Function (Velocity/Pressure)
for Window Glass (1/2" IG), Sash Frame (DH), and Window Sill
APG Building 2001; Mean Values for 29 Runs – 105 mm; 11/09/04**

At Building 4031 (Figure 4-12), the glass responded to the pressure pulse stronger than the sash frame, especially at frequencies above the first resonance. A plausible explanation for this is the glass thickness and poor condition of the window at Building 4031 compared to Building 2001.
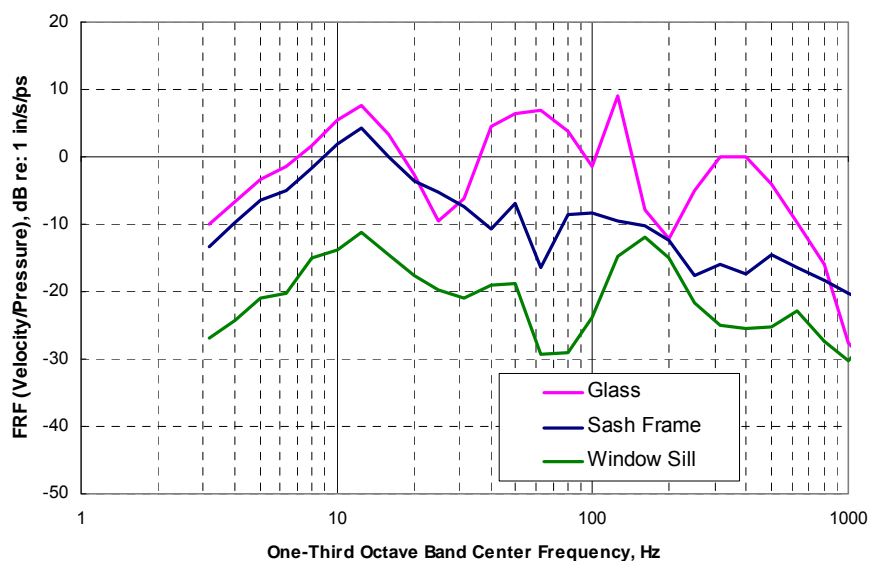
**Figure 4-12. One-Third Octave Frequency Response Function (Velocity/Pressure)
for Window Glass (ss), Sash Frame (DH) and Window Sill
APG Building 4031; Mean Values for 32 Runs – 105 mm; 11/09/04**

4.2.4 Various Microphone Positions

All FRFs presented and discussed above were obtained using sound pressure signals recorded with microphones located on the building walls, approximately 6 feet above the ground. A similar analysis was also performed utilizing the sound pressure signals simultaneously measured with microphones located on poles, which were situated in open spaces at a distance from the buildings, as seen (for example) in Figure 3-6. These microphones were positioned at 4, 20, and 40 feet above the ground.

A typical comparison between the FRFs determined using the wall and pole microphones is shown in Figure 4-13. In the figure, the one-third octave mean FRFs for glass velocity/pressure are presented for all four microphones at Building 2001 (105 mm guns on November 9). Very similar results were obtained for individual tank gun rounds, as well. It can be seen that the FRFs for the three pole microphones are almost identical at frequencies below approximately 100 Hz. At these low frequencies the vertical distance between the pole microphones is no more than twice longer than the sound wave length. At higher frequencies (shorter sound waves), small differences between the pole microphones can be observed.
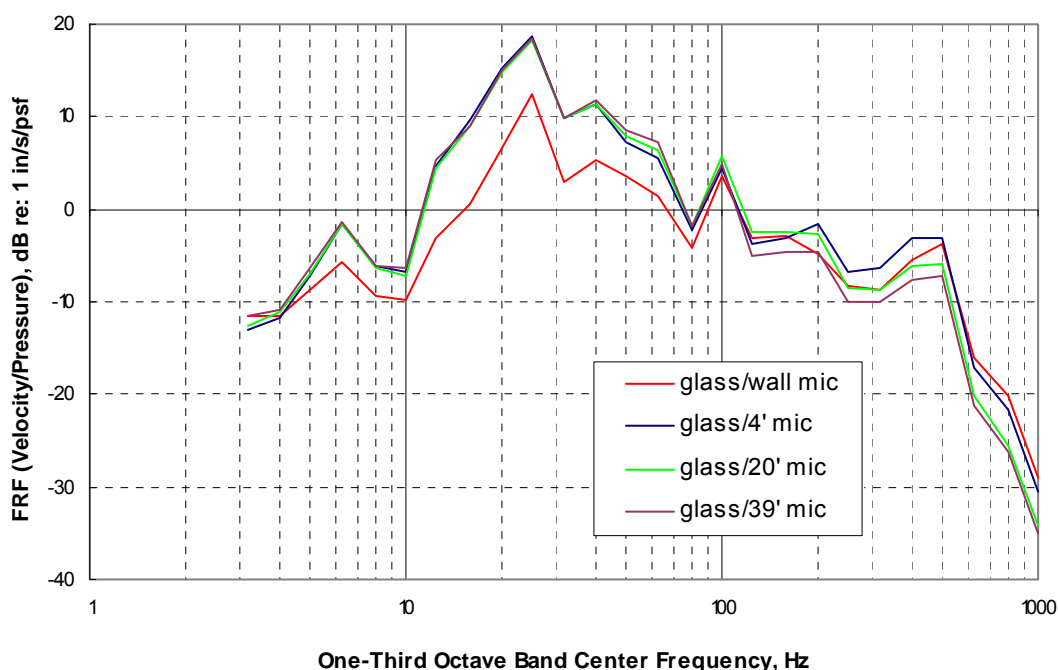
Figure 4-13. One-Third Octave Frequency Response Function (Velocity/Pressure) for Window Glass/Wall or Pole Microphone APG Building 2001, Mean for 29 Runs - 105 mm; 11/09/04

The FRF determined using the wall microphone, however, is consistently lower than the FRFs for the pole microphones at low frequencies. This is an indication of higher sound pressure at the wall compared to the pole. As a result of the well known effect of sound pressure doubling at acoustically hard surfaces, the FRF for the wall microphone is approximately 6 dB lower than

the FRFs for the pole microphones in the vicinity of the peak value at the first resonance of interest. The FRF relative to load on the wall is always consistent, but the difference between local pressure on the wall and the pressure measured in open space a short distance away must be noted.

4.3   Waveforms and Spectra of Various Blast Noise Sources

Typical examples of transient pressure loads recorded for various blast noise sources at the three installations is provided in Figure 4-14. The plot shows the sound pressure time histories measured for 105 mm and 120 mm tank gun shots received at APG Site B (Building 4031) on 9 November 2004, an ordinance disposal blast received at MCAAP Site A (Cabin 75A) on 12 August 2005, and a howitzer muzzle blast received at Fort Sill Site C (Building 216). The data provided are for a 4-foot pole microphone at each site. The recordings shown were performed at various distances from the noise sources (except for the two APG blasts), and the examples selected are intended to compare the waveforms of the blasts, rather than the blast intensities. Individual time scales for each signal indicated along the horizontal axis were expanded (maintaining identical time intervals) to show the blast signature details, and shifted relative each other to fit the signatures within the overall time frame for the comparison.
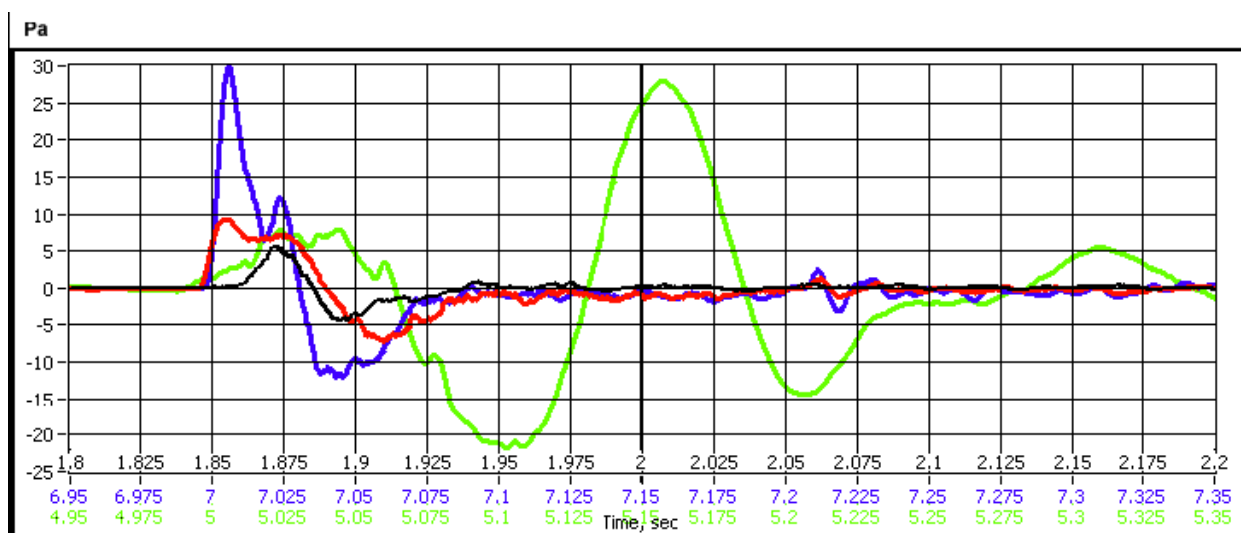
**Figure 4-14. Microphone Signal Time Histories: Red - APG 105 mm Tank Gun;
Blue – APG 120 mm Tank Gun; Black - Fort Sill Howitzer; Green – MCAAP Ordinance Disposal**

The amplitudes of the signals for the APG 105 mm and 120 mm tank gun shots are different, but they have similar wave shapes and spectral characteristics. Maximum overpressure of artillery shots (tank guns and a howitzer) occur during the first positive pressure phase, but the absolute maximum peak for the ordinance disposal appears during the second positive phase. Overpressure from all sources at observed distances did not exceed 1 kPa, or 154 dB. Disposal blasts indicated more energy associated with very low frequencies than artillery shots, as is evident from Figure 4-15 for the sound spectra of the three blasts.
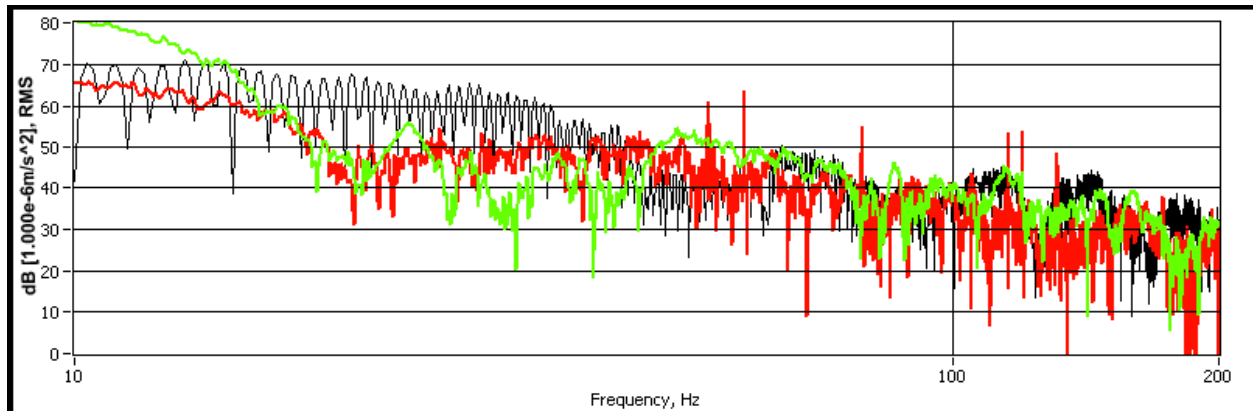
**Figure 4-15. Sound Frequency Spectra: Red - APG 105 mm Tank Gun;
Blue – APG 120 mm Tank Gun; Black - Fort Sill Howitzer; Green – MCAAP Ordinance Disposal**

4.4   Transfer Functions

The measured Transfer Functions, in the form of FRFs, have been prepared for all validated recordings at the three measurement sites, APG, Fort Sill and MCAAP. The analysis process developed with the 01dB system, as described above, was replicated as an automated LABVIEW script. Because it is customary to measure (or model) sound levels away from reflecting surfaces such as buildings, these production FRFs were prepared using the pole microphone, and are equivalent to the sample APG result presented in Figure 4-13. They contain the free space to wall factors as well as the structural response, and are thus appropriate for use with BNOISE2 predictions or field survey data. The FRFs were prepared in digital form, appropriate for use in the Damage Model Formulation task of the current project, described in Subsection 4.7 and Reference 41.

4.4.1   Single-Degree-of-Freedom Approximation

Analytical evaluation of the transient response of a structure to an idealized blast pressure wave is performed initially for a damped linear single-degree-of-freedom (SDOF) system in Reference 41. Equation 17 of Reference 41 defines the complex displacement frequency response (transfer) function normalized by the static displacement for such a simplified model of a structure. For comparison with the measurement results, removing the normalization from that equation and multiplying the result by the complex angular frequency jω leads to the following expression for the absolute value of the velocity FRF:

$$\text{FRF} = (\omega/\omega_0)^2/m/[(1-(\omega/\omega_0)^2)^2+(2\delta\omega/\omega_0)^2]^{1/2} \qquad (4.2)$$

where:

ω = angular frequency;
ω_0 = angular natural frequency of the structural element;
m = surface mass of the structural element;
δ = critical damping ratio, $\delta = \eta/2$, where η is the loss factor.

The loss factor was determined from the recorded accelerometer outputs for different structural elements during blast impacts, using the usual relationship:

$$\eta = 1/(2\pi)*\ln(A_1/A_2) \tag{4.3}$$

where A_1 and A_2 are two consecutive amplitude peaks of the acceleration signal.

The loss factor of coupled structural elements is significantly higher than the internal loss factor of the element material. From the measurement results it was found in a range from 0.02 to 0.5.

The equivalent mass used to describe the SDOF system was derived at the resonance ($\omega = \omega_0$) from the maximum measured value of the FRF as:

$$m = [2\delta*FRF(\omega_0)]^{-1} \tag{4.4}$$

Figure 4-16 shows an example comparison of the measured FRF with the FRF calculated using the SDOF model. In the majority of cases, when the experimentally determined loss factor is used for calculations, the analytical and experimental data are in a good agreement around the first resonance of the system.
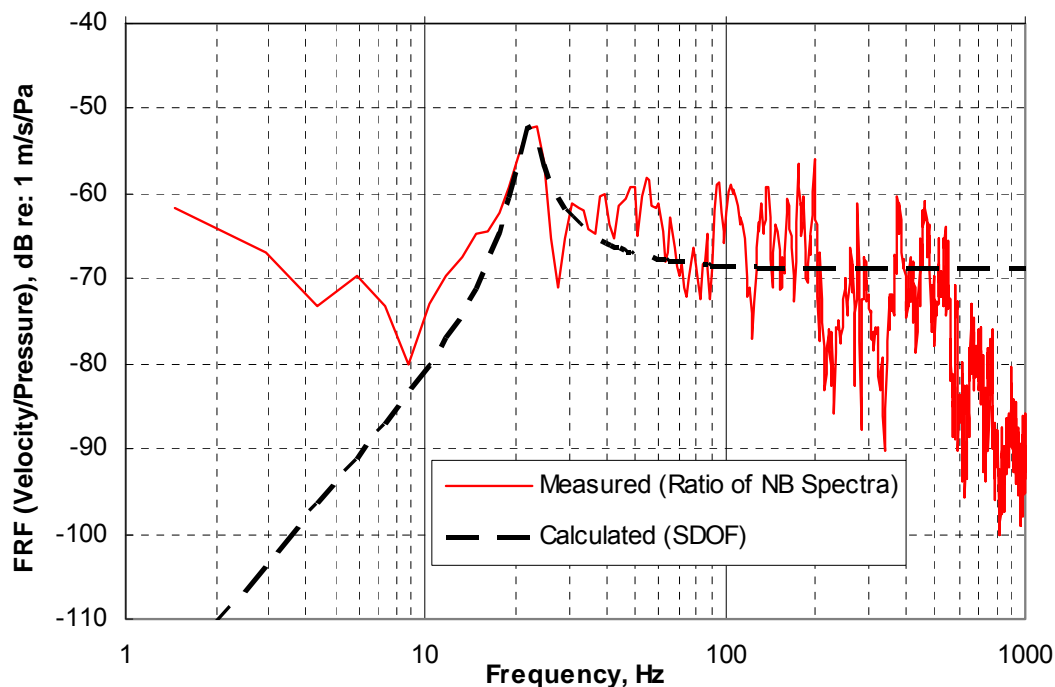
Figure 4-16. Comparison of Measured and Calculated FRFs: APG Building 2001, 105 mm Tank Gun, Run 025, 11-10-04 (glass)

4.5 Experimental Results of Building Vibration Monitoring

As described in Section 3.0, certain buildings at each military installation were instrumented with building-specific accelerometers for modal testing and recording global building motion response to ordnance firing. These accelerometers were set in key locations to monitor the vibration responses most relating to global building movements. Typically, the movements of most interest include the side-sway (horizontal) deflections in the transverse or longitudinal orientations.

The main focus of the results collected is to provide an understanding of the dynamic behavior of the building due to impulsive noise events. The responses measured due to the known stimuli provide control measurements to which to confirm stationary building behavior (i.e., properties of the building are not changing) and as another set of data from which system parameters are extracted for comparison (such as comparing identified natural frequencies, damping estimates, and deflection shapes at the identified natural frequencies). The main global movements of interest of the building typically concerns side sway (lateral) motions with respect to each axis of the building in plan (i.e., swaying parallel to the width and parallel to the length) and twisting (torsional motions) of the building in plan. Predominant frequency responses of buildings exist that resemble combinations of these three deflection movements hypothesized. The deviations from what would be expected from a purely geometric observation of the building dimensions in plan and number of stories are due to the actual distribution of lateral and torsional stiffnesses throughout the building.

One prediction of the fundamental mode of rectangular building provided in the Uniform Building Code (UBC) design code for earthquake engineering design and evaluation procedures is based on the formula to calculate the fundamental period, in seconds, as the number of stories times 0.1. Thus, for a one-story building a fundamental period is 0.1 seconds, or a first predominant frequency equals to 10 Hz. This assumes the building's stiffness does not greatly vary between the two axes and is symmetric.

The measurement data from all accelerometers were recorded as time histories, in digital form, using a nominal 16-bit analog to digital (A/D) conversion recording. The time histories were then post-processed for selected events for further analysis. The results are in the form of acceleration time histories, computed velocity time histories, and computed displacement time histories. Further post-processing also provided the following results: corrected acceleration time histories; computed and corrected velocity and displacement time histories; acceleration Fourier amplitudes; Residual Velocity Shock Spectra (RVSS), and acceleration auto-spectral density (ASD) functions. The data processing and results are discussed in more detail below.

4.5.1 Structural Vibration of APG Building 2001

Figure 4-17 shows a plot of raw acceleration data for a series of six consecutive gun firing events (B1-B6) recorded at APG Building 2001 on 9 November 2004 within a three-minute interval. The data were collected using 14 accelerometers (channels 01 through 14) installed at the building as described in Subsection 3.1.2.1. Figure 4-18 shows an example of how the events were selected for the ensuing analysis. The dotted box around each of the events for channels 01 and 12 in this example show the corrected event in red. The raw data was processed, in order, by selecting points before and after the event of interest, applying a Tukey window (a half cosine

tapering window to reduce leakage effects when calculating frequency transforms), removing the linear trend, applying a 5-pole low-pass butterworth filter, padding with zeros or truncating the selected record, as necessary (creating a 16,384-point data record). The data records were saved in a MATLAB format. Another MATLAB m-file processed the selected acceleration time records to calculate velocity time histories, displacement time histories, and frequency functions of interest. Figure 4-19 shows the result of the processing procedure for the selected event B1 for all channels.

Examples of corrected acceleration time histories with computed and corrected velocity and displacement time histories for event B1 are shown in Figure 4-20 for channels 01 and 12. Location 1 for accelerometer channel 01 is shown in Subsection 3.1.2.1, Figures 3-8 through 3-13. Referring to Table B-1 of Appendix B, the location of channel 01 is noted as: 1-x. This indicates that the sensor on channel 01 had the positive polarity pointing in the "-x" direction with respect to the x-y coordinate system for the building in plan.

The next step was computing spectral functions from the time histories. The acceleration ASD functions are easily converted to energy spectral density functions by multiplying each value by the value of the signal length (as number of points). The last row of every ASCII file includes a number which indicates the number of points of the original signal of the event selected, L. This matters when the signal length required padding with zeros to bring the total number of data points to the next power of 2 for the most efficient Fast Fourier Transform (FFT) calculations. The auto-spectral density functions and RVSS functions use L for the length of signal in which the energy resides. The FFT calculation uses a number of FFT points, nfft, which is the next power of 2 if the record was padded with zeros. Because of spurious transients recorded among the blast events of interest it was necessary, when selecting time events as described above, not to include other events, when possible, not caused by the gun firings.

Examples of acceleration Fourier amplitude $|A(f)|$ and of acceleration ASD function $|Ga(f)|$ for event B1 are shown in Figure 4-21 for channels 01 and 12. The acceleration ASD functions for a group of blast events from B1 through B20 are shown in Figure 4-22 (a) and (b) for channels 01 and 12, respectively, including the mean value for the group. Example of plots of RVSS and the mean value for that data group are shown for channels 01 and 12 in Figure 4-23.
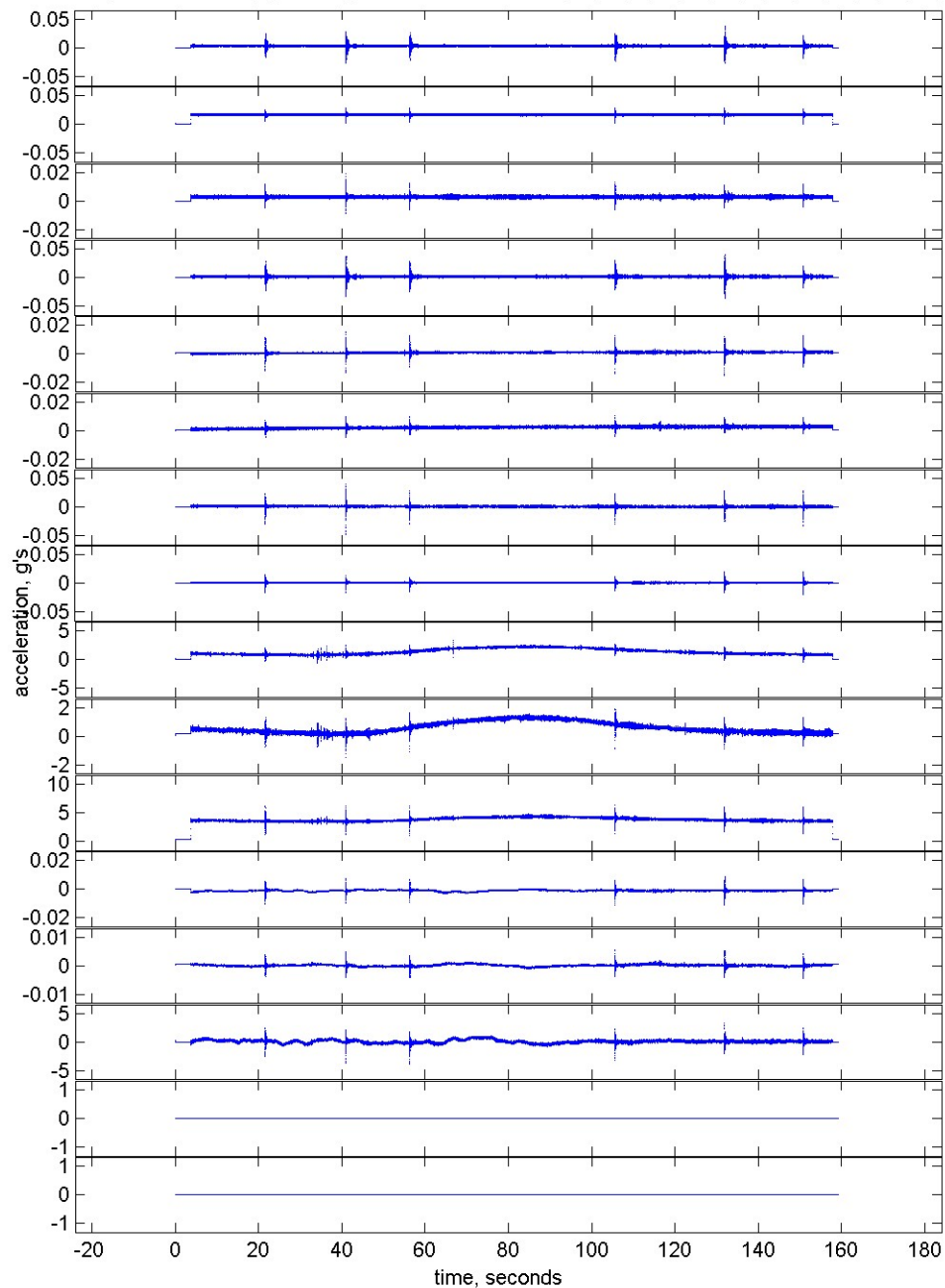
Figure 4-17. Example of Structural Acceleration Data Recorded at APG Building 2001 for 105 mm Tank Gun Firing
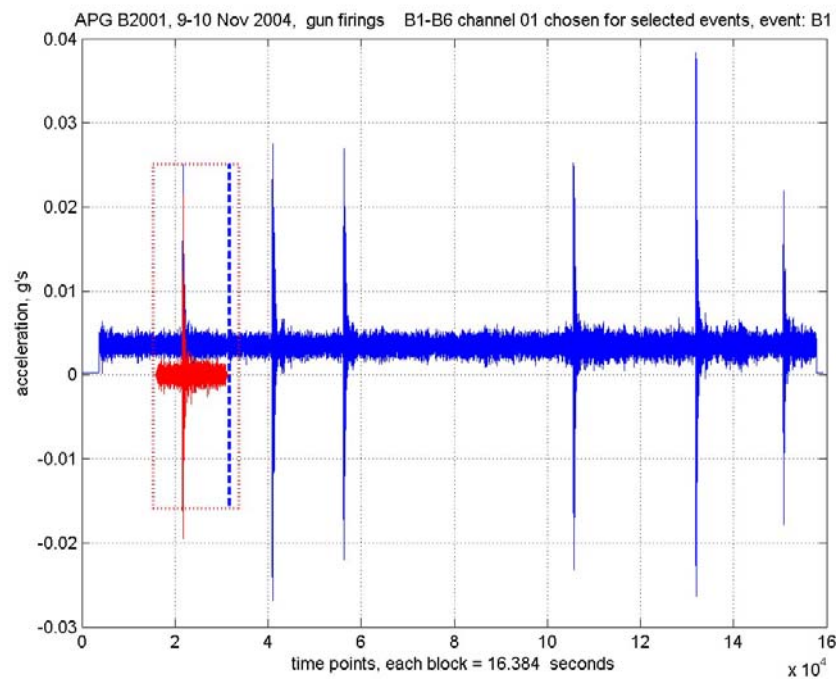
(a) Channel 01
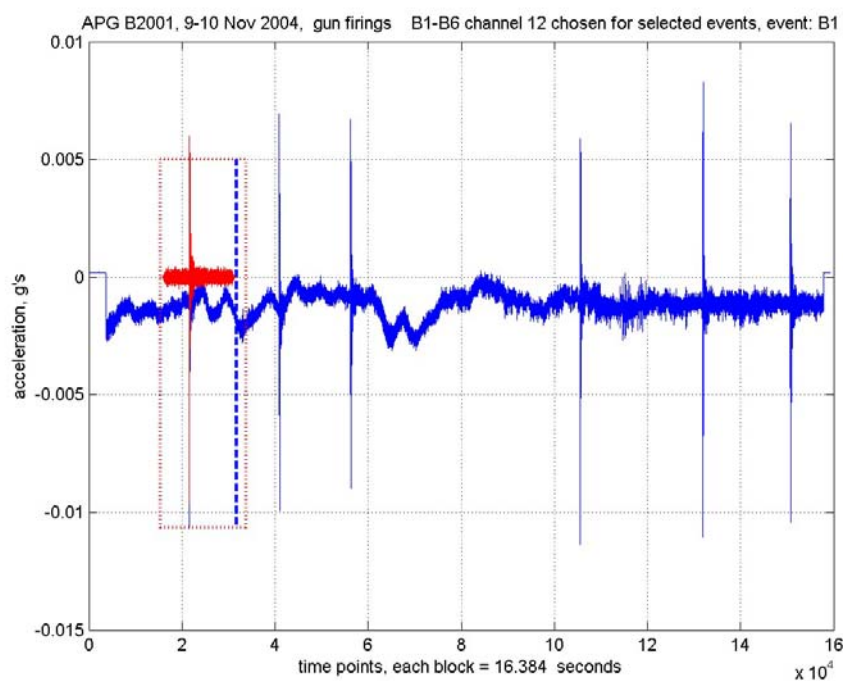
(b) Channel 12

**Figure 4-18. Example of Event Data Selection and Correction for:
(a) Channel 01 and (b) Channel 12; Corrected Events Shown in Red**
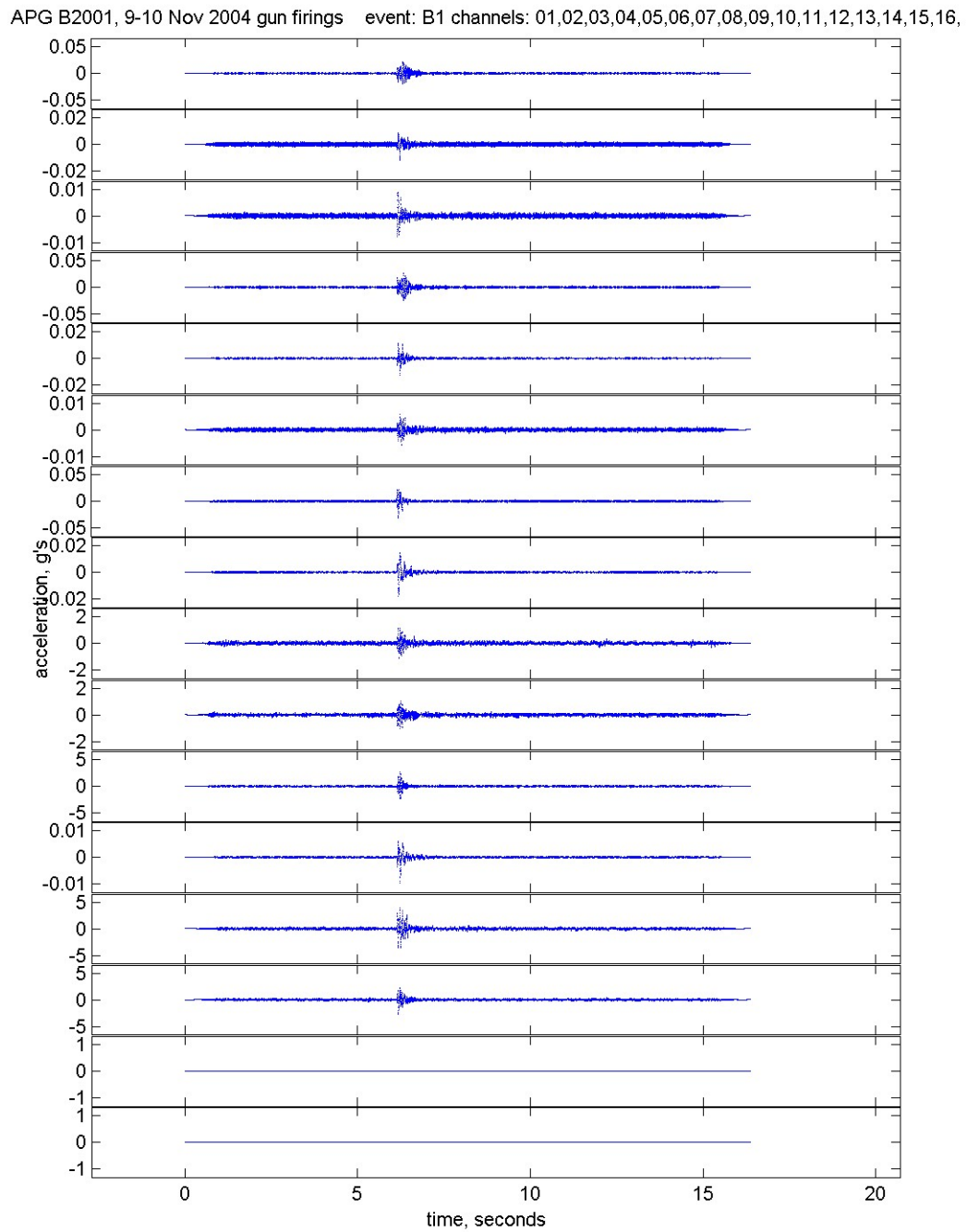
Figure 4-19. Corrected Acceleration Time Histories for Event B1
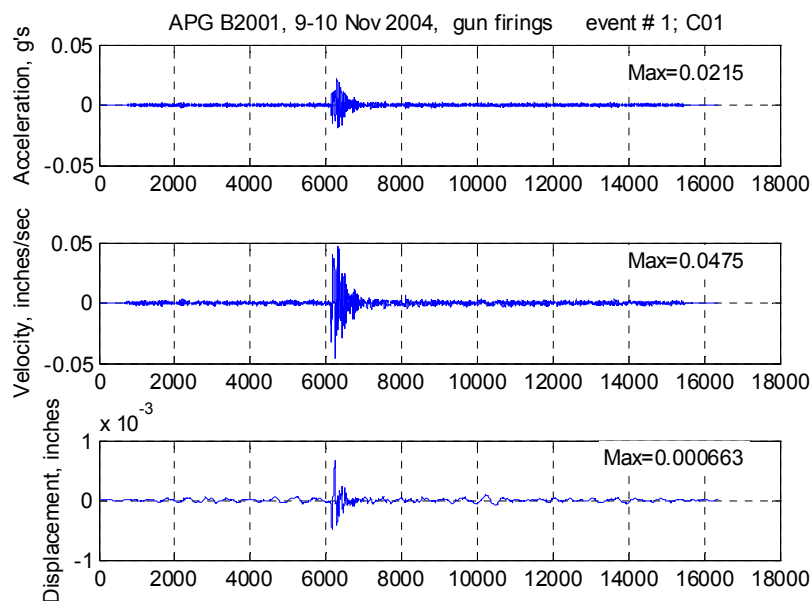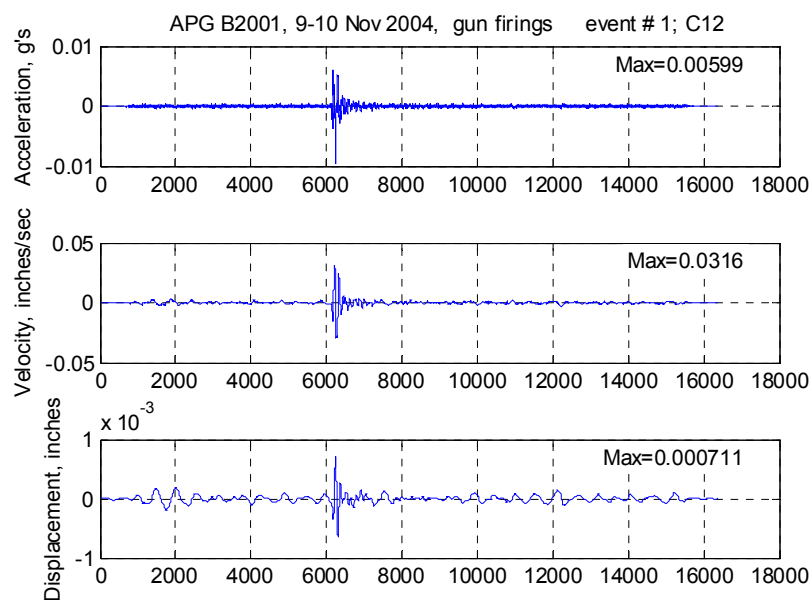
(a) Channel 01

(b) Channel 12

**Figure 4-20. Corrected Acceleration, Velocity, and Displacement Time Histories for
Event B1: (a) Channel 01; and (b) Channel 12 (Time in msec)**
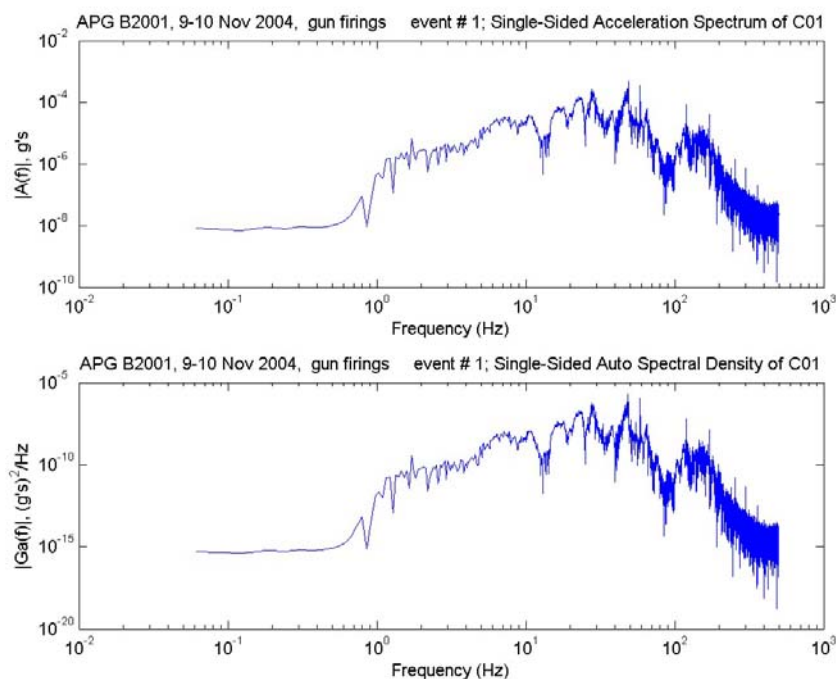
(a) Channel 01
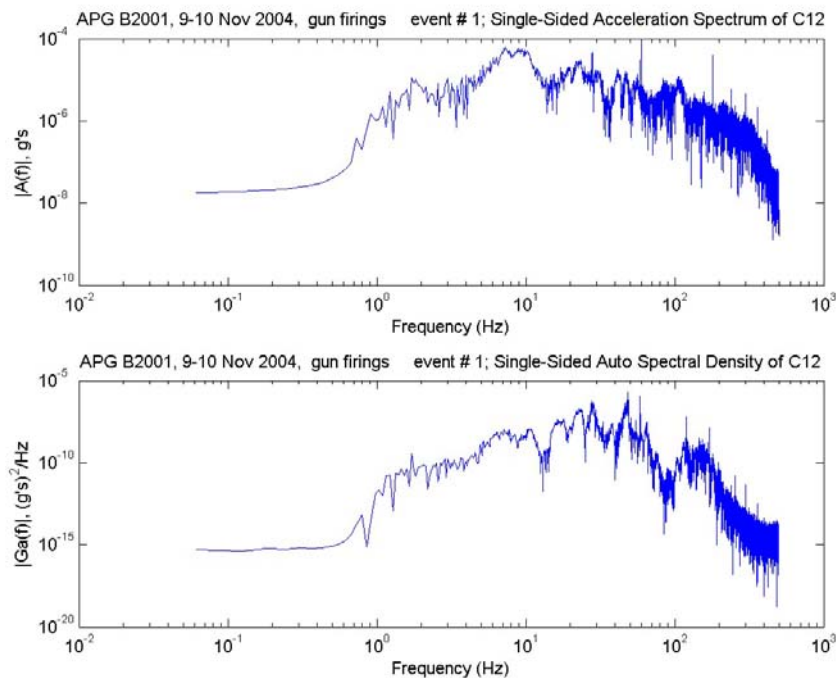
(b) Channel 12

**Figure 4-21. Acceleration Fourier Amplitude |A(f)| and ASD |Ga(f)| for
Event B1: (a) Channel 01; and (b) Channel 12**
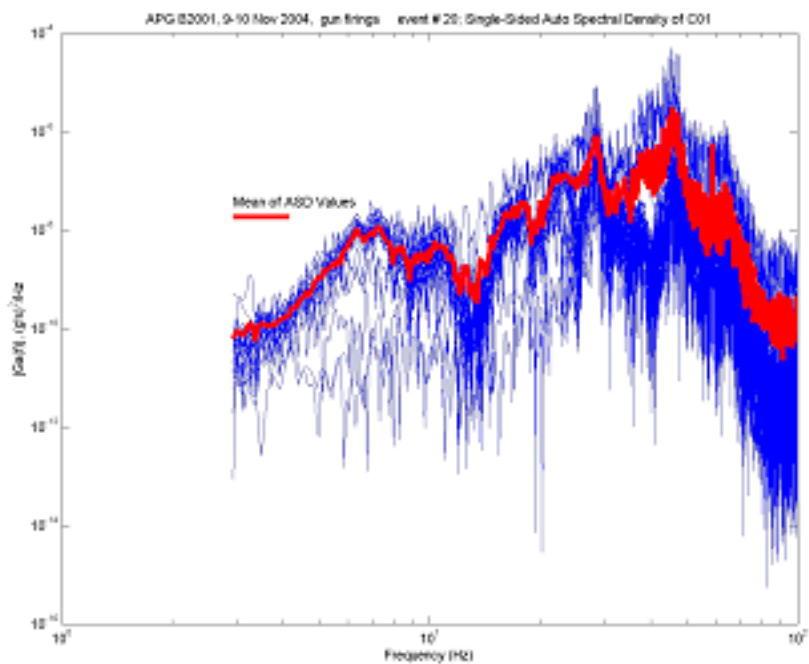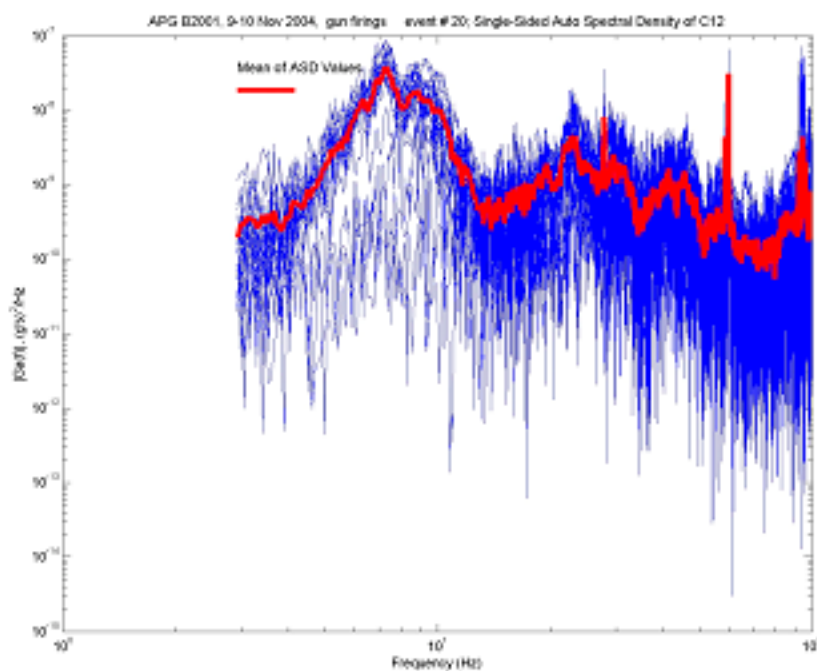
(a) Channel 01

(b) Channel 12

Figure 4-22. Acceleration Auto-Spectral Density for Events B1 through B20 for:
(a) Channel 01 and (b) Channel 12
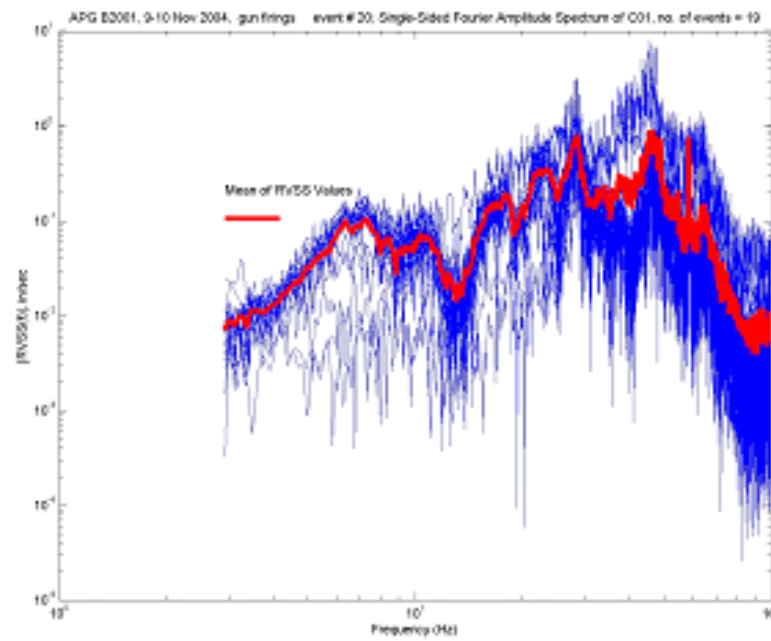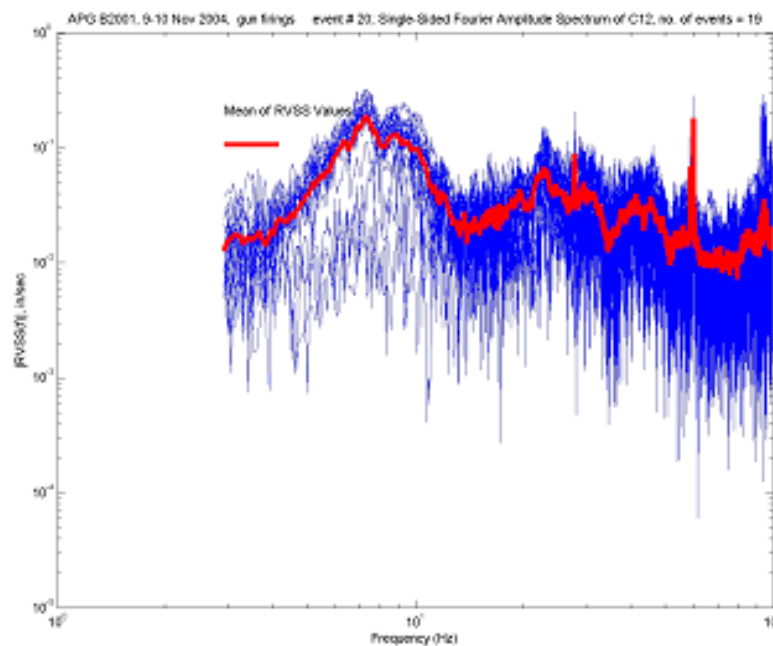
(a) Channel 01

(b) Channel 12

**Figure 4-23. Residual Velocity Shock Spectra for Events B1 through B20 for:
(a) Channel 01 and (b) Channel 12**

4.5.2   Structural Vibration of MCAAP Building 72

Several measurements were recorded and analyzed for MCAAP Building 72 using the processing procedure described in the previous subsection. A description of the building is given in Subsection 3.1.4.2. The data analysis is performed for a tri-axial accelerometer mounted to the roof rafter in the SW corner of the building.

The critical feature of the recorded vibrations is that each pit blast at this measurement site is similar, well spaced between events (approximately 25 to 30 seconds), and well identified. This is illustrated in Figure 4-24, showing acceleration recorded on three data channels 01 through 03 (from top to bottom) of the tri-axial accelerometer from pit blast events on 11 August 2005.
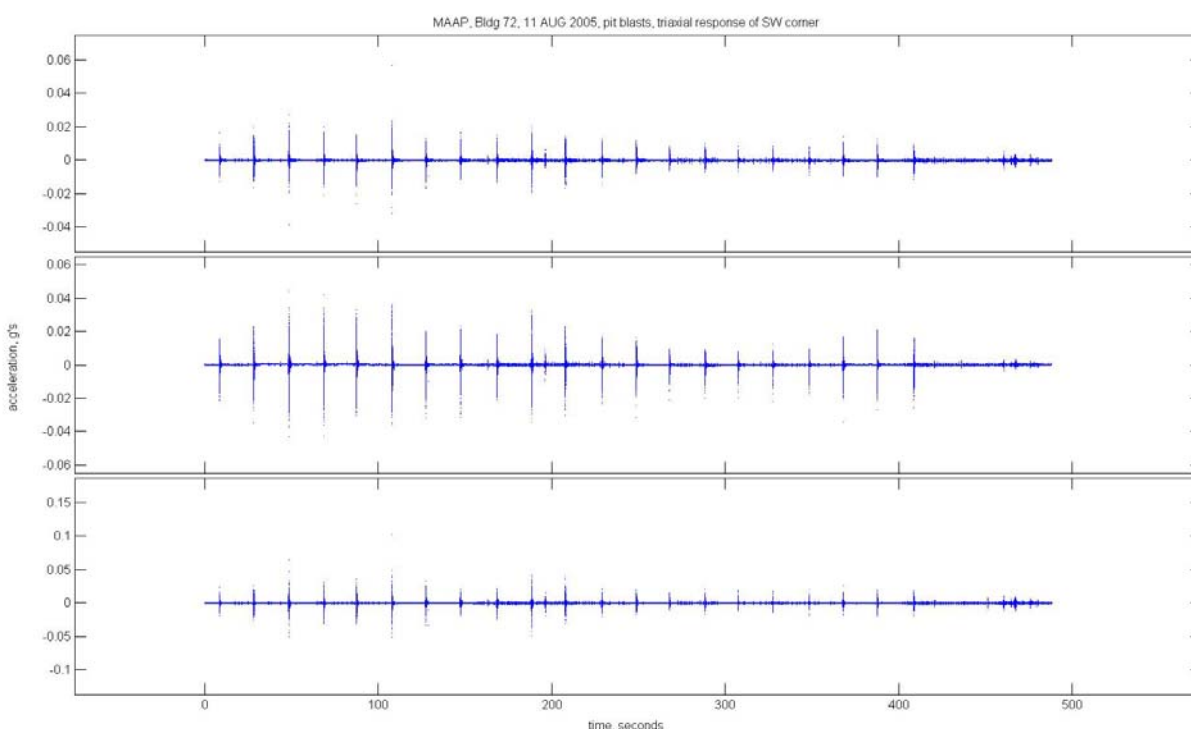
Figure 4-24. Acceleration Time Histories from Tri-Axial Accelerometer at MCAAP Building 72

The pit blast events subject the buildings to consistent stimuli and thus each event is independently treated as separate transient event, very similar to response vibrations of a building (or structure) subjected to impacts during a hammer modal test. Each transient response is segmented and the resulting auto-spectral density functions are averaged, producing a statistical frequency function. From these results, it is reasonable to apply cross-spectral techniques to estimate phase relationships between response points, estimates of coherence, and estimates of mode shape vectors assuming that the operational deflection shapes (amplitudes estimated from peak amplitudes at selected frequencies) is a good representation of the true mode shape for a specific natural frequency. Also, damping is estimated using a half-power

bandwidth method, where the peaks in the auto-spectral density function reveal well separated modes (such that the half-power points do not intersect or overlap).

A closer view of the acceleration data for an individual event (one pit test blast before a series of actual detonations of the pits) is shown in Figure 4-25 for channel 01 of the tri-axial accelerometer in a time window of about six seconds.
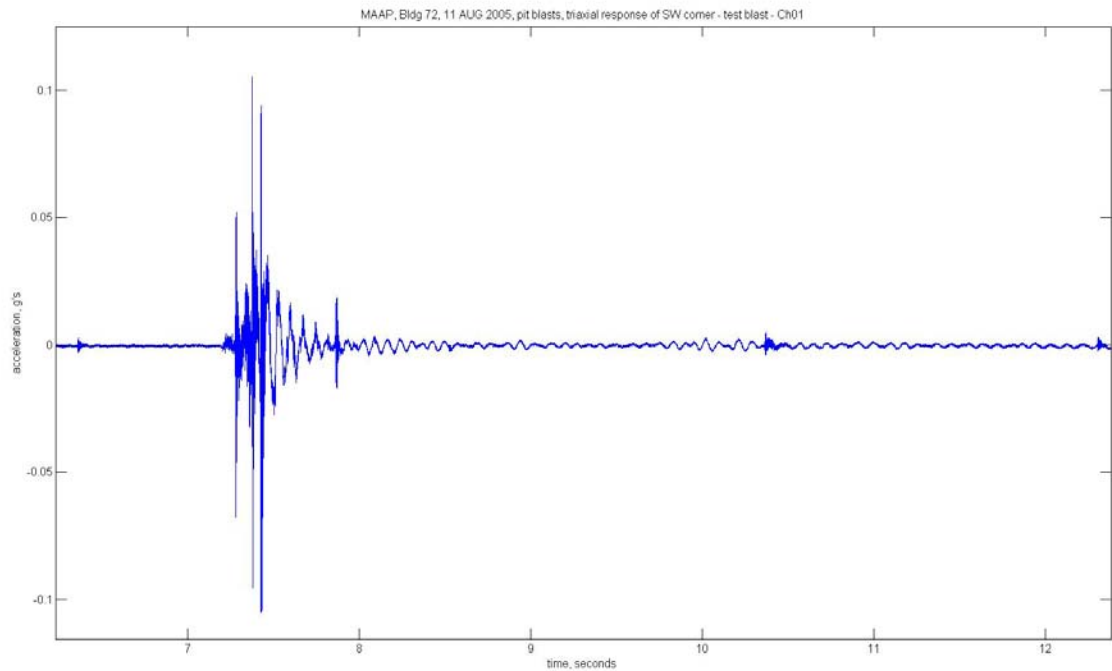
**Figure 4-25. Acceleration Time History from Channel 01 of Tri-Axial Accelerometer for
Test Blast at MCAAP Building 72**

It can be seen from the figure that the higher frequency vibration responses of the building (at the beginning of the response signature) attenuate first, after which a predominant building mode is revealed.

4.6   Experimental Results of Building Modal Testing

Modal testing performed at selected DoD facilities as described in Section 3.0 included electro-dynamic shaker excitation (controlled with random and sinusoidal signals) and instrumented hammer impacts.

The objective for the modal tests is to identify the global building resonances that occur when subjected to noise impulses as from gun firing that occur as a result of military training activities. The identification of these global building responses is then used to correlate to measurements on particular components of windows to understand more fully the interaction response effects of the building with general window system (window sill, frame and glass) when subjected to noise impulses. In this way, with modes identified from an impact modal survey, forced-vibration

excitation from electro-dynamic shakers, or Operating Deflection Shapes (ODS), it is possible to relate resonant frequencies at other measurement locations during the gun firings to global building responses. The basic excitation methods applied, such as the impact modal survey and using electro-dynamic shakers to excite residential structures were documented by Chiarito and Hall.[42] A broad description of many applications of forced-vibration testing to identify dynamic properties important for understanding structural responses due to impulse loadings is also summarized from case studies noted by Crowson.[43]

From measured response data alone it is possible to estimate linear parameters for the natural frequencies, mode shapes (as operating deflection shapes, ODS), and damping (as estimated from a half-power bandwidth method) (see References 44, 45, 46). Ideally, it is desirable to measure directly the force input time history simultaneously (as in independent and parallel data acquisition) with the measured responses of motion sensors (e.g., accelerometers) in orientations of interest (see References 47 and 48). For example, to measure side sway or torsional responses of a building, sensors are mounted horizontally near the corners (on or close to the connections of the structural framing elements) at upper floor or attic levels. Thus, the global movements of the building are measured and identified with particular resonant frequencies. It is at these resonant frequencies the energy content of stimuli in the form of air blast, wind, or other energy inputs from noise or vibrations is amplified or dissipated by the building structure subjected to the stimuli.

4.6.1 Modal Estimation Procedure

The general method to estimate ODS parameters follow that cited in Bendat and Piersol[45] and also discussed by others (e.g., Richardson and Schwarz[49]; Batel[50]). This is the most basic procedure before resorting to more sophisticated techniques of operational modal analysis. The basic procedure works well for well separated resonant and linear responses and assuming the damping ratios of interest are less than values of 0.1. The basic procedure outlined in Bendat and Piersol is applied here as follows:

1. The resonant frequencies are estimated as frequencies at which peak values are identified in the auto-spectral density (ASD) functions of measured responses.
2. The damping ratio estimate for any identified resonant frequency is given by the half-power bandwidth method.
3. The coherence function computed between paired channels of data is used to identify and confirm presence of suspected normal modes – a value close to 1.0 indicates 100 per cent linear correlation.
4. The cross-spectral density (CSD) is computed and the phase component establishes whether paired channels are in phase (0 degrees) or out of phase (180 degrees) at suspected or identified resonant frequencies.
5. The magnitude of the mode shape vector is approximated by the square root of the magnitude of the ASD functions associated with the identified or suspected resonant frequency.

The simplest FRF curve permits estimating the mode shape vector amplitude from the imaginary (quadrature or "quad") part of the FRF corresponding to a near zero value of the real (coincident or "co" part of the FRF). This method is sometimes called the "peak-picking", the "quadrature

peak", or the "co-quad" method. This method works well when normal modes are well separated (i.e., the half-power points of the nearest resonances do not overlap). If normal modes are separated adequately, then multiple degree-of-freedom curve fitting methods are available. For the measurements obtained it was determined that the results from the peak-picking method were sufficient to understand the building responses occurring at selected resonant frequencies. The direction or phase (in relation to other measurement locations) is determined from the phase of the FRF. For normal modes, where the force input is directly measured, the phase angles between a measurement location and the input-force is either 90 or 270 degrees out-of-phase. For modal estimates for ODS, the phase calculated between measurements locations from the cross-spectral density functions serve to identify the direction, as either the phase angle is 0 (in phase) or 180 degrees (out of phase). It is possible that even with the measured force time history, that ODS are applicable for a comparison to parameters estimated from various curve fits of FRFs.

The damping ratios are estimated using the half-power bandwidth method. Figure 4-26 illustrates the use of the half-power bandwidth method to estimate the damping ratio from computed ASD. The method is valid when the vibration modes are sufficiently separated (at the very least when half-power points of neighboring modes do not overlap) and the damping ratio is less than 0.1, i.e., for lightly damped systems.
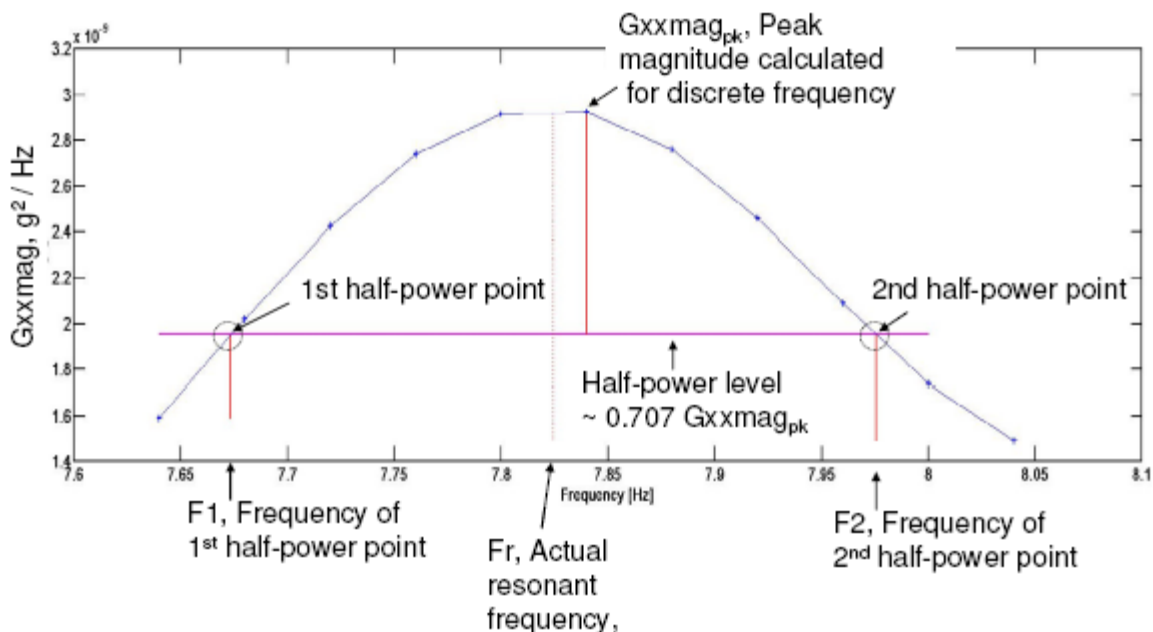
Figure 4-26. Application of Half-Power Bandwidth Method

The approximate fundamental period for a building plain in plan, can be estimated also as a function of the number of stories (typically up to 10-ft story heights, somewhat of a nearly square plan in geometry and with a center of mass nearly at the geometric center in plan) as $T^f = 0.1N$, where N is the number of stories and T^f is the fundamental period in seconds. Thus, for any general one-story building the fundamental period is estimated at 0.1 second, or a frequency of 10 Hz. More accurate estimates of fundamental periods involve the use of a

procedure to estimate the mass and stiffness distributed along the height of the building. Also, first estimates of calculated mode shape vectors are obtained using this procedure. However, calculating refined estimates of the fundamental periods and corresponding mode shapes of the buildings tested was beyond the scope of the current effort.

The application of the modal estimation procedure is described in details in the next subsection using an example of APG Building 2006, followed by the general discussion of the modal results obtained for the other tested buildings.

4.6.2   Modal Analysis for APG Building 2006

Modal results for APG Building 2006 are natural frequency estimates from measured transient responses of selected hammer impacts and forced-vibration excitations from an electro-dynamic shaker during November 2004 activities. Also, responses from gun firing events provided another estimate of modal parameters estimated using the ODS approach. The measurements included data from setups where two to eight channels of acceleration were measured at the ceiling (just below the attic) level. The building and instrumentation setup are described in Subsection 3.1.2.2. These measurements included channels oriented to monitor motions in the approximate east-west direction and six channels oriented to monitor motions in the approximate north-south direction. With this layout the lowest side sway modes and first torsional mode was identified. Other higher order modes are present as indicated by distinct peaks in the frequency response functions, but spatial resolution of the measurement locations limits the ability to discern accurately the full picture of the mode shapes for these higher order normal modes.

The most significant responses, as evident from the peak magnitudes of the acceleration ASDs, of the building exist between 10 to 35 Hz. The modal results are the estimates of the resonant frequencies identified from the peaks of calculated FRF functions, estimates of the damping ratios for the identified resonant frequencies, and estimates of the mode shape vectors identified from fits to the picked peaks of the FRF at the corresponding resonant frequencies. An example of the procedure follows for processing time response data to estimate the modal parameters.

Figure 4-27 shows a set of measured responses from instrumented hammer impacts. The hammer impacts create transient responses generally comprised of several resonances. The figure shows an example of two measured acceleration time histories which were selected as time ensembles for analysis. Time limits for each ensemble are shown by dotted boxes. Some overlap, or using some data from previous or subsequent ensembles, may occur. However, the selection of a portion of the data prior to the peak response (a pre-trigger or delay portion) and a selection of data past the peak response to where the record sufficiently decays was chosen, such that independent responses were obtained.
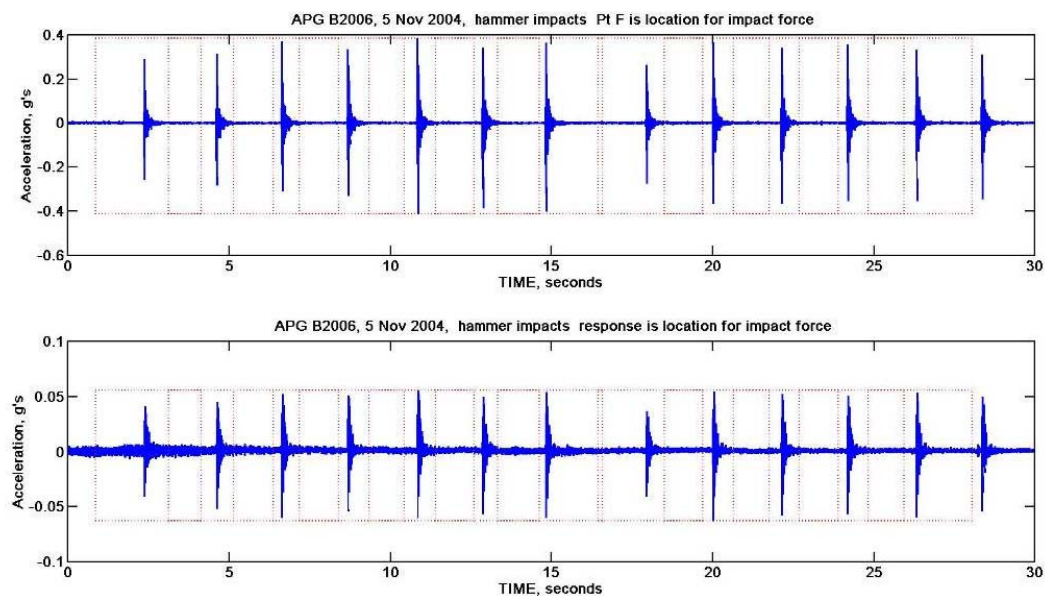
Figure 4-27. Example of Selected Acceleration Response Time Ensembles for ODS Modal Processing

Figure 4-28 shows four ensembles concatenated with padding of zeros where necessary to obtain sufficient record lengths for specified frequency resolution. The frequency resolution is 0.04 Hz for all modal analyses.
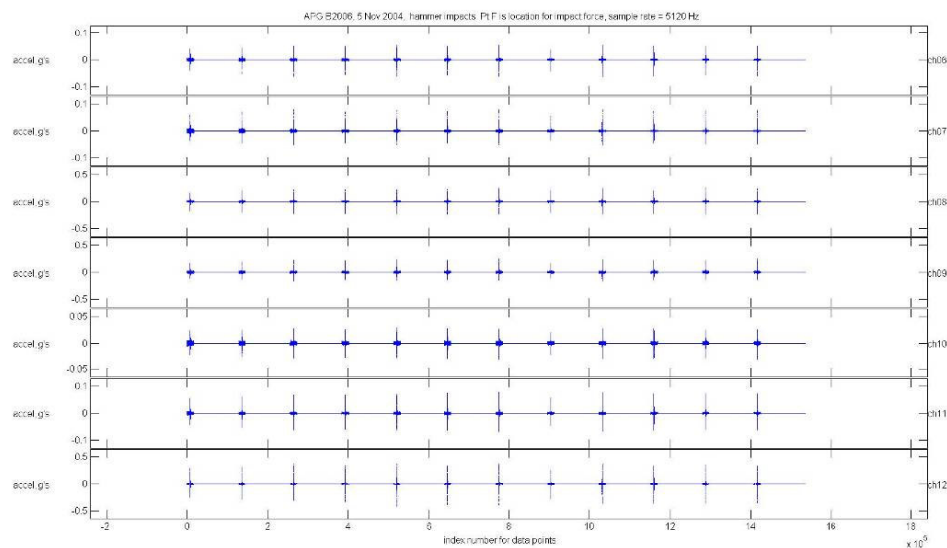
Figure 4-28. Example of Concatenated Acceleration Response Time Ensembles

Figure 4-29 shows an example of three spectral results for a cross-reference, or correlation, between two measurement points (i.e., 1x and 5x): CSD phase, CSD magnitude, and coherence.
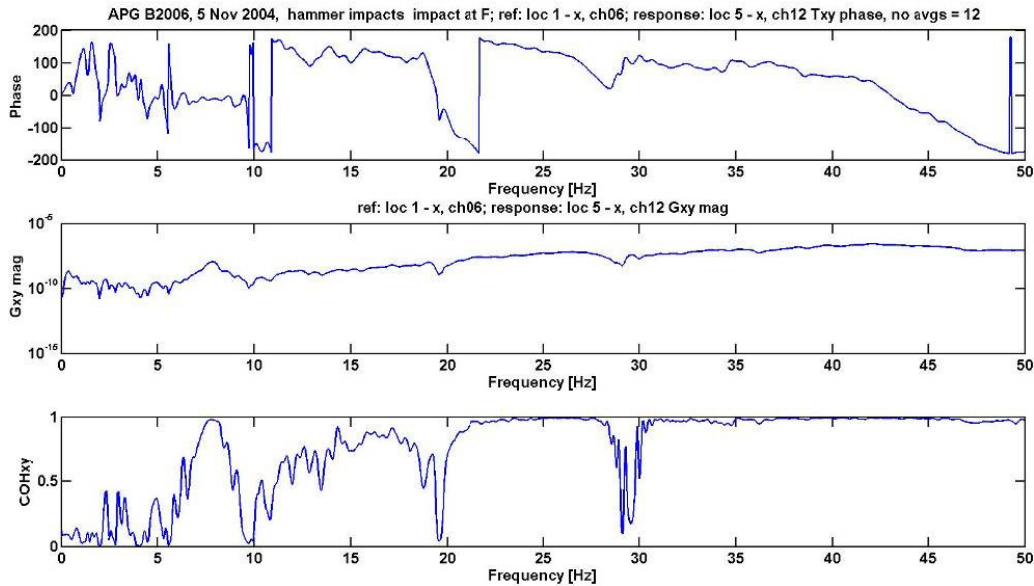
Figure 4-29. Example of Computed CSD Phase, CSD Magnitude and Coherance Functions

Figure 4-30 shows CSD magnitude values for all measurement points and a sum of all the CSD magnitudes (shown as a black dashed line as the upper bound). The latter set of values provides an initial approximate "mode indicator function" (MIF) to help identify most likely resonant frequencies in terms of an absolute upper bound. Also in Figure 4-30, the bottom plot shows all the coherence values for the computed CSDs. The red dotted portions of both sets of plots indicate where the coherence values are less than ideal (approximately 0.5 or less), and where the portions are plotted as solid blue lines, the coherence values are above 0.5. The coherence value of 0.5 was chosen as an initial criterion to help decipher where true normal mode (linear) responses are possible to identify.
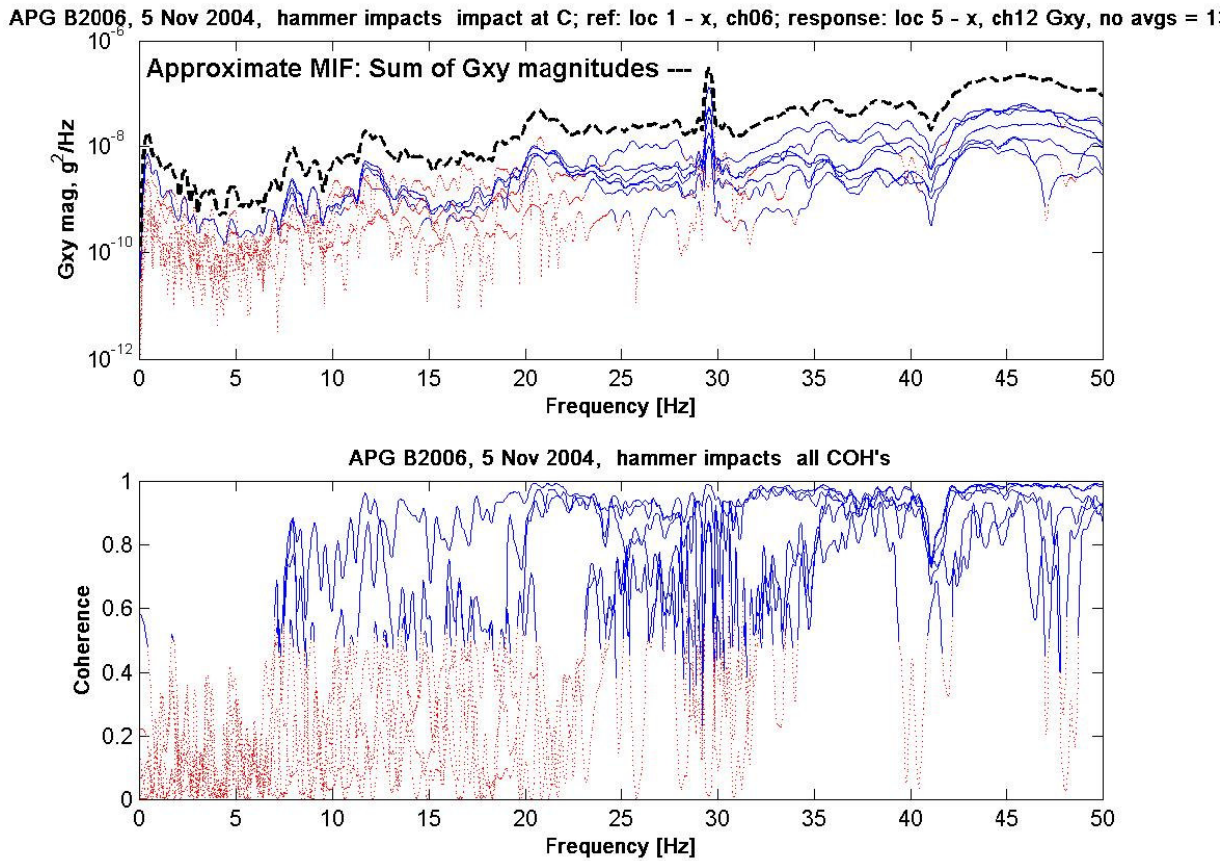
Figure 4-30. Example of Overlaid Functions for CSD Phase, CSD Magnitude and Coherence for Entire Set of Response Measurements

Table 4.1 summarizes the resonant frequencies identified for the largest resonances from sets of cross-spectral density (CSD) functions. The range and mean of damping ratios are also listed. Damping ratio estimates were obtained from each measurement where criteria for adequate values were met. It can be seen from Table 4.1 that many modal responses are evident below 20 Hz. At 30 Hz the energy was from harmonics of the HVAC fan motor (near measurement location 4).

**Table 4-1. Summary of Dynamic Parameters for Identified Resonances of
Maximum Responses for APG Building 2006**

ODS Description	ODS Mode ID	Frequency (Hz)	Damping Ratio		
			Min	Max	Mean
Side sway in N-S with some front wall bending and local response of west wall	1	6.99	0.023	0.075	0.046
Side sway in N-S and local response of west wall	2	7.82	0.005	0.043	0.031
Predominant side sway in E-W coupled with some N-S response	3	9.06	0.023	0.055	0.042
Some side sway in E-W, coupled with some torsion, local response of NE corner and SW corner	4	10.26	0.005	0.047	0.024
Torsional response	5	11.09	0.004	0.081	0.028
Torsional response	6	11.07	0.010	0.061	0.025
Side sway in E-W coupled with torsion	7	13.15	0.037	0.067	0.052
Local mode of West wall	8	16.19	0.006	0.041	0.023
Local mode of west in E-W, some torsion	9	17.52	0.007	0.032	0.021
Local mode of west in E-W, some torsion	10	18.34	0.008	0.027	0.015
Local mode of west in E-W, some torsion	11	19.30	0.034	0.046	0.040
Local mode of west in E-W, some torsion	12	20.30	0.012	0.071	0.043
Local mode of west in E-W, some torsion	13	23.49	0.007	0.075	0.027
Local mode of west in E-W, some torsion	14	26.86	0	0.097	0.026

The mode shapes are depicted as scaled vectors added to the coordinates of the measurement locations. Figure 4-30 shows the outline of building 2006 in plan and the corresponding position of measurement locations. The mode shapes only use the vector data recorded. For example, at measurement location 5 the component in the x-direction was recorded, but not the component of motion in the y-direction. Therefore, any y-direction (approximate east-west) response is not depicted relative to measurement location 5 in Figures 4-32 through 4-45, where the mode shapes for the selected frequencies are shown. As evident from observing the mode shapes displayed in Figures 4-32 through 4-45, not all represent truly global responses, where the measurements indicate the whole building movement following expected kinematics.
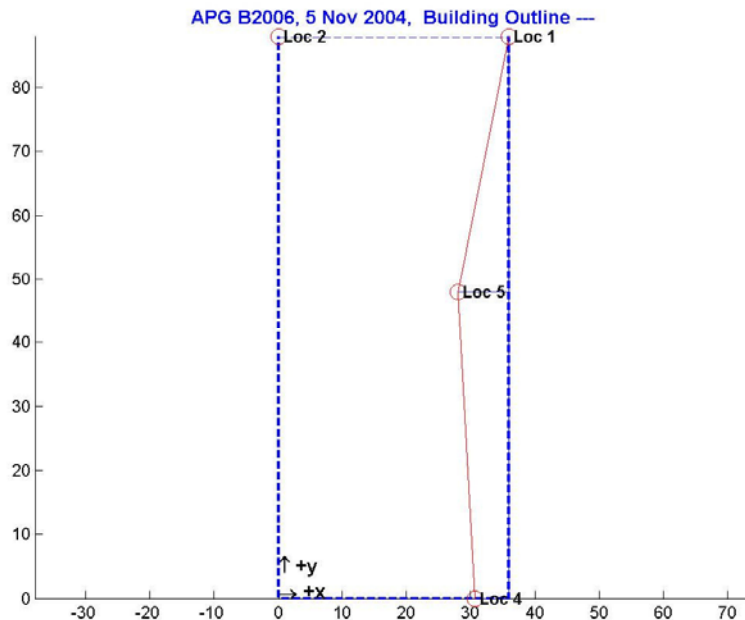
Figure 4-31. Undeformed Building Outline and Annotated Measurement Locations; x, y in feet
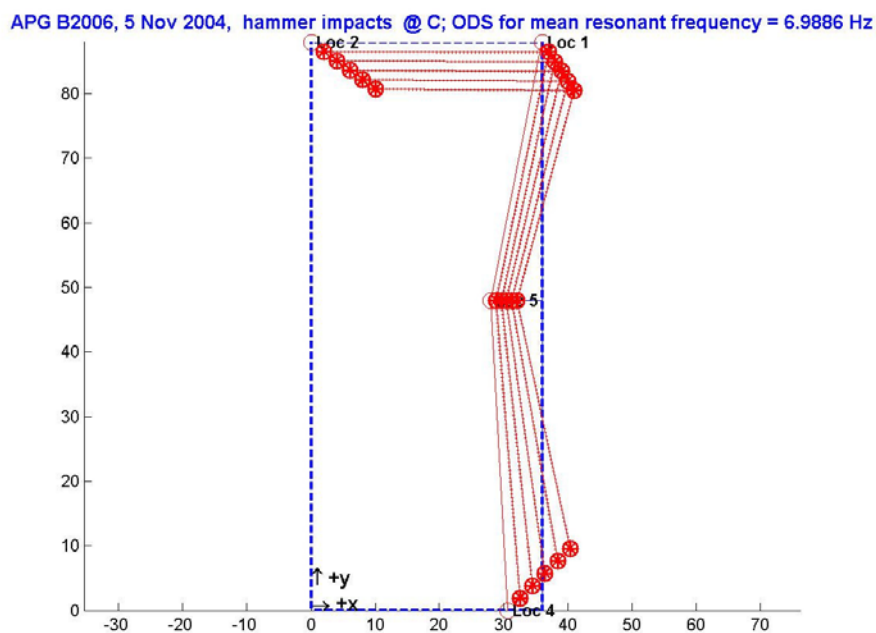
Figure 4-32. APG Building 2006 ODS Mode Shape Displayed Statically in Plan for 6.99 Hz; x, y in feet
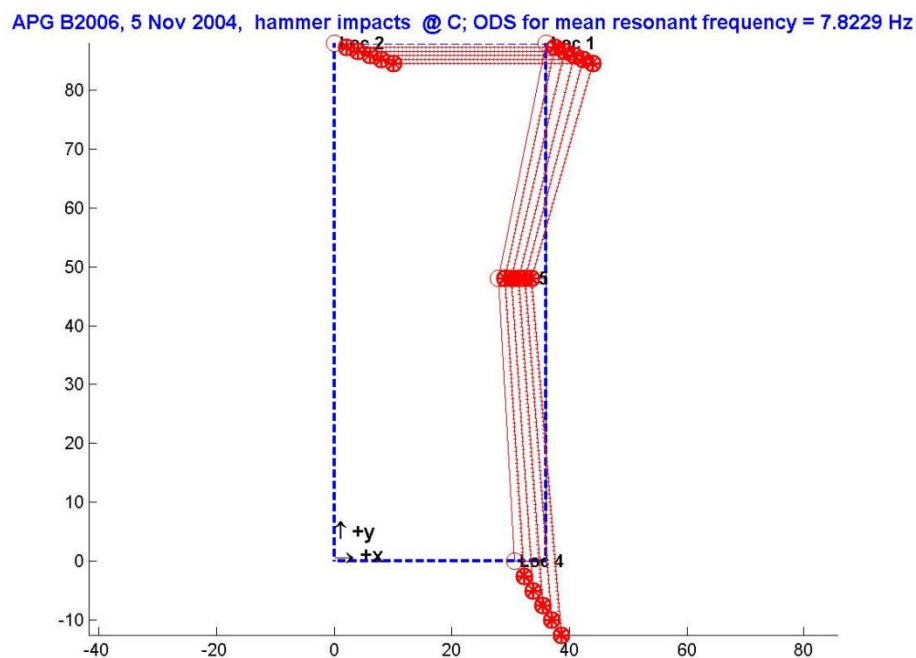
Figure 4-33. APG Building 2006 ODS Mode Shape Displayed Statically in Plan for 7.8 Hz; x, y in feet
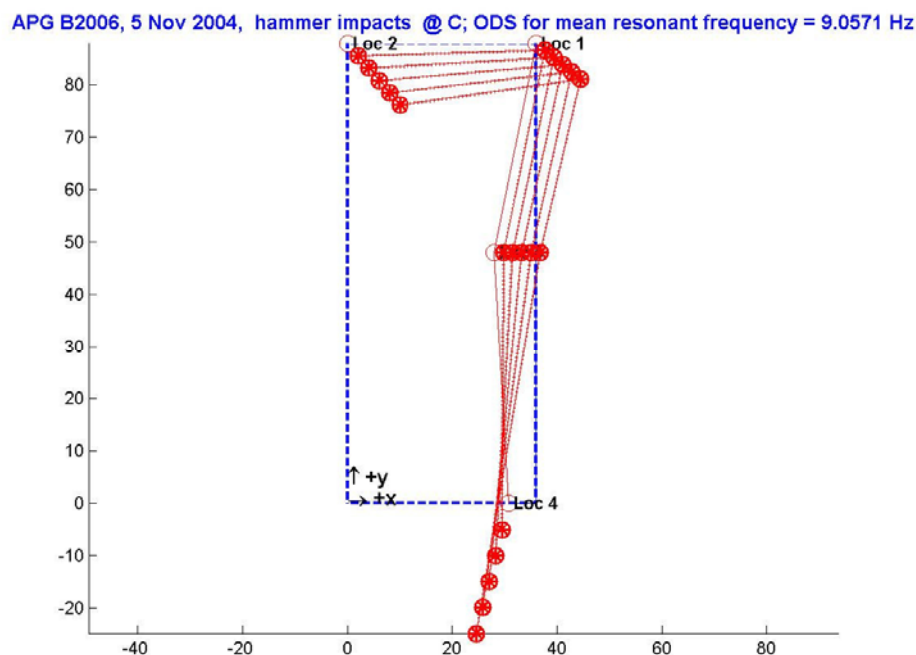
Figure 4-34. APG Building 2006 ODS Mode Shape Displayed Statically in Plan for 9.1 Hz; x, y in feet
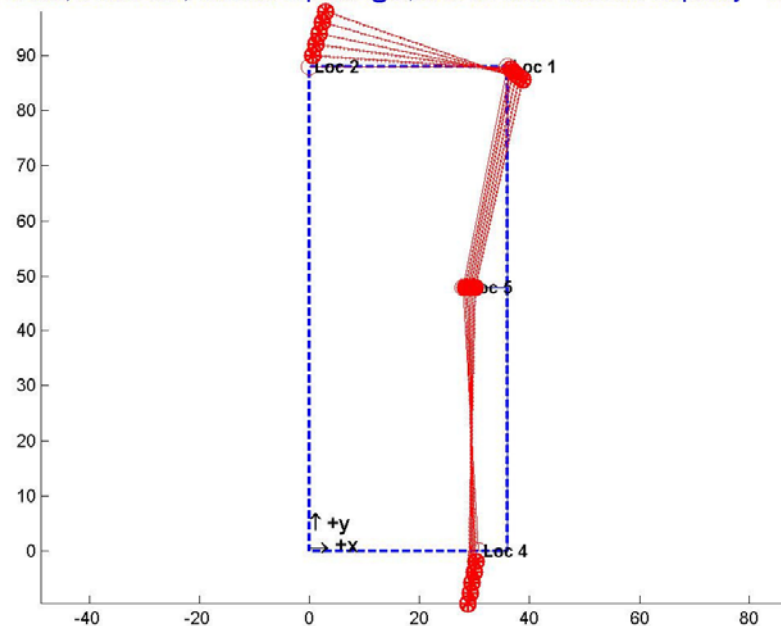
Figure 4-35. APG Building 2006 ODS Mode Shape Displayed Statically in Plan for 10.3 Hz; x, y in feet
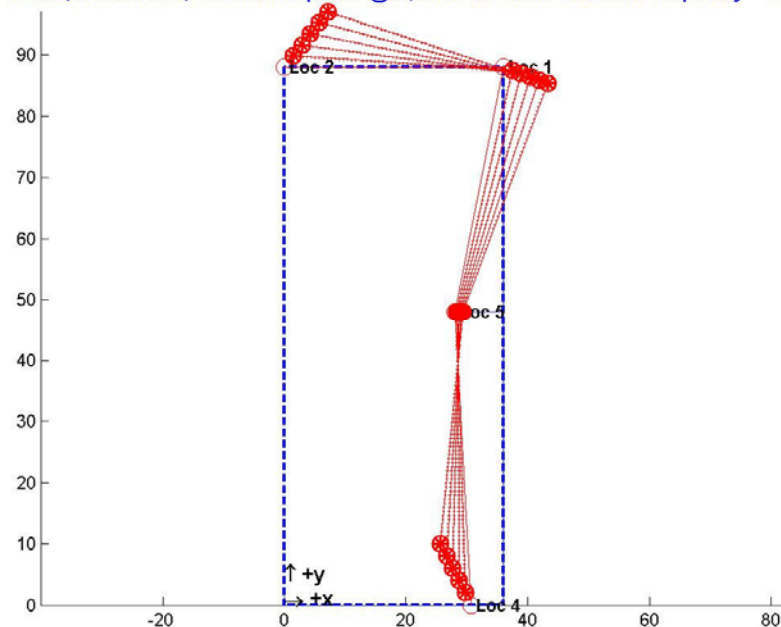
Figure 4-36. APG Building 2006 ODS Mode Shape Displayed Statically in Plan for 11.1 Hz; x, y in feet
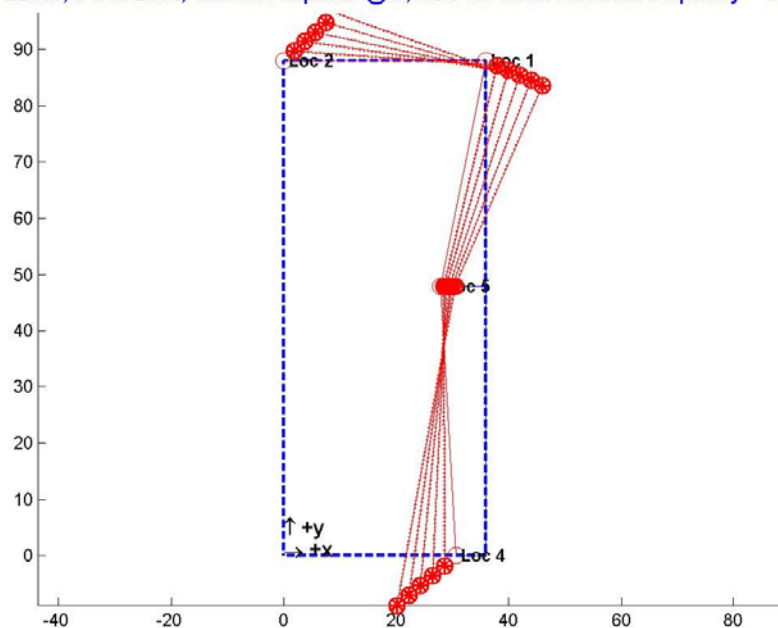
Figure 4-37. APG Building 2006 ODS Mode Shape Displayed Statically in Plan for 11.8 Hz; x, y in feet
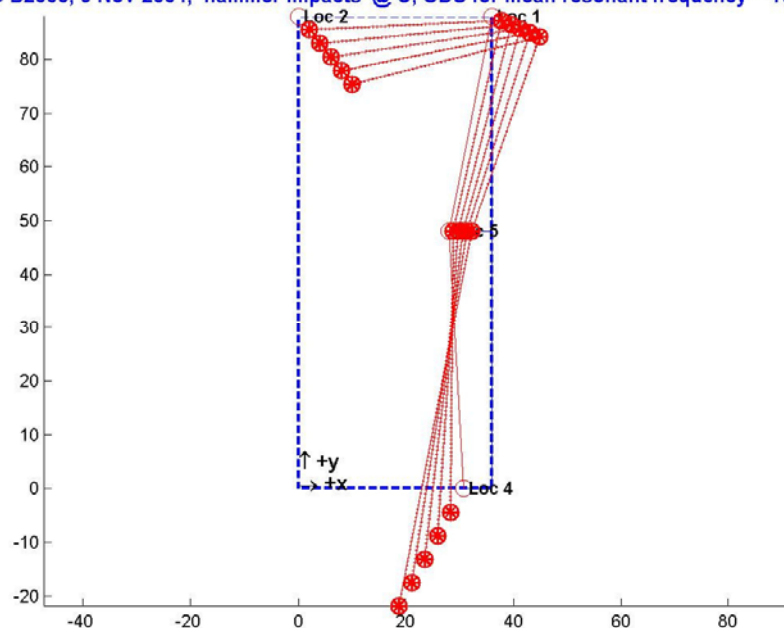
Figure 4-38. APG Building 2006 ODS Mode Shape Displayed Statically in Plan for 13.5 Hz; x, y in feet
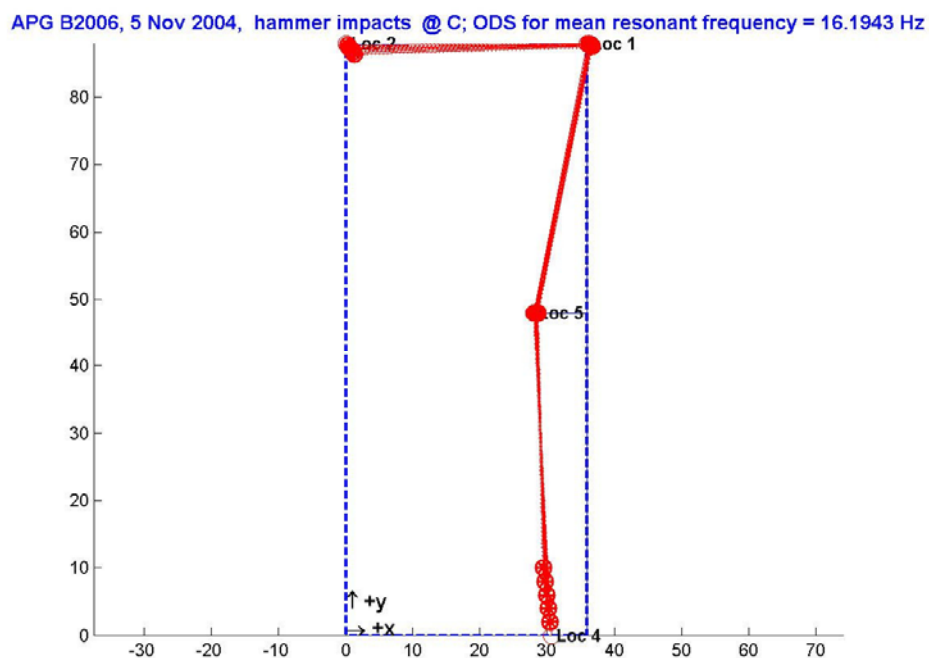
Figure 4-39. APG Building 2006 ODS Mode Shape Displayed Statically in Plan for 16.2 Hz; x, y in feet
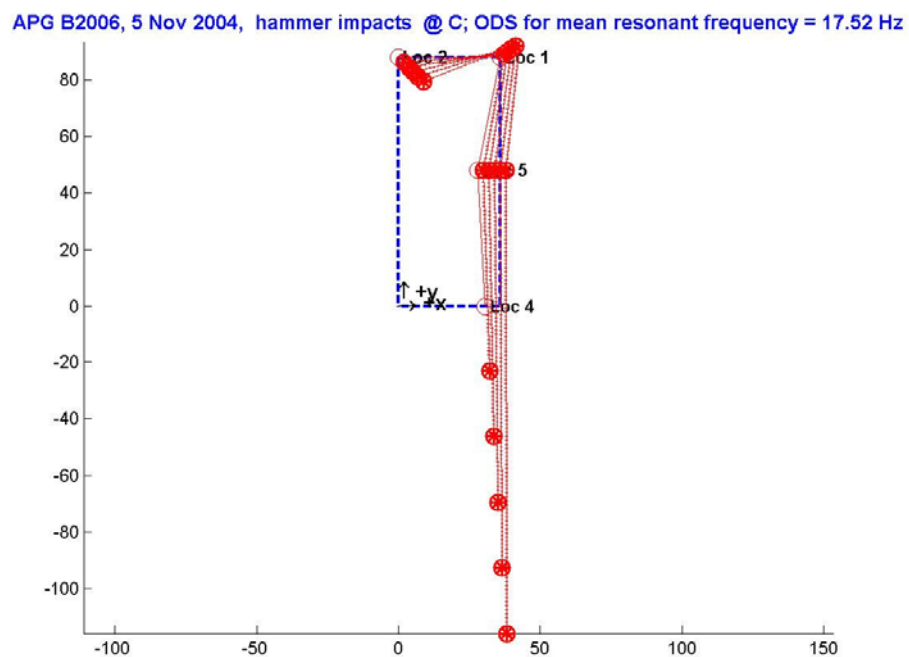
Figure 4-40. APG Building 2006 ODS Mode Shape Displayed Statically in Plan for 17.5 Hz; x, y in feet
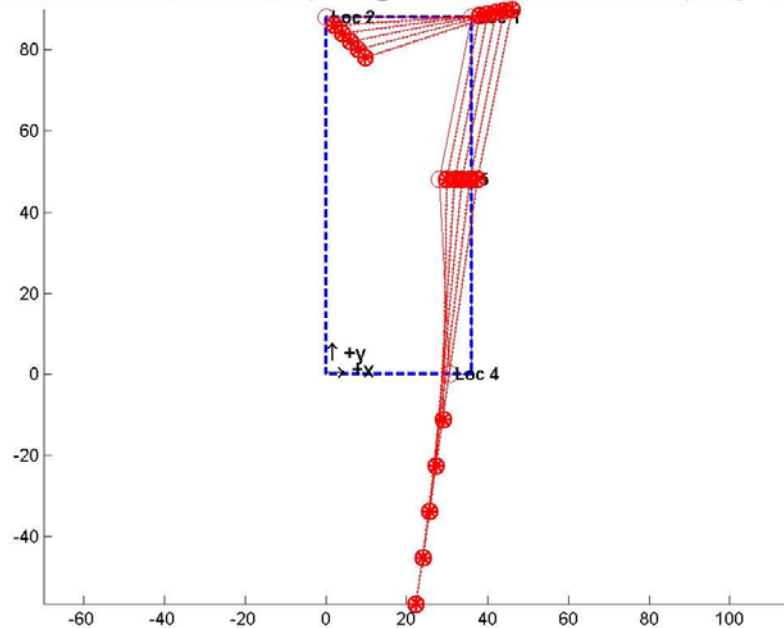
Figure 4-41. APG Building 2006 ODS Mode Shape Displayed Statically in Plan for 18.3 Hz; x, y in feet
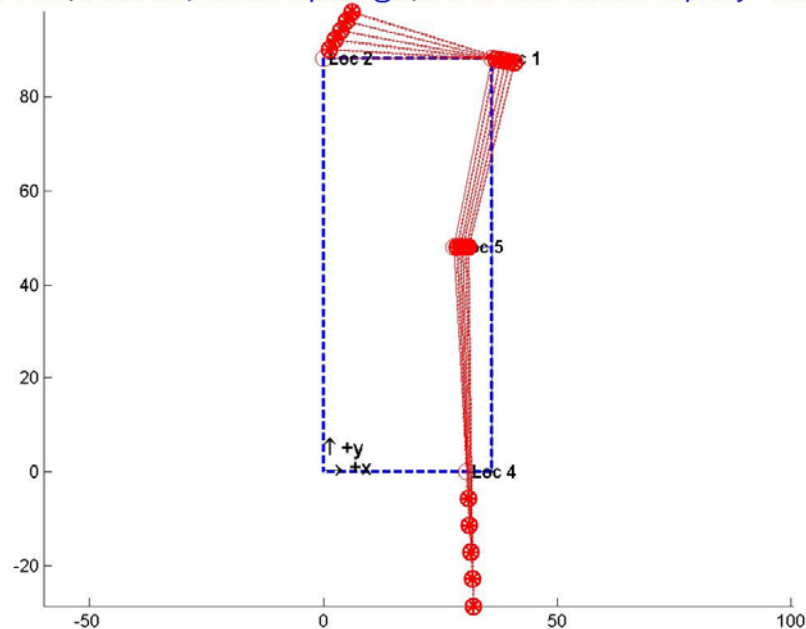
Figure 4-42. APG Building 2006 ODS Mode Shape Displayed Statically in Plan for 19.3 Hz; x, y in feet
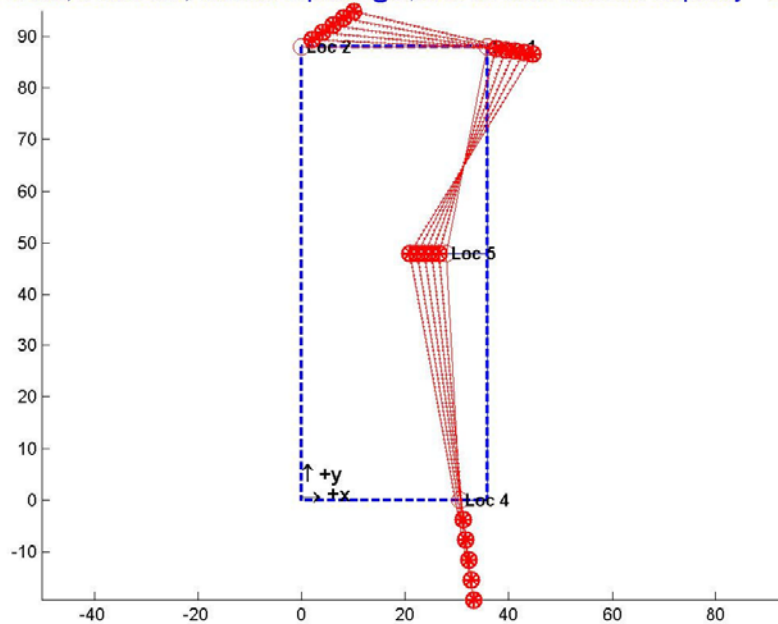
Figure 4-43. APG Building 2006 ODS Mode Shape Displayed Statically in Plan for 20.3 Hz; x, y in feet
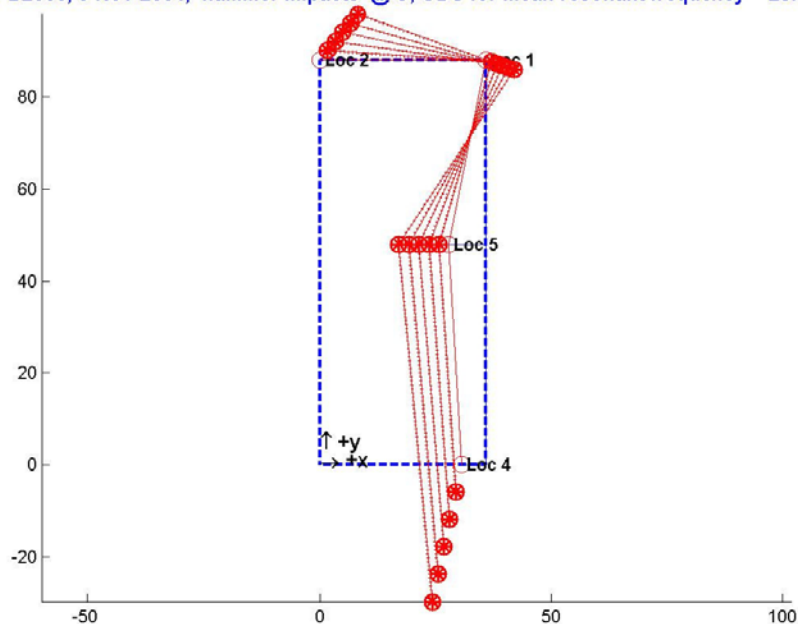
Figure 4-44. APG Building 2006 ODS Mode Shape Displayed Statically in Plan for 23.5 Hz; x, y in feet
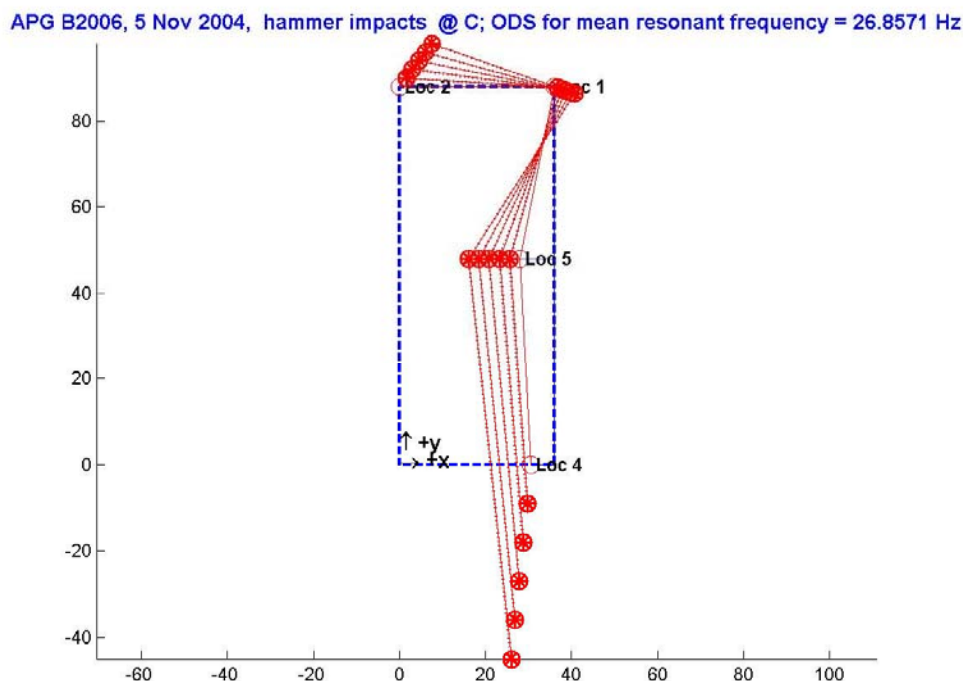
Figure 4-45. APG Building 2006 ODS Mode Shape Displayed Statically in Plan for 26.9 Hz; x, y in feet

4.6.3   Modal Results for APG Building 2001

Modal results for APG Building 2001 are natural frequency estimates from measured responses of selected forced-vibration excitations using an impact hammer and an electro-dynamic shaker during November 2004 activities. Also, transient responses from gun firing events provided another estimate of modal parameters estimated using the ODS approach. The building and instrumentation setup are described in Subsection 3.1.2.1. There were up to a total of thirteen channels of acceleration measured to monitor the building motions. Those included two channels at the ceiling level above the first level, two channels between the first level and the second level at the (above the ceiling) level, six channels on the floor of the second level, and three channels near the ceiling above the second level (below the attic). These measurements were oriented to monitor motions in the approximate east-west and approximate north-south directions. With this layout the lowest two side sway modes and first two torsional modes were identified. Other higher order modes are present as indicated by distinct peaks in the frequency functions, but spatial resolution of the measurement locations limits the ability to discern accurately the full picture of the mode shapes for higher order normal modes other than indicated. The most significant responses of the building, as evident from the peak magnitudes of the acceleration ASDs, exist between 10 to 35 Hz. The modal results are the estimates of the resonant frequencies identified from the peaks of calculated FRF functions, estimates of the damping ratios for the identified resonant frequencies, and estimates of the mode shape vectors identified from fits to the picked peaks fits of the FRFs at the corresponding resonant frequencies.

4.6.4   Modal Results for Fort Sill Building 216

Modal results for Building 216 at Fort Sill are natural frequency estimates from measured transient responses of gun firings from August 2005 activities and selected forced-vibration excitations using electro-dynamic shakers. The building and instrumentation setup are described in Subsection 3.1.3.1. There were a total of twelve channels of acceleration measured at the attic (above the ceiling) level. These measurements included six channels oriented to monitor motions in the approximate east-west direction and six channels oriented to monitor motions in the approximate north-south direction. With this layout the lowest side sway modes and first torsional mode were identified. Other higher order modes are present as indicated by distinct peaks in the frequency functions, but spatial resolution of the measurement locations limits the ability to discern accurately the full picture of the mode shapes for these higher order normal modes. The most significant responses of the building, as evident from the peak magnitudes of the acceleration ASD, exist between 5 to 30 Hz. The modal results are the estimates of the resonant frequencies identified from the peaks of calculated ASD functions, estimates of the damping ratios for the identified resonant frequencies, and estimates of the mode shape vectors identified as ODSs at the corresponding resonant frequencies.

4.6.5   Modal Results for Fort Sill Building 1230

Modal results for Building 1230 at Fort Sill are natural frequency estimates from measured transient responses of selected hammer impacts and forced-vibration excitations from an electro-dynamic shaker during August 2005 activities. The building and instrumentation setup are described in Subsection 3.1.3.3. The installation of accelerometers to monitor the building responses was not completed in time to measure discernable transient responses from gun firings. There were a total of twelve channels of acceleration measured at the attic (above the ceiling) level. These measurements included six channels oriented to monitor motions in the approximate east-west direction and six channels oriented to monitor motions in the approximate north-south direction. With this layout the lowest side sway modes and first torsional mode were identified. Other higher order modes are present as indicated by distinct peaks in the frequency functions, but spatial resolution of the measurement locations limits the ability to discern accurately the full picture of the mode shapes for these higher order normal modes. The most significant responses of the building, as evident from the peak magnitudes of the acceleration ASD, exist between 10 to 35 Hz. The modal results are the estimates of the resonant frequencies identified from the peaks of calculated FRF functions, estimates of the damping ratios for the identified resonant frequencies, and estimates of the mode shape vectors identified from fits to the picked peaks fits of the FRF at the corresponding resonant frequencies.

4.6.6   Modal Results for Fort Sill Building 6479

Modal results for Building 6479 at Fort Sill are natural frequency estimates from measured transient responses of selected hammer impacts during August 2005 activities. The building and instrumentation setup are described in Subsection 3.1.3.2. The measurements included one channel oriented to monitor motions in the approximate east-west direction and one channel oriented to monitor motions in the approximate north-south direction. With this layout, from the impact excitation method (recording the force input) the lowest side sway modes and first torsional mode were identified. Other higher order modes are present as indicated by distinct

peaks in the frequency functions. The most significant responses of the building, as evident from the peak magnitudes of the acceleration ASD, exist between 5 to 30 Hz.

4.6.7   Modal Results for MCAAP Building 72

Modal results for MCAAP Building 72 are natural frequency estimates from measured transient responses of detonations from 11 August 2005 activities. The building and instrumentation setup are described in Subsection 3.1.4.2. There were two channels of acceleration measured at the ceiling (inside, just below the attic) above the ground floor, near one corner of the building. These measurements included two channels of acceleration to monitor the horizontal motions in each direction of the building plan. The modal results are the estimates of the resonant frequencies identified from the peaks of calculated ASD functions, estimates of the damping ratios for the identified resonant frequencies, and estimates of the mode shape vectors identified as ODSs at the corresponding resonant frequencies. The most significant responses of the building, as evident from the peak magnitudes of the acceleration ASDs, exist between 7 to 33 Hz.

4.6.8   Modal Results for MCAAP Building 75

MCAAP Building 75 is very similar in plan, shape, and size to Building 72. Modal results for Building 75 are natural frequency estimates from measured transient responses of detonations from 10-13 August 2005 activities and from selected hammer impacts. The building and instrumentation setup are described in Subsection 3.1.4.1. There were a total of four channels of acceleration measured at the ceiling (inside, just below the attic) above the ground floor, near each front corner of the building. These measurements included two sets of accelerations recorded for the horizontal motions in each direction of the building plan. The modal results from the detonation activities are the estimates of the resonant frequencies identified from the peaks of calculated ASD functions, estimates of the damping ratios for the identified resonant frequencies, and estimates of the mode shape vectors identified as ODS' at the corresponding resonant frequencies. The most significant responses of the building, as evident from the peak magnitudes of the acceleration ASDs, exist between 7 to 33 Hz. The results from the impact modal survey are the estimates of the resonant frequencies identified from the peaks of calculated FRF functions, estimates of the damping ratios for the identified resonant frequencies, and estimates of the mode shape vectors identified from fits to the picked peaks fits of the FRF at the corresponding resonant frequencies.

4.6.9   Modal Results for MCAAP Building 97A

Modal results for MCAAP Building 97 are natural frequency estimates from measured transient responses of detonations from 10-13 August 2005 activities, from selected hammer impacts, and from selected forced-vibration excitations using an electro-dynamic shaker. The building and instrumentation setup are described in Subsection 3.1.4.3. There were a total of four channels of acceleration measured at the ceiling (inside, just below the attic) above the ground floor, near each front corner of the building. These measurements included two sets accelerations recorded of the horizontal motions in each direction of the building plan. The modal results from the detonation activities are the estimates of the resonant frequencies identified from the peaks of calculated ASD functions, estimates of the damping ratios for the identified resonant frequencies, and estimates of the mode shape vectors identified as ODSs at the corresponding resonant

frequencies. The most significant responses of the building, as evident from the peak magnitudes of the acceleration ASDs, exist between 7 to 33 Hz. The results from the impact modal survey and forced-vibration shaker excitations are the estimates of the resonant frequencies identified from the peaks of calculated FRF functions, estimates of the damping ratios for the identified resonant frequencies, and estimates of the mode shape vectors identified from fits to the picked peaks fits of the FRF at the corresponding resonant frequencies.

4.6.10 Modal Results for MCAAP Building 92

Modal results for MCAAP Building 92 are natural frequency estimates from measured transient responses of selected hammer impacts and detonations during 10-13 August 2005 activities. The building and instrumentation setup are described in Subsection 3.1.4.4. There were two channels of acceleration measured near the ceiling (outside, just below the attic) above the ground floor, near one front corner of the building these measurements included one channel oriented to monitor motions in the approximate east-west direction and one channels oriented to monitor motions in the approximate north-south direction. Due to channel limitations the input force during the impact modal survey was not measured. Thus, the modal parameters for both types of activities were estimated using the approach to identify ODSs. Other higher order modes are present as indicated by distinct peaks in the frequency functions. The most significant responses of the building, as evident from the peak magnitudes of the acceleration ASDs, exist between 8 to 38 Hz.

4.7   Formulation for Probability of Structural Damage

Initial analytical assessment of the structural response to blast waves was developed for simple structures, including a simply supported panel. The response parameter of primary interest is the peak structural velocity, since it is directly proportional to the peak stress in the structure. This development is based, in part, on a prior study for the response of structures to sonic booms[38]. For response to explosive blasts, however, a significant difference is the mathematically-infinite duration of the idealized pressure load compared to a finite duration of the impulsive pressure signature of a sonic boom. This difference requires a thorough development of the analytical background for the problem using distinct analytical approaches rather than the one used in Reference 38.

While most results in this study are presented in metric units, as generally preferred, the English units employed in Reference 38 are widely used for structural damage analysis. Those units are adopted here as necessary for consistency.

Sutherland[39] has reviewed applicable analytical methods for response to blast. Three methods were considered: the classical Duhamel integral, the complex Fourier transform, and Laplace transform approaches. First considered is the response of an SDOF system as a basic building block to the more complex response of a simply-supported panel, which serves as an approximate model for a window or a building wall exposed to a blast wave.

This analytical background was then used for the development of prediction models for the probability of structural damage to, or rattle of, building components from the impulsive blast sounds.[41] These models are intended to assist in development of improvements to the DoD planning guidelines and criteria for structural damage or community impact from blast sounds.

Emphasis is placed on potential blast damage to windows as the most vulnerable structural component of buildings.

This damage formulation is presented in the following subsections: response modeling based on Reference 39 in Section 4.7.1, and probability of damage based on Reference 41 in Section 4.7.2. Practical application in a user tool is presented in Section 4.8.

4.7.1 Formulation of Vibration Response to Blast Loads

The first level of analytical prediction of impulsive noise transmission into structures is "lumped parameter" Single Degree of Freedom model (SDOF). Motion of a lightly damped single degree of freedom system is fairly simple. For a spring-mass-damper, the equation of motion is:

$$m\ddot{x} + c\dot{x} + kx = F(t) \tag{4.5}$$

where

m = mass
c = damping
k = spring constant
x = coordinate
$F(t)$ = time-varying force

The response of this system to a unit impulse load at time 0 is

$$h(t) = \frac{1}{m\omega_d}\exp(-\delta\omega_n t)\sin\omega_d t \tag{4.6}$$

where displacement has been written as h rather than x to emphasize that it is a unit response, and where

$$\begin{aligned}
\omega_n &= \sqrt{\frac{k}{m}} &&= \text{undamped natural frequency} \\
c_c &= 2\sqrt{km} &&= \text{critical damping constant} \\
\delta &= c/c_c &&= \text{critical damping ratio} \\
\omega_d &= \omega_n\sqrt{(1-\delta^2)} &&= \text{damped natural frequency}
\end{aligned} \tag{4.7}$$

Figure 4-46 shows the response, Equation 4.6, of a lightly damped SDOF system to an impulse. It is the product of a sinusoidal wave, at the natural frequency, with an envelope that is a decaying exponential, as seen in Equation 4.6. The rate of decay of this envelope from one peak to another is a convenient measure of the amount of damping in the system. Between any two successive peaks, this envelope will decrease by a constant factor for linear damping. Thus, a useful term to describe this decay is the natural logarithm of the ratio of two successive peaks which are separated by the period, to = 2 π / ωd. This quantity is called the log decrement, Δ, and is readily shown to be

$$\Delta = \log\left[X(t_{n,\max})/X(t_{n,\max}+t_0)\right] = 2\pi\delta/\sqrt{(1-\delta^2)} \tag{4.8}$$

This expression can then be used to define the critical damping ratio, δ, in terms of the conveniently-measurable log decrement by

$$\delta = \Delta \big/ \sqrt{4\pi^2 + \Delta^2} \qquad\qquad (4.9)$$

For typical small values of δ (< 0.2), $\delta \approx \Delta/2\pi$.

For evaluation of response to a transient blast wave, however, damping does not play a strong role in defining the maximum response to the pressure pulse. This is in contrast to the dominant role damping plays in defining the maximum response to a steady state excitation.
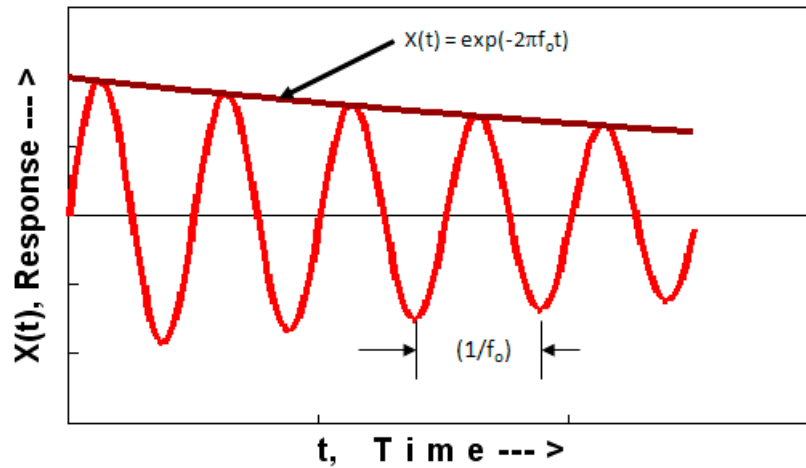
Figure 4-46. Transient Response of a Damped SDOF System to an Impulse

Equation 4.6 and Figure 4.46 represent the response to a concentrated impulse. As shown in Figure 2-3, blast waves have a particular waveform. In normalized form, the waveform an idealized blast waveform is given by

$$P(t) = P_0 (1 - t/T) \exp(-t/T) \qquad\qquad (4.10)$$

where P_0 is the initial peak pressure and T is the duration of the positive phase of the blast pulse. Figure 4-47 shows this waveform, normalized to a unit initial amplitude. Reference 39 discusses some alternate waveform models, including one with a finite duration negative phase and a simple triangular model for the positive phase, and concludes that the details are not critical.
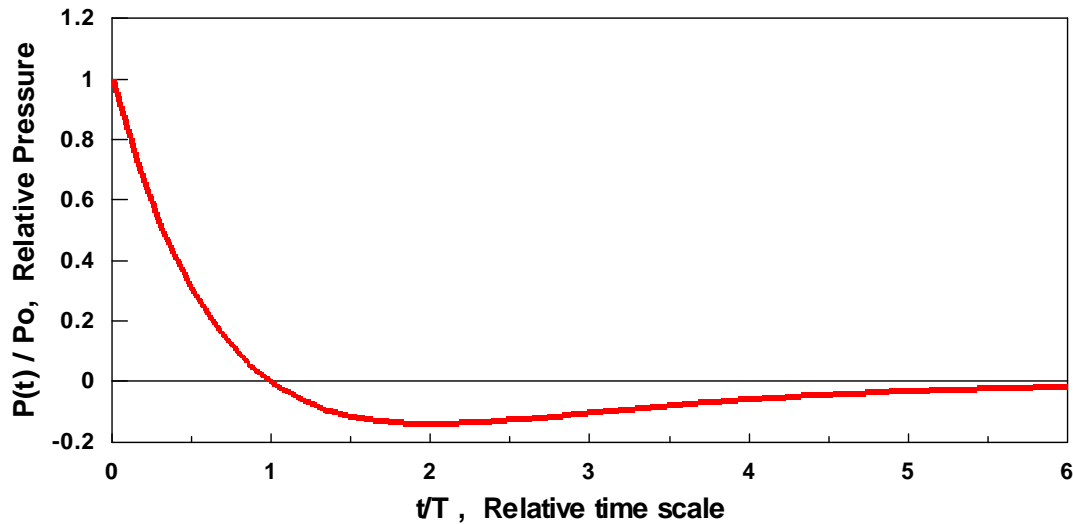
Figure 4-47. Time History of an Idealized Blast Wave

The response to an arbitrary time varying load, including a blast wave, is given by the Duhamel integral,[11,51] which is simply a convolution of the waveform with the impulse response:

$$x(t) = \int_0^t h(t - \tau) F(\tau) d\tau \qquad (4.11)$$

Reference 39 presents analytic solutions for velocity and stress responses, using Fourier and Laplace transform methods. With today's abundance of computing power, however, numeric evaluation of the Duhamel integral is practical. This approach was successfully employed in recent studies of transmission of sonic booms into buildings.[52] Figure 4-48 shows the SDOF response of a simple panel to a 2 psf blast wave with a 200 msec positive duration. The program, denoted SDOF, used for this calculation is described in Appendix C. The input waveform is shown in the upper left. Its power spectral density is shown in the upper right. The structural response is shown in the bottom two quadrants, displacement time history on the left and power spectral density on the right. The lower left quadrant shows the lumped parameter panel mass density, resonant frequency, and damping ratio.
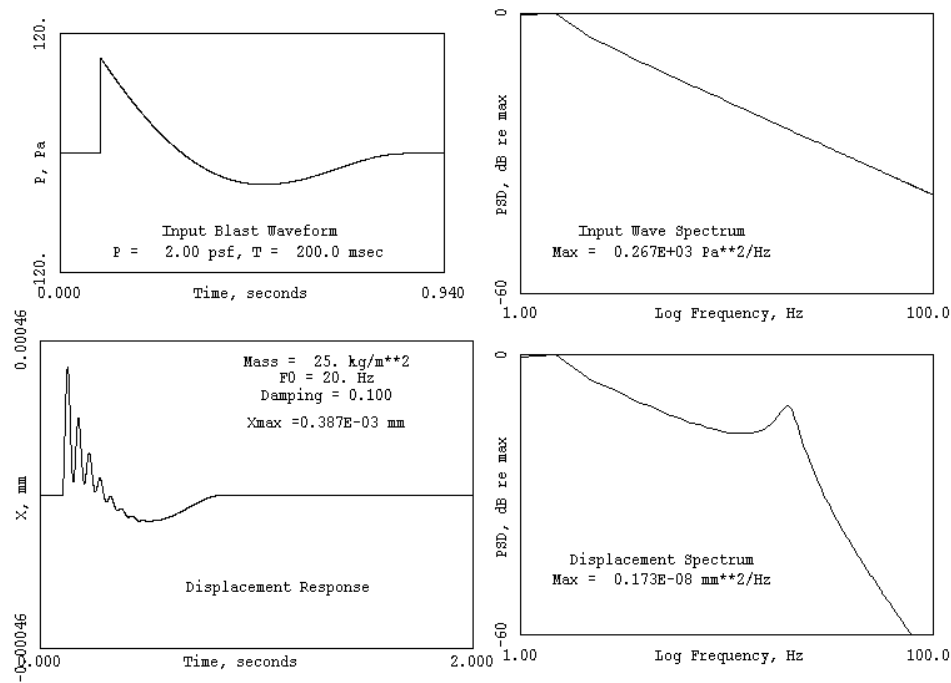
Figure 4-48. SDOF Response to a Blast Wave, from Duhamel Integral

Modeling a wall as a SDOF system entails lumping some of the physics. The fundamental for a simply supported rectangular panel is generally a half sine in each direction, with maximum displacement in the middle. One defines an effective *x* averaged over this shape. There is also corresponding spring constant, mass and damping. Equation 4.5 is then written with *m*, *c* and *k* as modal mass, damping and stiffness. The load becomes the pressure of the sound wave times the area of the wall. Since the wall moves in a modal shape (half-sine in each direction), the integration of the pressure over this shape yields a factor called the joint acceptance. For the analysis in Figure 4-48, the panel stiffness is embodied in the resonant frequency. Table 4-2 lists the resonant frequencies of common building elements. Table 4-3 lists the loss factor η (= 2δ) for common building materials. Data in Tables 4-2 and 4-3 are taken from Reference 38. As noted earlier, damping is of less importance for impulse response than for resonant response.

While the SDOF analysis presented here provides good estimates of structural vibration, corresponding to the measurements conducted in this project, and would be directly applicable for assessment of human response and tolerance, the probability of damage requires estimates of stress in the affected structures. That analysis is presented in the next section.

Table 4-2. Resonant Frequencies for Common Building Elements

Structure	f_0, Hz	Standard Deviation, Hz
Wood Wall	16	4
Brick Wall	12	6
Metal Wall	14	3
Concrete Block Wall	25	N/A
Plaster Ceiling	14	1
Windows, 0-2 ft^2	95	35
Windows, 2-10 ft^2	60	22
Windows, 10-50 ft^2	15	6
Windows, 50-100 ft^2	6	2
Windows, > 100 ft^2	6	2

Table 4-3. Loss Factors for Common Building Materials

Material	Range of η	Average η
Wooden Boards	0.02 - 0.10	0.045
Brick	0.01	0.010
Concrete	0.01 - 0.12	0.035
Glass	0.002 - 0.03	0.008
Gypsum	0.001 - 0.03	0.006
Metals	0.001 - 0.003	0.002
Overall Mean	-	0.011

4.7.2   Formulation of Probability of Damage

The probability of structural damage from blast loading depends on the nominal value and statistical variation of three basic parameters: the effective blast pressure loading on a structure, the vibration and corresponding stress response to this loading, and the thresholds for damaging or failure stress to such loading. Probability of Damage (POD) is a statistical, determined in terms of the statistical distribution of the Factor of Safety (FOS). FOS is the ratio of the failure stress limit of the structure to the peak stress imposed on the structure by the blast load. By definition, structural damage is presumed to occur whenever the FOS is equal to or less than 1:

$$\text{FOS} = S_d/S_{pk} \tag{4.12}$$

where

S_d = stress at which damage occurs

S_{pk} = peak stress resulting from blast load

The peak stress depends on a series of factors:

$$S_{pk} = P_0 \frac{P_f}{P_0} \frac{P_e}{P_f} \frac{V_{pk}}{P_e} \frac{S_{pk}}{V_{pk}} \tag{4.13}$$

where

P_0 = nominal peak blast pressure

$\dfrac{P_f}{P_0}$ = ratio of actual free field blast pressure to nominal, accounting for propagation effects

$\dfrac{P_e}{P_f}$ = ratio of effective blast pressure on the structure to free field

$\dfrac{V_{pk}}{P_e}$ = ratio of the peak structural velocity to the effective peak pressure

$\dfrac{S_{pk}}{V_{pk}}$ = ratio of peak stress to peak structural velocity

The first term (P_0) is the nominal blast pressure, as obtained by simple charge weight and distance relations as will be presented shortly.

The second term (P_f/P_0) represents effects of weather and terrain on propagation of the blast wave. In the measurements conducted in this study, the microphones on the 10 meter towers essentially measured P_f. A blast wave propagation model such as SIPS[8] or NAPS[9] will predict P_f.

The third term (P_e/P_f) represents the effect of local reflections at the structure (e.g., pressure doubling at the surface) and diffraction effects around it (e.g., self-shielding of the sides or back).

The fourth term (V_{pk}/P_e) is the vibrational response, as described in Sections 4.1 and 4.7.1.

The fifth term (S_{pk}/V_{pk}) relates stress to velocity.

Each of these quantities is statistical in nature, either from variation in propagation and terrain effects, or from the variations among seemingly similar structures in the community. POD for a particular case thus becomes a statistical analysis depending on the distribution. This is

illustrated in Figure 4-49 for a sample case. The distribution is log normal, and the FOS is the integral of the distribution for FOS less than 1.
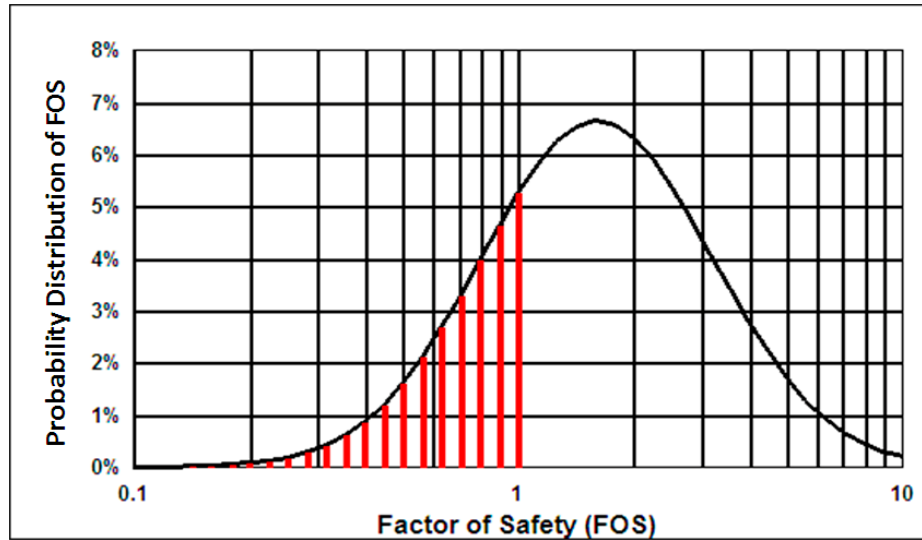
Figure 4-49. Example FOS Distribution; POD is red shaded area where $FOS \leq 1$

Sections 4.7.2.1 through 4.7.2.6 address each of the factors in Equations 4.12 and 4.13. These are based on Sections 1 through 6 of Reference 41. In accordance with Reference 41, English units of lb, in, sec are used, with distances in feet. The final model, with plots of POD for a range of windows and wall structures taken from Reference 41, is presented in Section 4.8. The final charts are presented in two forms:

- Method 1 - The free field blast loading is presumed to be known in advance from blast propagation models in terms of two parameters: the peak free field blast pressure and the positive phase duration;

- Method 2 - The mean value of the nominal pressure or equal free field blast pressure is defined by two parameters: the distance between the blast source and the receiving structure and the TNT-equivalent weight of the blast charge.

4.7.2.1 Blast Pressure Loading

The nominal peak blast pressure P_0 (see Equation 4.10 and Figure 4-47) that would be measured well above the ground in the absence of nearby structures has been established analytically (e.g., References 12 and 53) and experimentally. Peak pressure has been found to correlate well with scaled distance $Z = R/W_T^{1/3}$, where R is the distance and W_T is the equivalent TNT weight. Figure 4-50, taken from Reference 41, is a collection of measured data over a wide range of explosive yields, scaled according to Z. The regression line (red) is very close to fit defined by ANSI (blue), and is given by

$$\log_{10} P_0 = 2.72 - 1.79 \log_{10} Z + 0.090 \left(\log_{10} Z \right)^2 \tag{4.14}$$

$$Z = R/W_T^{1/3}, \text{ ft/lb}^{1/3}$$
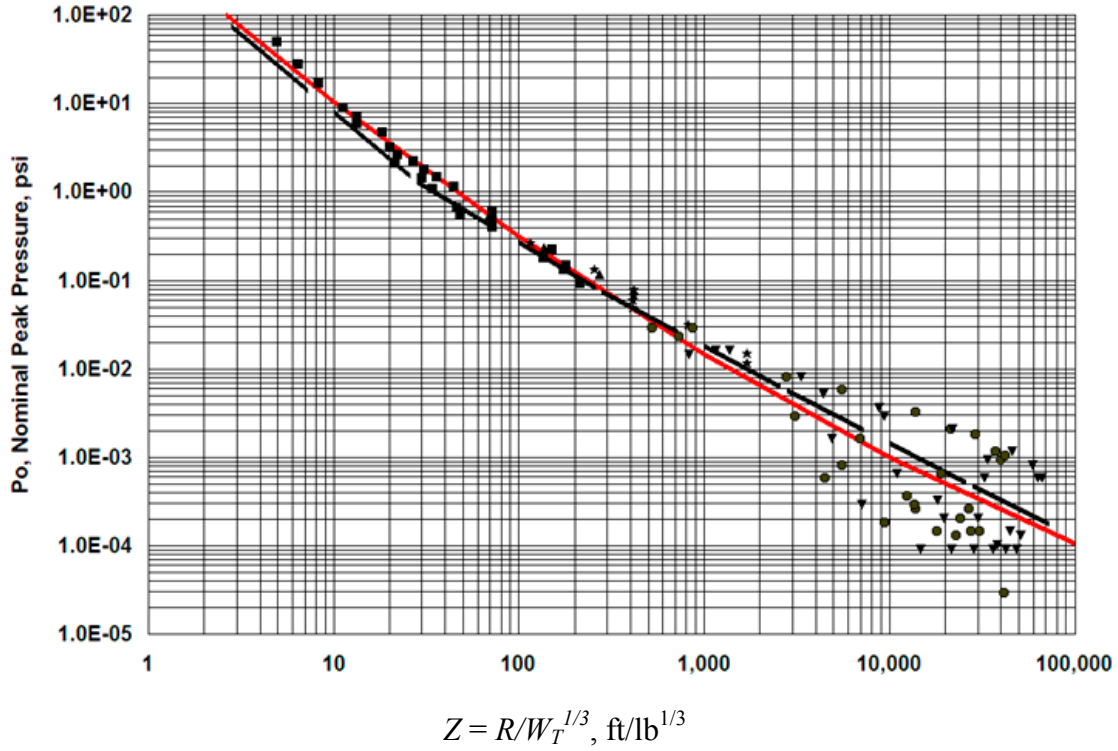
Figure 4-50. Correlation Between Peak Pressure and Scaled Distance Z

The positive phase duration, T, also correlates with Z, and is given by[39]

$$T = W_T^{1/3} \frac{1.74 \cdot 10^{-4} Z^{1.58}}{\left(1 + 0.028 Z^{2.4}\right)^{1/1.9}} \quad , \text{ sec}/lb^{1/3} \tag{4.15}$$

Equations 4.14 and 4.15 are based on data from free field explosions. Charges near (at or above) the ground are enhanced by ground reflection, while charges below the surface are attenuated. Raspet and Bobak[54] obtained an adjustment A^b, dB, based on parameter $Z^b = d/WT^{1/3}$, where d is the burial depth or burst height, in dB. The adjustment is

$$
\begin{aligned}
&= 0.0 &&, \quad Z_b \geq 0.216 \\
A_b &= -3.0 + 13.92 Z_b &&, \quad -2.21 \leq Z_b < 0.216 \\
&= -30.74 + 1.45 Z_b &&, \quad Z_b < -2.21
\end{aligned}
\tag{4.16}
$$

4.7.2.2 Statistical Patterns of Blast Wave Propagation

The second factor in Equation 4.13, P_f/P_0, represents propagation variations, primarily due to atmospheric effects. The statistics of these variations have been established by measurements presented in References 55-58. The distribution of data from Reference 55 is summarized in Figure 4-51, taken from Reference 41. Those data, which were obtained from 20 days of measurements, at 8 km, of explosions of 5 lb C4 charges. The variation was found to have a log normal distribution, corresponding to the example FOS distribution in Figure 4-49. The data fell into two regions. For the peak levels of interest in the current study, only the upper ("Favorable") group is of interest. The favorable conditions correspond to downwind or inversion conditions, which enhance sound. Unfavorable conditions correspond to inversion or upwind propagation, which result in lower peak levels that are generally not an issue for damage.
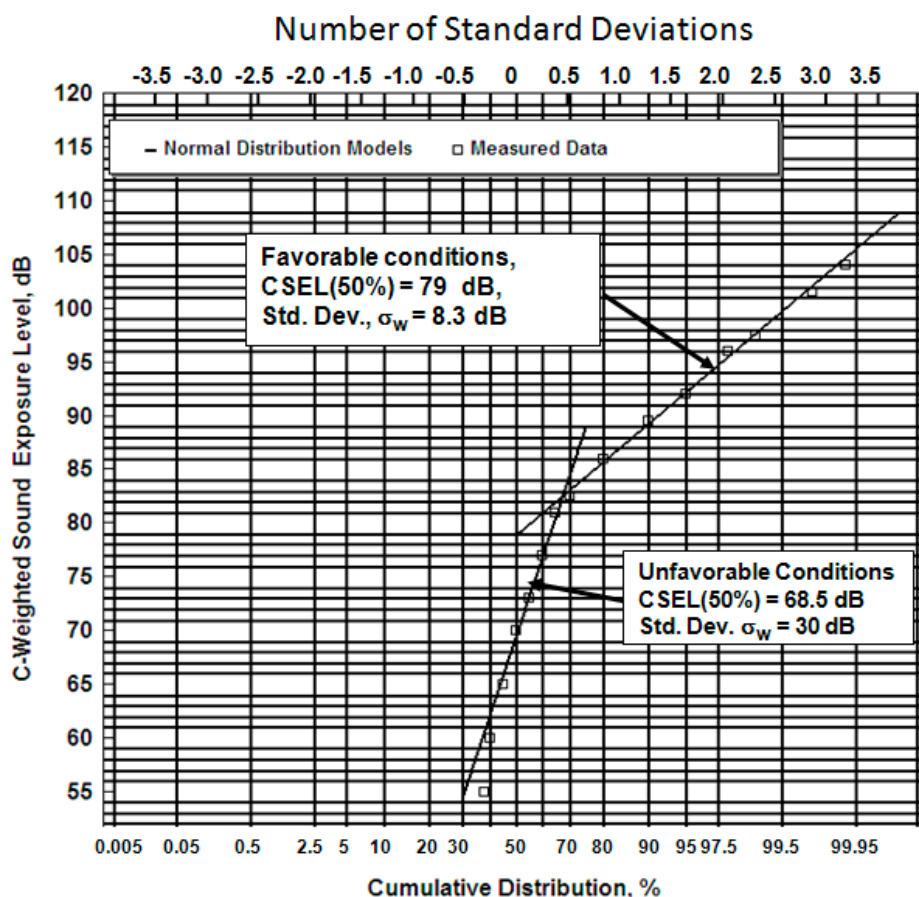
Figure 4-51. Cumulative Distribution of C-Weighted Sound Exposure Levels from Reference 55

Figure 4-51 shows data from only Reference 55. Sutherland[41] analyzed all of the favorable condition data from References 56 and 58. They are plotted in Figure 4-52. Variance depends on distance and the type of surface, with variance over soft surfaces being greater than hard. The regression lines in Figure 4-52 are

$$\sigma = -2.88 + 1.44 \log_{10} R \text{ , hard surfaces}$$
$$\sigma = -4.60 + 2.30 \log_{10} R \text{ , soft surfaces}$$

(4.17)

When recast in terms of the pressure ratio (P_f/P_0) rather than level ($20 \log_{10} (P_f/P_0)$), the standard deviations of the log normal distributions are

$$\sigma_L = -0.144 + 0.072 \log_{10} R \text{ , hard surfaces}$$
$$\sigma_L = -0.23 + 0.115 \log_{10} R \text{ , soft surfaces}$$

(4.18)

Because levels are 20 times the logarithm of the pressure ratio, Equations 4.17 and 4.18 differ by the factor of 20. Equations 4.17 or 4.18 are to be used for POD analysis only if blast levels are estimated by Equation 4.14, rather than a full propagation model such as SIPS.
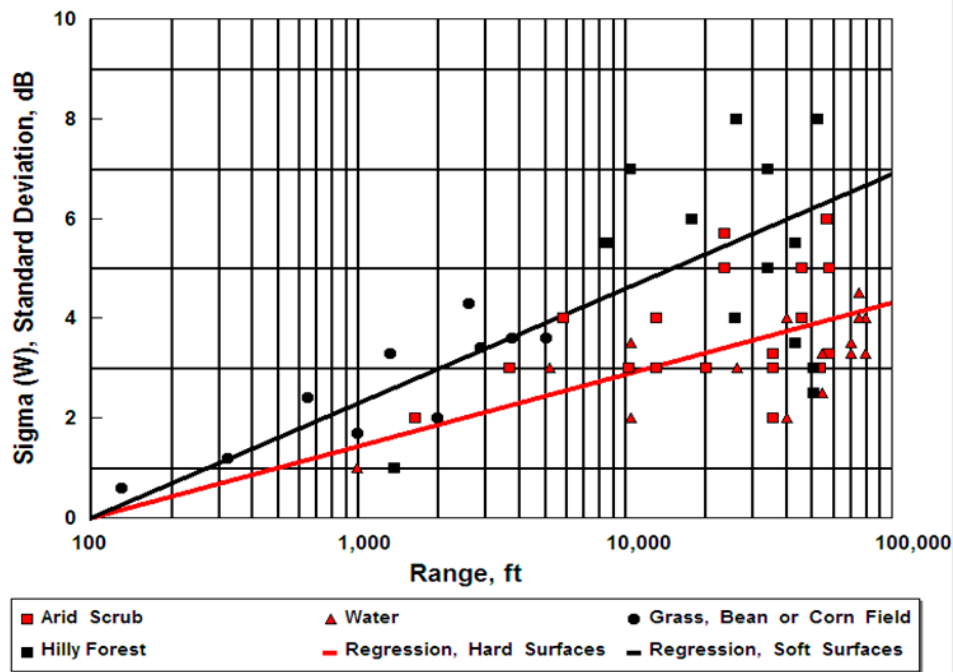
Figure 4-52. Weather-induced Variation in Blast Sound Levels,[56,58] Categorized by Surface Type

4.7.2.3 Reflection and Diffraction Effects

The third factor in Equation 4.13, P_e/P_f, represents the effect of the structure being impacted on the pressure field. For a wave impinging normally on a smooth infinite surface, this is a factor of two, pressure doubling. For finite surfaces, diffraction associated with the edges cause the pressure to vary across the surface. Faces of a structure that do not have line of sight to the blast are not directly impinged, but receive load from parts of the wave diffracted around the edges.

Diffraction theory has been applied in this context for a considerable time, e.g., References 59 and 60. It is well established, with measurements generally agreeing with theory, as shown in Figure 4-53, taken from Reference 59.
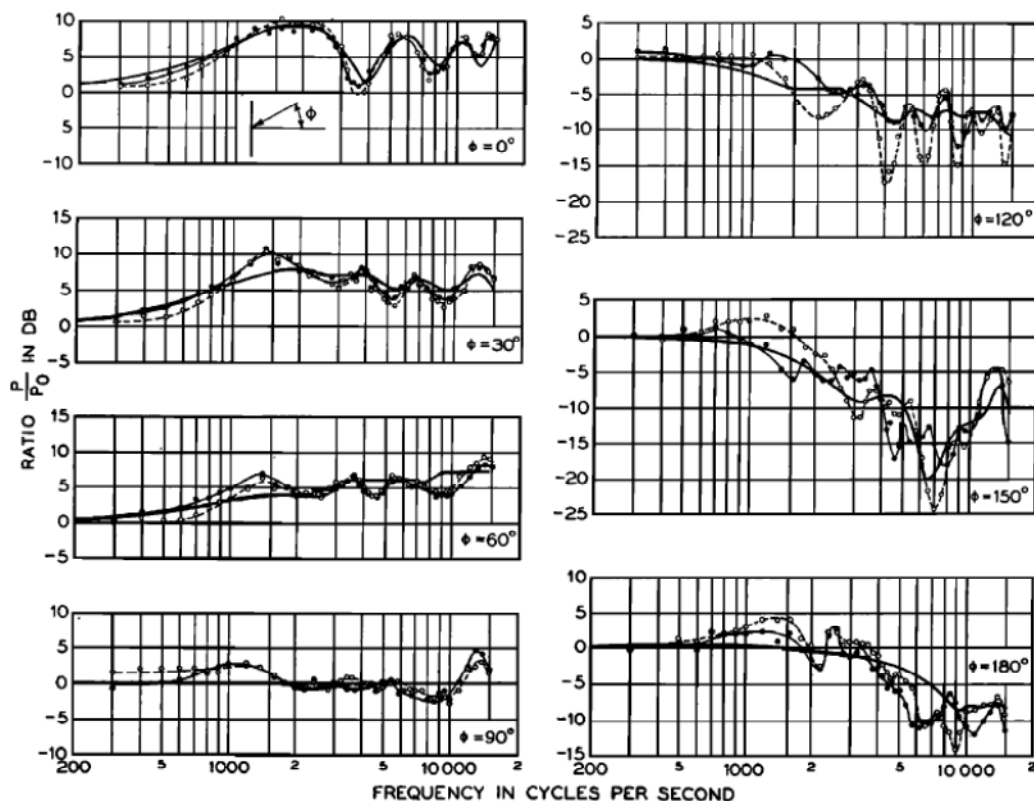
Figure 4-53. Experimental and Theoretical Diffraction Results for a Six Inch Cube[59]
(*P/P₀* corresponds to *Pₑ/Pf*.)

The most relevant idealized diffraction analysis for this study is impingement of waves on cubes or rectangular parallelepipeds. Figure 4-54 shows diffraction results, from References 11 and 61, at the center faces of rectangular parallelepipeds consisting of a single cube or two stacked cubes. Figure 4-55 shows additional data from Reference 61 as analyzed in Reference 41, showing the average amplification factor on the front, side and back of a single 10 foot cube and a stack of two 10 foot cubes.

Sutherland[41] drew several observations from data as shown in Figures 4-53 through 4-55 and the extensive measurements in Reference 61. These may be summarized as:

- The effective blast pressure on the front face of a cube or stacked two story cube is approximately twice the incident pressure (+ 6 dB) at all locations across the face.

- The space averaged reflection/diffraction adjustment on the side of a single or double stacked cube is on the order of 0 ± 3 dB. This is the pressure, and does not account for the more complex structural response for a grazing incidence wave.

- The space averaged reflection/diffraction adjustment on the back side of a single or double stack cube varies widely from -5 to -15 dB for the double stack, and about +3 to -6 dB for the single cube.

Based on these observations, average values and variations presented in Table 4-4 were determined to be appropriate for generic probability of damage estimates on residential structures. The nomenclature in Table 4-4 is:

- A_r = reflection/refraction adjustment in dB = $10 \log_{10}(P_e/P_f)$.

- C_r = reflection/refraction adjustment as a ratio = P_e/P_f.

- $\sigma_L(C_r)$ = standard deviation of log of C_r; $20 \, \sigma_L(C_r)$ is the standard deviation of A_r.

This nomenclature is retained for consistency with the relations developed in Reference 41.
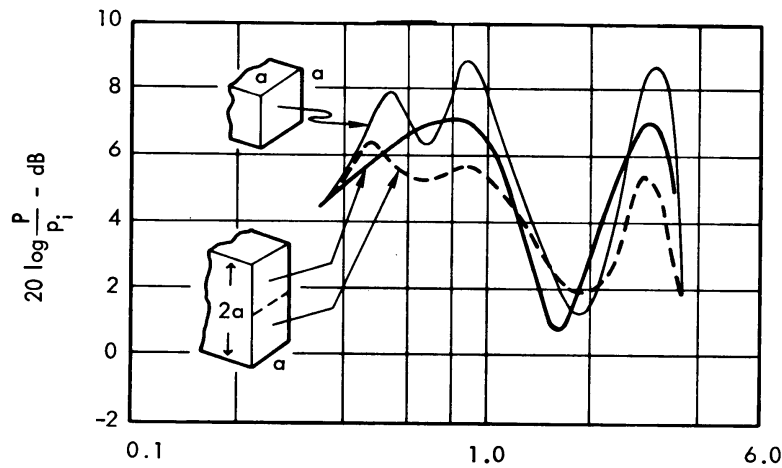
Figure 4-54. Reflection Adjustment at the Center of the Face of a Single and Double Stack of Cubes
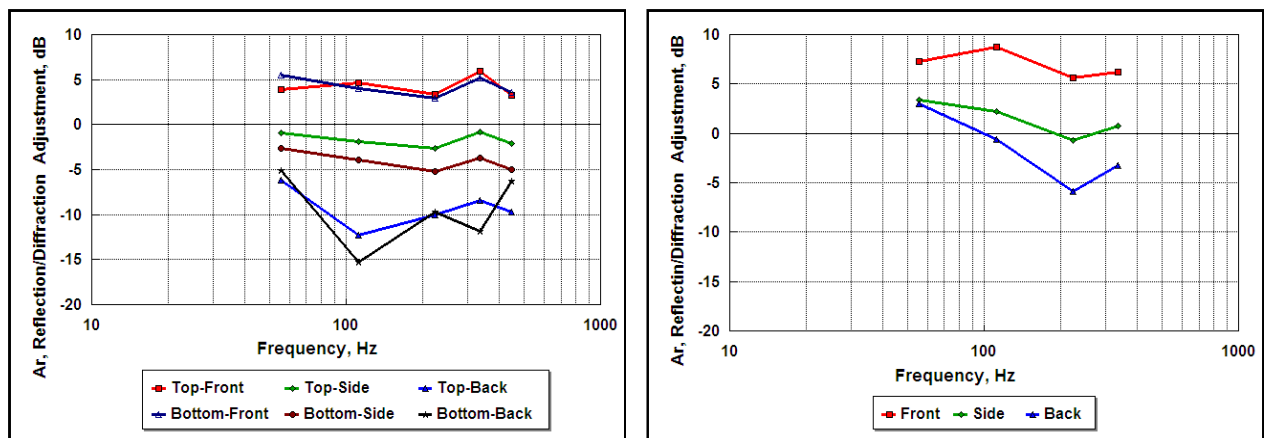
(a) Stack of two cubes

(b) Single cube

Figure 4-55. Area-averaged Reflection/diffraction Adjustment, $A_r = 20 \log_{10} (P_e/P_f)$

Table 4-4. Ar and Cr for Single and Double Stack Cube, and Default for Any Façade

	One-cube stack			Two-cube stack					
				Top			Bottom		
	Front	Side	Back	Front	Side	Back	Front	Side	Back
Mean, A_r, dB	7.0	1.4	-1.7	4.5	-1.6	-9.2	4.4	-3.9	-10.5
$20\sigma_L(C_r)$, dB	1.2	1.5	3.3	0.9	0.7	2.2	1.0	0.9	3.7

	Average values, both stacks			Default values for any building façade		
	Front	Side	Back	Front	Side	Back
Mean, A_r, dB	5.3	-1.3	-7.1	6 dB	1 dB	- 6 dB
Mean C_r				2.0	1.12	0.5
$20\sigma_L(C_r)$, dB	1.0	1.1	3.1	1 dB	1 dB	3 dB

4.7.2.4 Prediction of Structural Velocity Response to Blasts

The velocity response of a single degree of freedom system was presented in Section 4.7.1. The detail lost in lumping the motion of a panel into a single mode loses information that is essential to the next factor, relating velocity to stress. To accurately define the response of real structures, especially windows, to blast loads, it is therefore necessary to shift from a simple SDOF model to a multi-degree of freedom model to account for the modal behavior of the structure. This was briefly addressed in Section 4 of Reference 39 and is considered in more detail here. The same basic concepts of "generalized force" for the blast response of a simply supported panel are applied. That is, the "lumped" peak pressure P_0 becomes the "generalized pressure" [$4P_0/(m n\pi^2)$] for the m,nth mode and the lumped "surface weight" w becomes the "generalized" surface weight, w/4. As shown in Reference 39, the time variation $V_{m,n}(t)$ for the odd modes of the velocity at the center of a simply-supported (SS), undamped panel to a normally-incident classical blast wave, whose time history is given by Equation 4.10, is given by

$$\frac{V_{m,n}(t)}{P_0/w} = \left\{ \frac{16gT/(nm\pi^2)(\omega_{m,n}T)^2}{[(\omega_{m,n}T)^2 - 2\delta\omega_{m,n}T + 1]^2} \right\} \qquad (4.19)$$

where

P_0 = pressure load
$V_{m,n}$ = modal velocity
m,n = odd mode numbers
$\omega_{m,n}$ = undamped modal frequencies
δ = critical damping coefficient
w = panel surface weight
T = duration of positive phase
g = acceleration due to gravity

The damped resonance frequency, $\omega_{d,m,n}$ for the m,n^{th} mode is defined, as it was the SDOF model, in terms of the undamped resonance frequency, $\omega_{m,n}$ and the critical damping coefficient, δ. Based on measured blast response data for a window,[62] a critical damping coefficient of 0.075 was assumed to be the same for all modes for windows. Damping effect on response for other structural systems is considered later.

The convention of normalizing the time history of the velocity by the ratio P_0/w will help later to define the Factor of Safety (FOS) and the Probability of Damage (POD). (For convenience, the symbol P_0 is used in this section to denote the peak pressure when it reality it should be labeled as the effective peak pressure, P_e in accordance with Equation 4.13.

The total velocity response over all modes will simply be the sum of the responses for each mode. The resulting final expression for the time history of the total modal velocity response, $V_{m,n}(t)$ for a damped, simply supported plate to a normally-incident blast wave is:

$$\frac{V_{m,n}(t)}{P_0/w} = \sum_{m,n}^{odd} \left\{ \left[16gT/(mn\pi^2)\right]\left[Z_{m,n}/\left(Z_{m,n}^2 - 2\delta Z_{m,n} + 1\right)^2\right]\left[V_1(t) + V_2(t)\right]\right\} \quad (4.20)$$

where

$$V_1(t) = \left\{2(Z_{m,n} - \delta)\cos(BZ_{m,n}(t/T)) + \left[\left[Z_{m,n}^2 - 1 - \delta\left(2Z_{m,n} - \delta\left(1 + Z_{m,n}^2\right)\right)\right]/B\right]\right.$$
$$\left.\sin(BZ_{m,n}(t/T))\right\}\exp\left[-\delta Z_{m,n}(t/T)\right]$$
$$V_2(t) = \left\{\left[\left(Z_{m,n}^2 - 2\delta Z_{m,n} + 1\right)/Z_{m,n}\right](t/T) - 2(Z_{m,n} - \delta)\right\}\exp(t/T)$$
$$Z_{m,n} = \omega_{m,n}T$$

and $\omega_{m,n}$ is the undamped angular resonance frequency for the m,n^{th} mode, given by

$$\omega_{m,n} = 2\pi f_0\left[(m\,b/a)^2 + n^2\right]/\left[(b/a)^2 + 1\right] \quad (4.21)$$

where a, b are the shortest and longest sides of the panel, respectively.

The damped angular resonance frequency, $\omega_{d,m,n} = B\,\omega_{m,n}$ where $B = \sqrt{1 - \delta^2}$.

By symmetry of: a) the loading for normal incidence for a blast wave and b) the mode shapes for the SS panel, the response is zero for even modes for a normally incident acoustic load such as a blast wave. (While this Equation is not valid for blast wave incident on the side or back of buildings, any error is considered compensated for by using the experimentally-verified values[41] for the "reflection/ diffraction" corrections in Table 4-4 for these non-normal incidence cases.)

The key parameters needed to apply Equation 4.20 are: a) the undamped resonance frequency, $\omega_{m,n,}$ for the m,n^{th} mode as derived from the value of the fundamental frequency, f_0 using Equation 4.21, and, b) the positive phase duration, $T,$ of the blast wave.

The structures of concern for this report can be divided into two groups:

1. Solid or built-up wood, steel or aluminum walls or homogeneous masonry, (i.e., concrete or brick) walls for which the aspect ratio, a/b and f_0 does not vary appreciably for most of these wall types and,

2. Windows which have a wide range for aspect ratios and modal resonance frequencies for various sizes and shapes.

Thus, there is a more complex relationship between structural velocity and stress for windows than for walls, and for windows velocity and stress must be considered together. The remainder of this velocity response section will consider walls with a typical aspect ratio a/b of 0.75.

In order to evaluate the maximum multi-modal velocity response of this kind of wall with Equation 4.20, the range for the key dependent parameters must be defined. These are the fundamental resonance frequency f_0 and positive phase duration T.

The typical fundamental resonance frequencies for walls, other than windows, falls within a relatively narrow range of about 12 to 25 Hz. One exception is concrete block walls which can have a fundamental resonance frequency of the order of 100 Hz.[61] For analysis purposes, the frequency range was extended from a low end of 5 Hz to an upper end of 100 Hz.

The range for T was estimated for a range of the distance from 50 to 10,000 ft and equivalent TNT weight explosive from 2 to 2,000 lbs. The resulting range for T varied from about 0.005 to 0.1 sec. For the sake of the evaluation of Equation 4.20, the corresponding range of $f_o T$ was extended from 5 x 0.005 = 0.02, to 100 x 0.1 = 10.

Over this range of $f_0 T$, the maximum absolute values of the positive or negative velocity response was determined over a range for a dimensionless time, $f_0 t$, of 0 to 6 corresponding to a value for the time, t, equal to 6 cycles of the panel response at the fundamental frequency. For these velocity Shock Spectra, the critical damping coefficient δ was set, for now, to 0.075 – a value at the bottom of the expected range. The result, considering all of the first 25 odd modes, is shown in Figure 4-56. For a practical graphical evaluation of Equation 4.20, the parameter gT was moved to the left hand side so that the envelope of the response can be defined entirely as a function of just $f_o T$.
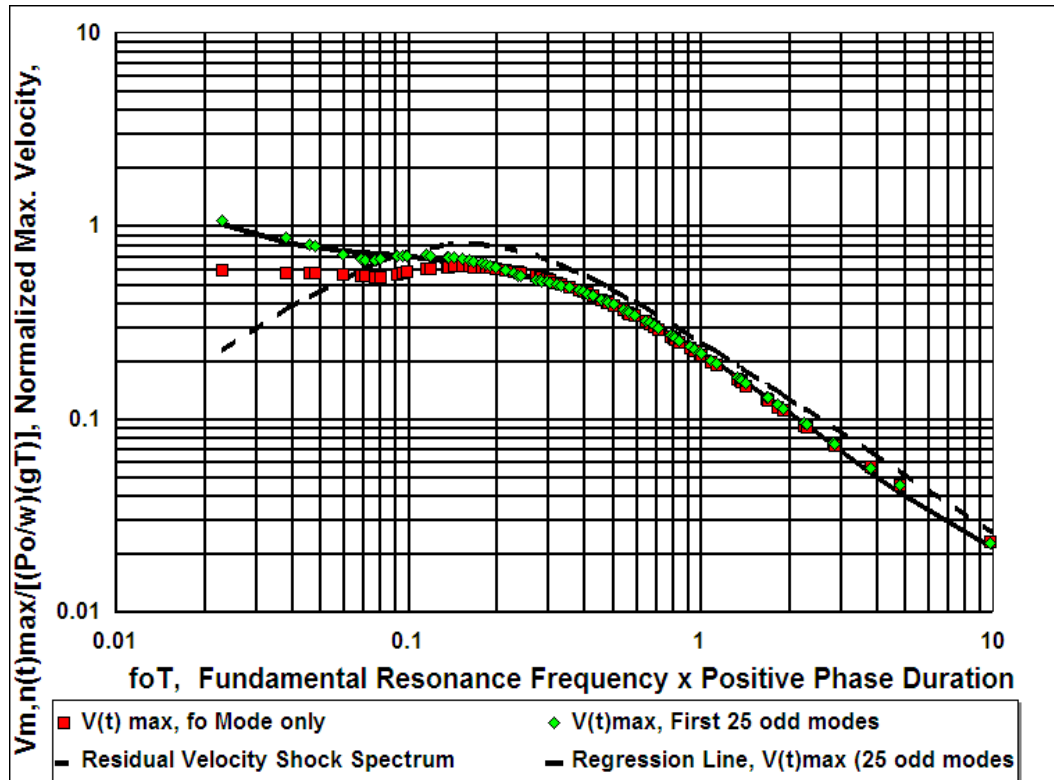
Figure 4-56. Velocity Shock Spectrum of Maximum Values of Time Histories for Structural Response to Blasts; Also shown are the Velocity Shock Ppectrum for the Fundamental Mode and the Residual Velocity Shock Spectrum

The Residual Velocity Shock Spectrum, also shown in Figure 4-56 by a dashed line, is defined in the same normalized form used for this figure instead of the normalized form used for Equation 29 in Reference 39. It includes the multimodal adjustment for just the fundamental mode f_0 ($m,n = 1,1$) and is given by:

$$\frac{V_R(f_0)}{(P_0/w)gT} = \frac{16}{\pi^2} \frac{\omega_0 T}{\left[1+(\omega_0 T)^2\right]}$$

(4.22)

The Residual Velocity Shock Spectrum slightly overestimates the total multi-modal, Velocity Shock Spectrum for values of f_0T greater than about 0.1 and increasingly under-predicts the maximum velocity response for lower values of f_0T. For this reason, the Residual Velocity Shock spectrum is only utilized briefly in relation to sonic boom response.

A regression line fit to the full Velocity Shock Spectrum for all of the first 25 odd modes shown in Figure 4-56 can be expressed in terms of a polynomial to $L = \log_{10}(f_oT)$:

$$\frac{V_{m,n}(t)_{max}}{(P_0/w)gT} = 10^{\left(-0.6528-0.9337L-0.3978L^2+0.1805L^3+0.1386L^4\right)}$$ (4.23)

The rms deviation of this regression is 0.35 dB, which is negligible. The only significant dependent variable is f_oT. Note that the spectra in Figure 4-56 are for the absolute value of the positive or negative peaks in the velocity response time history. It will be shown later, when evaluating the peak stress response of windows, that the maximum absolute stress response, for at least the first mode, is often negative.

Equation 4.23 is an interim key result for this analysis since this simple expression can be used to define the maximum multi-modal velocity response to blasts for many types of structural panels that can be approximated as simply supported plates with a fixed aspect ratio of 0.75.

The stress response corresponding to this velocity response can now be determined for such structures. To apply Equation 4.23 it is necessary to define the following appropriate parameters for the structure and the blast environment:

1) For each structure, the fundamental resonance frequency f_0 and surface weight w

2) For the blast environment, the effective peak pressure P_e and the blast duration T as a function of the scaled distance $R/Wt^{(1/3)}$.

The preceding results can also be applied to define the stress response of windows. One complication must, however, be taken into account. The proportionality factor between structural stress and structural velocity varies with the panel aspect ratio a/b. Since this parameter also affects modal resonance frequencies of the panel and the peak velocity response to a blast, it is necessary to combine multi-modal vibration analysis and corresponding stress response of windows to blast waves into one integrated approach. This is done in the next section.

4.7.2.5 Structural Stress as a Function of Structural Velocity

4.7.2.5.1 General Formulation

The peak stress, S_{pk} (generally expressed in psi), in a simply supported plate vibrating in a normal mode has been shown by Hunt[63] to be given by

$$S_{pk} = K_S(E/C_L)V_{pk}$$ (4.24)

where

K_S = a vibration/stress proportionality factor, typically 0.7 - 2
E = the Young's Modulus of Elasticity of the material, psi
C_L = the longitudinal speed of sound, in the material, in/s
V_{pk} = the peak modal velocity, in/s

Note that V_{pk}/C_L could be considered as a structural response Mach number.

Nominal values for E, C_L, and the estimated standard deviation of $\log_{10}(E/C_L)$, are given in Table 4-5 for a range of common building materials based on data in Table 4-6. These two tables are taken from Reference 39; the original data sources are identified in each Table.

The standard deviation of $\log_{10}(E/C_L)$, dB, is given in the last column for convenient indication of its magnitude at this point. The (log) mean value of E/C_L and the standard deviation of its log, or $\sigma_L(E/C_L)$, will be used later for computations of the Probability of Damage (POD). In an earlier study[38], it had been assumed that E/C_L was a deterministic variable with zero standard deviation. However, the range of this parameter for some of the materials listed in Table 4-5, especially masonry/stone and brick, indicated that this assumption was no longer tenable. Thus, $\sigma_L(E/C_L)$ is greater than 0.

The dimensionless stress/vibration proportionality factor, K_S in Equation 4.24, was defined by Hunt[63] as

$$K_S = \sqrt{3/(1-\mu^2)}\left\{\left[1+\mu((a/b)/(m/n))^2\right]/\left[1+((a/b)/(m/n))^2\right]\right\} \qquad (4.25)$$

where μ is Poisson's ratio for the structural material and a/b is the panel aspect ratio (≤ 1) with mode numbers m, n for sides a and b, respectively.

Table 4-5. Mean and Range of the Stress Parameters E, C_L, and E/C_L and the Standard Deviation of the Log of E/C_L for Common Building Materials

Material	Ref.	E		C_L		E/C_L		St.Dev. $\log_{10}(E/C_L)$
		Mean	Range	Mean	Range	Mean	Range	dB*
		10^6 psi		10^5 in/s		psi/(in/s)		
			+/-		+/-		+/-	
Adobe (*E* Range estimated)	64	0.023	0.0027	0.11	0.011	2.0	0.43	0.93
Aluminum Frame Wall	11,65	10.40	0.65	2.07	0.039	50.2	4.09	0.35
Brick Walls	11	1.72	0.87	1.00	0.280	17.2	14.7	3.67
Concrete Block	11	2.10	0.10	0.96	0.046	21.9	2.10	0.42
Glass	11	10.70	1.70	2.16	0.200	49.5	12.6	1.10
Masonry/Stone	11,66	9.30	4.60	1.93	0.510	48.2	39.3	3.53
Steel Frame Walls	11	29.80	0.40	2.01	0.015	148.0	3.10	0.09
Wood Frame Walls + Gypsum	11,38,65	0.54	0.047	0.75	0.081	7.2	1.41	0.85
Wood Frame Walls + Plaster	11,38,65	2.15	0.25	1.18	0.050	18.2	2.90	0.69
Wood Frame Walls + Wood	2,5,30	1.60	0.40	1.95	0.310	8.2	3.44	1.81

*Estimated standard deviation, in dB, of $\log_{10}(E/C_L) = 20\,[\pm$ Range of $\log_{10}(E/C_L)/2]$

Table 4-6 summarizes the available data on Poisson's ratio, μ, for the materials listed in Table 4-5. They are condensed into five groups for which the value of μ is approximately equal: (1) adobe, brick, etc, (2) aluminum, steel, (3) Douglas fir (for wood frame walls), (4) glass, and (5) gypsum materials. It is not necessary to estimate a standard deviation of the log of μ since it

is only an indirectly dependent variable and is not directly included in defining the statistical parameters of the probability of damage.

Table 4-6. Poisson's Ratio μ for the Materials Listed in Table 4-5, Collected into Five Groups

Poisson's ratio by material group	Ref.	μ	
		Mean	±Range
Adobe, Brick, Concrete Wall, Masonry, Stone	64	0.10	NA
Aluminum, Steel	11,65	0.31	0.025
Douglas fir (for wood frame walls)	11	0.32	0.11
Glass	11	0.22	0.045
Gypsum Plaster, Wall Board	11,67	0.04	NA

For simply-supported beams vibrating in their fundamental mode, the value of K_S is needed for evaluating the stress response of built-up structural assembles.[63]   This is given by

$$K_S = c(I/A)^{1/2} \tag{4.26}$$

where c = the distance from the neutral (unstressed) plane of the beam to the outer most fiber, I = the area moment of inertia of the beam and A is the area of its cross section.   This expression is utilized later to define values for K_S for built-up structures which consist of a combination of plates and beams.

4.7.2.5.2 Fundamental Resonance Frequency and f_0T for Windows

Since both the modal frequency $f_{m,n}$ and proportionality factor K_S vary with the aspect ratio of windows, it is necessary to establish a model for the fundamental resonance frequency of windows. Table 4-7, based on data in Reference 38, lists window types to be considered.

The theoretical value for the fundamental resonance frequency, f_0, for a simply supported homogeneous panel of thickness h, and short and long side lengths a and b respectively, was given by Equation 55 in Reference 39. It is recast in a more convenient form as

$$f_0 = \frac{\pi}{2}\frac{h}{a^2}\left[1+\left(\frac{a}{b}\right)^2\right]\frac{C_L}{[12(1-\mu^2)]^{1/2}} \tag{4.27}$$

Using the mean value for the longitudinal speed of sound $C_L = 0.216 \times 10^6$ from Table 4-5 and the Poisson's ratio $\mu = 0.22$ for glass from Table 4-6, this fundamental frequency for a simply supported window pane is

$$f_0 = 104,000\frac{h}{a^2}\left[1+\left(\frac{a}{b}\right)^2\right] \tag{4.28}$$

Application of Equation 4.28 requires the window thickness, h, which is not as readily found as the window dimensions.   Glass thickness usually varies with window size, so that if the actual value of h is not known it can be estimated from the empirical relation[41]

$$\frac{h}{a} = \log_{10}\left(1.035A^{-0.0027}\right) \tag{4.29}$$

so that, for glass,

$$f_0 = 76,000 \log_{10}\left(1.035A^{-0.0027}\right) \frac{\left[1+\left(\dfrac{a}{b}\right)^2\right]}{\sqrt{A\dfrac{a}{b}}} \tag{4.30}$$

Equation 4.30 includes empirical adjustments described in Reference 41, and is expected to be within 10% of actual resonant frequencies. Given the ease of obtaining window area and aspect ratio, versus obtaining actual glass thickness, this is of significant practical use.

Table 4-7. Representative Physical Parameters for Typical Windows

Type of Window	Range of Area, A, ft²	Geom. Mean, A, in²	Shortest Side, a, in	Thickness, h, in	h/a
A	1-2	200	12.2	3/32	0.00765
B	2-10	640	21.9	3/16	0.00856
C	10-50	3,200	49.0	1/4	0.00510
D	50-100	10,000	86.6	5/16	0.00361
E	> 100	14,400	103.9	3/8	0.00361

Table 4-8 provides a matrix of values for f_0 computed from Equation 4.30 for the five different window types (A through E) and four different aspect ratios from 0.25 to 1.0. Also included are values for the surface weight based on the nominal thickness from Equation 4.29 glass density of 0.0868 lb/in³. The estimated standard deviation, $\sigma_L(w)$, of the log of the surface weight is also shown.

Table 4-8. Matrix of Computed Values of f_0 for Various Window Configurations

Window Type	Mean Area, in²	f_0, Hz				Surface Weight w, psi.	$\sigma_L(w)$
		a/b					
		0.25	0.5	0.75	1.0		
A	200	99.7	82.9	84.6	93.8	0.00814	0.005
B	640	47.0	39.1	39.9	44.2	0.0163	0.005
C	3,200	15.6	13.0	13.3	14.7	0.0217	0.005
D	10,000	6.69	5.56	5.68	6.29	0.0271	0.005
E	14,400	5.00	4.16	4.24	4.70	0.0326	0.005

An initial range for f_0T of 0.02 to 10 was defined earlier for evaluation of Equation 4.20 for non-window structures with resonance frequencies ranging from about 15 to 50 Hz. Considering the greater range for f_0 for windows from about 4 to 100 Hz indicated in Table 4-8, the range for f_0T for window stress analysis was extended from a lower limit of 0.01 to the same upper limit of 10.

This accommodated the range in the 4 x 5 matrix of 20 values of f_0 in Table 4-8 and a 3 x 4 matrix of 12 values of T based on R = 50, 500 and 5,000 ft. and W_T = 2, 20, 200 and 2,000 lbs, providing a total of 200 cases with a corresponding range for f_0T of 0.01 to 10. Figure 4-57 summarizes the distribution for the resulting 200 values of f_0T. This distribution fits a log normal form.
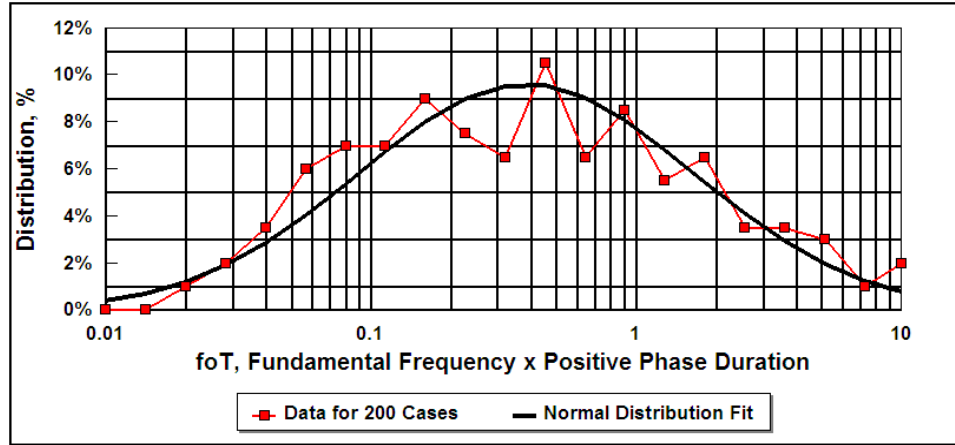
Figure 4-57. Distribution of f_0T for 200 Combinations of Window Dimension and Blast Loading

4.7.2.5.3 Stress Response of Windows to Blasts

Combining Equations 4.20, 4.23 and 4.24, a normalized expression for the total multi-modal stress response, $S_{m,n}(t)$ of windows can be given as

$$\frac{S_{m,n}(t)}{(P_0/w)gT} = \frac{E}{C_L}\sum_{m,n}^{odd}\frac{16K_S}{mn\pi^2}\frac{Z_{m,n}}{\left(Z_{m,n}^2 - 2\delta Z_{m,n}+1\right)^2}\{V_1(t)+V_2(t)\} \tag{4.31}$$

where $Z_{m,n}$, $V_1(t)$ and $V_2(t)$ are the same as defined for Equation 4.20, E and C_L are the elastic modulus and sound speed and K_S is the aspect-ratio, mode-dependent vibration-to-stress proportionality factor given earlier by Equation 4.25.   Since K_S is mode-dependent, it must be included within the mode summation sign.

  As was done for the evaluation of the velocity response, the quantity gT is on the left side of the Equation so that the normalized total stress response spectra varies only with f_0T. Equation 4.31 was used to determine the maximum positive or negative stress response from the time histories for all the types of windows, by area and shapes, in Table 4-7, for the range of values of f_0T indicated above. The velocity response analysis was carried out over a range of a dimensionless time, f_0t, from 0 to 6 to insure, conservatively, that the peak blast response was found.   As indicated earlier, based on available information, a critical damping coefficient, δ of 0.075 was assumed for all windows. Thus, the damping correction factor, C_d (to be introduced shortly), was 1.0 for windows. Figure 4-58 presents two examples of the resulting time histories for the computed stress response of two windows.
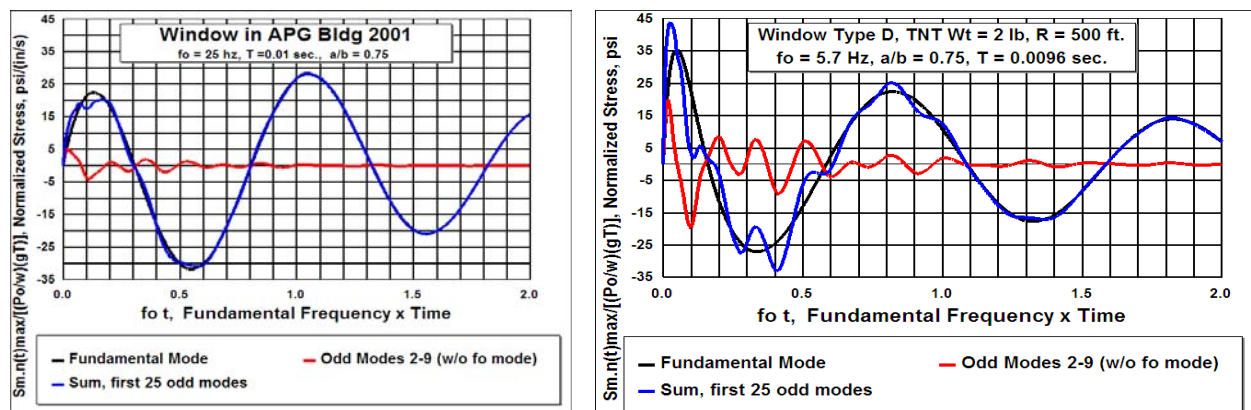
a. Window similar to APG Building 2001[62]   b. Type D window, Table 4-7

Figure 4-58. Time Histories of Stress Response to Blast for Two Windows

Figure 4-58a represents the stress response for a window similar to that in building 2001 at Aberdeen Proving Ground, which was measured as reported in Reference 62. Consistent with the measurements, very little evidence of significant response for odd modes beyond the fundamental mode is apparent. The response for modes 2-9 is for m,n = 1,3 and 5 but excluding the fundamental (m,n = 1) mode. The response differs slightly from that for the fundamental mode. The response for modes 10-25 is for m, n up to 9 without the first 9 modes. In this case, the response for these higher modes is barely discernible. Note that the highest response for the fundamental mode occurs at the beginning of the second cycle at f0t $\cong$ 1.0 or at t $\cong$ (1/f0).

Figure 4-58b is for a large (Type D) window with alternative parameters identified in the figure where much greater modal response is evident. The envelope or Stress Shock Spectrum of the maximum (positive or negative) stress response from these time histories is shown in Figure 4-59.

As expected, these Stress Shock Spectra collapse into four window groups according to their aspect ratio, a/b. Each of these groups can be defined, empirically, by the following fourth order regression expressions similar to that for the velocity response given earlier by Equation 4.23. The regressions, which combine the fourth and fifth factors of Equation 4.13, are

$$\frac{S_{m,n}(t)_{max}}{(P_0/w)gT} = 10^{\left(A_0 + A_1 L + A_2 L^2 + A_3 L^3 + A_{41} L\right)} \qquad (4\text{-}32)$$

where $L = \log_{10}(f_0 T)$ and the coefficients A_i are given in Table 4-9 along with the standard deviation of the log of the ratio of values for $S_{m,n}(t)_{max}/[(P_o/w)(gT)]$.
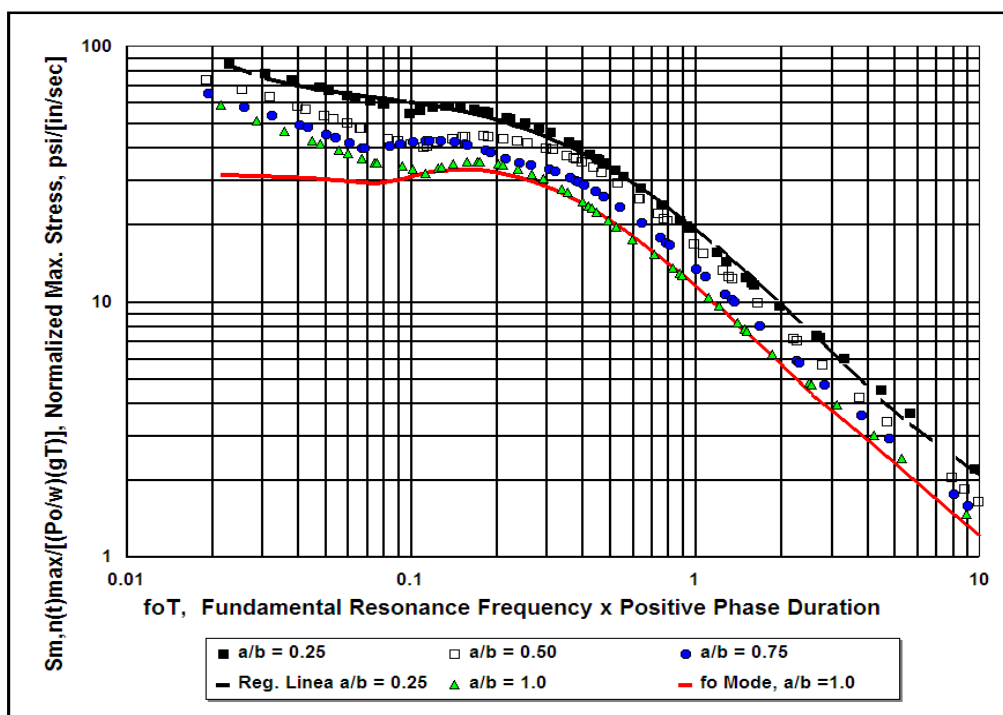
**Figure 4-59. Stress Shock Spectra for Response of Windows to Blasts Grouped by Aspect Ratio, *a/b*;
The solid red line is the regression line for the fundamental mode for *a/b* = 1.0;
The dashed black line, at the top, is one of the four regression lines for the
Shock Spectrum for the first 25 odd modes, in this case, for *a/b* = 0.25**

Table 4-9. Regression Coefficients for Equation 4.32

a/b	A_o	A_1	A_2	A_3	A_4	σ_L(Reg'sn)
0.25	1.2865	-0.9005	-0.3549	0.1711	0.1207	0.0190
0.50	1.2334	-0.9381	-0.4636	0.2236	0.1814	0.0249
0.75	1.1473	-0.9449	-0.4027	0.2239	0.1590	0.0163
1.00	1.0829	-0.9151	-0.3916	0.2024	0.1534	0.0263

4.7.2.5.4 Stress Response of Other Structures to Blasts

From Equations 4.24 and 4.25, the stress response of a structure to blast-induced vibration varies directly as the vibration/stress proportionality factor, K_S. The average ratio of K_S over the first 9 odd modes to K_S for the first mode was computed for all the structural material groups listed in Table 4-6 except glass. The average ratio was 1.07 with a standard deviation of ± 0.04 corresponding to a variation in the maximum stress response of 0.59 dB ± 0.32 dB, relative to a value for K_S for the f_0 mode. The modal response is always highest for the fundamental mode. Thus, the value of K_S for only the fundamental mode will be used for evaluation of stress for non-window structural materials.

A further consideration was to modify the value for K_S for built-up structures such as wood-, steel- or aluminum-frame wall assemblies. This required application of Equation 4.26 for the value of K_S for beams that make up the frame-work for such built-up structures. This analysis was carried out in Section 4.5 of Reference 38 and in Section 2.4.12 of Reference 66 and an example for a built-up wood wall is repeated here.

From Equation 4.26 the general expression for K_S of a beam is $c/(I/A)^{1/2}$ where c is approximately one half of the built-up wall thickness, I is the area moment of inertia of a unit width of the beam and A is its cross-sectional area.

For example, assuming a typical 2 in. x 4 in. x 8 ft. wood stud wall with studs 16 in. on center, for external and internal skin coverings 3/4 in. thick, K_S has a value of approximately 1.13. A similar analysis for built-up steel and aluminum frame wall assemblies gave a value of K_S of 0.89.

The resulting design values for K_S for such built-up structural wall assemblies and for homogeneous wall assemblies, other than windows, are given in Table 4-10 along with the previously-defined values for E/C_L and the product $K_S(E/C_L)$. The latter thus defines the magnitude of the fifth term, S_{pk}/V_{pk} in Equation 4.13 for all the structural assemblies except windows. (Note that V_{pk} is considered to be the same as the maximum multi-modal structural velocity, $V_{m,n}(t)_{max}$.)

Table 4-10 also defines the standard deviation, $\sigma_L(E/CL)$ of the log of E/C_L and identical values for the standard deviation, $\sigma_L[(E/C_L)K_S]$ of the log of $K_S(E/C_L)$ since the standard deviation of the log of K_S is assumed to be zero. Any variance in K_S can be assumed to be already included in the variation of the other important structural parameters for built-up walls such as their resonance frequency and surface weight. Estimates, primarily from References 11, 38 and 66, of the latter parameters, f_0 and w, and the corresponding standard deviation of the log of their values, $\sigma_L(f_0)$ and $\sigma_L(w)$ are also given in Table 4-10.

Table 4-10. Stress Response Parameters for Wall Materials and Assemblies (based primarily on data in References 11, 38 and 66)

Wall Material & Assemblies	a/b Mean[2]	K_S[2] Mean	E/C_L Mean psi/(in/s)	$\sigma_L(E/C_L)$[3]	(E/C_L) xK_S Mean psi/(in/s)	$\sigma_L[(E/C_L)$ x $K_S]$[3]	f_0 Mean Hz	$\sigma_L(f_0)$ -	w Mean psi.	$\sigma_L(w)$ -
Adobe, 12 in Thick	0.25-1.0	1.30	2.0	0.022	2.60	0.022	13	0.057	0.804(4)	0.095
Aluminum Frame Walls[1]	0.17	0.89	50.2	0.018	44.7	0.018	14	0.054	0.004	0.022
Brick Wall	0.25-1.0	1.30	17.2	0.230	22.4	0.230	12	0.109	0.460	0.093
Concrete Block	0.25-1.0	1.30	21.9	0.021	28.5	0.021	95	0.109	0.260	0.125
Glass (See Table 4-8)	Various	(5)	49.5	0.055	(5)	0.055	Tbl 4-8	0.138(6)	Tbl 4-8	0.005(8)
Masonry/Stone	0.25-1.0	1.30	48.2	0.177	62.6	0.177	25	0.109	0.760	0.105
Steel Frame Walls[1]	0.17	0.89	148	0.005	132	0.005	14	0.054	0.0115	0.022
Wood Frame Walls+Gypsum Interior	0.17	1.13	7.2	0.043	8.10	0.043	17	0.076	0.0347	0.065
Wood Frame Walls+Plaster Interior	0.17	1.13	18.2	0.035	20.6	0.035	16	0.066	0.0677	0.064
Wood Frame Walls+Wood Panel Int.	0.17	1.13	8.2	0.090	9.27	0.090	15	0.051(7)	0.0591	0.087

Notes:

(1) K_S computed for built-up structure using Equation 4.26 with typical 8 ft. wall with 16 in. stud spacing. Assumed, also for wood and steel frame walls.

(2) Average for a/b = 0.25 to 1.0 for non-window elements.

(3) Estimated Standard Deviation of $\log_{10}(E/C_L)$ = (1/2) [+/- Range of $\log_{10}(4$-$5)$]. See Table 3. Since $\sigma_L(K_S) = 0$,
$\sigma_L[K_S E/C_L] = [\sigma_L(E/C_L)^2 + \sigma_L(K_S)^2]^{0.5} = \sigma_L(E/C_L)$.

(4) w for 12 in. adobe walls based on average from data sources cited in Note 6, for Table 4-2 of Reference 38.

(5) K_S for windows included in the computation of their stress response using Equation 4.32.

(6) $\sigma_L(f_0)$ based in range for f_0 specified in Reference 68 is provided for information only – it is not used for damage prediction.

(7) Assumed Std Dev of $\log_{10}(f_0)$ for wood panel interior to be average for wood walls with plaster or gypsum board interior.

(8) $\sigma_L(w)$ based on estimated standard deviation of $\log_{10}$[Density of glass].

4.7.2.5.5 Damping Effects on blast response of non-window structures

Consider the assumption made earlier about the critical damping coefficient, δ. For the analysis thus far, δ was assumed to be 0.075. This was based, primarily, on the measurements on one window in APG Building 2001[62] and is considered a reasonable value for δ for acoustically-driven vibration of windows but not for other types of structural elements.

While large bodies of data exist on the gross structural vibration response of structure to blasts and sonic booms (e.g., References 11, 38, 69-71), very little information is available on damping effects for such impulsive sounds. Thus, the effect of damping on multi-modal velocity or stress response to blasts is briefly considered here. It was only necessary to evaluate damping effects on velocity response since damping effects are the same for velocity and stress response.

Damping has a first order effect on maximum structural response to excitation by steady broad-band sound such as aircraft noise. Similar laboratory data, summarized in Table 4-11, were available to better define this first order effect of damping. The data covered a wide range of built-up wall structure mock-ups, including, a wall with a window,[11,61] and are presented here for analysis of Specific Acoustic Mobility, M_{SA}, and critical damping coefficients.

The maximum rms acceleration response, $A(f_0)_{max}$, g, in a one-third octave band for the fundamental frequency f_0, at the center of a simply supported panel driven by a normally incident broad-band continuous sound is[11,66]

$$A(f_0)_{max} = 4\left[\pi P_b^2(f_0) J_{11}^2(f_0) Q / (2 B_w w^2)\right]^{1/2} \tag{4.33}$$

where

$P_b^2(f_0)$ = mean square sound pressure in the 1/3rd octave band centered at f_0,

$J_{11}^2(f_0)$ = square of the Joint Acceptance at f_0 at the center of a simply supported panel for a normal incident sound wave,

Q = the resonance amplification factor for a SDOF system

B_W = bandwidth of one third octave band filter relative to its mid band frequency

w = the surface weight of the panel in the same units as $P_b(f_0)$.

In this case[11,66], $J^2_{11}(f_0) = (2/\pi)^4$ and $B_W = 0.2308$ for a one third octave band so that

$$A(f_0)_{max} = 4.23 P_b\left(f_0 \sqrt{Q}/w\right) \tag{4.34}$$

For the tests summarized in Table 4-11, the maximum acceleration response, $A(f_0)_{max}$ to broad-band sound was measured at the fundamental frequency, f_0 of the structure. This maximum response is conveniently defined in a non-dimensional form by a term called the Specific Acoustic Mobility, M_{SA} equal to:[11,66]

$$M_{SA} = A(f_0)_{max} w / P_b(f_0) \tag{4.35}$$

Table 4-11. Damping Parameters of Building Components other than Windows

Type of Structure	M_{SA}	δ (Eq. 4-6)	$σ_L(δ)$ (1)
B-1 PART A Design values for damping constant derived, in part, from Part B data.			
Adobe wall (12 in.)	7.1	0.18	0.23
Aluminum Metal Frame Buildings	4.5	0.44	0.30
Brick	5.6	0.29	0.15
Concrete Block	5.6	0.29	0.15
Masonry-Stone	5.6	0.29	0.15
Steel Frame Buildings	4.5	0.44	0.30
Wood Frame Bldg with Gypsum Board Interior	6.7	0.20	0.27
Wood Frame Bldg with Plaster Interior	10.0	0.09	0.27
Wood Frame Bldg with Wood Paneling Interior	7.4	0.16	0.27
PART B Measured Vibro-acoustic structural response data			
B.1 Wyle, Ref. 61			
Wall W1-1, 8'x10' Wood Frame Wall Mock-up			
¾" Wood siding, 1/8" asbestos shingles	32.8	0.008	
No Window. No Insulation	82.4	0.001	
Wall W1-2, Same Mock-up			
¾" Wood siding, 1/8" asbestos shingles	31.7	0.009	
No Window + Insulation	10.6	0.080	
Wall W2, Same mock-up			
¾" Wood siding, cedar shingles	3.72	0.65	
Wood double hung window + Insulation	6.62	0.21	
Wall W3, Same mock-up			
½" Fiberboard w/ Aluminum Siding	4.18	0.52	0.51
Aluminum Awning Window + Insulation	6.62	0.21	0.20
Wall W4, Same mock-up			
18" x 8" cinder blocks	3.06	0.96	
Roof			
Roof (10 ft x 16.5 ft mockup, wood gabled roof	4.55	0.44	
With sheet rock ceiling and insulation			
Steel Industrial Bldg Wall + Insulation (2)	3.5	0.73	0.30
Steel Industrial Bldg Wall, No Insulation (2)	5.5	0.30	0.30
B.2 CERL, Reference 72			
3 sided, 13 ft. x 19 ft. Resid. Bldg. Mockup.			
Avg. North, South Wall & Ceiling combined	19.3	0.024	0.062
Picture Window	28.2	0.011	
Sash Window	37.6	0.006	

(1) Standard deviation for published or estimated range of Lg(δ).
(2) Data for steel industrial buildings from vibro-acoustics tests of a 18 ft. x 20 ft.

mockup. Only data for 2 walls designed for 25 psf. wind loads were considered.[2,16]

Comparing Equations 4.34 and 4.35, since the critical damping coefficient δ is equal to $1/(2Q)$, the value of δ can be derived from experimentally-determined values for $M_{SA.}$, measured for structural response to continuous, broad-band sound, by:

$$\delta = \frac{1}{2} 4.23^2 / M_{SA}^2 = 8.95 / M_{SA}^2 \approx 9 / M_{SA}^2 \qquad (4.36)$$

Table 4-11 summarizes these experimentally-derived values for $M_{SA.}$. The values for M_{SA} in Part A are used to define δ from Equation 4.36 for a wide range of structural components of concern for this report. These will be applied for estimating the relative stress response of damped, non-window structures to define a damping adjustment factor for this stress response. This is considered later.

Part B summarizes key experimental data from References 61 and 72 for which some of the values for M_{SA} were derived. Where possible, estimates of the standard deviation, σ_L of the variation in the log of δ is also provided.

In Part B, the average M_{SA} measured for the various wood walls with insulation was 10.6 which compares very well with an average M_{SA} of 8.0 in Part A for wood walls. Absent more measurements, Part A values are assumed suitable for design.

The change in the Velocity Shock Response Spectrum for other values of δ, relative to the value of 0.075 applied for Figure 4-65, has been computed. This involved finding the envelope of the maximum time histories of velocity response of simply-supported plates to blasts for three different values of f_0T. For this evaluation of damping effects, the range of δ considered corresponded to the approximate minimum ($\delta = 0.01$) and maximum ($\delta = 0.8$) that had been observed in the tests summarized in Part B of Table 4-11. The higher values of δ, inferred from these measurements, reflects the complex damping patterns of built-up structural assemblies.

Figure 4-60 shows the ratio of the corresponding values of $V_{m,n}(t)_{max}/[(P_o/w)(gT)]$ relative to its value default $\delta = 0.075$, which is representative for windows. For convenient interpretation, the ordinate, in decibels, is simply $20 \times \log_{10}$ of the ratio of $V_{m,n}(t)_{max}/[(P_o/w)(gT)]$, for the specified δ on the abscissa scale, to its value for $\delta = 0.075$. The values for $V_{m,n}(t)_{max}$ are the maximum total velocity response (positive or negative) over the first 25 odd modes of a simply supported plate considered reasonably representative for most types of structures for purposes of this analysis.

Values are shown for this ratio, in dB, in Figure 4-60 vs δ for $f_0T = 0.02$, 0.4 and 8. These values for f_0T correspond to approximately the log mean (0.4), and $\pm$ 1 standard deviation about this log mean, for the log normal distribution of f_0T shown earlier in Figure 4-57. Each of these data points is the value for this relative, multi-mode velocity response for a default aspect ratio of 0.75 considered reasonably representative for all types of structures. Clearly, the data indicate an expected trend of a moderate, not first order, increase in velocity response as the damping coefficient decreases. A regression line, describing the average trend over all three values of f_0T, Is given by a relative damping adjustment A_d, in decibels, equal to

$$A_d = -0.859 + 4.49 \log_{10}(\delta) + 7.10 [\log_{10} \delta]^2 + 2.16 [\log_{10} \delta]^3 \qquad (4.37)$$

where $A_d = 20 \log_{10} \dfrac{V_{m,n}(t)_{max} \text{ for any } \delta}{V_{m,n}(t)_{max} \text{ for } \delta = 0.075}$

For damage probability calculations, the relative damping correction factor, $C_d = 10^{(A_d/20)}$ will be used. This expression, equal to 1.0 for $\delta = 0.075$, defines the magnitude of the peak velocity and/or stress response amplitude of structures for values of $\delta \neq$ 0.075 relative to the amplitude for $\delta = 0.075$. The anomalous behavior of the data for $f_0T = 0.4$, for an abnormally high $\delta > 0.6$, is ignored for current purposes.

As indicated at the top of Figure 4-60, the standard deviation from the regression line of all values of A_d for the three values of f_0T was $\pm$ 0.71 dB for $\delta \leq 0.6$.   Thus, for damage prediction analysis purposes, the standard deviation of the log of C_d, or $\sigma_L(C_d)$, will be set equal to 0.71/20 or 0.036 for all non-window structures.
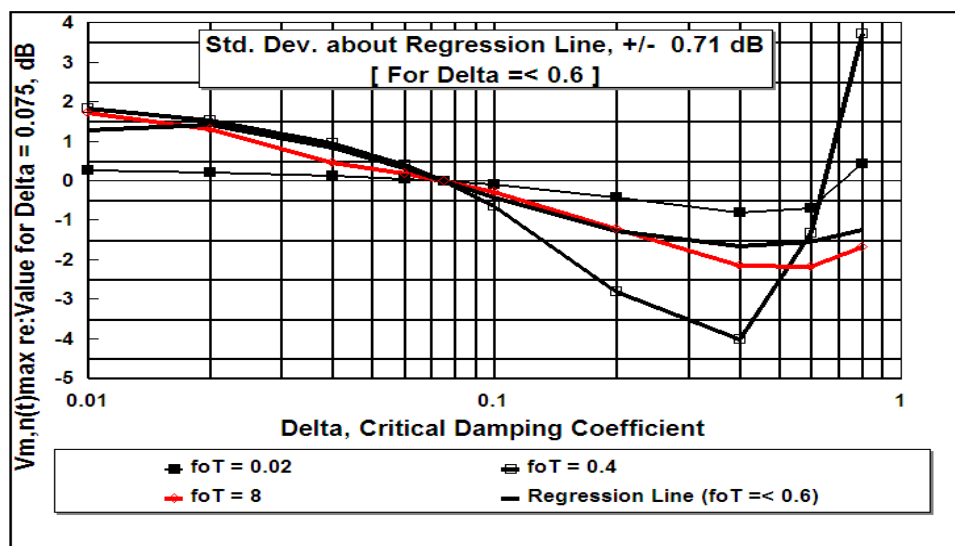
Figure 4-60. Damping Adjustment, A_d in dB, to Maximum Multimodal Velocity Response Relative to the Value for δ = 0.075 used for Glass; The same damping effect applies to the stress response

The effect of damping on blast response illustrated in Figure 4-60 will apply to all types of structures since the underlying multi-modal damped vibration response model of Equation 4.20 is independent of the type of structure. However, since δ is assumed to be 0.075 for all windows, the value of C_d for windows is 1.0. The corresponding Standard Deviation of the log of C_d, and the relative damping adjustment A_d, are both equal to 0 for windows.

The predicted values for the critical damping coefficient, listed on the right side of Table 4-11, are very high, in some cases, and reflect the expected higher damping of built-up structural assemblies made of steel or aluminum.   However, for conservative damage estimates, a maximum value of δ = 0.44 will be assumed for these highly damped structures. This corresponds to a maximum value for the damping adjustment factor, A_d, from Equation 4.37 or Figure 4-60, of −1.7 dB.

4.7.2.5.6 Summary of structural stress response to blasts.

All the parameters needed for the first five terms of Equation 4.13 to predict the stress response to blasts have now been defined. Anticipating their employment for damage assessment, it is desirable to summarize the practical form that these parameters will have, and the steps used in their employment for this purpose.

Returning to the specific symbology indicated in Equation 4.13, the effective peak blast pressure, P_e acting on a structure will be given by:

$$P_e = P_0 \left[P_f / P_0 \right] \left[P_e / P_f \right] \tag{4.38}$$

where P_o is the nominal free field blast pressure given by Equation 4.14 or other blast wave prediction model.

The second term, $[P_f/P_o]$, represents the nominal variation in the free field blast pressure due to propagation effects. By virtue of the statistical model for these effects, developed in Section 4.7.2.2, the log mean value of this ratio is assumed to be 1.0 in all cases. The standard deviation of the log of this ratio will be zero for the baseline damage prediction method (Method 1) or it will be defined by Equation 4.17 for Method 2.)

The third term, $[P_e/P_f]$, or reflection/diffraction correction factor C_r, represents the change in the true free field blast pressure due to reflection and diffraction as developed in Section 4.7.2.3. While this change has a complex pattern of variation with frequency, a simplified version is provided, in Table 4-4, by a diffraction correction, in dB, A_r equal to $20 \log_{10}(C_r)$ for cubical shaped structures. For the default case for a blast wave at normal incidence on a large structure, C_r has the default value of 2 (i.e., $A_r = 6$ dB).

The fourth term, V_{pk}/P_e, in Equation 4.13, is the ratio of the peak velocity response to the effective peak pressure. For structures other than windows, this is obtained from the regression (Equation 4.23) for $V_{m,n}(t)_{max}/[(P_o/w)(gT)]$. In this case, the symbol P_o is understood to actually represent the effective pressure, P_e and V_{pk} is the same as $V_{m,n}(t)_{max}$ so that the term V_{pk}/P_e is equal to $V_{m,n}(t)_{max}/[(P_o/w)(gT)]$ x $[(gT)/w] = $ [Eq. (4.23)] x $[(gT)/w]$. Clearly, this requires that the structure variable, w and the blast source variable, T be defined for each case. (Note that since in-lb-sec units are employed and w is in psi, the acceleration of gravity, g is 386 in/s^2.)

The fifth term in Equation 4.13, S_{pk}/V_{pk}, is the ratio of the peak stress response, S_{pk}, to the peak velocity, V_{pk}.

For all structures, this ratio, derived from Equation 4.24, is equal to the product KS [E/CL] . The appropriate values for this quantity for structures other than windows are given in Table 4-10.

For such structures, one adjustment can be applied to the stress-to-velocity ratio to account for damping effects. Thus, for these non-window structures, the ratio S_{pk}/V_{pk} will actually be given by:

$$S_{pk}/V_{pk} = C_d K_S E/C_L \tag{4.39}$$

where C_d is a relative damping correction factor, a function of the critical damping coefficient, δ. Values for δ were given in Table 4-11 for structures other than windows. As stated earlier, the standard deviation of the log of the relative damping correction factor, C_d, was set equal to 0.036

(= 0.71/20) as indicated by the standard deviation, 0.71 dB, of the data points about the regression line in Figure 4-60.

For windows, damping is already included in the assessment of stress response for blast. Thus, for windows, $C_d = 1.0$ and the corresponding standard deviation, $\sigma_L(C_d) = 0$. The fourth and fifth terms in Equation 4.13 are combined to define the ratio, S_{pk}/P_e, of the peak stress response to the peak effective pressure. As stated earlier, this approach is necessary due to the complex interaction of velocity response modes and stress for the modal behavior of windows. This ratio is defined by the set of normalized regression equations defined by Equation 4.32 with aspect ratio dependent coefficients listed in Table 4-9. Thus, for windows, the ratio S_{pk}/P_0 is given by

$$S_{pk}/P_0 = \left\{S_{m,n}(t)_{max} / [(P_0/w)(gT)]\right\}(gT/w) = 10^{F(L,a/b)}(gT/w) \qquad (4.40)$$

where $F(L,a/b)$ represents the polynomial exponent in Equation 4.32.

Having defined the peak stress response to blasts, the damage prediction model concludes with an evaluation of the last term Equation 4.13 involving the structural failure or damage threshold stress, S_d.

4.7.2.6 Damage Stress Thresholds and Material Strength Data

Damage stress thresholds and material strength data employed for this study are based primarily on:

1) Available, directly applicable, data on damage or failure stress (or strength) of materials, listed in detail with many source citations at the end of Reference11
2) Data from the extensive work carried out by the U.S. Bureau of Mines on structural damage from blast loading: References 67, 69, and 70
3) Engineering estimates based on related information on structural damage from dynamic loads: References 11, 38 and 66
4) Re-analysis, as needed, of the prior data used in References 38 and 66

These data are well established, so it is not appropriate to attempt a detailed review. Rather, they are summarized in Table 4-12 and supported by limited comments for some materials and a plot demonstrating the all-important lognormal distribution of the values for the damage stress or material strength values (S_d) for glass. This will draw heavily on the more detailed review of the topic in References 38 and 66 plus additional references cited in the table.

Table 12. Damage Stress Thresholds for Building Materials

No.	Building material or Assembly	S_d Damage Stress, psi	$\sigma_L(S_d)$	Reference
1	Adobe, New	8.5	0.239	38, p 3-24
2	Aluminum Frame Walls (1)	10,055	0.0988	73, p 12-67, 68
3	Brick Wall	55	0.239	66, 67
4	Concrete Block	88	0.328	66, 67 (2)
5	Glass, New (60 sec. load)	11,600	0.216	Eq. (4.41), Fig 4.61
6	Glass, Old (60 sec load)	2,940	0.216	Eq. (4.41), Fig 4.61
7	Masonry/Stone, in good repair	430	0.179	66, 67 (2)
8	Steel Frame Walls	15,000	0.150	38, 66, p 3-34
9	Wood Frame Walls + Gypsum Interior	234	0.072	66 (2)
10	Wood Frame Walls + Plaster Interior	150	0.185	66, p 3-31
11	Wood Frame Walls + Wood Panel Interior	470	0.210	38, p 4-45 (2)

(1) For aluminum alloys 3S, 53S, & 61S, commonly used in construction.
(2) The table entries are based on a re-analysis of the original data.

4.7.2.6.1 Damage Stress Threshold for Glass

Unlike the other structural elements considered in this report, "damage" to glass is assumed to correspond to actual failure of the glass pane. Glass panels fail under dynamic or static pressure loads due to the combination of bending and membrane or tensile stresses and their interaction with the very important influence of stress-raising surface flaws.[74] Due to the influence of membrane stresses, the stress response of a typical window does not increase linearly as a function of load. This nonlinear response behavior cannot be readily included in the statistical failure model employed in this report. However, it is possible to rationalize an assumption of linear response with the following argument employed by Hershey and Higgins[71] in their analysis of window damage from sonic booms.

1) A linear stress response model will over-predict the probability of a window failure since it will not account for reduced stress response due to non-linearity at stress levels approaching failure.

2) This over-prediction of failure will be partially compensated for by the fact that used, or older, glass panels have a lower failure stress.

Static pressure failure tests of 2,500 panes of new glass covering a wide range of window sizes, conducted by a glass manufacturer, were reported by Hershey and Higgins[71]. The lognormal probability distribution of these data is shown in Figure 4-61 which is based on the original plot in Reference 71. The log mean failure stress S_d of the primary distribution was 11,600 psi and the standard deviation $\sigma_L(S_d)$ of the log of S_d, for this part, was 0.216

Each of these static tests had a duration of about 60 sec. which requires consideration of the dynamic strength characteristics of glass to short duration loading, as from a blast. For sonic booms lasting about 0.1 sec., Hershey and Higgins assumed that the distribution of failure stress

in Figure 4-61 was about the correct value for used glass in good condition for such a short duration load based on the counterbalancing effect of two factors.

1) From their limited data, used glass had a failure stress about one-half that of new glass. (A lower failure stress for old glass is given later.)

2) The failure stress under the short duration (0.1 sec) sonic boom loading is about twice as high as the failure stress for the typical 60 sec. duration of static tests.

For blast loads, however, the duration can be substantially different than 0.1 sec. The increase in glass failure stress for short duration loading has been examined,[75] leading to the following expression for the ratio of the glass failure stress, $S_d(T)$ for load duration, T (not to be confused with blast wave duration T), in sec. to the 60 sec. static failure stress, $S_d(60)$.

$$S_d(T)/S_d(60) = (T/60)^{-1/n} \tag{4.41}$$

The reported[75] value of n, varying from 12 to 20, had an average value of 16 which is used here. The resulting value of $S_d(T)/S_d(60)$ is shown in Figure 4-62.
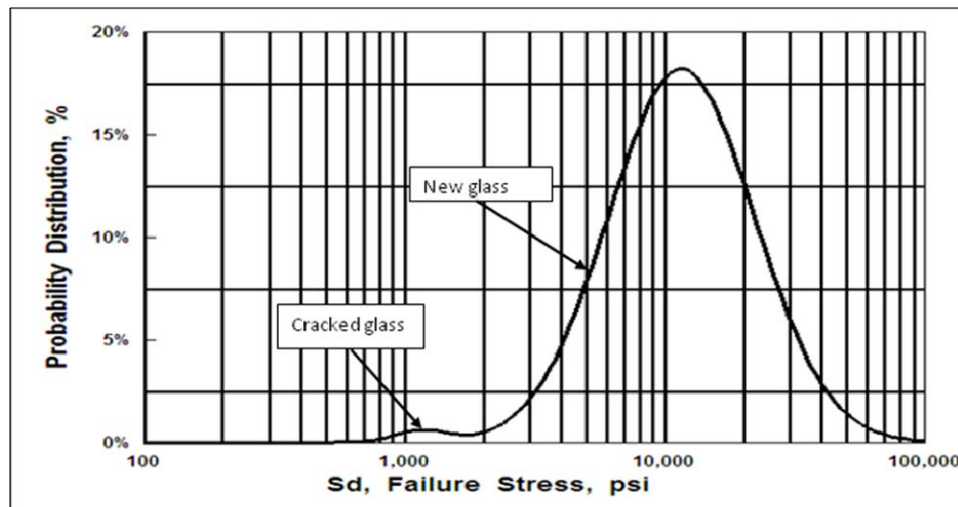
Figure 4-61. Failure Stress, S_D from 60 sec. Static Tests of 2,500 New Glass Panes of Various Sizes as Reported by Hershey and Higgins
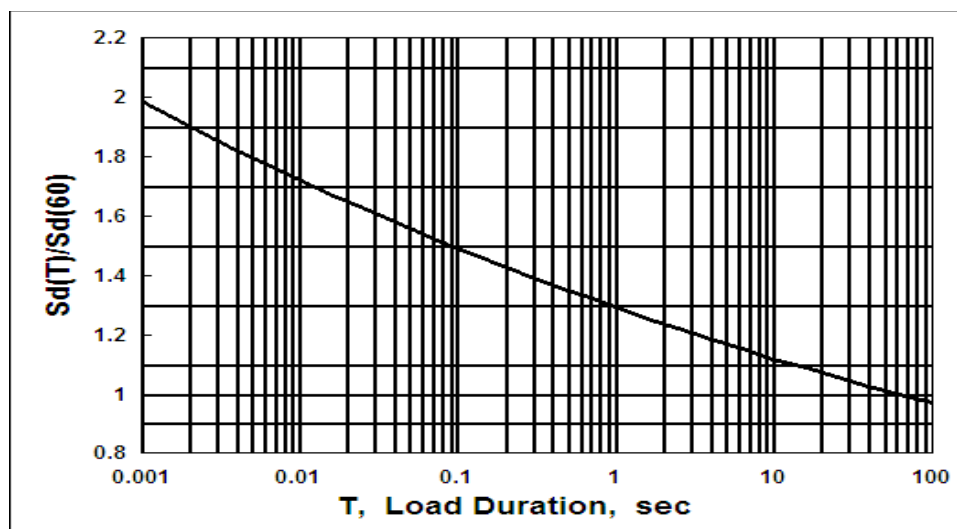
Figure 4-62. Increase in Failure Stress for Glass as the Load Duration, T, Decreases Below the 60 sec Duration for the Static Failure Test Data in Figure 4-61; Based on data in Reference 75

For expected blast load durations for the range of equivalent TNT weights (2-2,000 lb) and ranges (50–50,000 ft) considered in this report, blast wave duration T will vary from about 0.005 to 0.2 sec. The corresponding increase in the static failure stress for glass can vary from about 1.4 to 1.8 times the 60 sec. static failure stress, according to Figure 4-61 or Equation 4.41. Thus, for prediction of the Probability of Damage (POD) for windows, this significant variation in the expected failure stress of glass due to loading duration effects is included in the POD prediction model.

For old glass, tests by Beason and Morgan[74] on 62 twenty-two year old panes, ranging in thickness from 1/4 to 7/32 in, and with areas from 320 to 1,720 in^2, showed a log mean failure stress of 2,940 psi. (See Table 4-4 in Reference 66). (Coincidentally, this is almost exactly one quarter the strength of new glass.)

For damage predictions for glass, the 60 sec. static test damage threshold stress, for new and old glass will be taken as 11,600 and 2,940 psi. respectively. The blast damage threshold stress for different blast durations will then be computed using Equation 4.41 for all windows. The standard deviation of this loading duration correction from will be assumed to be zero.

The same dynamic strength phenomenon of a material under short time loading, compared to static loading, also applies to other materials.[76,77] This increase, utilized for the design of blast-resistance structures, can be of the order of 10% to 20% for concrete and steel structures. Absent more detailed data for other building wall materials, in the form available for glass, it was considered practical and acceptably conservative to ignore this small dynamic strength increase for building materials other than glass.

The standard deviation $\sigma_L(S_d)$ of the log of the failure stress of glass, in Figure 4-61, of 0.216 will be used later for damage prediction for both new and old glass.

One final consideration for damage assessment for glass is the potential "fatigue" effect of repeated blast loads. Two laboratory tests of the fatigue of windows under simulated sonic boom loading have been conducted.[78,79] The results are shown in Figure 4-63. The Wyle data[78] permitted using a regression line, for analysis purposes, since reference failure stress data were

also available for just one load application (i.e., N = 1). This regression line, which defines the apparent reduction in failure stress due to repeated simulated sonic boom loads, is defined as a "Fatigue Factor" *F*, given by

$$F = [\text{Failure Stress}(N \text{ loadings})]/[\text{Failure Stress}(N=1)] = N^{-0.033} \tag{4.42}$$
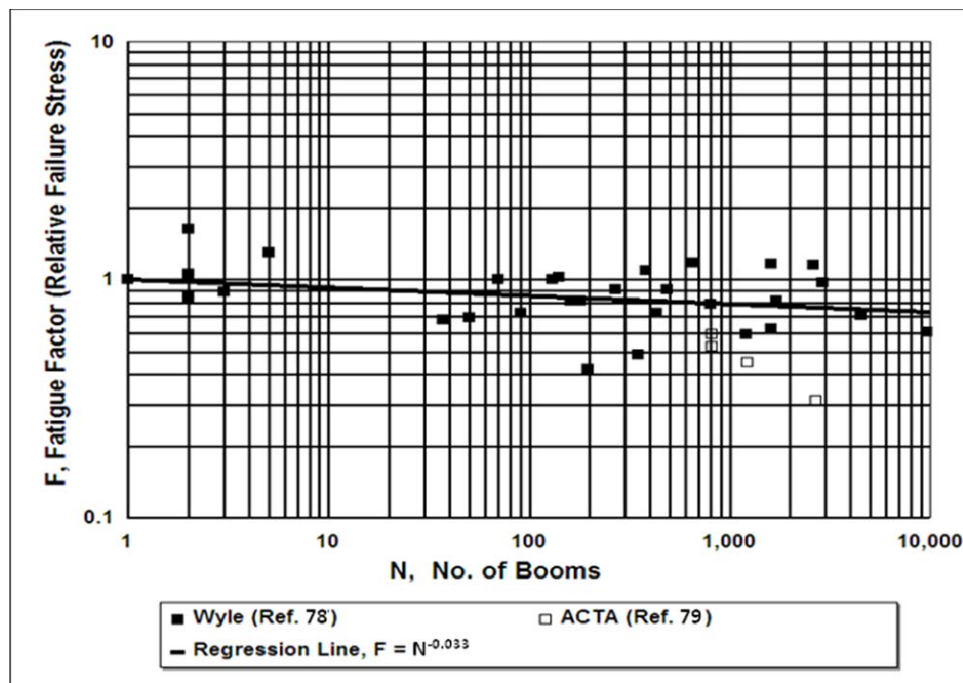
Figure 4-63. "Fatigue Factor" or Reduction in Damage Stress Threshold with Repeated Cycles of Simulated Sonic Boom Loading for Glass Panes[78,79]

As expected, the data exhibit considerable scatter (r = 0.34) reflecting the wide variation in failure stress of glass due to the many factors involved such as surface conditions, age and stress risers at the edges.[75] For comparison, fatigue effect test results were also available for concrete[61] and plaster[80] walls subjected to repeated cyclic loading. For concrete, the Fatigue Factor exponent in Equation 4.42 was -0.039, very nearly the same as for glass. For plaster walls, a pseudo "Fatigue Factor" was assumed equal to the inverse of the observed increase in the length, number or area of cracks in the plaster walls from repeated loading by simulated sonic booms.[80] In this case, the Fatigue Factor exponent varied from – 0.30 to – 0.43. This indicates the likely presence of a significant true fatigue effect for plaster walls. This is not, however, evaluated further.

In summary, these results show consistent evidence of a "fatigue factor" for glass and concrete with similar Fatigue Factor exponents of - 0.033 to - 0.039 and a probable much larger fatigue effect for plaster. Assuming the same fatigue effect applies to blast damage, according to Figure 4-63, the failure stress, Sd would decrease by about a factor of about 0.86 and 0.80 respectively for 100, and 1,000 identical blast loadings. Applying the failure prediction methods defined latter, such reductions would increase the Probability of Damage (POD) by a factor of 4.3 at 1,000 ft. for 100 blasts vs just one blast for a typical window and by a factor of 8.8 at 1,000 ft. for 1,000 blasts of the same magnitude.

4.7.2.6.2 Damage Stress Threshold for Masonry Walls

Bureau of Mines damage criteria[67,69,70] for masonry structures (e.g., adobe, brick, concrete and stone) subject to damage from blasting operations and data from static load tests on such walls provided the estimates of failure (or damage) threshold stress values in Table 4-12. Estimates of the standard deviation of the log of these damage stress levels were based on the information available on their variation.

Siskind used the following Bureau of Mines Level of Damage classification scheme for assessing damage from blasting operations:[69]

- Threshold: Loosening of paint; small plaster cracks at joints between construction elements (i.e., bricks, wall panels, etc.); lengthening of old cracks.

- Minor: Loosening and falling of plaster; cracks in masonry around openings near partitions; hairline to 3 mm cracks (0 to 1/8 inch); fall of loose mortar.

- Major: Cracks of several millimeters in walls; rupture of opening vaults; structural weakening; fall of masonry, e.g. chimneys; load support ability affected.

For this study, damage is taken to be greater than "minor." Masonry falls into three general groupings: adobe, brick and concrete block.

4.7.2.6.2.1 Adobe walls

For adobe walls, in the absence of other data, the relative compressive strengths of 400 psi. for adobe[38] and an average of 2,565 psi for conventional (fired clay) bricks[66,67], were used as to define a correction factor to adjust the damage threshold stress of brick walls of 55 psi to provide an estimated damage threshold stress for adobe walls. The resulting value was equal to (400/2,565) x 55 = 8.5 psi (rounded to the nearest 0.5 psi). Thus, 8.5 psi is the baseline estimate for the damage stress threshold for an adobe wall.

As cited in References 38 and 66, static loading tests reported by Smith[81] were conducted on a total of approximately 290 adobe bricks of various types from many different manufacturers. The results of these tests provided a substantial statistical data base for the static load strength of adobe bricks, typically about 10 x 4 x 14 inches in size. While the method of quantifying the adobe static load for these tests did not provide a directly applicable measure of failure stress, the statistical distribution of the measure of the failure load was clearly lognormal (See Figure 4-6 in Reference 38) and was therefore considered useful and reliable. Based on a lognormal fit to the data, the corresponding value for the standard deviation, $\sigma_L(S_d)$ of the log of the static failure

load was 0.239. An alternative (Weibull) model was also explored in a prior Wyle study[82] to define the probability distribution for the failure stress of adobe. However, the difference between a lognormal and a Weibull probability distribution for the failure stress was minimal indicating that for adobe, a lognormal probability distribution is a reasonable approximation.

Hershey and Higgins[71] also found that the probability distribution of failure stress, S_d for other materials, in addition to glass and adobe, could be closely approximated by lognormal distributions.

4.7.2.6.2.2 Brick walls

For brick walls, the damage threshold stress was developed primarily from the BOM data by Stagg.[67] There was a very large range, as much as 400 percent, in the values of static load for failure or damage of bricks walls This wide range is apparently due to real differences in the strength of brick walls as a function of their geometry and type or mix of mortar. (See the partial data summary on brick wall strength in Hershey and Higgins.[71]) Thus, the damage threshold stress in Table 4-12 for brick walls must be considered nominal for an average brick.

A large statistical data base was not available for these estimates of damage threshold stress values for brick so it was assumed that the more extensive data base on strength of adobe bricks, considered above, should be used to define the same standard deviation, $\sigma_L(S_d) = 0.239$ for the log of the damage threshold stress for conventional (fired clay) brick walls.

4.7.2.6.2.3 Concrete block walls

For concrete block walls, the damage threshold stress in Table 4-12 is 88 psi based on the referenced BOM data. The standard deviation $\sigma_L(S_d)$ of the log of this damage stress threshold for concrete blocks was based on the variation in the data for S_d.

4.7.2.6.3 Damage stress threshold for interior walls of wood frame buildings

Wood frame buildings of current construction usually have an interior wall finish of: a) gypsum wallboard (also called plasterboard or drywall), b) plaster or c) wood paneling.

4.7.2.6.3.1 Wood frame buildings with gypsum wallboard interiors

The basic dynamic stress prediction model developed in Section 4.7.2.5 is strictly applicable only for homogeneous walls and must be modified to predict stress and estimate damage probability for such non-homogeneous built-up walls of standard wood frame construction. For the same reasons, stress in such panels under static loads must be evaluated differently from stress in homogeneous plates under the same type of load. The resulting modifications to the stress prediction models for non-homogeneous walls were developed in detail in References 38 and 66 and are summarized here.

The modifications consisted of accounting for the differences in bending stresses in a homogenous 16 in. by 96 in. "plate" equivalent to one section between studs of a standard 8 ft.

wood stud wall. In this way, it was possible to use BOM data[67,69,70] on damage thresholds for static loading tests for such walls to estimate dynamic stresses in the interior wall materials under blast loading.   In some cases, BOM criteria for building damage in the form of damage thresholds for the velocity of building elements or building foundations were converted into estimated failure stresses for these various types of interior wall panels under blast loads utilizing the stress-to-velocity relationships developed in Section 4.7.2.5.   Again, details of these calculations are provided in References 38 and 66.

4.7.2.6.3.2 Wood frame buildings with plaster interior walls and ceilings

Tensile strength or failure stress data on a variety of plaster materials was available from Hershey and Higgins[71], Stagg, et al.[67] and from a variety of sources summarized in the Appendix of Reference 11.   These indicated a range of failure stresses from 140 to 300 psi. Based on considerations discussed in References 38 and 66, a value of 150 psi near the lower end of this range was selected for design purposes. From the Hershey and Higgins statistical data on mortar strength of plaster walls, a standard deviation, $\sigma_L(S_d)$ of the log of failure strength, 0.185, is used for plaster walls.

4.7.2.6.3.3 Wood frame buildings with wood panel interior walls

The same concepts relating the substantial data base for static failure loads to the resulting failure stresses applied in Section 4.7.2.6.3.1 were used in Table 4-12 to define a log mean failure stress S_d, and standard deviation, $\sigma_L(S_d)$ for walls with wood panel interiors.[38]

4.7.2.6.4 Damage Stress Threshold for Interior Walls of Metal Frame Buildings

The same process outlined for wood frame buildings was applied to the type of lightweight steel or aluminum frame utility buildings that are used on farms or as commercial buildings in many locations.   Such buildings commonly have vertical metal channel studs or columns, and horizontal stiffeners or girts, covered by a thin corrugated metal skin.

Again, the same well known theory[38,66] for predicting stress in such built-up structures was applied as for wood frame structures.

4.7.2.6.4.1 Steel frame buildings

A typical steel frame structure can consist of an 18 gage (0.049 in.) steel skin supported by 3 in., channel, 18 gage, steel columns, spaced 16 in. on centers.

Based on the estimates of failure stresses from static load test data[73] or from estimated dynamic stresses from blast pressures[69], failure stresses for the metal skin of steel frame buildings ranged from 4,000 to 4,700 psi.   Allowing for common stress concentration factors of 2 to 4, the resulting failure stresses were estimated to fall in the range of 8,000 to 18,800 psi – bracketing a working stress for common steel[73] of 15,000 psi. Thus, the latter was considered a reasonable value for design purposes. The value for $\sigma_L(S_d)$ for steel frame buildings of 0.15 was based on an assessment of the variation in the above estimates of failure stress.

4.7.2.6.4.2 Aluminum frame buildings

The same rationale was applied to aluminum frame buildings except that the design failure stress was estimated as the log mean, 10,055 psi., of published tensile strengths of a variety of common aluminum alloys used in construction (3S, 52S and 61S)[73]. The value of 0.0988 for the standard deviation, $\sigma_L(S_d)$, of the log of S_d was based on the variation in these tensile strengths.

With the limited data available, it was not always possible to validate the assumptions used here and by Hershey and Higgins[71], that the strength or damage threshold stress values had lognormal distributions. However, Hershey and Higgins[71] justified this assumed lognormal behavior for the strength of materials lacking failure distribution data "on the basis of the brittle nature of these materials and their similarity to glass and mortar".

For this report, when necessary, the required values of the standard deviations of the log of the quantities involved were estimated from information on the statistical variation of the variable (i.e., its own standard deviation or its range of extreme values). In the latter case, for example, it was assumed that $\sigma_L(x)$ was equal to one-fourth the log of the ratio of the maximum to minimum value of x assuming this corresponded approximately to the ±2 sigma range of the log of the variable, x.

4.7.2.7 Statistical Model for Blast Damage to Structures

All but the last element – the statistical prediction model needed to assess structural damage from blast - have now been established. In this section, the essential details of this statistical damage assessment model are defined. This is followed in Section 4.8 by specific estimates of the statistical probability of blast-induced damage to structures.

4.7.2.7.1 Factor of Safety and its Components

Recalling the basic starting point illustrated in Figure 4-49, blast damage is expected when the log of the Factor of Safety, or $\log_{10}$(FOS) is less than 0 and thus the FOS is less than 1. The value of the FOS is obtained from Equation 4.12, with the factors defined in Equation 4.13. Two additional optional correction factors have been included. The first is C_b, to correct the peak blast pressure for charge burial depth when needed, and the second is C_d. This is the correction, obtained from Equation 4.37 (using $C_d = 10^{(A_d/20)}$) for the peak velocity or stress response for structures, other than windows, due to damping being greater or less than the default value for δ of 0.075 of assumed for windows. Equations 4.12 and 4.13 may be written in combined form (as they are in Reference 41) with these factors as

$$S_{pk} = S_d \bigg/ \left(P_0 C_b \frac{P_f}{P_0} \frac{P_e}{P_f} \frac{V_{pk}}{P_e} \frac{S_{pk}}{V_{pk}} C_d \right) \tag{4.43}$$

The computation or specification of each of the terms in this expression for the FOS has been defined in the preceding sections. Now consider, more carefully, the statistical nature of these. This is summarized in Table 4-13.

For convenience, the standard deviation, $\sigma_L(x)$, the log of the various parameters, are expressed in dB as $20\sigma_L(x)$ in the last column. Note that rows are included for the surface weight, w and blast duration, T since the normalized maximum velocity and stress responses are directly proportional to these two parameters.

Table 4-13. Name and Source for Log Mean and Standard Deviation of Log of Statistical Parameters to Define the Factor of Safety

Parameter, x	Name	Source for log Mean(x)	Source for Std. Dev. of log(x) = $\sigma_L(x)$ (listed as $20\sigma_L(x)$, dB)
P_o	Blast Pressure	Equation 4.14	0. Equation is nominal
C_b (1)	Charge Depth Cr'ctn	Equations 4.16	0 Equations are nominal
(P_f/P_o)	Propagation effect	Log Mean = 1.0 (2)	Figure 4-52, Equations 4.17 and 4.18, 0 to $\pm$ 5 dB
$C_r = (P_e/P_f)$	Reflection/Diffraction	Table 4-4	Table 4-4, Default,$\pm$1.0 dB (3)
$(V_{pk}/[(P_e/w)(Gt]$	Velocity/Pressure	Equation 4.23 or Figure 4-56	$\pm$ 0.3 dB, ($\approx$ 0) See Equation 4.23 and Figure 4-56
(S_{pk}/V_{pk})	Stress/Velocity	Equation 4.24, for K_SE/C_L	$\pm$ 0.10 to $\pm$ 4.6 dB, Table 4-10
$(S_{pk}/[(P_e/w)(gT)]$	Stress/Pressure (4)	Equation 4.23, windows	$< \pm$ 0.6dB, ($\approx$ 0) See Table 4-9.
W	Surface weight	Table 4-10	$\pm$0.44 to $\pm$ 2.5 dB, Table 4-10
T	Duration of Blast	Equation 4.15	0
C_d (5)	Damping Correction	Equation 4.37, $C_d = 10^{(Ad/20)}$	$\pm$ 0.71 dB, as in Figure 4-60
S_d	Damage Threshold	Table 4-12	$\pm$ 1.4 to $\pm$ 6.6 dB, Table 4-12
FOS	Factor of Safety	Equation 4.44	{Sum of $\log_{10}[\sigma_L(x)]^2\}^{(1/2)}$

(1) Charge burial depth correction, C_b, applied as needed.
(2) Log mean value of the propagation effect = 1.0.
(3) Default value for front and side faces. (See Section 4.7.2.3.)
(4) Applicable only for windows.
(5) C_d = 1.0 for windows

Since FOS $= (S_d/S_{pk})$, then the log of FOS can be expressed as

$$\log_{10}(\text{FOS}) = \log_{10}(S_d/S_{pk}) = \log_{10}(S_d) - \log_{10}(S_{pk}) \tag{4.44}$$

Two key principles, from basic statistics, are utilized by Hershey and Higgins,[71] concerning the parameters in Equation 4.43. The first key principle, from statistics, is that the difference of two normally distributed, independent variables, e.g., $[\log_{10}(S_d) - \log_{10}(S_{pk})]$ will tend to also be normally distributed for large sample sizes.[71]

Note that this would not necessarily be so if the stress variables themselves, instead of their logarithms, were normally distributed since the quotient of two normally distributed variables is not necessarily normally distributed.

Statistical independence of S_{pk} and S_d is assured since the variations in the blast pressure environment will be uncorrelated with variations in the material strength properties of the buildings exposed to these blasts.

The second basic principle in statistics invoked by Hershey and Higgins is that the standard deviation of sums or differences of two or more independent, normally distributed variables is equal to the square root of the sum of their variances (i.e., the sum of the squares of their standard deviations). Thus, the standard deviation of the log of the FOS is the square root of the sum of the squares of individual values for the $\sigma_L(x)$ terms identified in Table 4-13 which make up the FOS. Thus, if each term in Equation 4.43 has a lognormal distribution (or is deterministic with a fixed value, i.e., the standard deviation of its log is zero), then the

distribution of the final result – the Factor of Safety (FOS) - also has a lognormal distribution. The standard deviation of the log of the FOS is thus the square root of the sum of the squares of the standard deviation of the log, $\sigma_L(x)$ of each of the values identified in Table 4-13.

As mentioned earlier in Section 4.7.2.6, Hershey and Higgins also found that the probability distribution of the failure stress, S_d for other materials, in addition to glass and adobe, could also be closely approximated by a lognormal distribution. Furthermore, they also found that the structural response functions, (i.e., ratios of peak stress to velocity or peak pressure) similar and/or identical to those employed for this study, can also be closely approximated by lognormal distributions. Finally, it has already been established in Section 4.7.2.2 that, when applied, the weather-induced variation in peak blast pressures, (P_f/P_o) is very well defined by a lognormal distribution.

In summary, each of the terms in Equation 34 has been shown to have, or can be reasonably be assumed to have, a lognormal distribution or, in some cases, a deterministic value with a zero standard deviation.

4.7.2.7.2 The Statistical Basis for the Probability of Damage (POD)

For a normal (or Gaussian) distribution of any variable x, the probability of occurrence of any specific value of x can be specified in terms of its probability distribution (or probability density) P(x). This is a function of the difference between x and its mean value, x_m and the standard deviation, σ_x of x and is given by the general expression for a normal distribution[25].

$$P(x) = \frac{1}{\sigma_x \sqrt{2\pi}} \exp\left[-\frac{(x - x_m)^2}{2\sigma_x^2} \right] \qquad (4.45)$$

For a lognormal distribution of the FOS, (S_d/S_{pk}), the same expression holds except that x is now the log of the FOS, the mean, x_m is now the arithmetic mean (the log mean) of $\log_{10}(\text{FOS})$. The standard deviation σ_x of x is now the standard deviation of $\log_{10}(\text{FOS})$ or, in the terminology used here, $\sigma_L(\text{FOS})$.

This log distribution is illustrated in the Figure 4-64 for a hypothetical case. While a linear abscissa is equal to $\log_{10}(\text{FOS})$ and would go from - 1 to 1, the lognormal behavior is more clearly demonstrated by plotting the FOS on a log scale as shown at the bottom of the figure.

For this hypothetical case, the Probability of Damage (28%) is represented by the area under that portion of the distribution for which the FOS is < 1. Thus, the POD is simply the integral of the lognormal probability distribution of $\text{Log}_{10}(\text{FOS})$, from minus ∞ to 0:

$$\text{POD} = \frac{1}{\sigma_L(\text{FOS})\sqrt{2\pi}} \int_{-\infty}^{0} \exp\left[-\frac{(x - x_m)^2}{2[\sigma_L(\text{FOS})]^2} \right] dx \qquad (4.46)$$

where $x = \log_{10}(\text{FOS})$, x_m = the log mean of x and $\sigma_L(\text{FOS})$ = standard deviation of $\log_{10}(\text{FOS})$.

The right side of Equation 4.46 is the cumulative value, $F_n(y)$, of the normal distribution function, i.e.,

$$F_n(y) = \int_{-\infty}^{y} P(x)dx \qquad (4.47)$$

where in this case $y = (x-x_m)/[\sigma_L(FOS)]$ and $y=0$ is of interest

Values in the published tables of the cumulative value of a normal distribution function, $F_n(y)$ are customarily given for only positive values of y. The symmetry property of the cumulative normal distribution[83] is utilized here, which means that $F_n(-y) = 1 - F_n(y)$.
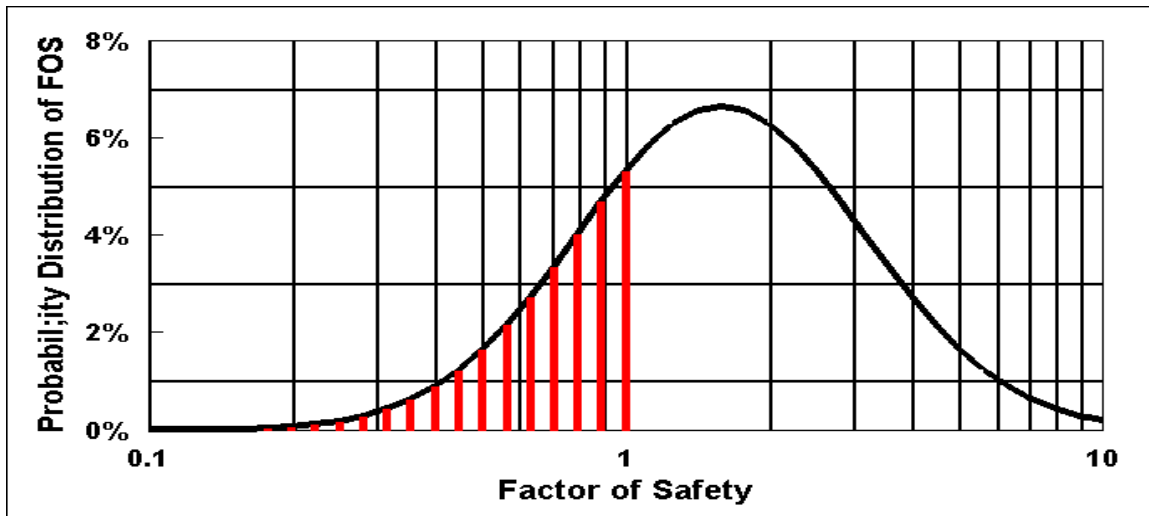
Figure 4-64. A Lognormal Distribution of the FOS;
The log mean of the FOS is 1.6, the standard deviation of the log of the FOS is 0.3 and the POD is 28%

The positive variable, y, identified by capital Y, is the normalized variable $Y = x_m/((\sigma_L(FOS)$ and the Probability of Damage, POD is

$$POD(Y) = 1 - F_n(Y) \qquad (4.48)$$

where

$Y = x_m/[(\sigma_L (FOS)]$
x_m = the mean value of $\log_{10}(FOS)$.
$\sigma_L(FOS)$ = the standard deviation of $\log_{10}(FOS)$.

Equation 4.49 is a regression equation that describes this cumulative normal distribution function for POD = $1 - F_n(Y)$, $Y = x_m/[(\sigma_L (FOS)]$, within an rms error of ± 0.1 % of values of POD(Y) and covering a range for the POD from 99% to 0.000,5% - e.g., from near certainty of damage to a negligibly small probability of damage.

$$POD(Y) = 10^{A+By+cY^2+DY^3+EY^4} \qquad (4.49)$$

where

A = 1.69816

B = - 0.34789

C = - 0.13605

D = - 0.01486

E = 0.00125.

An alternative expression to calculate the integral of Equation 38 in terms of the complimentary error function, erfc(Y) was used in Reference 38. However, ambiguity in the literature on exactly how this function is defined indicated the simpler approach using Equation 4.47 to define $F_n(Y)$ was much preferred. Figure 22 of Reference 38 presents a comparison of exact values of POD(Y) to values computed from the regression Equation 4.49.

In summary, the steps to compute the Probability of Damage (POD) are:

1) Equation 4.43 defines the FOS from the terms identified in Table 4-13.

2) The numerator of the lognormal distribution variable, Y, is the mean of $\log_{10}$(FOS).

3) The denominator of Y is the square root of the sum of the squares of the standard deviations, σL(xi) of the log of these terms as identified in Table 4-13.

4) The POD is then computed from Equation 4.49 in terms of Y.

4.8   Probability of Structural Damage

Predicting the probability of damage consists of the steps summarized at the end of Section 4.7, beginning with each of the factors in Equation 4.43 and Table 4-13 and finishing with the probability from Equation 4.49. This process is demonstrated below for blast waves and sonic booms.

4.8.1   Probability of Structural Damage from Blasts

4.8.1.1 Blast Load

Figures 4-65 through 4-67 present the basic parameters of a blast source for four values of equivalent TNT weight, W_T. Figure 4-65 shows the nominal free field blast pressure, P_0 vs distance. Figure 4-66 shows the value of the burial depth correction, adjustment, C_b in blast pressure for charges located at, or below the ground surface. (Note the sign convention for burial depth.) The discontinuous slope of the curves in Figure 4-66 reflects the discontinuous nature of the burial correction factor C_b. As mentioned earlier, note the marked effect burial has on the

blast pressure, especially for charges with values for W_T less than 200 lb. Figure 4-67 shows the variation in the positive phase blast duration T with distance, for the same four values of W_T.
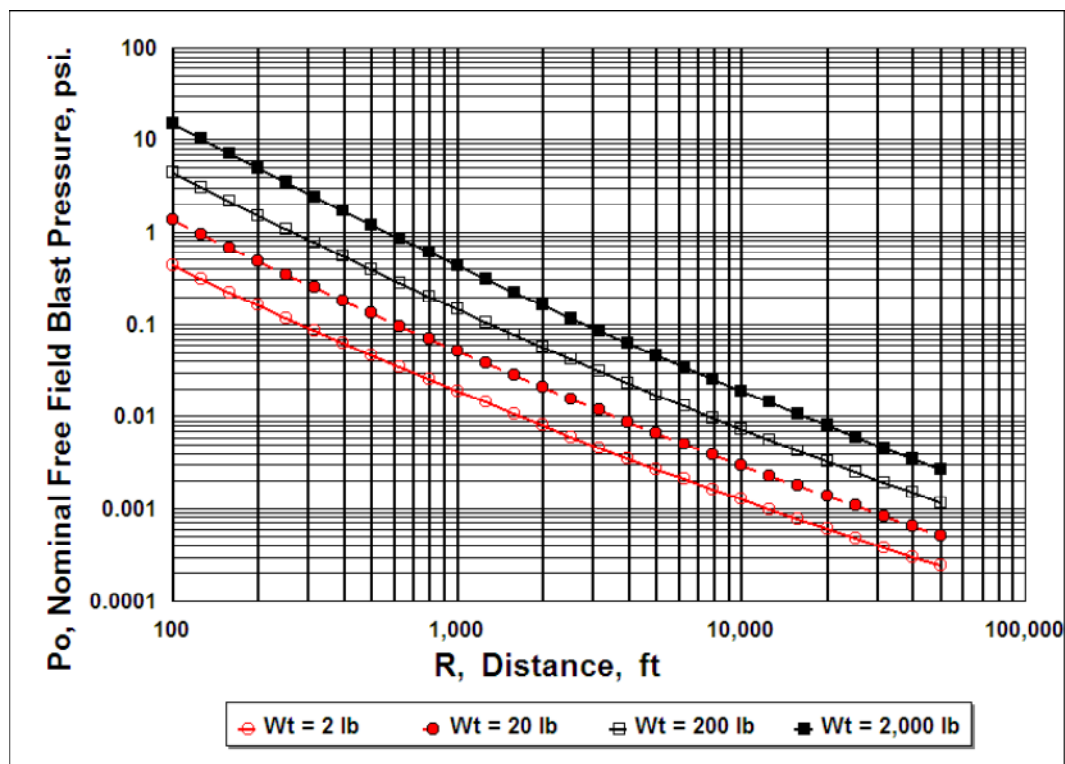
Figure 4-65. Nominal Free Field Blast pressure, P_0 vs distance for Four Values of Equivalent TNT Weight, W_T, as Computed from Equation 4.14
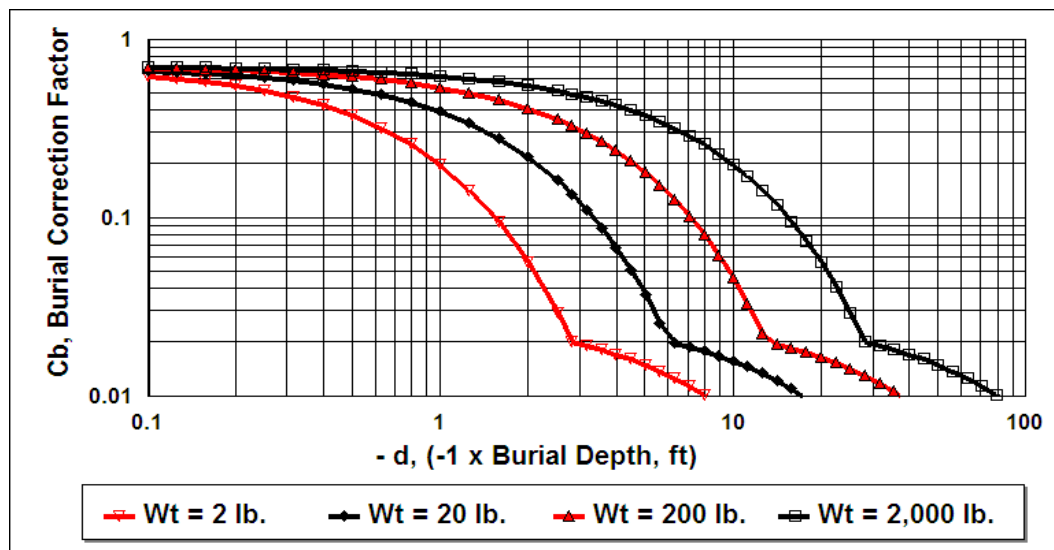
Figure 4-66. Decrease in Blast Pressure of Buried Charges re: a Free Field Blast
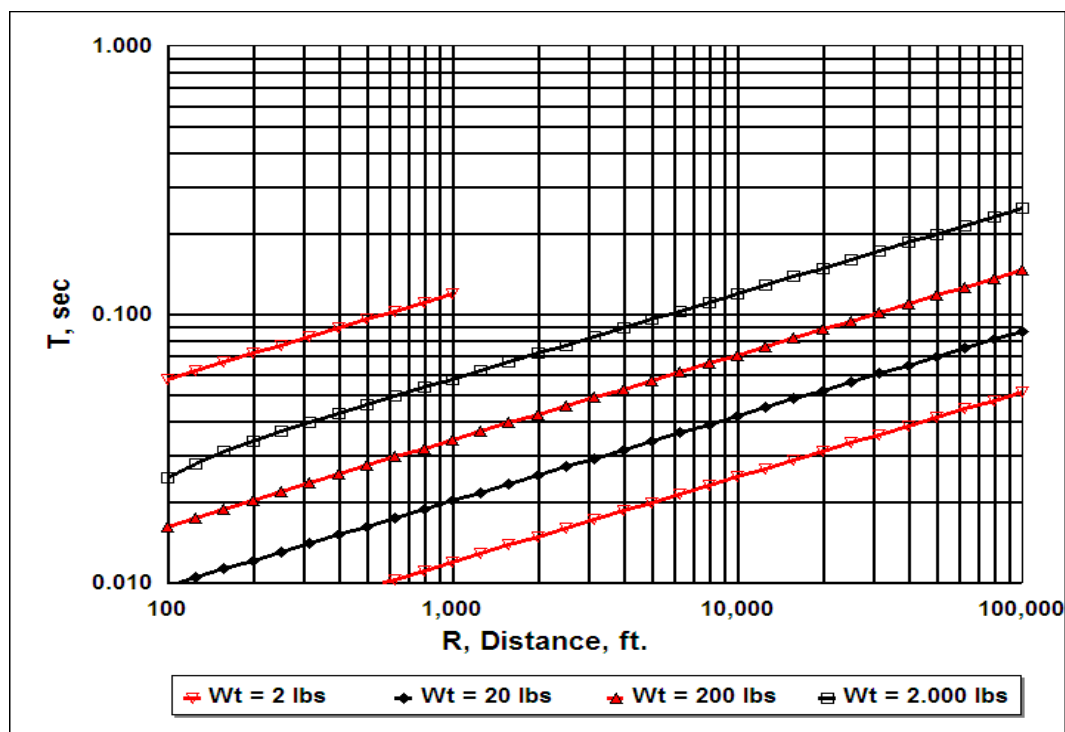
Figure 4-67. Positive Phase Duration, T, of the Blast Pulse for Four Values of Equivalent TNT Weight, W$_T$, based on Equation 4.15

Following the steps implied by Table 4-13, these source-specific data can now be combined with the structure-specific data in Tables 4-8 through 4-12, for various structure types, to define their response to the blast environment and the resulting variation in the Probability of Damage (POD). It will be convenient and practical to present this information, in graphical form, by two different methods:

- **Method 1**: The POD is plotted as a function of the incident free field (not reflected or diffracted) blast pressure, P_f (or P_0) with the blast positive phase duration, T as a parameter. This incident peak blast pressure can be chosen from the nominal value, P_0 defined in Figure 4-65 or Equation 4.14, or can be obtained from any independent measurement or prediction of P_0 using suitable sound propagation and/or ray tracing models. In this case, any statistical variation due to propagation effects in the actual incident (free field) blast pressure, P_f is either neglected [e.g. $\sigma_L(P_f/P_0) = 0$] or is already accounted for with use of an independent blast propagation measurement or prediction model. The structural response, and hence POD values, assume that the wall is facing the incident blast wave. That is, the effective blast pressure, P_e on the wall is just twice the incident free field blast pressure, P_f, – i.e. the reflection/diffraction correction factor, $C_r = P_e/P_f$, is 2.0. All the other elements of the statistical model for the POD, as embodied in Equation 4.43 and Figure 4-49 are accounted for. The blast duration T can be obtained from measurements, predicted with Equation 4.15, or obtained from Figure 4-67.

- Method 2: In this case, POD values are simply plotted as a function of distance R, with equivalent TNT charge weight W_T as a parameter. The same statistical model defined in this report is employed but it now includes the propagation-caused statistical variation $[\sigma_L(P_f/P_0) > 0]$ in the ratio P_f/P_0 of the incident free field blast pressure to the nominal blast pressure. Again, as for Method 1, the default reflection/diffraction correction factor, $C_r = P_e/P_f, = 2.0$, for a wall facing the incident blast wave, is applied when computing the structural response and POD.

Representative plots of the POD using these two methods will be given in this section for two examples of the more blast-sensitive structures listed in Table 4-11: adobe walls and windows.

4.8.1.2 Blast Damage Probability for Adobe Walls

Figure 4-68 presents values for POD for an adobe wall using Method 1: POD vs the free field peak blast pressure, P_f.

Figure 4-69 (a) and (b) presents values for the POD for an adobe wall using Method 2: POD vs range, for propagation over hard and soft ground, respectively.

A comparison of the Method 1 and 2 results is shown in Figure 4-70. This compares the POD for an adobe wall using Method 2 for propagation over hard or soft ground $[\sigma_L(P_f/P_0) > 0]$ with the POD values that would be computed from Method 1 $[\sigma_L(P_f/P_0) = 0]$.

Figure 4-70 shows values of the POD for four values of the charge weight, W_T from 2 to 2,000 lbs. For each value of W_T, three lines are shown. The lowest line shows the POD with Method 1. It is lowest since it assumes that the incident free field blast pressure is always the same as the nominal value ($P_f = P_0$). The middle line, in each group, is for Method 2 with propagation over hard ground. The highest line in each group is for Method 2 with propagation over soft ground. This order reflects the fact that the propagation-induced statistical variation in P_f is larger for Method 2 than for Method 1 as applied here, and is larger for soft ground surface for Method 2. That is, the standard deviation of the log of the FOS increases so that the below-one portion of the lognormal distribution of FOS increases, thus increasing the POD. A full solution from a propagation model such as SIPS would, of course, include the statistical distribution of the load and would also include the actual expectation for favorable or adverse propagation conditions, so that a full application of Method 1 would generally be more reliable, and would not necessarily exhibit the lower probability of this example.

Note that the lines for T = 0.05 and 0.2 sec. are nearly identical due to the non-monotonic change in the POD with positive phase blast duration T. This problem occurs frequently for prediction of POD vs the free field blast pressure, P_f using Method 1 as applied here, so Method 2 should be used if a full propagation model is not available.
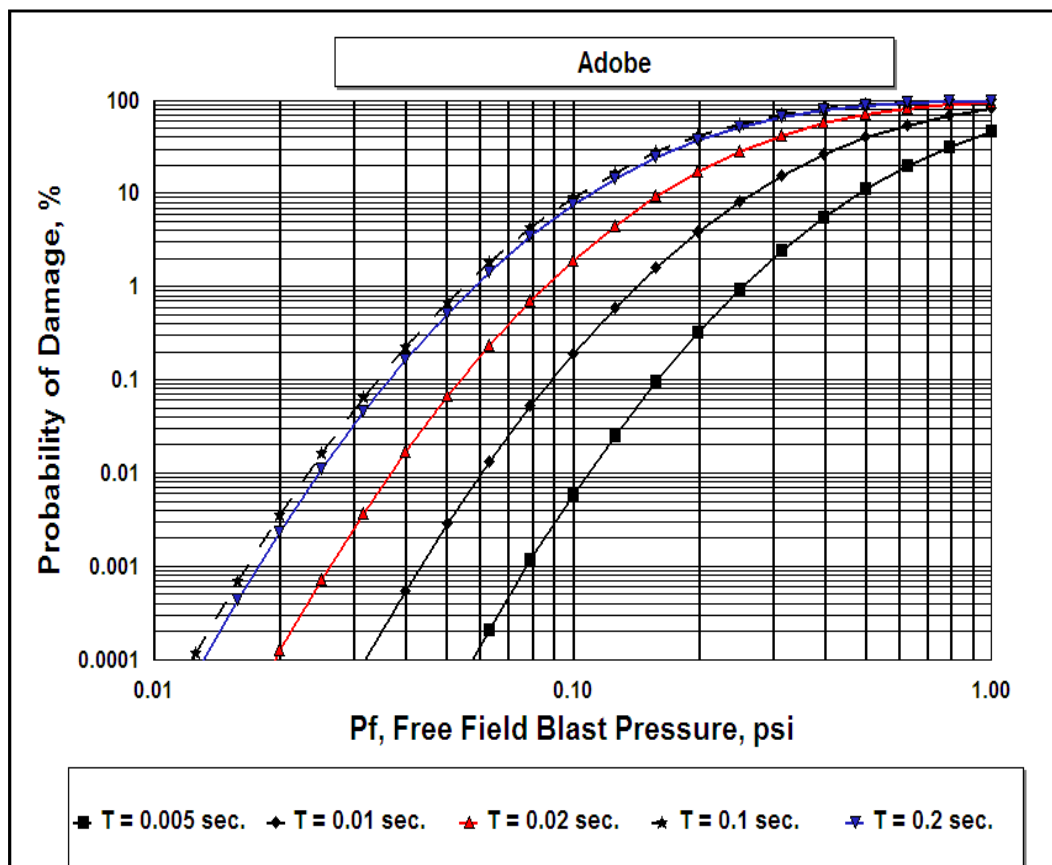
Figure 4-68. POD for an Adobe Wall Applying Method 1: POD vs Peak Free Field Pressure P_f, with the Positive Phase Duration T as a Parameter; the wall is facing the incident blast wave
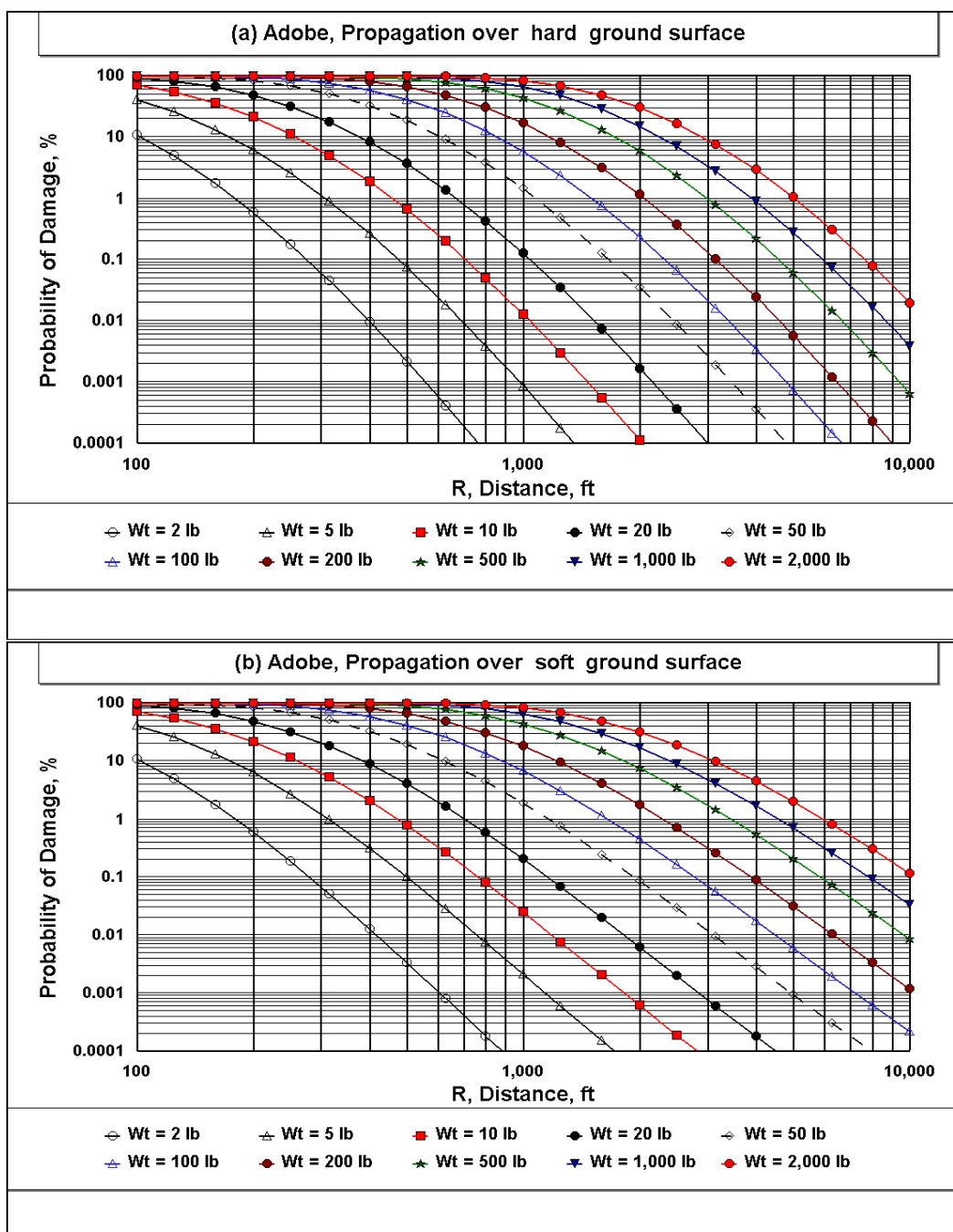
**Figure 4-69. POD for an Adobe Wall Applying Method 2 for:
(a) propagation over a hard ground surface; and (b) propagation over a soft ground surface;
The wall is facing the incident blast wave**
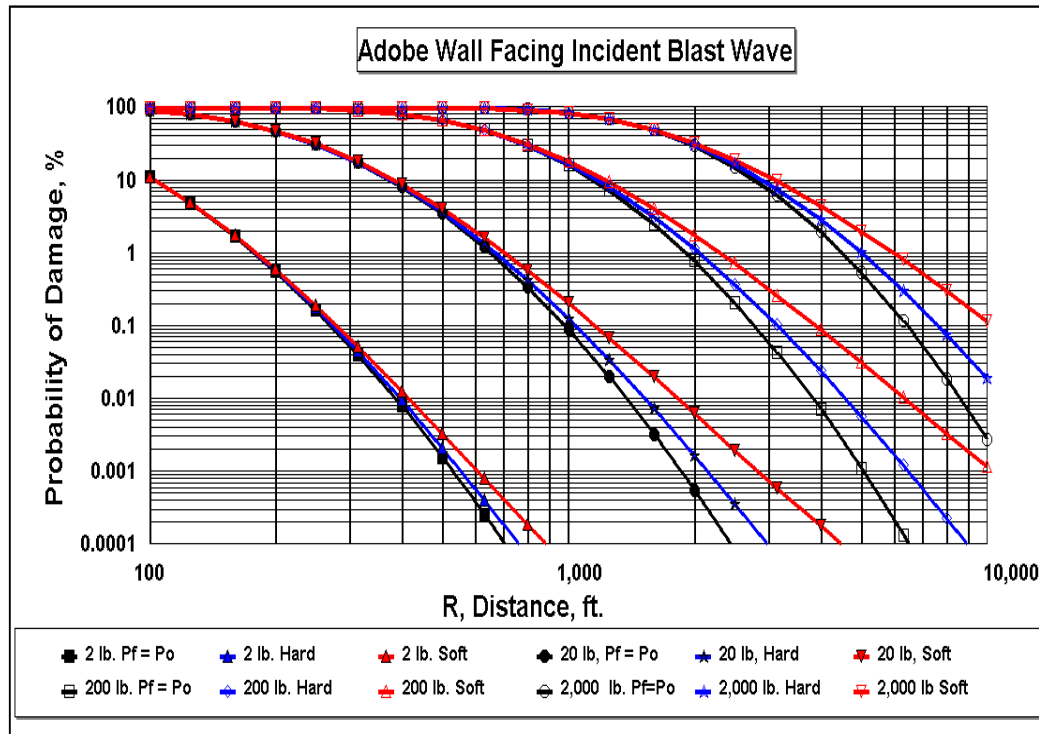
Figure 4-70. Comparison of the Probability of Damage (POD) for an Adobe Wall for Four Equivalent TNT weights using Method 1 and Method 2; For the former, $P_f = P_0$

4.8.1.3 Blast Damage Probability for Windows

Windows are the type of building component most vulnerable to damage from blast loads. Thus, it was desirable to provide some specific validation of the damage prediction method employed for windows. While there are considerable data on blast and sonic boom damage to windows in real dwellings[11,71], these data usually lack details concerning the orientation of the window with respect to the direction of the blast or sonic boom pressure wave front.

One partial exception is the data from sonic boom tests in 1972 at White Sands as analyzed by Hershey and Higgins[71]. The effective reflection/diffraction adjustment for these sonic boom data fit the relation

$$A_r = 20\log_{10}\left(\frac{p_e}{P_f}\right) = 2.85\cos(\theta) + 3.50\,\text{dB} \tag{4.50}$$

The effective reflected pressure load on the face of a building wall, as a function of the incidence angle θ of the sonic boom, was approximately the same as the default values for reflection data in Table 4-4 for normal and grazing incidence blast waves. The difference between the reflection adjustments for the sonic boom and blast data for normal ($\theta = 0^\circ$) and grazing ($\theta = 90^\circ$) incidence were just +0.4 and +0.5 dB respectively. For a wall facing away from the incident sonic boom or blast wave ($\theta = 180^\circ$), the reflection adjustments for the sonic boom data were 6.7

dB higher than the default values for the back side of a building for blast waves in Table 4-4. This larger difference is not surprising given the much larger wavelength of the sonic boom than for blast wave as compared to a characteristic building dimension. Thus, larger diffraction effects around the back side of a building would be expected for typical blast waves. Therefore, sonic boom building reflection/refraction data appear to be very comparable to values for blast loads for only normal and grazing incidence ,where values of about +6 dB and +3 dB, respectively, are expected.

A unique set of data are available on measured window blast damage in a nine-building apartment complex from an accidental blast in 1996 at a nearby Wyle test facility in Huntsville, AL. The data, summarized in Appendix F of Reference 41, allowed comparison of the observed vs predicted window failure rate for 17 different walls containing a total of 738 windows with incidence angles relative to the blast wave of approximately 0° (normal incidence), 90° (grazing incidence) and 180° (window facing away from the blast). These orientations are denoted later as "front", "side" or "back" windows, respectively. While no blast pressure measurements were obtained for this blast incident, the blast pressures could be accurately predicted since the equivalent TNT weight (30 lbs) of the blast source was well defined and the propagation distances were limited to a range of 435 to 885 ft. minimizing any uncertainty due to propagation anomalies. The reflection/diffraction adjustments, A_r, in Table 4-4, to the free field blast pressure were critical to achieving the reasonable agreement indicated below between the observed and predicted POD for these windows.
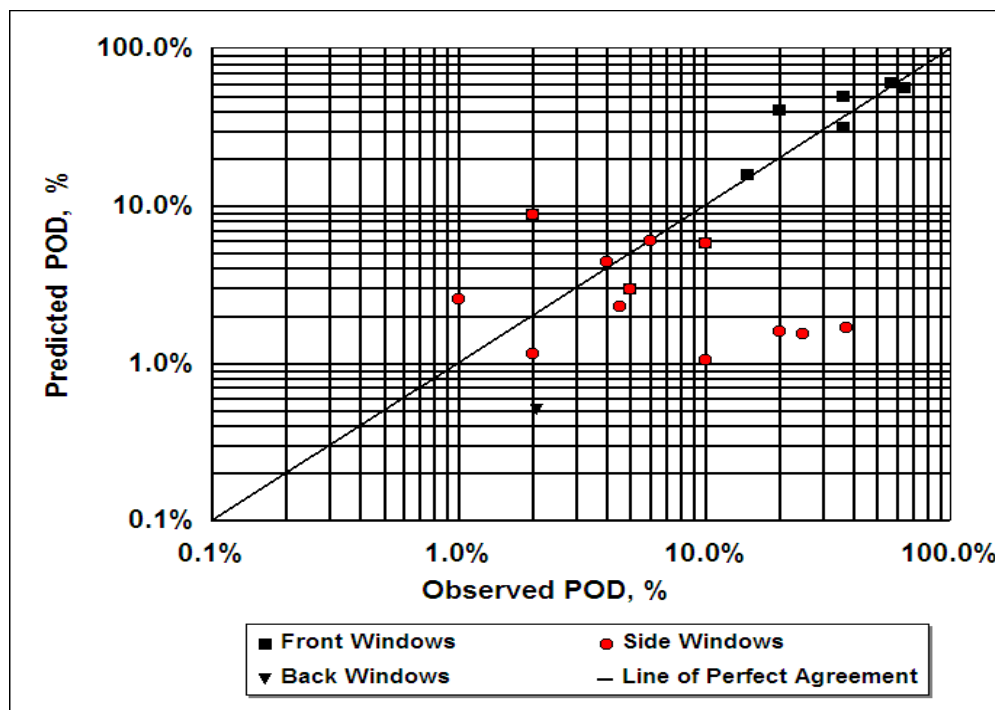
Figure 4-71. Predicted vs Observed Failure Rate for 738 Windows in 9 Buildings Exposed to an Accidental Blast of a 30 lb Equivalent TNT Weight Located 445 to 910 ft. from the Blast Source[41]

The damaged windows were grouped into 22 clusters of closely adjacent windows over the 17 window facades on the 9 buildings making up the 15 year old apartment complex. This clustering allowed an accurate estimate of blast pressure for windows located within in a limited

area. The predicted and observed Probability of Damage (POD) for the windows for this accident, are shown in Figure 4-71. The predicted POD values used Method 2 assuming soft ground. However, the predicted POD varied by 1% or less between Method 1 or 2 and between a hard or soft ground surface for Method 2.

The observed window breakage rate per window cluster varied from 0 to 64% for the 53 broken windows, out of 738 windows exposed to the blast. As shown on Figure 4-71, this compared reasonably well with the predicted failure rate, especially for the higher failure rates. The default values, from Table 4-4, for the reflection/diffraction adjustment, A_r used to define the effective blast pressure at the windows were: +6, +1 and –6 dB for "front", "side" and "back" facing" windows respectively. These are well within the standard deviation values of $\pm$ 1 to $\pm$ 3 dB for the single stack model data in Table 4-4. The +1 dB default value for A_r for "side" windows was 2.3 dB higher than the average -1.3 dB for the model data in Table 4-4 but 1 dB was selected to provide a close fit to the measured window blast damage POD data for the 520 "side" windows out of the 738 windows exposed. In this case, the results from the actual window damage data was considered as having more credibility than the model data on reflection/diffraction.

Figure 4-72 presents a comparison between the average predicted and observed window failure rates for each of the three window directions using the default values for A_r, and the failure stress value S_d for old glass computed according to Equation 4.41 using the predicted blast duration T at each cluster. For these accident data, the average and standard deviation of the predicted blast duration T values were 0.0194 and $\pm$ 0.0013 sec. respectively.

The predicted POD for each window direction in Figure 4-72 is the average of the product of the POD for each window cluster and direction and the number of windows in that cluster divided by the total number of windows in that direction. The agreement is as good or better than one could expect, especially for the windows facing the blast direction.
The agreement provides support for the basic validity of the structural damage prediction model employed here. Note that since the apartment complex was 15 years old, the basic failure stress used for 22 year old glass stated earlier was equal to 2,940 psi. This failure stress was corrected, according to Equation 4.41, for the variation in the failure stress S_d due to variation in duration T of the blast loads on the windows. From the accident data, this variation was less than $\pm$0.7 % about an average value of 4,790 psi for the average blast duration of 0.0194 sec.

An objective measure of the accuracy of any one predicted POD value is defined by the absolute value of the relative error in the predicted POD. This is the absolute value of the difference between the observed and predicted POD values divided by the observed POD. The averages of these relative POD errors, expressed as a percentage, were $\pm$ 29 % for the 80 front-facing windows, $\pm$ 88 % for the 520 side-facing windows and $\pm$ 76 % for the 138 back-facing windows.
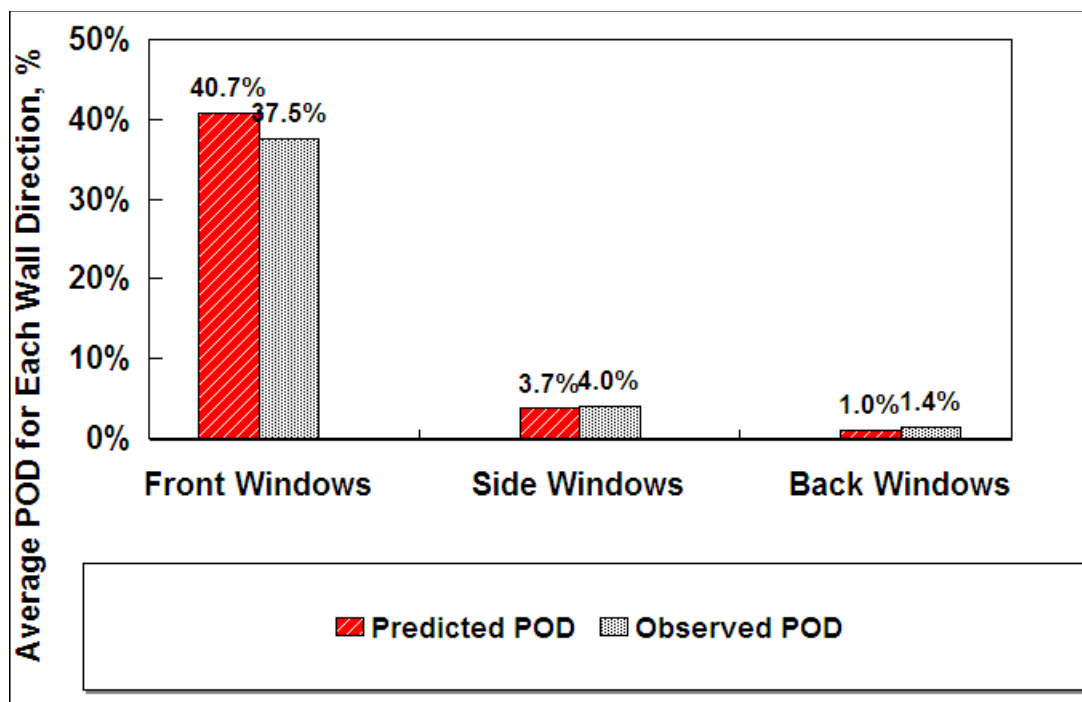
**Figure 4-72. Average Predicted versus Observed POD for the Window Orientation;
re: the blast direction for N = 80 front, N = 520 side and N = 138 back windows**

These accuracy figures for this one substantial data set are considered representative of the probable accuracy of POD values predicted by this method. The net result is expected to be an accuracy in the relative POD predictions of the order of ±30% for structures or windows facing a blast wave and of the order of ±80% for structures or windows facing 90° or 180° to the blast wave. For example, if the predicted POD for a structure facing the blast was 20%, the true POD would be expected to fall between 14% and 26% , that is, equal to 20% x (1- 0.3) or 14% and 20% x (1+ 0.3) or 26%.

The scatter in the date in Figure 4-71 is also a realistic reflection of the many factors which influence the actual failure strength of windows, such as surface flaws, potential stress risers in the window frame and age of the window. In addition, local sound field anomalies such as reflected blast from adjacent buildings that could have occurred in some cases were not considered.   The larger variation in the reflection/diffraction correction for side (grazing incidence) or back windows indicated by the model data in Table 4-4 may also be a factor. These latter two effects are considered a likely cause of the large scatter for the POD Predictions vs Observed for the side and "back" windows. Nevertheless, the predicted average unweighted, POD over all 22 clusters of windows was 14.1%, very close to the observed average unweighted POD over all clusters of 16.3%.

Not shown in Figure 4-71 are data for three groups of windows, consisting of 2 and 40 windows on back walls of two buildings facing away from the blast, and 100 on the side wall in one building. These were predicted to have an average failure rate of 4.0 % but showed no damage. However, even including these discrepancies, the overall agreement between predictions and observations, as indicated in Figures 4-71 and 4-72, and the above averages, is reassuring, especially for the higher POD values.

In summary, the agreement between observed and predicted failure rates from blast for windows implied by Figures 4-71 and 4-72 and the average POD values is a reasonable confirmation of the blast damage prediction model presented here. The predicted failure rates tested the validity of all elements of the prediction model including blast pressure, propagation, reflection/diffraction adjustments, stress response to the blast and failure strength of the glass including the standard deviations of the logs of the pertinent variables as outlined in Table 4-13.

Applying the presentation used for Figures 4-68 and 4-69, Figure 4-73 parts a and b compare the two POD presentation methods for a window. For Method 2, the ground surface was assumed to be hard.

One additional analysis is shown in Figure 4-74 for the change in the POD for windows facing towards, to the side or at the back side of a building facade re: the blast direction. The figure, using Method 2, is for an equivalent TNT weight W_T of 200 lbs and a hard ground surface. Consideration of this change, reflected in the choice of the appropriate default reflection/diffraction adjustments given in Table 4-4, (i.e., +6 dB, for front, +3 dB for side, and -6 dB for back facing walls), was a key part of the window damage validation illustrated in Figures 4-71 and 4-72.

The change in the POD from front to side or from front to back orientation of the windows varies widely, being generally smaller for closer distances and for larger charge weights. The mean and standard deviation of the relative PODs (re: the front windows) for a range from 100 to 1,000 ft. for equivalent TNT weights of 20 lbs. (not used for Figure 4-74), and 200 lbs. (as shown in Figure 4-74) were:

- $W_T = 20$ lbs: POD(side)/POD(front) = 0.25 ±0.36
                    POD(back)/POD(front) = 0.20 ± 0.38

- $W_T = 200$ lbs: POD(side)/POD(front) = 0.30 ± 0.31
                    POD(back)/POD(front) = 0.082 ± 0.13

One final note: All the windows considered herein are single pane windows. The higher surface weight and probable higher damping of double pane or laminated windows would tend to reduce their POD values.
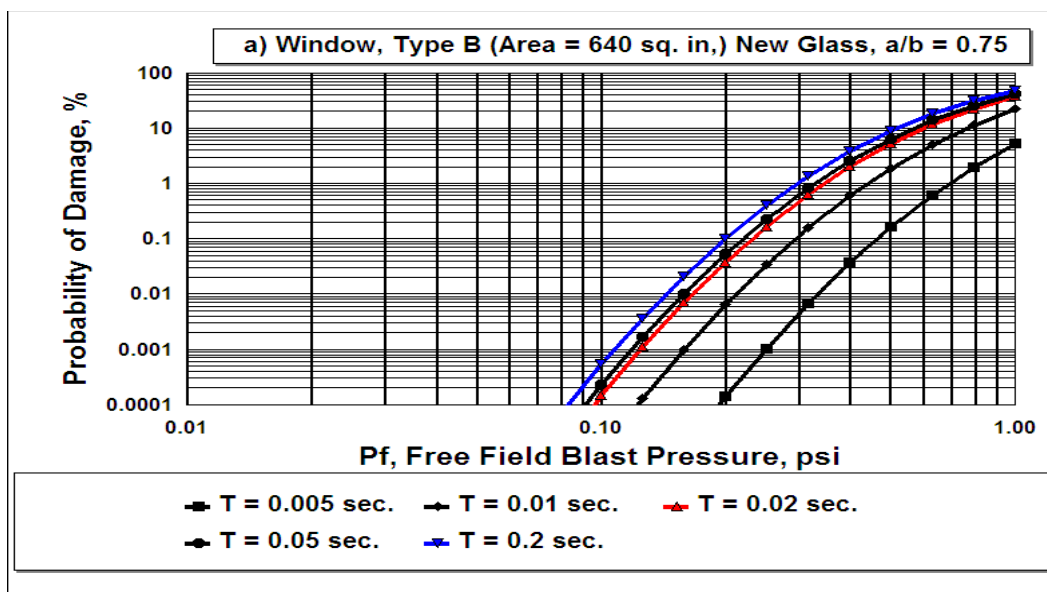
(a) Method 1
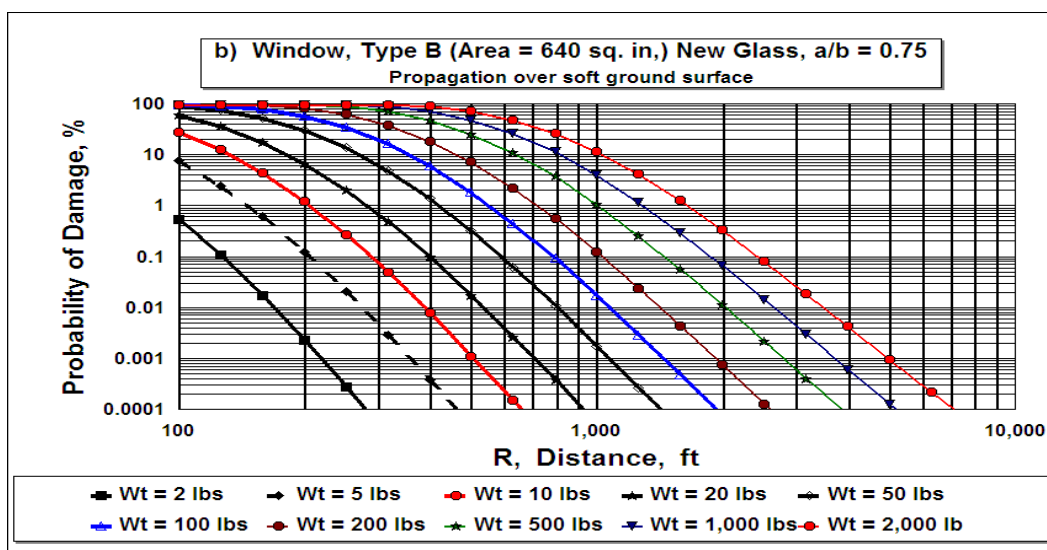
(b) Method 2

**Figure 4-73. POD for a typical window type portrayed using Methods 1 and 2.
Normal incidence (e.g. pressure doubling) applies in each case.**
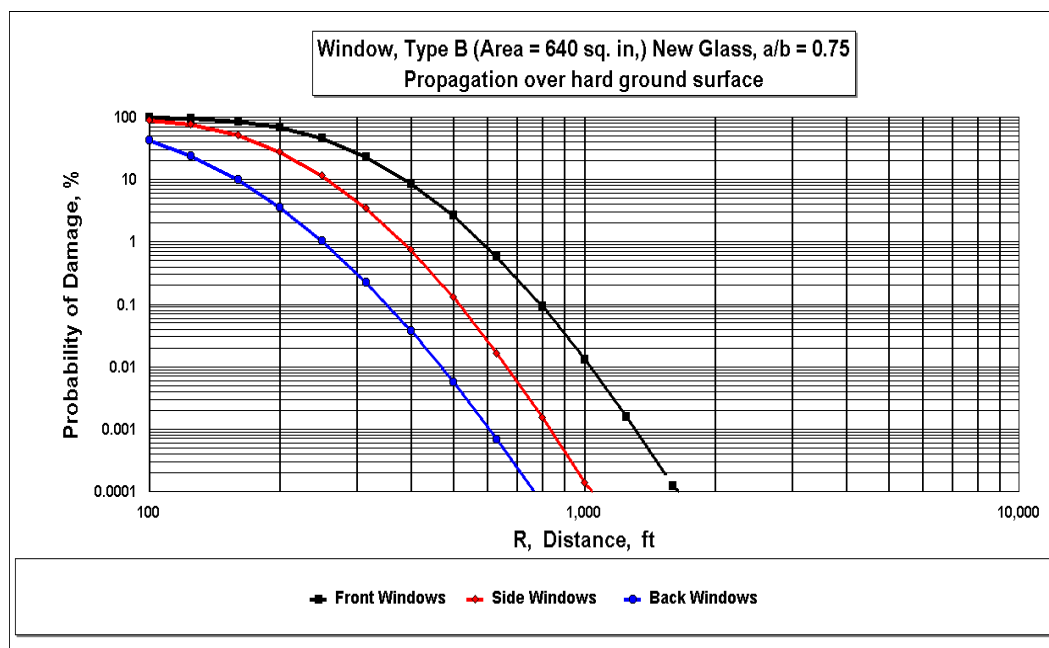
Figure 4-74.   POD for a Typical Window for the Three Orientations and the Corresponding Reflection/Diffraction Adjustments from Table 4-4; The equivalent TNT weight, W_T was 200 lb.

4.8.2 Structural Response and Probability of Damage for Sonic Boom Loading

Structural damage from one other impulsive pressure load considered for this project is that from sonic booms. This topic was treated extensively for unconventional structures in Reference 38 applying essentially the same statistical damage model employed here. Thus, the topic is only treated briefly in this report. The first, and most significant point, concerning damage response from sonic booms compared to blasts is illustrated in Figure 4-75 for building vibration response data acquired by NASA[84] for various types of sonic loads. The figure shows the stress response of a wall stud in a residential building to sonic booms and explosive charges as well as from other acoustic or dynamic loads. As indicated on the figure, the average Dynamic Amplification Factor (DAF) for sonic booms, relative to that for blasts, was 1.8. The DAF is the ratio of the peak dynamic response of a structure for a dynamic load to the static response of the same structure to a static load with the same peak pressure.
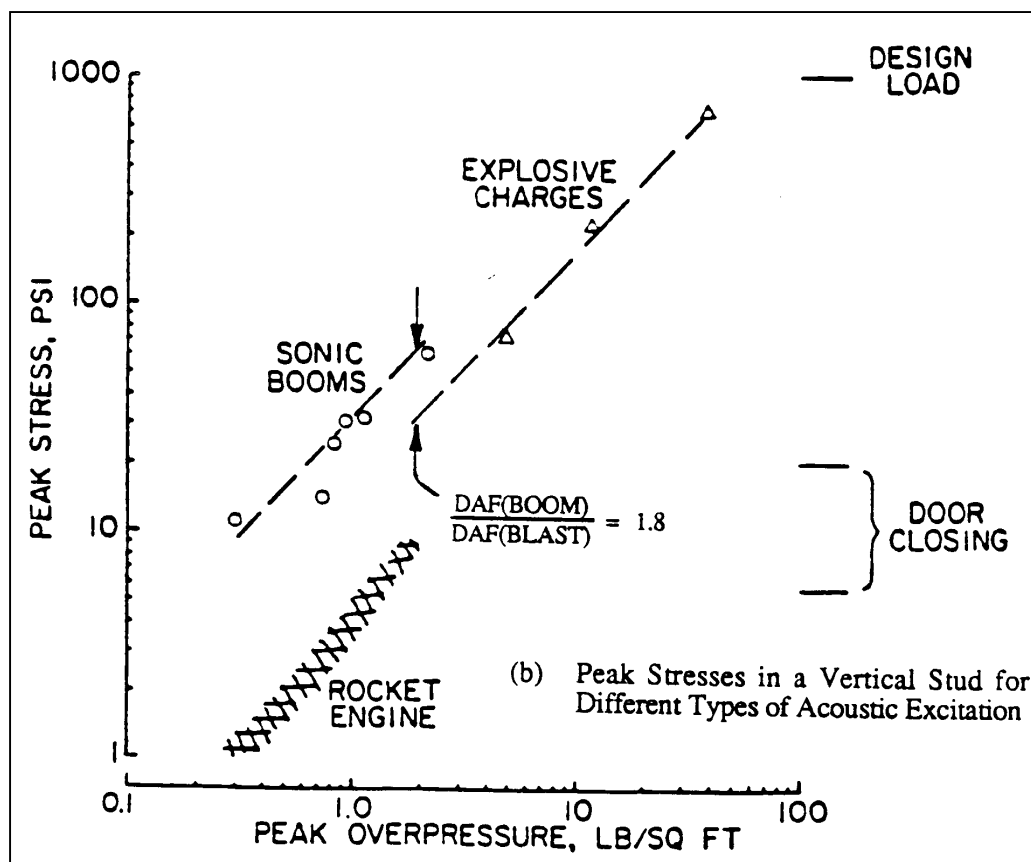
Figure 4-75. Comparison of Peak Stress Responses of a Wall Stud in a Residential Building to Various Acoustic Loads[84]

The approximately 2 to 1 increase in structural stress (e.g., - or velocity) response for sonic boom loads relative to blast loads with the same peak pressure is consistent with theoretical expectations. The simplest way to illustrate this relative structural response for sonic booms vs blast loads is to compare the Residual Velocity Shock Spectrum for each type of loading. For values of the basic parameter, f_oT > about 0.2, this Residual Velocity Shock Spectrum provides a close approximation to the full Velocity Shock Spectrum for both blast (see Figure 4-56) and for sonic booms (see Appendix C of Reference 38).

When expressed in the same normalized form employed for Figure 4-56 using Equation 4.22, the Residual Velocity Shock Spectrum for blast loads for the m,nth structural mode with resonance frequency, $f_{m,n}$, is

$$\frac{V_R\left(f_{m,n}\right)}{\left(P_0/w\right)gT} = \frac{16}{\pi^2}\frac{2\pi f_{m,n}T}{1+\left(2\pi f_{m,n}T\right)^2}$$

(4.51)

From Appendix C of Reference 38, it can be shown that the Residual Velocity Shock Spectrum, for sonic boom loading, is the absolute value of the sin, cos functions given by:

$$\frac{V_R(f_{m,n})}{(P_0/w)gT} = \frac{16}{\pi^2} \frac{2}{(2\pi f_{m,n}T)} \left[\frac{\sin(2\pi f_{m,n}T)}{2\pi f_{m,n}T} - \cos(2\pi f_{m,n}T) \right]$$

(4.52)

For both expressions, T is the duration of the positive phase of the impulse loading, i.e., half the 2T total duration of a classic sonic boom N-wave.

A typical range for T, as defined here, for sonic booms from DOD aircraft, such as an F-15 or an F-22, is 0.04 to 0.1 sec. The range of fundamental resonance frequencies for typical structures was shown in Table 4-10 to be about 12 to 95 Hz. The resulting range for the product f_0T would be about 0.5 to 10. As suggested by plots of Equations 4.51 and 4.52 in Figure 4-76 over this range of f_0T, the asymptotic values for the normalized Residual Velocity Shock Spectrum for sonic booms is just two times that for blasts.

Thus, for prediction of damage from sonic booms, the free field blast pressure, P_f, using the plots of POD vs P_f for blast damage, applying Method 1, should be doubled to predict sonic boom damage. For an equivalent process with Method 2 (POD vs range), increasing the parametric equivalent TNT weight, W_T, by 5, increases the free field blast pressure P_f by a factor of $2 \pm 8\%$.

An approximate validation of this method for estimating damage from sonic booms is provided by the following. For a peak sonic boom pressure of 0.2 psi, the Hershey and Higgins empirical window damage prediction model predicted POD values from 6 to 29% with a log mean of 13.4% for five different window types listed in their report[71]. Their prediction model does not account for the variation in the POD with duration of the sonic boom. However, based on knowledge of the type of supersonic aircraft on which their data are based,[85] the range for the positive phase duration, T was estimated to vary from 0.02 to 0.05 sec. The prediction model in this project was applied for a doubled blast pressure of 0.4 psi for six window types that closely match the area and aspect ratio of these defined by Hershey and Higgins. The POD from blasts with P_f = 0.4 psi and the above values for T = 0.02 and 0.05 sec. over the six windows types varied from 1.4 to 66 % with a log mean of 13.0%. This excellent agreement with the Hershey-Higgins sonic boom damage log mean value of 13.4% tends to validate both the basic blast damage model and the "double the peak blast pressure" method defined here to estimate damage from sonic booms. However, this method includes consideration of effect of the time duration, T, not included in the Hershey and Higgins, data-based, prediction model.
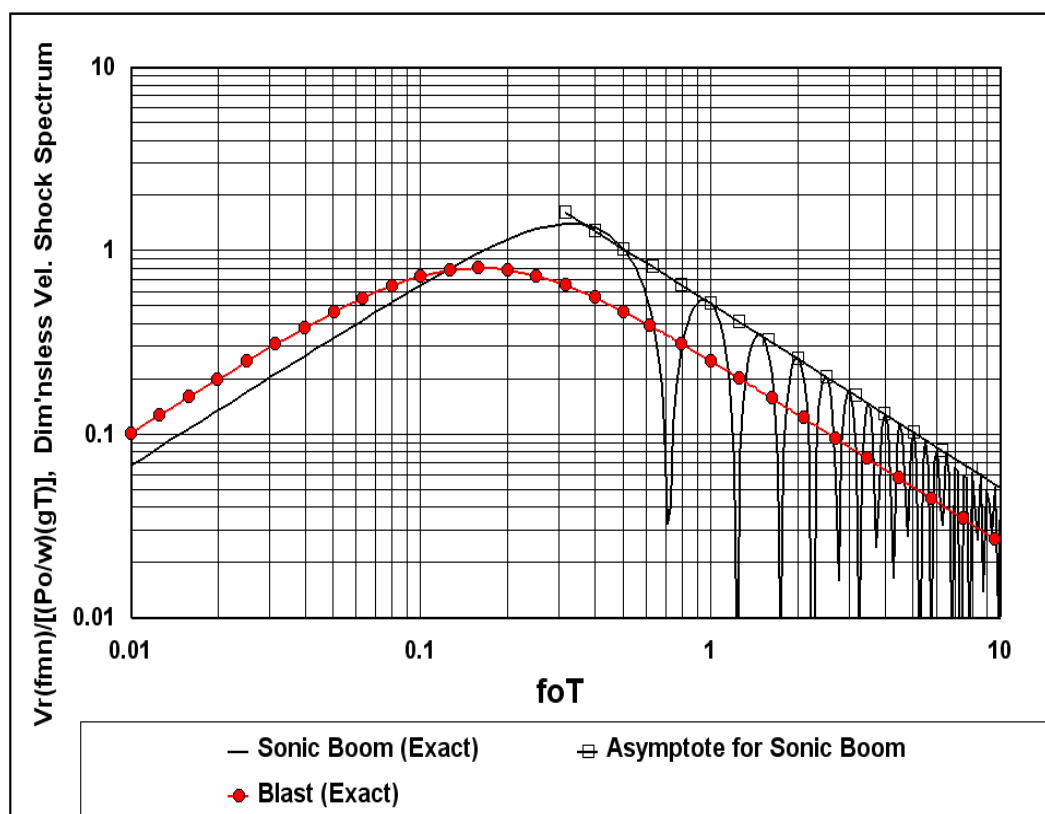
Figure 4-76. Residual Velocity Shock Spectra for Sonic Booms and Blasts;
The envelope for sonic booms is just twice that for blasts for values of $f_0T > 0.4$ which covers the expected
range for f_0 for typical structures and the range for T for sonic booms from military aircraft

5.0 Conclusions and Implications for Future Research/Implementation

To accomplish the goals of Project WP-1398, the following tasks were performed:

- Airborne and groundborne propagation mechanisms from blast sound sources were reviewed and analyzed.

- Field measurements of impulsive airborne and groundborne noise propagation from the blast source were conducted at three military installations.

- Field monitoring of structural vibration response to impulsive blast noise were conducted for a number of buildings at three military installations.

- Field modal testing was conducted for a number of buildings at three military installations.

- Structural response to impulsive loads was assessed and transfer functions were determined for critical structural elements.

- Damage model from blast loading was formulated for different structural types and materials.

- Prediction model and guidelines for probability of damage or rattle of structural elements were developed.

The following overall conclusions have been drawn as the result of the study:

- For air and surface impulsive military sources of interest in this project, airborne sound propagation is dominant compared to seismic groundborne propagation.

- Generally, many modal responses of the building are excited from the impulsive noise load. For typical residential structures, the main global response of interest to impulsive loads is a combination of movements with respect to the building axes, i.e. side sway (lateral) motions parallel to the width and length, and twisting (torsional motions) of the building in plan. These three deflection movements and their combinations determine predominant frequency response (resonant frequencies) of the building. Actual distribution of lateral and torsional stiffnesses throughout the building determine individual variations of the deflection shapes and resonant frequencies of the building global response in the typical range from 7 to 15 Hz.

- Local response of individual structural elements (walls, windows, etc.) is typically characterized by resonant frequencies in the range from 15 to 50 Hz. These local responses may not depend on the global building response, for example - if the window pane itself responds at a higher frequency than the building structure or walls. Higher modal responses of the walls are more likely to interact with the window than global building modal responses.

- The Frequency Response Function (Transfer Function) describing structural vibration response of a building element to acoustic excitation is an attribute of the specific construction and is independent of the type of acoustic load (artillery firing, ordnance disposal, steady transportation noise, etc.). It is determined primarily by the resonant frequencies and damping properties of the structure itself.

- An interactive computer model for the prediction of SDOF vibration response of structures to blast and sonic boom loads was developed.

- The probability of structural damage from blast loading depends on the nominal value and statistical variation of three basic parameters: the effective blast pressure loading on a structure, the vibration and corresponding stress response to this loading, and the thresholds for damaging or material failure stress to such loading. The prediction of potential structural damage from blasts can be defined by a statistical Probability of Damage (POD) function. POD is determined in terms of the statistical distribution of the Factor of Safety (FOS), which is the ratio of the load capacity of the structure in terms of its failure stress to the stress imposed by the blast loading. Structural damage is presumed to occur whenever the FOS is equal to or less than 1.

A procedure for computing POD was developed, consisting of easily applied formulae and material/structural data. The prediction model and updated noise and damage criteria are intended to assist in development of improvements to the DoD planning guidelines for structural damage and community impact from impulsive military activities at DoD installations.

5.0 Conclusions and Implications for Future Research/Implementation

A study has been conducted on the effect of impulsive noise on structures. The study addressed propagation of blast noise from the source to the receiver, the structural response of buildings, and the probability of damage. Field measurements of impulsive airborne and groundborne noise propagation and structural vibration response were conducted at three military installations. Field modal testing was conducted for a number of buildings at each installation.

5.1   Conclusions and Damage Model

For the air and surface impulsive military sources of interest in this project, it was found that airborne sound propagation dominates relative to seismic groundborne propagation. This is consistent with other quantitative studies, and counters the common belief among the public that impulsive noise propagates through the ground. The SIPS model is recommended for calculation of airborne propagation. Alternatively, nominal propagation may be computed via standard distance and explosive weight formulae, which are included in this report.

Impulsive noise loads generally excite many response modes of a building. For typical residential structures, the main global response of interest to impulsive loads is a combination of movements with respect to the building axes, i.e. side sway (lateral) motions parallel to the width and length, and twisting (torsional motions) of the building in plan. These three deflection movements and their combinations determine predominant frequency response (resonant frequencies) of the building. The distribution of lateral and torsional stiffnesses throughout the building determines individual variations of the deflection shapes. Resonant frequencies of building global response were found to be typically in the range from 7 to 15 Hz. Local response of individual structural elements (walls, windows, etc.) is typically characterized by resonant frequencies in the range from 15 to 50 Hz. These local responses may not depend on the global building response. For example, a window pane itself may respond at a higher frequency than the building structure or walls, and its relation to the containing wall may be primarily through the edge boundary conditions at its perimeter. Higher frequency modal responses of the walls are more likely to interact with the window than would global building modal responses.

The Frequency Response Function (Transfer Function) describing structural vibration response of a building element to acoustic excitation is an attribute of the specific construction and is independent of the type of acoustic load (artillery firing, ordnance disposal, steady transportation noise, etc.). It is determined primarily by the resonant frequencies and damping properties of the structure itself.

An interactive computer model for the prediction of single degree of freedom (SDOF) vibration response of structures to blast and sonic boom loads was developed.

The probability of damage from impulsive noise was found to depend on higher order modes, not just the lumped SDOF mode. A probability of damage (POD) model was developed that accounts for the stress associated with those loads.

POD depends on the nominal value and statistical variation of three basic parameters: the effective blast pressure loading on a structure, the vibration and corresponding stress response to this loading, and the thresholds for damaging or material failure stress to such loading. POD is determined in terms of the statistical distribution of the Factor of Safety (FOS), which is the ratio of the load capacity of the structure in terms of its failure stress to the stress imposed by the blast loading. Structural damage would occur whenever the FOS is equal to or less than 1.

A procedure for computing POD was developed, consisting of easily applied formulae and material/structural data. The procedure is described in Section 4.7, with step-by-step instructions presented in 4.7.2.7.2. Section 4.8 presents sample calculations, with charts of POD for a variety of structures as a function of distance and explosive size (Equivalent TNT weight). The following tables present example values for three distances, three explosive sizes, and four structure types. The four structure types are adobe walls, frame walls with gypsum board interior, and two qualities of glass. "Old" glass is presumed to have half the strength of new glass. Both window types are 200 square inches, aspect ratio of 0.75. These example values are for propagation over hard ground, with the structure facing the blast. Peak pressure, P_0, is free field, prior to doubling at the facing surface.

Table 5-1. POD (Percent), 10 Pounds Equivalent TNT Weight

Distance, ft	P_0, psi	Adobe	Frame	New glass	Old glass
500	.0975	.3387	.3699	.0001	.0299
1000	.0386	.0051	<.0001	<.0001	<.0001
2000	.0159	<.0001	<.0001	<.0001	<.0001

Table 5-2. POD (Percent), 100 Pounds Equivalent TNT Weight

Distance, ft	P_0, psi	Adobe	Frame	New glass	Old glass
500	.284	26.701	92.09	.317	7.466
1000	.108	2.486	8.285	.0004	.0718
2000	.0426	.0646	.0102	<.0001	<.0001

Table 5-3. POD (Percent), 1000 Pounds Equivalent TNT Weight

Distance, ft	P_0, psi	Adobe	Frame	New glass	Old glass
500	.868	92.929	>99.0	22.55	70.38
1000	.316	47.521	97.95	.5137	9.515
2000	.120	6.791	23.28	.0015	.1562

While the probabilities are not linear, there is a clear relation between distance and charge size, so that Tables 5-1 through 5-3 provide quick guidance for planning for the most common structures of concern. For the distances shown, up to 2000 feet, atmospheric refraction effects tend to be small and the nominal blast pressure calculation is reasonable. At longer distances - particularly beyond a few thousand feet - refraction effects should be taken into account via SIPS or similar calculations. It is worth noting that the closest structures at the three facilities visited - Aberdeen, Ft. Sill and McAlester - were around 1500, 10,000 and 15,000 feet, respectively.

Table 5-4 summarizes community noise thresholds used by DoD for land use planning.[86] The low risk threshold of 115 dB corresponds to 0.0016 psi. The high risk range of 130 dB to 140 dB corresponds to 0.0092 psi to 0.075 psi. Structural damage is thus expected to be rare at blast

levels that are acceptable on the basis of community annoyance. Damage probabilities are not zero, and cannot be discounted, but are sufficiently low that guidelines for community exposure remain dominated by the risk of complaints.

Table 5-4. Thresholds for Community Response to Impulsive Noise Levels

Predicted Sound Level, PK	Risk of Complaints	Action
< 115	Low risk of noise complaints.	Fire all programs
115 – 130	Moderate risk of noise complaints	Fire important tests. Postpone non-critical testing, if feasible.
130 – 140	High risk of noise complaints, possibility of damage.	Only extremely important tests should be fired.

5.2   Implications for Future Research and Implementation

This study has identified the characteristics of structural response and damage associated with military impulsive noise sources. The levels at which the probability of damage is significant are generally above those at which there is a high risk of noise complaints from the community. Occasional damage can occur, even if not common, and there are incidents where blast levels can be high enough to cause damage to structures. Two recommendations are made:

1. The POD model presented in this study should be validated by comparison with actual damaging explosion incidents. Two candidate incidents are the 1996 accidental explosion at Wyle's Huntsville, Alabama, facility[41] and the 1998 PEPCON explosion in Henderson, Nevada.[87]

2. Following validation, the POD model should be integrated into DoD range planning tools such as the Range Manager's Tool Kit (RMTK).[88]

Intentionally left blank

Literature Cited

1. Czech, J.J., Bradley, K.A., Noise and Vibration Study of Explosive Ordnance Disposal Activity at Naval Weapons Station Charleston, SC," Wyle Research Report WR 99-06, May 1999.

2. Downing, M., Plotkin, K., and Schomer, P, "Study Report on the Sound Intensity Prediction System (SIPS) for Application at Sierra Army Depot," Wyle Research Report WR 99-36, 1999.

3. Embleton, T.F.W., "Tutorial on sound propagation outdoors," *J. Acoust. Soc. Am*, Vol 100, pp 31-48, 1996.

4. White, M.J., "BNOISE2 Enhancements," ARA Project 0119, Applied Research Associates, Inc., January 2002.

5. Raspet, R., Lee, S.W., Kuester, E., Chang, D.C., Richards, W.F., Gilbert, R., and Bong, N., "A fast field program for sound propagation in the a layered atmosphere above an impedance ground," *J. Acoust. Soc. Am.*, Vol 77, 345-352, 1985.

6. Myers, M.K., and McAninch, G.L., "Parabolic approximation for sound propagation in the atmosphere," *AIAA Journal*, Vol 16, 836-842, August 1978.

7. Plotkin, K.J., and Grandi, F., "Computer Models for Sonic Boom Analysis: PCBoom4, CABoom, BooMap, CORBoom," Wyle Research Report WR 02-11, June 2002.

8. Kordich, M.M., and Pollet, D.A., "Sound Intensity Prediction System (SIPS): Volume 1 - Reference Manual," NSWCDD/TR-97/144, December 1997.

9. Dietenberger, M.A., Luers, J.K., and Smith, J.A., "Technical Reference Guide for Noise Assessment and Prediction System (NAPS)," UDR-TR-91-87, University of Dayton, Dayton, OH, September 1991.

10. Pater, L.L, "Far Field Overpressures from TNT Explosions: A Survey of Available Models," NSWC TR 81-132, NSWCDD, Dahlgren, VA, April 1981.

11. Sutherland, L.C., "Sonic and Vibration Environments for Ground Facilities - A Design Manual," Wyle Laboratories Research Staff Report WR 68-2, March 1968. Chapter 6: Source Characteristics.

12. Brode, H.L., "Numerical solutions of spherical blast waves," *Journal of Applied Physics*, No. 6, June 1955.

13. Lam, N., Mendis, P., and Ngo, T., "Response Spectrum Solutions for Blast Loading," *Electronic Journal of Structural Engineering*, Vol 4, pp28-44, 2004.

14. Blokhintzev, D.I., "The Propagation of Sound in an Inhomogeneous and Moving Medium I". *J.Acoust.Soc.Am.*, Vol 18, 322-328.

15. Sahl, Ibn, *On Burning Mirrors and Lenses*, Baghdad, 986.

16. "Digital Terrain Elevation Data (DTED) Level 1 Coverage, Edition 3," The National Imagery and Mapping Agency, Fairfax, VA, 20 July 1995.

17. Plotkin, K.J., McLaughlin, D.K., Morris, P.J., Sparrow, V.W., and McInerny, S.A., "Advanced Acoustic Models for Military Aircraft Noise Propagation and Impact Assessment," Wyle Report WR 10-17, August 2010.

18. Chan, P.C., "Field Validation of OBOD Noise Abatement Using Model Predictions," presented at Global Demilitarization Symposium and Exhibition, Coer d'Alene, Idaho, May 1998.

19. Plotkin, K.J., Hobbs, C.H., and Bradley, K.A., "Evaluation of the lateral Attenuation of Aircraft Noise," Wyle Research Report WR 99-10, July 1999.

20. Sharman, R., Liu, Y,. and Clough, C.A., "Application of a coupled meteorological forecast and sound propagation model to forecast blast noise at the Aberdeen Test Center," 11th Conference on Aviation, Range and Aerospace, October 2004.

21. Okrasinski, R., and Dennis, S, "Evaluation of the Noise Assessment and Prediction System Used at Aberdeen Proving Ground," ARL-CR-204, September 1995.

22. Plotkin, K.J., Ikelheimer, B., and Huber, J., "The effects of Atmospheric Gradients on Airport Noise Contours," Wyle Report WR 02-26, September 2003.

23. Calderone, J.J. and Garbin, H.D., "Demolition Range Noise Abatement Technique Demonstration and Evaluation for the McAlester Army Ammunition Plant," Sandia Report SAND2001-2267, August 2001.

24. Greenfield, R.J., and Moran, M.L., "Low Frequency Signals From Moving Vehicles," 2002 Meeting of the MSS Specialty Group on Battlefield Acoustic and Seismic Sensing, Magnetic and Electric Field Sensors, September 2002.

25. Anderson, T.S, Ketcham, S.A., Lacombe, J., and Moran, M.L., "Validation of FDTD Seismic Signatures From Moving Ground Vehicles," 2002 Meeting of the MSS Specialty Group on Battlefield Acoustic and Seismic Sensing, Magnetic and Electric Field Sensors, September 2002.

26. Wilson, D. K., G. L. Szeto, B. H. VanAartsen, and J. M. Noble, 2000: A prototype acoustic battlefield decision aid with interfaces to meteorological data sources and a target database," 2000 Meeting of the MSS Specialty Group on Battlefield Acoustic and Seismic Sensing, 2000.

27. Wilson, D.K., Moran, M.L., and Anderson, T.S., "Development of a Combined Acoustic/Seismic Tactical Decision Aid", 2002 Meeting of the MSS Specialty Group on Battlefield Acoustic and Seismic Sensing, Magnetic and Electric Field Sensors, September 2002.

28. Chien, C.F., and Soroka, W.W., "Sound Propagation Along an Impedance Plane," *J. Sound Vib.*, Vol 43, 9-20, 1975.

29. Chessel, C.I., "Noise propagation along an impedance boundary," *J. Acoust. Soc. Am.*, Vol 62, 825-834, 1977.

30. Delany, M.E., and Bazley, E.N.," Applied Acoustics, 3, 105-115, 1970.

31. Sabatier, J.M., Bass, H.E., and Bolen, L.N., "The interaction of airborne sound with porous ground: The theoretical formulation," *J. Acoust. Soc. Am*, Vol 79, 1345-1352, May 1986.

32. Attenborough, K., Sabatier, J.M., Bass, H.E., and Bolen, L.N., "The acoustic transfer function at the surface of a layered poroelastic soil," J. *Acoust. Soc. Am*, Vol 79, 1353-1358, May 1986.

33. Sabatier, J.M., Bass, H.E., Bolen, L.N., and Attenborough, K., "Acoustically induced seismic waves," *J. Acoust. Soc. Am*, Vol 80, 646-649, August 1986.

34. Sabatier, J.M., Bass, H.E., and Elliott, G.R., "On the location of frequencies of maximum acoustic-to-seismic coupling," *J. Acoust. Soc. Am*, Vol 80, 1200-1202, October 1986.

35. Albert, D.G., and Orcutt, J.A., "Observations of low-frequency acoustic-to-seismic coupling in the summer and winter," *J. Acoust. Soc. Am.*, Vol 86, 352-359, July 1989.

36. Van Moorhem, W.K., Reaveley, L., and Decker, R., "Open Burn/Open Detonation Risk Assessment Ground Motion and Related Effects," Center for Environmental Technologies, University of Utah, Salt Lake City, Utah, December 3, 1996.

37. Plotkin, K.J., "Test Plan for Impulsive Noise and Structural Response Measurements," Wyle Technical Note TN 05-01, April 2005.

38. Sutherland, L.C., Brown, R. and Goerner, D., "Evaluation of Potential Damage to Unconventional Structures by Sonic Booms", Report HSD-TR-90-021, by Wyle Laboratories for Brooks Air Force Base, TX, April 1990.

39. Sutherland, L.C., "Analytical background for Evaluation of Acoustically-Induced Vibration of Structures from Artillery or Ordinance Blasts", Consulting Report 2005-1 for Wyle Laboratories, Arlington, VA, September 2005.

40. *01dB-Stell, dBFA32 V. 4.4 Frequency Analysis Software Suite, User Manual*, MVI Technologies Group, France, 2002.

41. Sutherland, L.C., "Probability of Damage to, or Rattle of, Building Components From Military Impulsive Noise Sources," Consulting Report 2007-1R for Wyle Laboratories, Arlington, VA, March 2009.

42. Chiarito, Vincent P. and Hall, Robert, "Investigation of Damage to Structures in the McCuthanville-Daylight Area of Southwestern Indiana, Part VII: Experimental and Finite Element Studies of the Vibration Response of Residential Structures Due to Surface Mine Blasting," Office of Surface Mining Reclamation and Enforcement Technical Report, Vol.3., 1984.

43. Crowson, Roger D., "The Role of Forced Vibration Tests in Structural Dynamics," M.S. Thesis, Mississippi State University, Mississippi State, MS, 1978.

44. Ewins, D. J., *Modal Testing: Theory and Practice*, John Wiley & Sons, Inc, 1984.

45. Bendat, Julius S., and Piersol, Allan G., *Engineering Applications of Correlation and Spectral Analysis*, Wiley-Interscience, New York, NY, 1993.

46. Clough, Ray W., and Penzien, Joseph *Dynamics of Structures*, McGraw-Hill, New York, NY, 1975.

47. Halvorsen, William G., and Brown, David L., "Impulse Technique for Structural Frequency Response Testing," *Sound and Vibration*, November 1977, pp.8-21.

48. Hewlett Packard. (1986). "The Fundamentals of Modal Testing," Application Note 243, Palo Alto, CA.

49. Richardson, Mark, and Schwarz, Brian (2003). "Modal Parameter Estimation from Operating Data," *Sound and Vibration*, Vol. 37, No.1, pp.28-36.

50. Batel, Mehdi (2002). "Operational Modal Analysis – Another Way of Doing Modal Testing," *Sound and Vibration*, Vol. 36, No.8, pp.22-27.

51. Thompson, W.T., *Vibration Theory and Applications*, Prentice Hall, NJ, 1965.

52. Plotkin, K.J., Sizov, N.V., and Morgenstern, J.M., "Examination of Sonic Boom Minimization Experienced Indoors," AIAA Paper 2008-0057, January 2008.

53. American National Standards Institute, "Estimating Air Blast Characteristics from Single Point Explosions in Air, with a Guide to Evaluation of Atmospheric Propagation Effects," ANSI S2.20, 1997.

54. Raspet, R., and Bobak, M.T., "Procedure for Estimating the Flat-Weighted Peak Level Produced by Surface Mining Buried Charges," USA-CERL Technical Report N-88/07, 1988

55. Schomer, P.D. and Luz, G.A., "A Refined Statistical Analysis of Blast Sound Propagation", Noise Control Eng. J. , Vol. 42, May-Jun, (1994).

56. Schomer, P.D. "A Statistical Description of Blast Sound Propagation", Noise Control Eng. J. , Vol. 49, Mar-Apr, (2001).

57. Schomer, P.D., "A Statistical Description of Ground-to-Ground Sound Propagation", Noise Control Eng. J. , Vol. 51, Mar-Apr, (2003).

58. Schomer, P.D. and White, M.J., "A Statistical Description of Sound Propagation: A Comparison of Elevated and Near-ground Sources", Noise Control Eng. J. , Vol. 54, May-Jun, (2006).

59. Muller, G.G., Block, R., and Davis, T.E. "The Diffraction Produced by Cylindrical and Cubical Obstacles and by Circular and Square Plates", *J. Acoust. Soc. Am.* **10**, 6-13, (1938).

60. Boukamp, C.J., "Diffraction Theory", *Rpts. Prog. Phys.* **17**, 35-100, (1954).

61. Sutherland, L.C., Chan, G., and Andriulli, J. "Experimental Tests on the Response of Industrial and Residential Structures to Acoustic Excitation", Wyle Laboratories Report WR-68-2A, March, (1968).

62. Plotkin, K.J., Gurovich, Y., Bell, D., James, M. and Chiarito, V., "Prediction Model for Impulsive Noise on Structures, 2005 Annual Report", Wyle Report WR 06-06 prepared for SERDP/ESTCP, March 2006.

63. Hunt, F.V., "Stress and Strain Limits on the Attainable Velocity in Mechanical Vibration," *J. Acoust. Soc. Am.*, **32**, 1123-1128, 1960.

64. Smith, P.R., "Effects of 0.9 psi Overpressure on the McDonald House Walls," Letter report submitted to Kaman Tempo, New Mexico, Jan. 1986.

65. Pierce, A.D., *Acoustics, an Introduction to its Physical Principles and Applications,* McGraw-Hill Book Co., New York, 1981.

66. Sutherland, L.C., "Assessment of Potential Structural Damage from Low Altitude Subsonic Aircraft," Wyle Research Report WR 89-16(R), June 1990.

67. Stagg, M.S. et al, "Effects of Repeated Blasting on a Wood-Frame House," U.S. Dept. of the Interior, Bureau of Mines Report of Investigations RI-8896, 1984.

68. Haber, J.M., and Nakaki, D., "Sonic Boom Damage to Conventional Structures," HSD TR 89-001, February 1989.

69. Siskind, D. E. et al. "Structure Response and Damage Produced by Air Blast from Surface Mining", U.S. Dept. of the Interior Bureau of Mines Report of Investigations RI-8485, 1980.

70. Siskind, D.E., Stachura, V.J., and Radcliffe, K.S., 1976, "Noise and Vibrations in Residential Structures from Quarry Production Blasting", Bureau of Mines Report of Investigations, RI 8168, 1976.

71. Hershey, R.L. and Higgins, T.H. "Statistical Model of Sonic Boom Structural Damage", FAA-RD-76-87, 1976.

72. Eldred, K. McK., "Noise and Vibration Characteristics of the CERL Low Frequency Blast Pressure Facility Test House," KEE Report 85-29 for U.S. Army Construction Engineering Research Laboratory, 1985.

73. Eshbach, O.W. (ed), "Handbook of Engineering Fundamentals," Second Edition, Wiley Engineering, John Wiley and Sons, Inc., New York, 1952.

74. Beason, W.L. and Morgan, J.R., "Glass Failure Prediction Model," *J. Structural Engineering*, **110**: 197-212, February 1984.

75. McClellan, G.W., and Shand, E.B., "Glass Engineering Handbook," Third Edition, McGraw-Hill, New York, 1984.

76. Bramaimah, A., "Blast Effects on Structures," Canadian Explosives Research Laboratory, Ottawa, Canada, www.schulich.ucalgary.ca/Civil/csce_calgary/ Lecture2a-BlastEffects-on-Structures.pdf.

77. Naval Facilities Engineering Command, "Blast Resistant Structures," Design Manual 2.01, December 1986.

78. White, R.W., "Effects of Repetitive Sonic Boom Loads on Glass Breakage," Wyle Laboratories Report WR 72-4, 1972.

79. Haber, J.M., "Cumulative Damage to Window Panes," AFRL-HE-TR-2001-0093, 1998.

80. Haber, J.M., "Cumulative Sonic Boom Damage to Plaster," AIAA 93-4446, Octover 1993.

81. Smith, E.W., "Adobe Bricks in New Mexico," NM Bureau of Mines and Mineral Resources, 1982.

82. Sutherland, L.C., and Plotkin, K.J., "Feasibility Study of Potential Damage to Adobe Structures from Sonic Booms," Wyle Laboratories Technical Note TN 93-2, Prepared for BBN Systems and Technologies, 1993.

83. Abramowitz, M. and Stegun, I.A. (Eds.), *Handbook of Mathematical Functions with Formulas, Graphs, and Mathematical Tables*, National Bureau of Standards, Applied Mathematics Series 55, December 1972.

84. Clarkson, B.L. and Mayes, W.H., "Sonic-boom Induced Building Structure Responses Including Damage", *J. Acoust. Soc. Am.* **51**, 742-757, 1972.

85. Sutherland, L.C. and Czech, J., "Evaluation of Human Response to Structural Vibration Induced by Sonic Booms", NASA Contractor Report 189584, May 1992.

86. Pater, L., "Noise Abatement Program for Explosive Operations at NSWC/DL," Presented at the 17th Explosives Safety Seminar of the DOD Explosives Safety Board (Denver, CO, 1976).

87. Reed, J.W. and Zehrt, W.H. "Community Damages from the PEPCON Explosion", June (1998).

88. Swearingen, M.E., "The Range Managers Toolkit (RMTK) Noise Tool," ERDC/CERL TR 06-15, June 2006.

Intentionally left blank

Appendix A

Publications

Intentionally left blank

Publications

Plotkin, K.J., "Test Plan for Impulsive Noise and Structural Response Measurements," Wyle Technical Note TN 05-01, April 2005.

Plotkin, K.J., "Prediction Model for Impulsive Noise on Structures, 2004 Annual Report," Wyle Report WR 05-24 prepared for SERDP/ESTCP, October 2005.

Plotkin, K.J., Gurovich, Y., Bell, D., James, M. and Chiarito, V., "Prediction Model for Impulsive Noise on Structures, 2005 Annual Report," Wyle Report WR 06-06 prepared for SERDP/ESTCP, March 2006.

Sizov, N.V., Yuriy A. Gurovich, Y.A., and Plotkin, K.J., "Measured vibration response characteristics of building elements subjected to impulsive noise," Noise-Con 2007, Reno, NV, October 2007.

Plotkin, K.J., Sizov, N.V., and Morgenstern, J.M., "Examination of Sonic Boom Minimization Experienced Indoors," AIAA Paper 2008-0057, January 2008.

Intentionally left blank

Appendix B

Building Sensor Set Up Information

Intentionally left blank

**Table B-1. APG Building 2001: Measurement Set Up for
Gun Firings on 9 November 2004**

(x, y or z denotes the building axis; "+" or "-" denotes polarity of the sensor axis relative to the
building axis indicated for the location)

Channel	Sensor Model	Serial No.	Sensitivity	Units	Gain	Location
01	PCB393C	740	0.8897	V/g	5.0	1-x, SE corner, 6ft above ground floor
02	PCB393C	748	0.8865	V/g	1.0[a] 5.0[b]	2-x, midpoint of E side, on 2nd floor stair landing
03	PCB393C	738	0.8658	V/g	5.0	2+y, "
04	PCB393C	726	0.8945	V/g	5.0	1+y, SE corner, 6ft above ground floor
05	PCB393C	739	0.8525	V/g	5.0	3+x, midpoint of W side, on 2nd floor
06	PCB393C	728	0.8961	V/g	5.0	3-y, midpoint of W side, on 2nd floor
07	PCB393C	737	0.9217	V/g	5.0	5-x, E-¼-point of S side above 2nd floor at ceiling height
08	PCB393C	744	0.8621	V/g	5.0	4+x, midpoint of W side above 2nd floor at ceiling height
09	PCB393C	747	0.8842	V/g	5.0	6-x, near SW corner (on E side of door opening) on ground floor
10	PCB393C	741	0.8696	V/g	5.0	6+y, "
11	PCB393C	749	0.8913	V/g	5.0	6+z, "
12	PCB356B18[c]	12444	0.9960	V/g	5.0	7-x, SW corner above ground floor above ceiling height, just below 2nd floor level.
13	PCB356B18[c]	12444	1.005	V/g	10.0	7+y, "
14	PCB356B18[c]	12444	1.041	V/g	10.0	7+z, "
15[b]	PCB393A03	9303	1.0	V/g	1.0	T-x, midpoint of hallway on 2nd floor (near geometric center of plan of 2nd floor)
16[b]	PCB393A03	9301	1.0	V/g	1.0	T+y, "

Notes:

        (a) 9:00 - 13:00.

        (b) 14:00 - 19:00.

        (c) Tri-axial accelerometer.

**Table B-2. APG Building 2001: Measurement Set Up for Gun Firings
on 10 November 2004 and Modal Testing**
(x, y or z denotes the building axis; "+" or "-" denotes polarity of the sensor axis relative to the building axis
indicated for the location)

Channel	Sensor Model	Serial No.	Sensitivity	Units	Gain	Location
01	PCB393C	740	0.8897	V/g	5.0	1-x, SE corner, 6ft above ground floor
02	PCB393C	748	0.8865	V/g	5.0[a] 1.0[b]	2-x, midpoint of E side, on 2nd floor stair landing
03	PCB393C	738	0.8658	V/g	5.0	2+y, "
04	PCB393C	726	0.8945	V/g	5.0	1+y, SE corner, 6ft above ground floor
05	PCB393C	739	0.8525	V/g	5.0	3+x, midpoint of W side, on 2nd floor
06	PCB393C	728	0.8961	V/g	5.0	3-y, midpoint of W side, on 2nd floor
07	PCB393C	737	0.9217	V/g	5.0	5-x, E-¼-point of S side above 2nd floor at ceiling height
08	PCB393C	744	0.8621	V/g	5.0	4+x, midpoint of W side above 2nd floor at ceiling height
09[c]	PCB393C	747	0.8842	V/g	5.0	6-x, near SW corner (on E side of door opening) on ground floor
10[d]	PCB393C	741	0.8696	V/g	5.0	6+y, "
11[e]	PCB393C	749	0.8913	V/g	5.0	6+z, "
12	PCB356B18[f]	12444	0.9960	V/g	5.0	7-x, SW corner above ground floor above ceiling height, just below 2nd floor level.
13[d] or 10[g]	PCB356B18[f]	12444	1.005	V/g	10.0	7+y, "
14[d] or 11[g]	PCB356B18[f]	12444	1.041	V/g	10.0	7+z, "
15[h]	PCB356B18[f], z-axis	12409	1.0	V/g		z, mounted on shaker, 2nd floor (landing at top of stairs on E side)
16[i]	Tektronix CFG280signal generator	280TW51704	1.0	V/g	1.0	NA

Notes:
(a) For gun firings only.
(b) For shaker tests only.
(c) For gun firings from 10:00 to 12:00 and shaker tests; otherwise - open channel.
(d) For gun firings from 10:00 to 12:00 and shaker tests.
(e) For gun firings from 10:00 to 12:00; for shaker tests - open channel
(f) Tri-axial accelerometer.
(g) For gun firings from 13:00 to 14:00.
(h) For gun firings from 13:00 to 14:00 and shaker tests; otherwise - open channel.
(i) For shaker tests; otherwise - open channel.

**Table B-3. APG Building 2006: Measurement Set Up for Shaker and
Impact Hammer Tests**

(All gains are 1.0; x, y or z denotes the sensor component measured; "+" or "-" denotes polarity of the sensor axis
relative to the building axis indicated for the location)

Channel	Sensor Model	Serial No.	Sensitivity	Units	Location
01[a]	PCB356B18[b]	12409, z	0972	V/g	In direction of shaker
04	PCB393C	739	0.8525	V/g	3-x, shaker location
05	PCB393C	733	0.8850	V/g	3+z, shaker location
06	PCB356B18[b]	12598, x	0.9880	V/g	1-x, SE corner, ceiling height
07	PCB356B18[b]	12598, y	0.9510	V/g	1+y, SE corner, ceiling height
08	PCB393C	744	0.8621	V/g	4+x, near SW corner, ceiling height
09	PCB393C	741	0.8696	V/g	4+y, near SW corner, ceiling height
10	PCB356B18[b]	12412, x	0.9470	V/g	2+x, NE corner, ceiling height
11	PCB356B18[b]	12412, y	0.9780	V/g	2-y, NE corner, ceiling height
12	PCB356B18[b]	12444, x	0.9960	V/g	5-x, S midpoint, ceiling height
13[a]	OROS Signal Generator			V	
14	PCB393C	747	0.8842	V/g	3-y or 3-x, shaker location
15	PCB356B18[b]	12598, z	0.931	V/g	1+z, SE corner, ceiling height
16[c]	PCB Sledge GK291B50		1.0	mV/lb	Roving hammer (impact locations are shown in Figure 5.32

Notes:
   (a) For shaker tests only.
   (b) Tri-axial accelerometer.
   (c) For impact hammer tests only.

Table B-4. APG Building 379: Measurement Set Up for Gun Firings on 10 November 2004
(x, y or z denotes the building axis; "+" or "-" denotes polarity of the sensor axis relative to the building axis indicated for the location)

Sony SN - Channel	Sensor Model	Serial No.	Sensiti-vity	Units	Gain	Location
U2551 - 01	-	-	-	-	-	Not used
- 02	PCB3701G3FA3G	1261		V/g	1.0	Front window glass
- 03	PCB356A27, z-axis	21464	50 (nom.)	mV/g	1.0	Front window sill vertical, + z
- 04	PCB356A27, x-axis	21464	50 (nom.)	mV/g	1.0	Front window sill, horizontal, +x
U2545 - 01	PCB393A03	9301	1.0	V/g	1.0	2nd floor, conference room
- 02	PCB393A03	9303	1.0	V/g	1.0	2nd floor, conference room
- 03	PCB356B18	12412	1.0	V/g	10.0	2nd floor, under front window, +x
- 04	PCB356B18	12598	1.0	V/g	10.0	2nd floor, under front window, +y

Appendix C

Single Degree of Freedom Blast and Sonic Boom Response Program

Intentionally left blank

The SDOF vibration response model described in Section 4.7.1 has been implemented in Program SDOF. No special installation is necessary: just copy it into a working directory. It is run from the command line by typing

sdof case.sig

where "case.sig" is a definition of an impulsive noise signature. This can define a boom or a blast wave. For a boom, the contents are:

- Number of points
- t,p pairs - one pair to a line, enough lines to match number of points. Units are milliseconds and psf
- shock thickness parameter

For a blast wave, the contents are:

- 0
- P0 and T, psf and msec
- shock thickness parameter

The thickness parameter defines a Taylor shock structure with thickness inversely proportional to shock overpressure. The default value is 1. A value of 0 means no thickening. Values up to 2 or 3 are physically meaningful; higher values can be used for rhetorical purposes.

Shocks in an input boom signature are defined by places where successive values of t are the same. There must be some zero lead-in and lead-out before and after the signature. A blast wave has only one shock, and an appropriate lead-in is automatically generated.

If there is no command line argument, a default N-wave is built in. This has appropriate lead-in/out.

Figure C-1 is a screen shot of the program. There are two parts:

A graphical data display, as described in Section 4.7.1, with the following four plots:

- Upper left: original signature, Pa vs time (seconds)
- Bottom left: displacement response, mm vs time (seconds)
- Upper right: spectrum (psd, Pa**2/Hz) of the boom
- Lower right: spectrum (psd, mm**2/Hz) of the displacement

The plots contain annotation that is described in further detail in Section 4.7.1. Note that spectra are in dB relative to the maximum value. By default, the spectra appear in log-log coordinates (dB vs log frequency). The upper frequency range is five times f_0. The spectral plots can be switched to linear mode, where spectra will be shown in physical units. The frequency scales can also be toggled between logarithmic and linear.

The data plotted as a line in the signature plot is the signature sampled at 24000 samples/second. For sonic boom signatures circles are plotted, for reference, at the original input definition points.
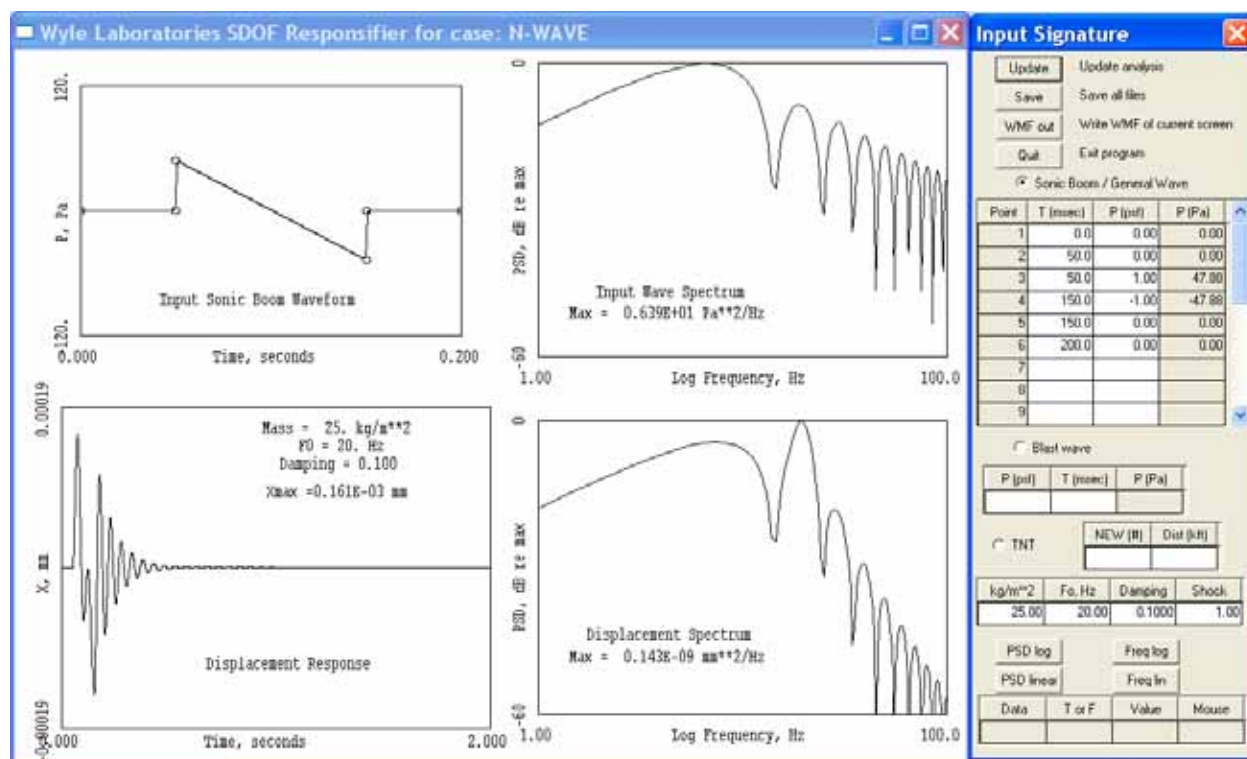

Figure C-1. Screen Shot of Program SDOF, Sonic Boom Case

A dialog windows appears to the right, with three tables and several buttons.

The top table lists the input sonic boom signature. This can be navigated with the cursor keys, and new or modified values entered. If the table is modified such that there are fewer values than original, delete the entries for the extra spaces.

The first column of the boom signature table is just an index, and is not editable. The last column is pressure in Pa, and is not editable: enter pressures in the psf column.

The second table consists of two parts, with radio buttons. The first part, if selected, allows definition of a blast wave via P_0 (psf) and T (msec). Pressure in Pa (not editble) is shown in a third column. The second part, when selected, allows definition of a blast wave via equivalent TNT weight (NEW, pounds) and distance (kilofeet).

The next table has the three structural parameters: surface weight, fundamental frequency and damping. It also has the shock thickness parameter. These can all be edited.

The "Update" button at the top causes the program to accept newly entered data. Pressing "enter" usually does the same as pressing the "Update" button.

Just below the structural parameter table are buttons to toggle the display, as noted above, and a display table for examining quantities in the graphs. If the mouse is clicked in one of the graphs, the graph name and the data values appear in the bottom table. The columns are:

- Data: name of the table you've clicked in
- T or F: time (seconds) or frequency (Hz)
- Value: the value of the data at the T or F. Units are whatever the graph shows
- Mouse: the value (in data units) of the mouse position when you clicked.

Clicking on the "Save" button near the top of the dialog writes the following five files:

- case.sig - the signature as defined in the table. Suitable for input.
- case.bpa - the boom at 24k. Binary file consisting of:
    – number of points (always 48000)
    – all time values, seconds
    – all P values, Pa
- case.xmm - the response time history. Binary file consisting of:
    – number of points (always 48000)
    – all time values, seconds
    – all X values, mm
- case.bsp - the power spectrum of the boom. Binary file consisting of:
    – number of frequencies (always 16384)
    – all frequencies, Hz
    – PSD, Pa**2/Hz
- case.xsp - the power spectrum of the response. Binary file consisting of:
    – number of frequencies (always 16384)
    – all frequencies, Hz
    – PSD, mm**2/Hz

The binary files are little-endian. Data count is 32 bit integer, the rest are real*4.

While the spectral files contain 16384 points, only the first 12800 are statistically meaningful.

Button "WMF out" writes a Windows Meta File image of the current screen display. This can be imported into most documents. Figure 4-48 was generated in that manner. Windows image previewer also appears to be able to display and print them, although there is no assurance that future versions of Windows will have that capability.

Both "Save" and "WMF out" bring up Windows dialogs for the file name. Defaults based on the input case are offered. There is an "Are you sure" query if you're about to overwrite an existing file.

Button "Quit" ends the program. You can also quit by clicking on the X in the main graphic screen, or by pressing ESC when the main graphic screen is active, i.e., it's the last thing you clicked on and its border is highlighted.